# Magnetic Resonance Imaging of Susceptibility Effects in Carotid Atherosclerosis

Pascal Peter Richard Ruetten

Fitzwilliam College

This dissertation is submitted for the degree of Doctor of Philosophy

Department of Radiology

University of Cambridge

January 2020

# Declaration

This thesis is the result of my own work and includes nothing which is the outcome of work done in collaboration except as declared in the preface and specified in the text.

It is not substantially the same as any work that has already been submitted before for any degree or other qualification except as declared in the preface and specified in the text.

It does not exceed the prescribed word limit of 60000 words.

# Acknowledgements

I would like to express my deepest gratitude and appreciation to Dr Martin J Graves. His continuous support and encouragement have been invaluable to this project and I greatly appreciate the time he has taken to support me and the insights he has shared with me in many meetings and discussions.

I would like to thank Professor Fiona Gilbert and Professor Jonathan Gillard for their supervision. They have provided me with a stimulating research environment and shared their advice and their continuous support.

Dr Andrew Priest has shared his endless knowledge on MR physics and always supported me. The meetings and discussions we have had were always inspiring end encouraging.

I would also like to thank everyone else who had been involved in my study. I am very grateful to Dr Ammara Usman for her work to recruit patients for the clinical study and she and Professor Gillard obtained the funding and ethical approval for imaging patients before and after administration of the USPIO. I would like to thank Dr Jianmin Yuan for the interesting talks about MR physics, countless evening scanning volunteers and phantoms together, and also for his support with the sequence development. Dr Alison Cluroe has been invaluable to the project through her histopathological validations of our MRI results and going over the histopathological results with me. Finally, the MR study was conducted in the MRIS unit of Addenbrooke's hospital and I would like to thank all of the radiographers who gave up their time to help in conducting this study.

In addition, I would like to acknowledge my funding from the Medical Research Council (MRC)/Sackler Stipend. The project was supported by the Addenbrooke's Charitable Trust and the National Institute for Health Research [Cambridge Biomedical Research Centre (BRC) at the Cambridge University Hospitals NHS Foundation Trust]. The views expressed are those of the authors and not necessarily those of the NHS, the NIHR or the Department of Health and Social Care.

To Dr Jason Tarkin, Dr Matt Stovell I would like to express my gratitude for the interesting conversations and the insights I got into clinical practice, laboratory work, and MRI studies in different anatomies through the participation in their studies.

The department of Radiology has been a great place to work and I would like to express my gratitude to everyone in our department.

I would like to especially thank my parents Rita and Hans-Peter Ruetten. Words cannot express how grateful I am for your support. Without you none of this would have been possible.

# Summary

This thesis explores the use of susceptibility-weighted imaging (SWI) and quantitative susceptibility mapping (QSM), to characterize carotid artery plaques with and without the use of ultrasmall superparamagnetic iron oxide (USPIO) nanoparticle contrast agents. The overall hypothesis is that QSM can serve to differentiate carotid artery plaque features of different susceptibility and provide a positive contrast mechanism for imaging the uptake of USPIOs.

Chapter 1 describes the pathophysiology of carotid atherosclerosis. Vulnerable plaques, i.e. those at risk of rupture, can be characterized by the presence of a lipid rich necrotic core (LRNC), intraplaque haemorrhage (IPH), and inflammation. In addition, plaques may develop calcifications that may be protective of rupture. The chapter describes the established multi-contrast imaging protocols used for characterizing plaques. Furthermore, the use of USPIO-contrast agents to image inflammation is described.

Chapter 2 describes the physical principles of MR image generation including the sensitivity to magnetic susceptibility. The principles of $T_2^*$w imaging, and susceptibility weighted imaging (SWI) are explained.

Chapter 3 reviews the principles and post-processing steps involved in commonly used algorithms for QSM in terms of the underlying physical and mathematical principles which are then demonstrated in the form of numerical simulations.

Chapter 4 presents the application of SWI to a group of patients who underwent USPIO enhanced MRI on a 1.5T MRI system. Images were acquired prior to infusion and 48 hours post infusion. SWI and gradient echo phase images were used to depict the field inhomogeneities generated by diamagnetic and paramagnetic materials within the plaques, calcification and USPIO-uptake. These results were then compared to a conventional carotid multi-contrast protocol, which includes $R_2^*$-mapping and $T_2^*$w imaging, and, where available, CT and histology.

In chapter 5 QSM is performed in the carotid artery wall of a cohort of normal volunteers on a 1.5T MRI system. Unlike the brain, the neck contains fat which can cause severe errors in the field estimate, which propagate into the susceptibility map.

Therefore, QSM was combined with water-fat separation for application in the neck to correct for these artifacts. This correctly estimated a high fat-fraction in fatty tissue in the neck and allowed for a detailed depiction of the anatomy of healthy volunteers. The susceptibility value measured in fatty tissue agreed with literature values.

Chapter 6 applies QSM with water-fat separation to a subset of the patient group on a 1.5T MRI system. On pre-contrast scans QSM successfully identified calcification as diamagnetic tissue and the water-fat separation identified a lipid core. On the post-contrast susceptibility maps, USPIO-uptake was identified as hyperintense signal. This allows QSM to provide quantitative contrast in carotid imaging that can identify multiple features simultaneously and to simplify the imaging of USPIO-contrast. The results were confirmed using the multi-contrast carotid MRI protocol and, where available, histology and CT.

Chapter 7 discusses the limitations of the current studies and the potential future improvements of the current methodology in terms of MR acquisition, post-processing algorithms and MR protocols.

Future studies could serve to further evaluate the potential of QSM in carotid imaging and use it as a novel tool to quantify USPIO uptake in atherosclerotic carotid arteries.

# Publications & Conference Proceedings

1. **Ruetten PPR**, Gillard JH, Graves MJ. Introduction to Quantitative Susceptibility Mapping and Susceptibility Weighted Imaging. Br J Radiol. 2019;92(1101):20181016. doi:10.1259/bjr.20181016.
2. **Ruetten PPR**, Cluroe AD, Usman A, Priest AN, Gillard JH, Graves MJ. Simultaneous MRI water-fat separation and quantitative susceptibility mapping of carotid artery plaque pre- and post-ultrasmall superparamagnetic iron oxide-uptake. Magn Reson Med. 2020;84(2):686–697. doi:10.1002/mrm.28151.
3. Yuan J, Graves MJ, Patterson AJ, Priest AN, **Ruetten PPR**, Usman A, Gillard JH. The development and optimisation of 3D black-blood R2* mapping of the carotid artery wall. Magn Reson Imaging. 2017;44:104–110. doi:10.1016/j.mri.2017.08.006.
4. Yuan J, Patterson AJ, **Ruetten PPR**, Reid SA, Gillard JH, Graves MJ. A Comparison of Black-blood $T_2$ Mapping Sequences for Carotid Vessel Wall Imaging at 3T: An Assessment of Accuracy and Repeatability. Magn Reson Med Sci. 2019;18(1):29–35. doi:10.2463/mrms.mp.2017-0141.

## First author abstracts:

1. **Ruetten PPR**, et al. “Quantitative Susceptibility Mapping of the Carotid Artery Wall using IDEAL”. In: Proceedings of the 34th Annual Scientific Meeting of ESMRMB. ; 2017:20
2. Yuan J, Usman A, **Ruetten PPR**, et al. “Three-dimensional Quantitative Magnetic Resonance Imaging of Carotid Atherosclerotic Plaque”. In: Proceedings of the 34th Annual Scientific Meeting of ESMRMB. ; 2017:18
3. **Ruetten PPR**, et al. “Quantitative Susceptibility Mapping of the Carotid Artery Walls”. In: Proceedings of the MRC Symposium. ; 2017
4. Yuan J, Usman A, **Ruetten PPR**, et al. “Optimization of 3D black-blood multi-echo T2* weighted sequence in carotid artery”. In: Proceedings of the 25th Annual Meeting of ISMRM. ; 2017:2787

5. **Ruetten PPR**, et al. “Phase Corrected Bipolar Acquisition for Simultaneous Water-Fat Separation and Quantitative Susceptibility Mapping of the Carotid Artery Wall”. In: Proceedings of the 26th Annual Meeting of ISMRM. ; 2018: 2194
6. Yuan J, Wiesinger F, **Ruetten PPR**, et al. “Head and Neck Vascular Calcification Imaging using Zero Echo Time”. In: Proceedings of the 26th Annual Meeting of ISMRM. ; 2018:3467
7. **Ruetten PPR**, et al. “Simultaneous Water-Fat Separation and Quantitative Susceptibility Mapping of the Carotid Artery Wall: Sequence and Processing Considerations”. In: Proceedings of the 30th Annual International Conference SMRA. ; 2018:A52
8. **Ruetten PPR**, et al. “Calcification and USPIO detection in Carotid Artery Plaque using QSM and SWI”. In: Proceedings of the 27th Annual Meeting of ISMRM. ; 2019:2090
9. **Ruetten PPR**, et al. “Plaque feature analysis using a joint method of QSM and water-fat separation”. In: Proceedings of the 27th Annual Meeting of ISMRM. ; 2019:2091
10. **Ruetten PPR**, et al. “Identification of USPIO-uptake in calcified Atherosclerotic Plaques”. In: Proceedings of the 36th Annual Scientific Meeting of ESMRMB. ; 2019:S13.04

# Table of Contents

# Table of Figures

# Table of Tables

# Abbreviations

| | |
|---|---|
| 2D | Two-dimensional |
| 3D | Three-dimensional |
| AD | Alzheimer's Disease |
| ASSET | Array coil Spatial Sensitivity Encoding |
| BMT | Best Medical Therapy |
| BOLD | Blood oxygen level dependent |
| CAS | Carotid Artery Stenting |
| CE | Contrast Enhanced |
| CEA | Carotid Endarterectomy |
| CNR | Contrast to noise ratio |
| CT | Computed Tomography |
| CTA | Computed Tomography Angiography |
| DANTE | Delay Alternating with Nutation for Tailored Excitation |
| DCE | Dynamic Contrast Enhanced |
| DIR | Double Inversion Recovery |
| ECST | European Carotid Surgery Trial |
| FC | Fibrous Cap |
| fMRI | functional Magnetic Resonance Imaging |
| FSE | Fast Spin Echo |
| GBCA | Gadolinium Based Contrast Agents |
| GRASP | Gradient Echo Acquisition of Superparamagnetic Particles |
| GRE | Gradient Echo |

| | |
|---|---|
| ICA | Internal Carotid Artery |
| IDEAL | Iterative decomposition of water and fat with echo asymmetry and least- squares estimation |
| IOSB | Inflow Outflow Saturation Band |
| IPH | Intraplaque Haemorrhage |
| IRON | Inversion Recovery ON Resonance |
| LDL | low density lipoprotein |
| LDL-C | Low Density Lipoprotein Cholesterol |
| LBV | Laplacian Boundary Value |
| LRNC | Lipid Rich Necrotic Core |
| MEDI | Morphology Enabled Dipole Inversion |
| MRA | Magnetic Resonance Angiography |
| MRI | Magnetic Resonance Imaging |
| MS | Multiple Sclerosis |
| NASCET | North American Symptomatic Carotid Endarterectomy Trial |
| NO | Nitric Oxide |
| oxLDL | oxidized low-density lipoprotein |
| PD | Parkinson’s Disease |
| PDF | Projection onto Dipole Fields |
| PVE | Partial Volume Effect |
| QSM | Quantitative Susceptibility Mapping |
| SHARP | Sophisticated Harmonic Artifact Reduction for Phase Data |
| SNR | Signal to Noise Ratio |
| SWI | Susceptibility Weighted Imaging |
| RES | Reticuloendothelial system |

| | |
|---|---|
| SENSE | SENSitivity Encoding |
| SGM | Susceptibility Gradient Mapping |
| TKD | Truncated k-space Division |
| TOF | Time of Flight |
| USPIO | Ultrasmall Superparamagnetic Iron Oxide |
| VCAM | Vascular Cell Adhesion Molecules |
| VSMC | Vascular Smooth Muscle Cell |

# Chapter 1 Stroke and Atherosclerotic Disease

## 1.1 Carotid Artery Disease

Cardiovascular disease is the leading cause of death worldwide (1) and stroke in particular, which affects the vasculature of the brain, has a very high mortality rate and is a leading cause of long-term disability, which causes a significant amount of social expenditure (1,2). This explains the high interest in continually improving understanding of the disease for better diagnosis and medical treatments, which includes life-style changes, medication and surgical intervention.

The improvements in medical treatment and risk factor control has had the effect of reducing the incidence of stroke and associated deaths over the recent decades (1–6), which may be due to improved understanding of the disease. In particular, controlling certain risk factors, for example, through lipid lowering therapy, blood pressure control or smoking cessation have decreased stroke incidence and mortality rates over the past decades (4–6). While this shows the importance of medical research in this field, the incidence rates are nonetheless high and the long-term effects severe (1,2,6).

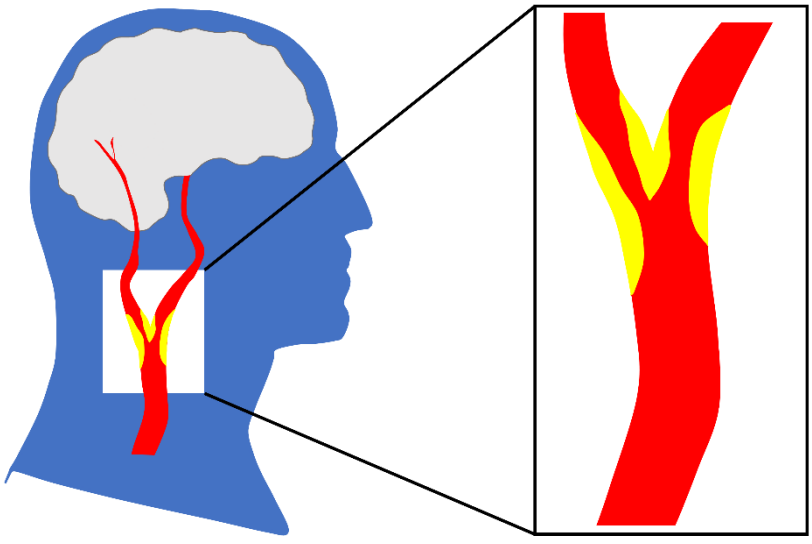

*Figure 1-1: Atherosclerotic plaque in the carotid bifurcation*

The most prevalent type of stroke is ischemic (~85%), while the remaining types of stroke are haemorrhagic (7). During an ischaemic stroke a thrombus (blood clot) or occlusion blocks the blood and nutrient supply to the brain. Of those a large part are caused by atherosclerotic carotid plaques, which are illustrated in Figure 1-1 (7). Atherosclerotic plaques typically grow more and more complex during the life of the patient, so that they may eventually rupture, which leads to the formation of a blood clot, which can cause the ischemic stroke. In spite of the decrease in incidence and mortality rates associated with stroke, there remain large areas for improvement in patient diagnosis: Currently, luminal narrowing (luminal stenosis) as diagnosed on Doppler Ultrasound is used clinically as a marker to identify patients at risk and decide on their treatment approach (8). Severe levels of stenosis have shown to be an important indicator of the risk of future events in patients who have shown stroke symptoms: Both the North American Symptomatic Carotid Endarterectomy Trial (NASCET) and European Carotid Surgery Trial (ECST) found that symptomatic patients with severe levels of stenosis had a great benefit in reduction of future events after carotid endarterectomy surgery (9,10). During this surgery, the carotid artery is opened so that the inner artery lining can be removed along with the plaque (8). As there is a perioperative risk associated with this procedure, it is important to carefully select the patients eligible for surgery to maximize the benefit to risk ratio of the surgery. However, the benefit of considering carotid stenosis as a sole risk factor in asymptomatic patients and those with mild to moderate levels of carotid stenosis remains questionable (9,11). Plaques may, for example, progress without occluding the lumen and expand outward, which is called positive remodelling (12,13). In vivo imaging of different patient groups and ex vivo analysis of excised carotid plaques have suggested that the presence of certain morphological features may render certain plaques more prone or vulnerable to rupture. These include plaques that contain intra plaque haemorrhage (IPH), a thin and/or ruptured fibrous cap (FC), a larger lipid rich necrotic core (LRNC), large amounts of inflammation, and to a lesser degree calcification (14,15).

## 1.2 Pathology

Atherosclerosis originates with the formation of fatty streaks, often early in the life of the patient. Over a long period of time, the fatty streaks may progress into more

complex atherosclerotic plaques, which may become increasingly unstable and eventually rupture. As the plaque ruptures, its thrombogenic core is exposed so that a thrombus may be formed in the vasculature. In the carotid arteries, this may lead to a blockage of the blood supply to the brain, which results in an ischaemic stroke (16).

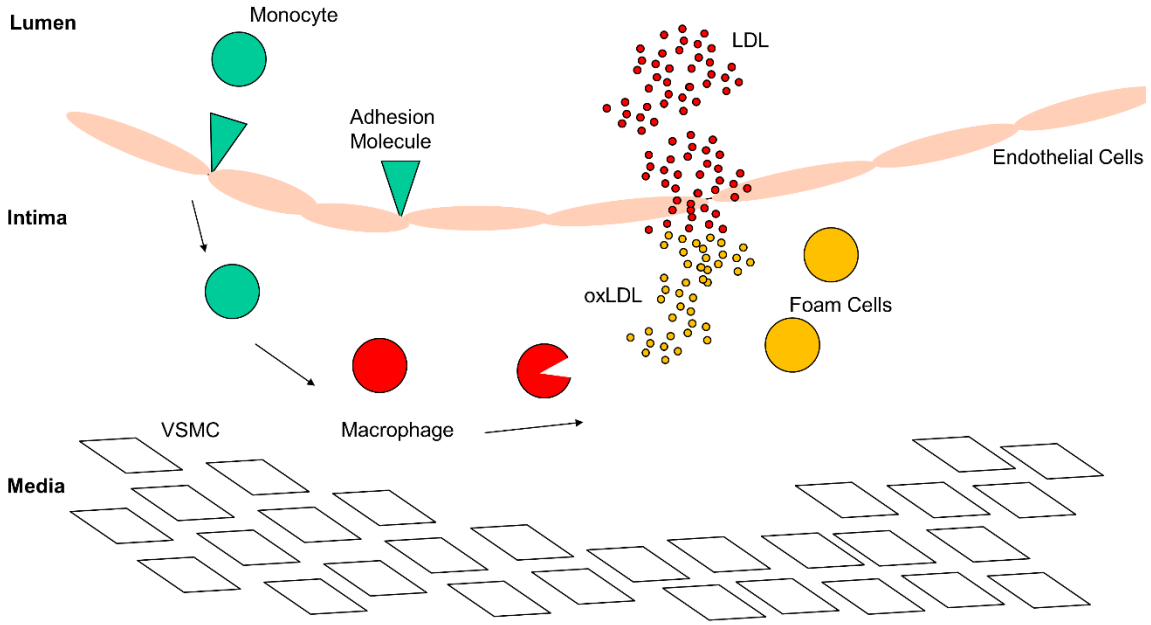


*Figure 1-2: The formation of carotid plaques involves the infiltration of lipids and macrophages* (17)

A particular risk factor of atherosclerosis is heightened low density lipoprotein (LDL) levels in the circulation (12). In areas with increased endothelial cell permeability LDLs may enter the subendothelial space (12,18). Increased endothelial cell permeability is an effect of endothelial dysfunction (19), which may be caused by other risk factors, such as smoking, diabetes mellitus, hypertension, or hypercholesterolemia (12,20). As LDLs enter the vessel wall, they undergo modification and become oxidized LDLs (oxLDLs) (12,20–22) which are cytotoxic, which means that they cause cell damage (20). OxLDLs cause further endothelial dysfunction (23,24), allowing for a heightened influx of LDL particles and also lead to an inflammatory response. This involves the expression of vascular cell adhesion molecules (VCAMs), which may bind monocytes and lymphocytes, which are then recruited into the plaque by chemokines (20,25–28). Inside the plaque, the monocytes can differentiate into macrophages (20,25,29) which take up oxLDLs until they become lipid laden macrophages or foam cells (20,25). The macrophages secrete cytokines, which are pro-inflammatory and lead to the upregulation of VCAMs and also the recruitment of further macrophages (12,30,31). Therefore, through the recruitment of macrophages, the inflammatory response is

further enhanced and can be seen as a marker for plaque progression. As macrophages and foam cells die, they form a lipid rich necrotic core, which was previously mentioned as a marker of unstable plaques (16).

In addition, growth factors and cytokines released by foam cells also attract vascular smooth muscle cells from the media into the intima (12,20,32,33). Within the intima, the VSMCs change their phenotype and release proteoglycans, which can bind and oxidize LDL (20,34–36) they attract and bind monocytes (20,35) and also secrete cytokines and chemokines (34,35), all of which enhances the accumulation of macrophages in the plaque. As the VSMCs can also take up lipids, they may also turn into foam cells (33,35,37–40). Similarly to the macrophages, these VSMCs may die and contribute to the lipid rich necrotic core (35,41).

This has demonstrated that the presence of inflammation in atherosclerotic plaques leads to positive feedback to increase inflammation even further. This is particularly problematic in regions of non-laminar flow, such as the carotid bifurcation (12). The reduction of shear stress caused by the altered flow pattern leads to a downregulation of the atheroprotective nitric oxide (NO) (12,20,42). NO has several functions such as preventing platelet aggregation (anti-thrombotic) (12,43) and the expression of adhesion molecules and therefore inhibiting macrophage infiltration (anti-adhesive) (12,20,43). Therefore, regions of turbulent flow, such as the carotid bifurcation, are especially predisposed for the formation of atherosclerotic plaques.

However, in addition to these pro-inflammatory, destabilizing effects, VSMCs also play a stabilizing role in atherosclerosis through the generation of a fibrous cap (12,44). VSMCs synthesize an extracellular matrix containing for example collagen (45,46), which together with the smooth muscle cells forms the fibrous cap (16,45). This protective structure covers the thrombogenic necrotic core and shields it from exposure to the lumen. However, when the fibrous cap of an atherosclerotic plaque ruptures, a thrombus can but does not have to be formed, which can but does not necessarily have to lead to symptoms (47–49). Furthermore, it is important to note that once a fibrous cap has ruptured it may remain thrombotically active so that multiple recurring events may follow (15). Therefore, fibrous cap rupture is an important feature of vulnerable plaques which is associated with thrombus formation (15,50) and also with other features of plaque instability such as a lipid rich necrotic core or intraplaque

haemorrhage (47). Cap rupture is caused by the thinning of the fibrous cap, which is enhanced by inflammation. Macrophages, which accumulate at the border of the lipid core and in the shoulder region of the plaque, or around neovessels, which are described in more detail below, release matrix metalloproteinases (MMPs) (18,50–52), which degrade the extracellular matrix, which leads to cap thinning (18,50–52).

A thick FC does not necessarily indicate a low risk of symptoms. Studies conducted in plaques in the coronary vasculature, for instance show that, a number of thrombi occur with an eroded and thick FC as opposed to a ruptured cap (53–56). In carotid artery plaques, plaque erosion is less frequent and occurs less often than plaque rupture in symptomatic patients (15,57,58).

Another feature of vulnerable plaques is intraplaque haemorrhage. Erythrocytes (red blood cells) can leak into the fibrous cap through fissures in the fibrous cap or a network of microvessels, the vasa vasorum. It is thought to be formed in response to plaque thickening. As the intima thickens, the diffusion path of nutrients and oxygen, that need to be supplied to the VSMCs, growths in length. The vasa vasorum is formed in response to this so that across its highly permeable walls the nutrients and oxygen can be supplied to VSMCs (59–67). Along with nutrients, erythrocytes also leak into the plaque, which is associated with an increased infiltration of macrophages (62–65). Higher levels of apoptotic macrophages and higher phagocytosis of erythrocytes increases the content of free cholesterol in the plaque and produces lipids and iron. Therefore, the development of intraplaque haemorrhage (IPH) has been shown to cause progression of the LRNC and an increase in wall volume while decreasing the lumen volume and exhibiting a high association with a thin and/or ruptured fibrous cap (63–66,68–71).

Advanced atherosclerotic plaques typically also contain calcification. While its role in plaque vulnerability is ambiguous, calcification is seen as an overall marker of cardiovascular risk and atherosclerotic disease burden and may increase with age (20,23,72). Calcification originates within apoptotic bodies or necrotic debris released by apoptotic macrophages and VSMCs or matrix vesicles released by VSMCs and macrophages as an inflammatory response (73–76). This process may be aided by the absence of mineralization inhibitors and VSMCs that transdifferentiate into osteochondrogenic precursors, which can regulate mineralization (73–76). The initial

formation of microcalcifications, which are of a size between 0.5-15 µm (77), is therefore associated with inflammation. This is even further enhanced, since microcalcifications may induce another inflammatory response, therefore enhancing plaque progression and destabilizing the atherosclerotic plaques (74,78). However, microcalcifications may also coalesce into larger sheets of macrocalcification which are greater in size than 15µm (77,79,80). This may be aided by the transdifferentiation of VSMCs into an osteoblast-like phenotype (75). These macrocalcifications are thought to have a stabilizing effect on the plaque as they may shield inflammation, therefore slowing plaque progression and potentially stabilizing the plaque (74,75,78,81).

## 1.3 Current Diagnosis and Treatment

Atherosclerosis is a complex process. Luminal stenosis is used as a risk evaluation criterion for making a decision on medical treatment (8). As previously described, the large-scale NASCET and ECST trials have demonstrated that surgical intervention was beneficial in high risk symptomatic patients with a high degree of stenosis by reducing the risk of recurrent strokes through carotid endarterectomy surgery (9,10). It has furthermore been shown that patients who have suffered from a recent event are at an increased risk of a recurrent event in the 30 days following the initial event so that they would benefit greatly from surgery (82). Therefore, patients who have suffered from symptoms will undergo screening for carotid artery stenosis, which is typically done using carotid doppler ultrasound/duplex ultrasound, and subsequently often undergo surgery in the two weeks subsequent to the initial event, where benefit has shown to be greatest (8,83,84). The benefit of surgery in symptomatic patients with lower degrees of stenosis was much lower (9). In asymptomatic patients, even with high levels of stenosis, careful consideration before surgery is recommended and the uncertainty about treatment strategies is higher (11). In combination with the overall low prevalence of atherosclerotic plaques in the general population and the questionable benefit of stenosis as a marker for risk of future events in asymptomatic patients have led to recommendations against a screening of the general population (85–87).

However, as many asymptomatic patients may suffer from stroke as well and because a high degree of stenosis is regarded as an increased risk of stroke (88), it would be

beneficial to identify subgroups of patients at risk. The common risk factors of atherosclerosis and increased stroke risk are known. In addition to examining symptomatic patients, the "ASA/ACCF/AHA/AANN/AANS/ACR/ ASNR/CNS/SAIP/SCAI/SIR/SNIS/SVM/SVS Guideline on the Management of Patients With Extracranial Carotid and Vertebral Artery Disease" has therefore recommended the screening of asymptomatic patients with duplex ultrasonography with symptomatic peripheral artery disease, coronary artery disease, atherosclerotic aortic aneurysm, carotid bruit, or two of the following: hypertension, hyperlipidaemia, tobacco smoking, family history of early onset of atherosclerotic disease (89,90).

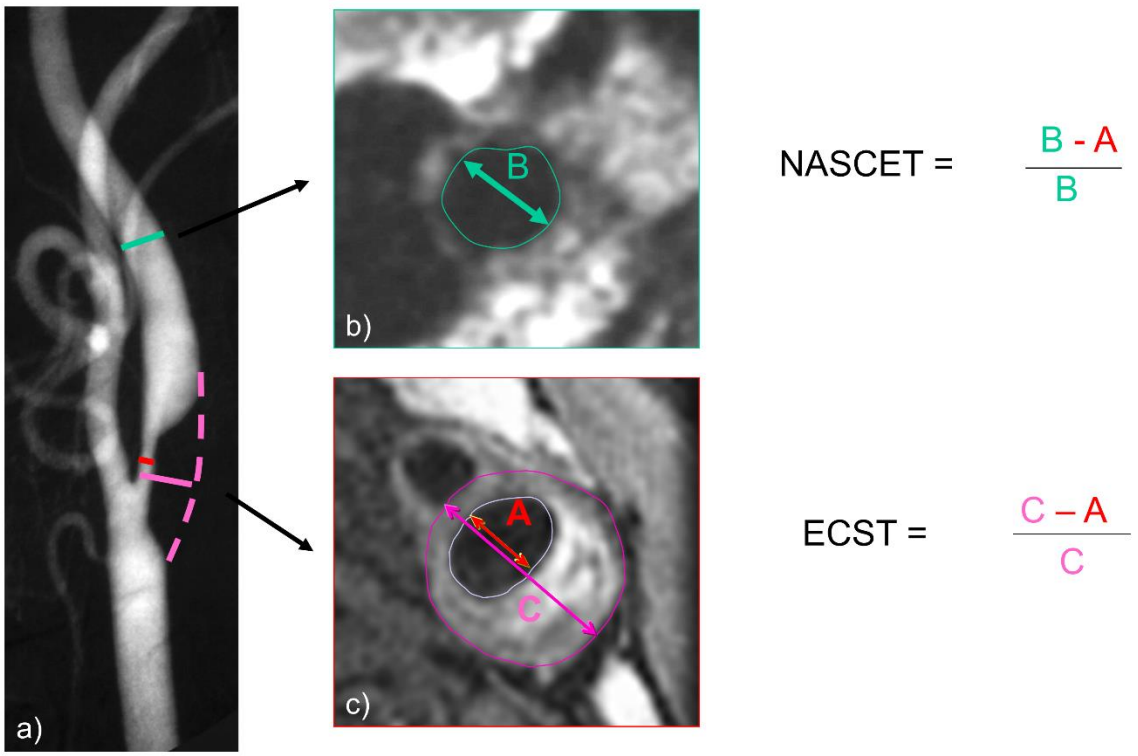


*Figure 1-3: Stenosis as calculated with the NASCET and ECST criteria. A) shows an X-ray angiogram where the narrowest diameter of the internal carotid artery, the estimated original diameter of the lumen at said location and the normal distal cervical internal carotid artery diameter are indicated in red, purple, and green respectively. B) and c) illustrate how these diameters can be measured on black blood MR images, also. (courtesy of Martin Graves)*

Carotid stenosis can be assessed with different methodologies. In the NASCET and ECST studies, two different methods of measurement and calculation have been proposed to measure stenosis in X-ray angiography as illustrated in Figure 1-3: In the NASCET study (10), the difference between the narrowest diameter of the internal carotid artery (ICA) and the normal distal cervical ICA diameter is measured relative to the normal distal cervical ICA diameter to give a percentage stenosis. In the ECST

study, stenosis was defined as the difference between the diameter of the lumen at the most stenotic part of the ICA and the estimated original diameter of the lumen at said location relative to this original diameter (9,91).

Carotid ultrasound imaging, is commonly used to assess carotid artery stenosis since it is cost-effective and non-invasive and does not expose the patients to ionizing radiation (8,89,92). Doppler ultrasound uses the Doppler effect to measure the blood velocity, which is elevated in stenotic regions and allows for grading of stenosis (93). If the results from this examination are ambiguous or further information is required for surgical planning, additional examinations such as X-ray angiography or Magnetic Resonance Angiography may be performed (89,92).

Once a patient has been diagnosed with carotid artery stenosis, several different steps are involved in order to provide the best medical therapy (BMT) according to disease severity. Initially lifestyle changes such as cessation of smoking, diet changes, and cardiovascular exercise are prescribed (89), which may be combined with medication. This can consist of antiplatelet and antithrombotic therapy to prevent further blood clotting (89,94), antihypertensive therapy to regulate blood pressure (89,95) and/or statin therapy to decrease low density lipoprotein cholesterol (LDL-C) level to a target level (89,96).

In especially severe cases, patients may undergo carotid revascularization surgery: in particular carotid endarterectomy (CEA) or carotid artery stenting (CAS). As these surgeries carry great perioperative risks, which may lead to ischemic events in itself, it is important to weigh the benefits against the risks of the surgery. CEA involves the excision of the carotid artery plaque from the carotid artery. This is a well-established technique and from the results of several studies, in particular the previously mentioned NASCET and ECST trials, a risk assessment according to the patient status can be made. In particular, in symptomatic patients with severe and, to a lesser degree, moderate cases of carotid artery stenosis, the removal of the plaque has shown to lower the overall risk of recurrent events (97,98). In patients with less than 50% of stenosis, however, medical management was shown to be more beneficial than surgery (97). Furthermore, the benefit was greatest two weeks after an ischemic event (83). An alternative procedure to CEA is carotid artery stenting, which involves the placement of a stent inside the region of the carotid artery plaque. The

perioperative risks and post-surgery reduction of risk of ischemic events have shown to be similar to CEA. It has been proposed that the advantages of CEA and CAS may differ on a case-by-case basis, depending on the individual patient and also the experience of the operating surgeon (89,99).

While the benefits of surgical intervention are clear in symptomatic and severely stenotic patients, a large group of patients who have never shown any symptoms or have a low level of stenosis may suffer from plaque rupture and ischemic events. In order to identify the patients at risk it is therefore necessary to find alternative strategies for patient screening and identifying patients eligible for surgery. An example for this is the identification of vulnerable complex plaques. MRI offers excellent soft-tissue contrast and therefore offers an excellent methodology for monitoring disease progression for research and clinical purposes.

## 1.4 Multi-Contrast MRI of Carotid Plaque

In order to characterize atherosclerotic carotid artery plaques MRI is a suitable imaging technique since it achieves high resolution, non-invasive in vivo imaging with excellent soft tissue contrast. A typical imaging protocol consists of multiple contrast weightings ($T_1$, $T_2$, PD, and 3D time-of-flight (TOF)), as shown in Figure 1-4. Their specific appearance on the individual images allows for the individual features of vulnerable plaques to be identified and distinguished. (See Table 1-1).

| | 3D TOF | $T_1$-w | PDw | $T_2$-w |
|---|---|---|---|---|
| Recent IPH | High | High/Moderate | Variable | Variable |
| Lipid Rich Necrotic Core | Moderate | High | High | Variable |
| Calcification | Low | Low | Low | Low |
| Fibrous Tissue | Moderate/Low | Moderate | High | Variable |

*Table 1-1: Signal intensities of different plaque features relative to the sternocleidomastoid muscle on different sequences of the multi-contrast protocol* (100)

Initial studies using $T_1$w 2D Fast Spin Echo (FSE), $T_2$w FSE, and PDw FSE and 3D TOF were able to detect IPH and a thin and/or ruptured FC with high reproducibility and high classification accuracy, sensitivity, and specificity when compared to the gold standard histology (101–107).

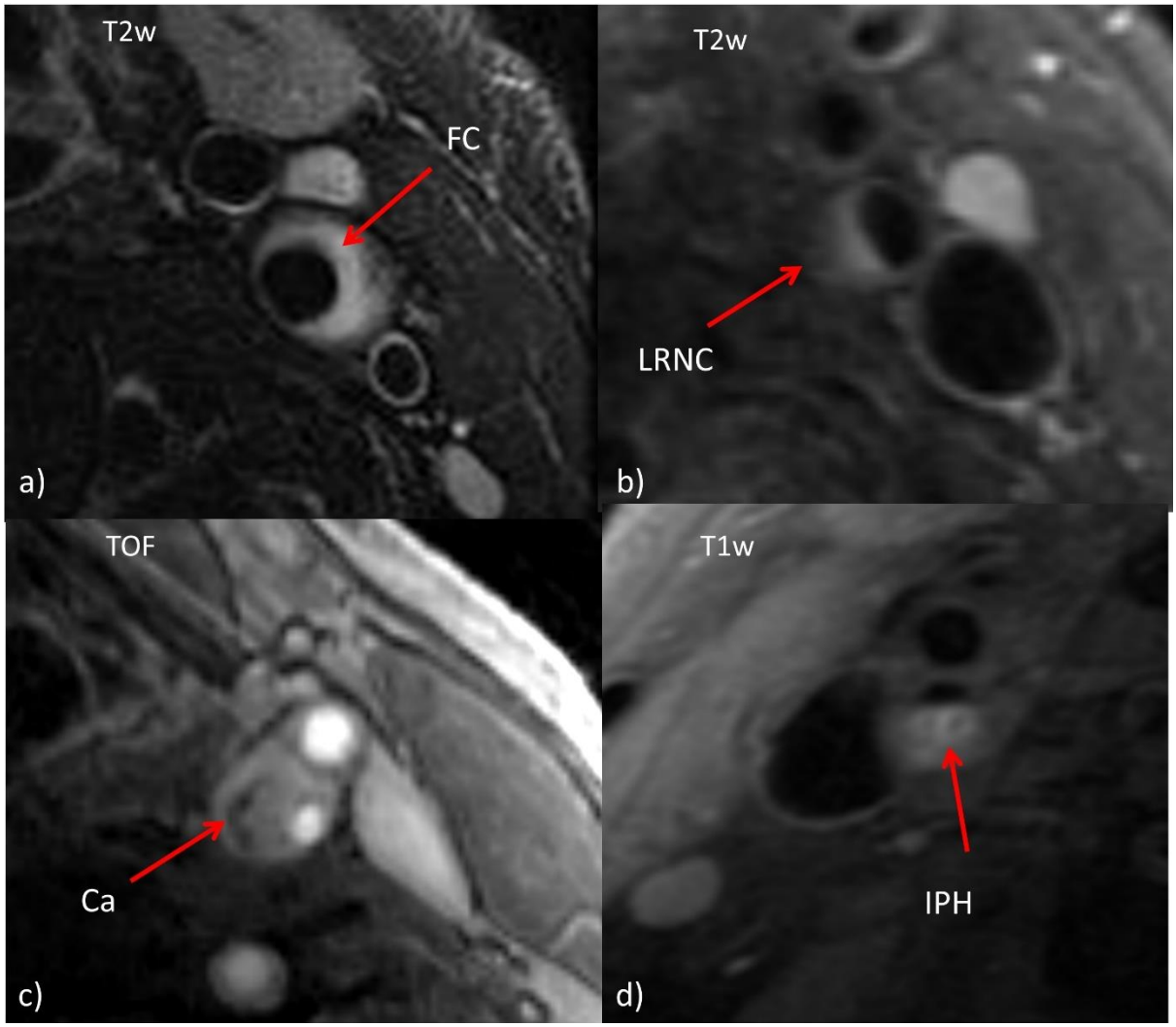


*Figure 1-4: Multi-contrast MRI of carotid plaques can identify features of vulnerable plaques (courtesy of Martin Graves)*

Progress in MRI research has allowed for the increase of field strength of the magnets from 1.5T to 3T (108–114), and in some applications even to 7T scanners (115–118). This improves the SNR of the acquired images, which can improve image quality or can be used to acquire higher resolution images or acquire images in a shorter acquisition time, as parallel imaging or less signal averages can be employed to acquire high quality images within a smaller time period (108–113). Additionally, the use of 3D instead of 2D imaging sequences further improved the SNR of the image acquisition (119,120). In 3D imaging a 3D volume, rather than a 2D slice is excited by the radiofrequency excitation pulse. For a given sequence, where all other imaging parameters are kept constant, 3D imaging increases the SNR by a factor of $\sqrt{N_{PE2}}$, where $N_{PE2}$ is the number of phase encode steps in the slice direction, since the

relationships between SNR, volume of interest and the resolution can be described as follows for 2D and 3D sequences:

$$SNR_{2D} \propto \frac{F_{seq}\Delta x\Delta y\Delta z\sqrt{NSA\ N_{FE}N_{PE1}}}{\sqrt{BW}}$$

$$SNR_{3D} \propto \frac{F_{seq}\Delta x\Delta y\Delta z\sqrt{NSA\ N_{FE}N_{PE1}N_{PE2}}}{\sqrt{BW}}$$

Here $F_{seq}$ is a sequence dependent factor that gives the signal strength relative to relaxation times, flip angle and echo and repetition times, $BW$ is the imaging bandwidth, NSA is the number of signal averages, $\Delta x$, $\Delta y$, and $\Delta z$ are the resolution in the x, y, and z-direction, $\mathrm{N_{FE}}$ is the number of frequency encode steps, and $\mathrm{N_{PE1}}$ and $\mathrm{N_{PE2}}$ are the number of phase encode steps (121). The acquired images therefore have a higher SNR or can be acquired at a higher resolution. This can be used to improve the resolution in the slice direction and image quality and partial volume effects (PVE) can be reduced (119,120).

Furthermore, specialist sequences have been developed for certain applications. Black-blood imaging aims to suppress the signal from flowing blood. This has the effect of eliminating plaque mimicking artifacts caused by slow or turbulent flow. Inflow-outflow saturation band (IOSB) and double-inversion recovery (DIR) are two techniques, successfully used in 2D FSE (112,122,123). IOSB places two parallel saturation bands on either side of the imaging slice prior to data acquisition. The spins that subsequently flow into the imaging slice then do not give any signal (112). DIR uses a train of pulses that achieves black blood preparation. The black blood preparation consists of two 180° radiofrequency (RF) pulses, the first of which is not spatially selective and therefore inverts the magnetization within the entire volume. The second, spatially selective RF pulse, only inverts the signal within the imaging slice and restores the magnetization. After an inversion time TI, the magnetization of the blood will have relaxed sufficiently to reach a null point and give zero signal. At this point, data acquisition starts. This technique requires that the blood inside the imaging slice will be replaced by that flowing in from the outside, which has only experienced the first RF pulse so that the lumen does not give any signal (112,122,123). However, both techniques rely on the inflow of magnetization prepared blood into the imaging slice, replacing any unprepared blood, which may give rise to signal within the lumen.

Insufficient replacement by magnetization prepared blood may occur particularly in thick imaging slices or in areas of slow or turbulent flow, such as the carotid bifurcation.

Therefore, alternative blood suppression techniques which are better suited for 3D imaging of the carotid artery bifurcation have been proposed, such as Delay alternating with nutation for tailored excitation (DANTE) (124). DANTE employs a black blood preparation module in advance of the imaging sequence. A pulse train with small flip angles (3-15°), which have a fixed phase advance, are interspersed with gradients. Blood suppression is achieved as static spins only have a linearly increasing phase component. In combination with a fixed increment of the phase of the flip angle, this leads to phase coherence. Spins, that move along the direction of the gradient will accumulate a quadratic phase. This results in a spoiling mechanism similar to RF spoiling. This leads to a large attenuation of the longitudinal magnetization of flowing spins, which leads to a robust flow compensation relatively independent of flow velocity (124).

In addition to that, specific properties of the individual plaque features have allowed for specialized pulse sequences to simplify their detection. A commonly used example is MR direct thrombus imaging (125). IPH contains methaemoglobin, which has a particularly short $T_1$ relaxation time. Magnetization preparation is combined with a $T_1$-weighted sequence, in order to suppress blood flow. Overall this improves the contrast between IPH and the surrounding tissues as demonstrated in Figure 1-5 (125).

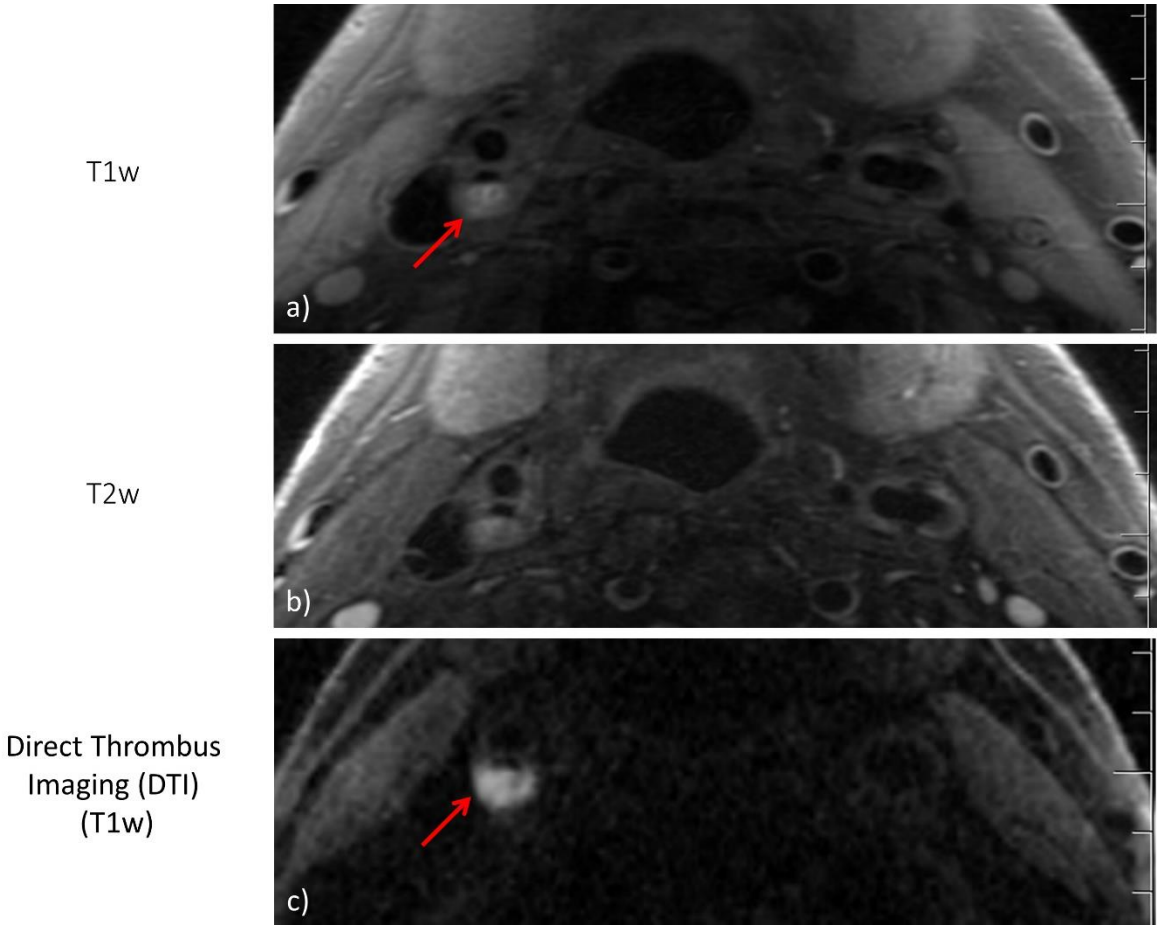


*Figure 1-5: Appearance of intraplaque haemorrhage on $T_1$w and $T_2$w contrast in comparison with MR DTI (courtesy of Martin Graves)*

## 1.5 Imaging of Carotid Artery Plaque Inflammation Using USPIO-Contrast Agents

### 1.5.1 USPIO Contrast Agents

While the multi-contrast protocol cannot image inflammation in plaques, this can be achieved with a macrophage selective contrast agent. Ultrasmall Iron Oxide (USPIO) nanoparticles are contrast agents with a mean diameter of less than 50 nm. As they do not accumulate in the reticuloendothelial system (RES) as rapidly as larger iron oxide particles, they stay in the blood circulation for a sufficiently long time to serve as an attractive blood pool agent (126,127). As such USPIOs have found application in contrast enhanced MRA (128,129), perfusion imaging and to evaluate tumour vascularity (130,131). Additionally, USPIOs are taken up by the lymph node system

(132). Tumour metastases located in the lymph node system, can be detected as they do not show any change on the MR images post-contrast administration (132).

Furthermore, USPIO-contrast agents are taken up by macrophages. In Abdominal Aortic Aneurysm USPIO uptake by macrophages was shown to image inflammation (133,134) which appeared to be a sign for more rapid expansion (133). In strokes, which result from a disruption in the blood supply to the brain, there are macrophages in the infarct zone (135). Furthermore, increased USPIO uptake within the infarcted and remote myocardium after acute myocardial inflammation could be detected (136).

In addition to that, USPIO nanoparticles have also been used as a contrast agent for imaging carotid artery plaques. They enter the plaque through a leaky endothelium and are subsequently taken up by macrophages, typically within the first 24 hours after an intravenous bolus injection (126,137–140). Due to their paramagnetism (positive susceptibility), USPIO-uptake causes an increase in $R_2^*$-relaxation rate and manifests as signal hypointensities on $T_2^*$w gradient echo MRI when compared to a pre-contrast acquisition as shown in Figure 1-6 (137,138,141–143). The macrophage-specific property of USPIOs allows MRI to detect areas of high macrophage activity which could potentially help assessing pathogenesis and prognosticating disease severity. USPIOs also shorten $T_1$. Especially in low concentrations they appear as hyperintensities on $T_1$ weighted images (127).

The carotid coils are typically phased array surface coils that are placed on either side of the neck. The carotid coil sensitivity is highly inhomogeneous so that the signal intensity within the plaque may vary drastically between pre- and post-contrast scans. Therefore, the $T_2^*$w signal within the plaque is typically normalized by the signal intensity in the sternocleidomastoid muscle to make pre- and post-contrast signal intensities comparable (138,141). However, this technique is nonetheless susceptible to inaccuracies and variability, due to the same issues concerning the scan location and coil positioning changes between the pre- and post-contrast acquisition. Therefore, $T_2^*$/$R_2^*$-mapping may offer a more reliable and quantitative assessment independent of the imaging variables. However, the non-local properties of the field inhomogeneities (field inhomogeneities extend beyond the source of the susceptibility variation) can cause errors on $R_2^*$-maps and lead to errors in the estimation of the amount of USPIO-uptake (144). Furthermore, areas of USPIO-uptake may be

overestimated due to non-local effects (144). A pixelwise comparison of pre- and post-contrast images requires advanced image co-registration. Therefore, $T_2^*$w and $R_2^*$-mapping based analyses divide the plaque area into quadrants (126,141,143) or octants (137) in order to compare the values for each section on pre- and post-contrast administration. While this allows for an operator independent analysis, the decline in resolution may lead to decreased detection sensitivity of small areas of USPIO uptake. USPIO uptake within carotid atheroma was found to be a good indicator of plaque inflammation (141) and USPIO uptake has also been shown to be more frequent in symptomatic patients (145).

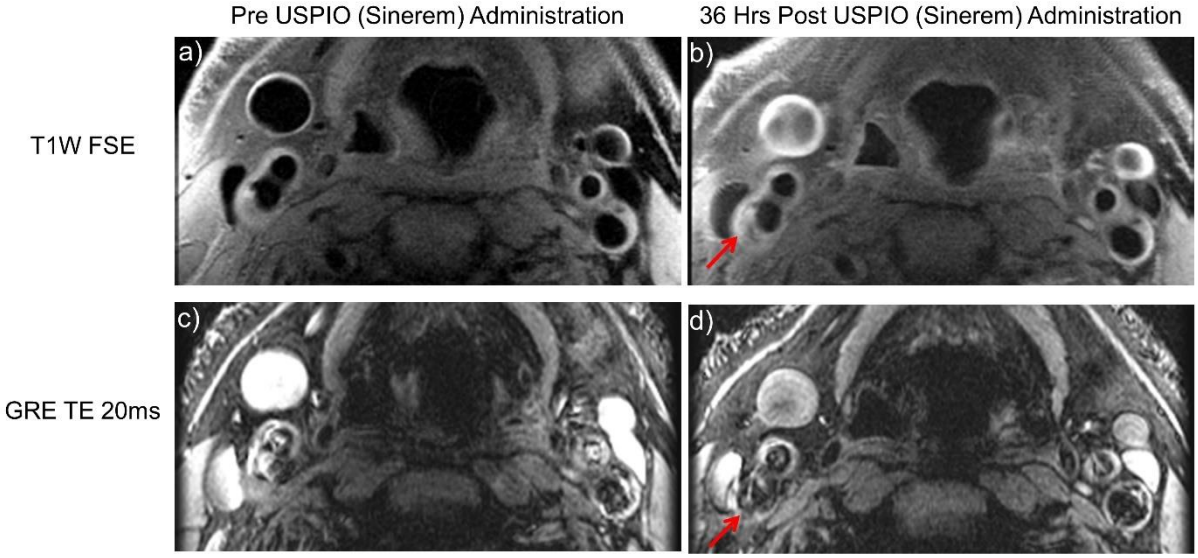


*Figure 1-6: MR images acquired before and 36 hrs after administration of the USPIO contrast agent Sinerem. Hyperintensity can be observed on post-contrast $T_1$w imaging and hypointensity on the post-contrast $T_2^*$w image (GRE TE = 20 ms) (courtesy of Martin Graves)*

In the following chapters the USPIO contrast agent ferumoxytol will be used. Ferumoxytol is an iron oxide agent originally used to treat anaemia, which has been widely used in research and also used as an off-label clinical contrast agent (146). It is important to consider its safety profile. The risk assessment is based on its use as a therapeutic drug for anaemia treatment. In 2015 the FDA issued a boxed warning for ferumoxytol since in 1.2 million therapeutic doses, 79 anaphylactic reactions with 18 fatalities occurred (146,147). However, these results were all based on therapeutic applications. It is important to note that the ferumoxytol doses administered for imaging are much lower in comparison with therapeutic doses. For imaging, the administered doses typically ranged from 1 to 7.5 mg/kg, while the full therapeutic dose was 1020

mg, which for a 70 kg adult would correspond to 14.6 mg/kg (146). During administration, the dose is typically diluted and a slow infusion is recommended (146,147). In comparison to ionic iodinated and gadolinium-based contrast agents the reported risks were comparable and higher respectively. However, it has been suggested that ferumoxytol offers a comparatively lower risk in patients with renal disease and could therefore be used as an alternative contrast agent (146).

### 1.5.2 Positive Contrast in USPIO-Imaging

The described techniques, that have been commonly used in imaging USPIO-contrast agents rely on the detection of a reduction in signal intensity on post-contrast images due to the increase in magnetic susceptibility caused by the uptake of USPIO particles, which is associated with $T_2^*$-shortening. Therefore, USPIO-uptake is imaged with negative contrast. The distinction from other sources of signal hypointensities, for example originating from bone, calcification or haemorrhages, is therefore difficult to impossible on a single scan. Therefore, as previously described, a comparison of pre- and post-contrast images is required for the detection of USPIO-uptake.

It has been suggested that imaging USPIO-uptake as “positive” contrast, i.e. hyperintensities, may improve the detection of USPIO uptake, render pre-contrast imaging obsolete and, therefore, eliminate the associated registration errors (144,148). Several techniques have aimed at creating positive contrast images:

***The IRON technique: spectrally selective pulses***

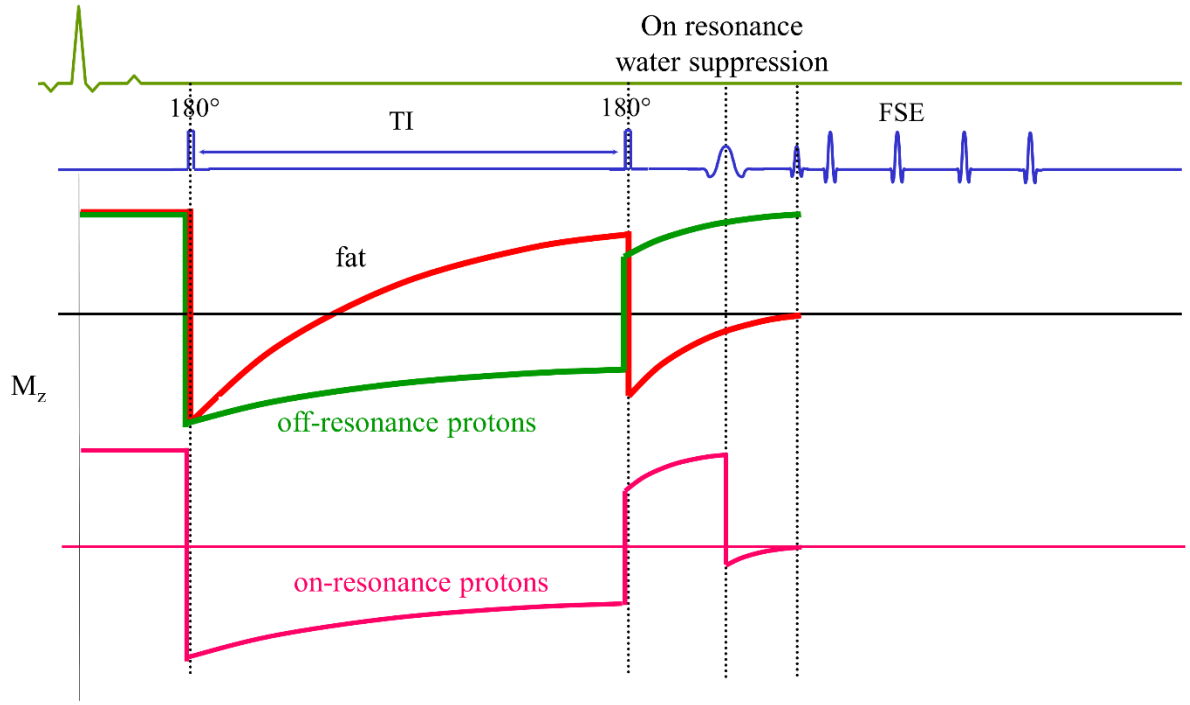


*Figure 1-7: Pulse sequence diagram IRON (courtesy Martin Graves)*

The IRON (Inversion Recovery ON Resonance) technique (148), pictured in Figure 1-7, uses a sequence of spectrally selective saturation preparation pulses in order to suppress signal from all other sources besides USPIO nanoparticles. Due to their high paramagnetism, the USPIO nanoparticles cause an inhomogeneity in $B_0$. This causes a local change in precession frequency in the surrounding voxels. IRON saturates only on-frequency spins, that contain minimal changes in precession frequency. Voxels in proximity to the USPIO nanoparticles contain large $B_0$ field inhomogeneities, and precess at a different frequency. Therefore, they remain unsuppressed and are highlighted and are presented as hyperintensities as shown in Figure 1-8. Exciting/saturating the correct frequency shifts, requires knowledge of the expected frequency shifts and therefore the amount of contrast agent taken up. Furthermore, large-scale field inhomogeneities also cause a change in precession frequency which may cause errors in this technique (148,149).

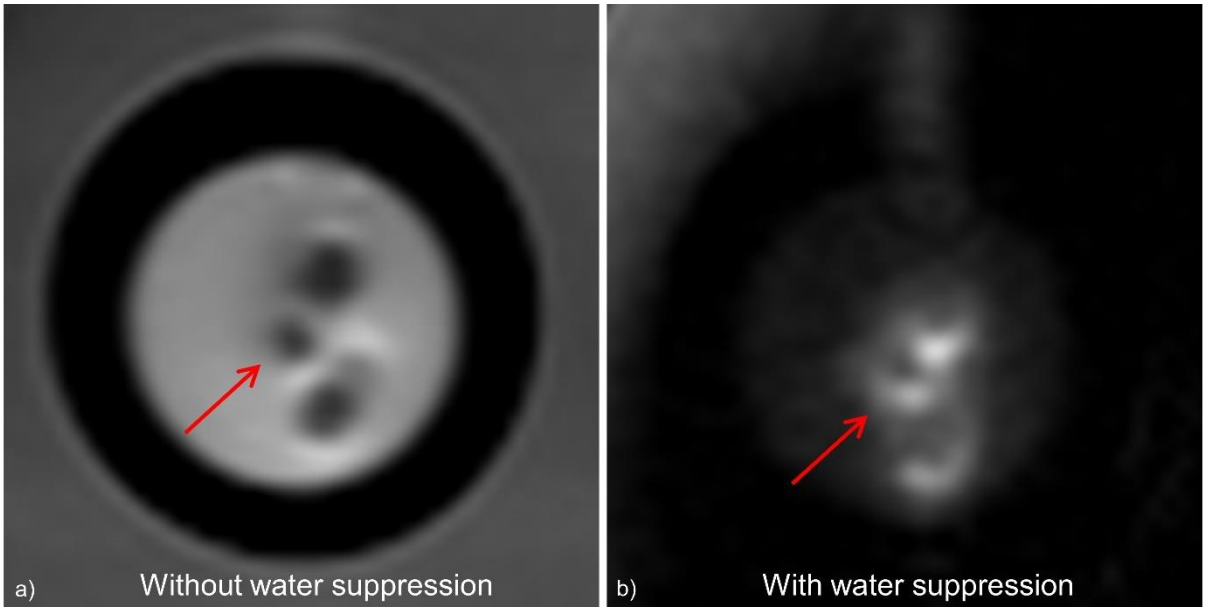


*Figure 1-8: The IRON sequence selectively suppresses signal from water but signal hyperintensities can be observed in the vial stemming from USPIO (courtesy Martin Graves, images also appear in* (150)*)*

### *GRASP technique*

Another, similar technique to generate positive contrast is called GRASP (151). In conventional imaging, the slice select gradient is followed by a re-phasing gradient in order to eliminate the de-phasing caused during slice selection. By estimating the amount of rephasing achieved by the $B_0$ field inhomogeneities alone, the re-phasing gradient can be reduced by an appropriate amount so that the change in $B_0$ leads to an enhanced signal recovery: The spins within voxels where the $B_0$ field inhomogeneity in the direction of the slice select gradient is insufficiently large or is of the wrong polarity, will not be fully re-phased and only the relevant voxels where the USPIO contrast have caused a phase shift appear hyperintense. This technique requires a careful selection of the re-phasing gradient strength, based on a priori knowledge of the magnitude and orientation of the $B_0$ field inhomogeneity caused by the contrast agent.

### *SGM technique*

Alternatively, in susceptibility gradient mapping (SGM) susceptibility gradients may be mapped when considering the complex signal of a gradient echo acquisition. This delineates the region of interest by signal hyperintensities surrounding areas of USPIO uptake. Since there is an increase in the local field inhomogeneity (152).

All of these techniques simply highlight the presence of larger field inhomogeneities and suffer from dependence on the sequence or assumptions about the amount, orientation, or geometry of the areas containing USPIO contrast agents and are non-quantitative.

# Chapter 2 Principles of MRI

Aspects of this work have been published in “Ruetten PPR, Gillard JH, Graves MJ. Introduction to Quantitative Susceptibility Mapping and Susceptibility Weighted Imaging. Br. J. Radiol. 2019;92:20181016 doi: 10.1259/bjr.20181016.” (153)

## 2.1 MRI Physics

### 2.1.1 MR Signal and Spin Relaxation

The human body consists of atoms, whose nuclei have an associated charge and spin. Hydrogen atoms which are typically imaged in MRI are positively charged. As they spin around their own axis, they constitute moving charges which generate a magnetic moment, so that a hydrogen nucleus constitutes a magnetic dipole. The spin, also defined as angular momentum $J$ is characterized by the nuclear spin quantum number $I$, which is ½ for hydrogen nuclei (121,154–157):

$$J = \hbar[I(I+1)]^{\frac{1}{2}} \qquad 2\text{-}1$$

Here, $\hbar$ is the reduced Planck’s constant ($\frac{h}{2\pi}$). The z-component of $J$ is given by:

$$J_z = \hbar m_I \qquad 2\text{-}2$$

Here, $m_I$ is the magnetic quantum number, which for hydrogen, ($I = \frac{1}{2}$) may take on the values -½ and ½ (121,154–157) This means that there are two potential orientations for the hydrogen spins. When placed within a static magnetic field, such

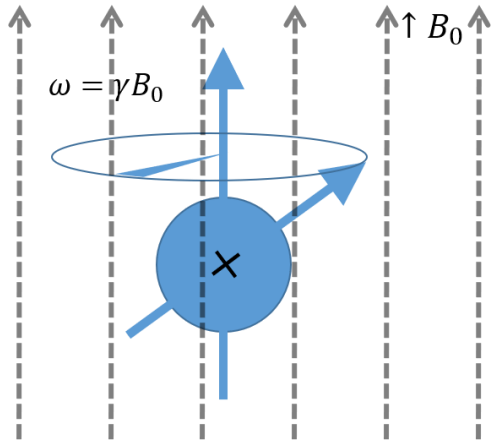


*Figure 2-1: The proton spins precess around the magnetic field of the scanner $B_0$ with the Larmor frequency: $\omega = \gamma B_0$ (Courtesy of Martin Graves)*

as that of an MRI scanner, all the z-components of $J$ align either in parallel or anti-parallel with the field of the scanner $B_0$. The relationship between the magnitude of $J$ and $J_z$ is defined as $J_z = |J|\cos(\alpha)$. The angle $\alpha$ is in between the direction of $B_0$ and $J$. By evaluating $J$ and $J_z$ in the above formulae with the known values for the spin quantum number and magnetic quantum number, this gives:

$$\frac{\hbar 1}{2} = \hbar\left[\frac{1}{2}\left(\frac{1}{2}+1\right)\right]^{\frac{1}{2}}\cos(\alpha) \qquad 2\text{-}3$$

From this, $\alpha$ can be determined as:

$$\alpha = \cos^{-1}\left(\frac{1}{2}\Big/\sqrt{\frac{3}{4}}\right) = \cos^{-1}\left(\frac{1}{\sqrt{3}}\right) = 54.7° \qquad 2\text{-}4$$

Therefore $J$ is at an angle of 54.7° (the magic angle) in relation to $B_0$.The spins precess around the z-axis of the magnetic field $B_0$ with a specific frequency, the Larmor frequency, as shown in Figure 2-1. This is analogous to a gyroscope. The Larmor frequency is calculated as the product of the rationalised gyromagnetic ratio and the magnetic field strength of the scanner:

$$f = \gamma B_0 \qquad 2\text{-}5$$

The rationalised gyromagnetic ratio $\gamma = \frac{\gamma}{2\pi}$ is 42.56 MHz/T for hydrogen and is a nucleus-specific constant so that the spins of different nuclei precess at different frequencies around the direction of $B_0$ (121,154–157).

The anti-parallel and parallel spin orientations correspond to the two distinct quantized energy states the spins may be in. The anti-parallel spins are at a slightly energetically higher state. The energy difference between the two states is given by

$$\Delta E = \hbar\gamma B_0 \qquad 2\text{-}6$$

Here, ħ is the reduced Planck's constant and $\gamma$ is the gyromagnetic ratio. The presence of the two distinct energy states is known as the nuclear Zeeman effect (121,154–157).

This is illustrated in Figure 2-2. The ratio of the parallel (N↑) to anti-parallel (N↓) spins is given by the Boltzmann distribution as (121,154–157):

$$\frac{N\uparrow}{N\downarrow} = \exp\left(\frac{\Delta E}{kT}\right) \qquad 2\text{-}7$$

Here $k$ is the Boltzmann constant and $\Delta E$ is the energy difference between the two states. This formula can be simplified to:

$$\frac{N\uparrow}{N\downarrow} = 1 + \frac{2\pi\gamma\hbar B_0}{kT} \qquad 2\text{-}8$$

This is possible as $2\pi\gamma\hbar B_0 \ll kT$, at body temperature and a clinical field strength. Here $\hbar$ is the reduced Planck's constant ($\frac{h}{2\pi}$), $\gamma$ is the rationalised gyromagnetic ratio, and k the Boltzmann constant (121,155). Since the overall magnetization is given by the difference of nuclei aligned parallel and anti-parallel to $B_0$ and the parallel spins are in a slight majority ($\frac{N\uparrow}{N\downarrow} = 1.000004$; at $B_0$ = 1.5T, T = 37° C) they produce a net magnetization $M_0$ in the direction of $B_0$. This superimposed magnetic field change is however very small (several μT) compared to $B_0$, which is typically several tesla, e.g. 1.5 T or 3.0 T, and therefore impossible to detect (121).

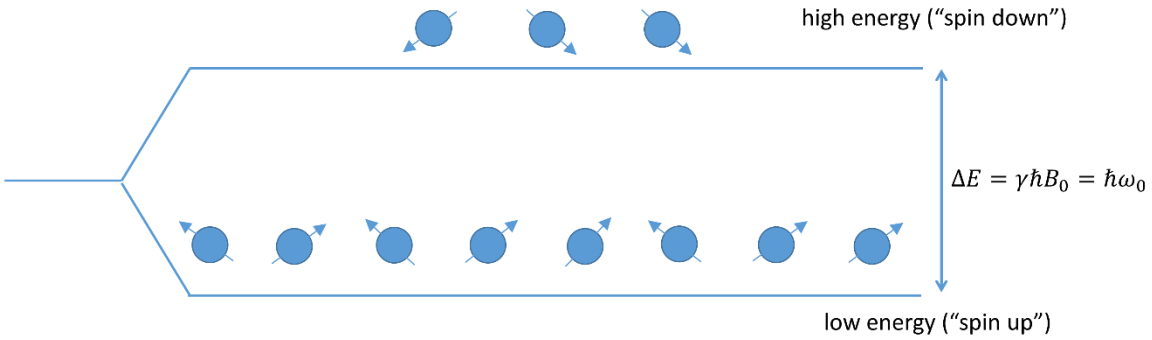


*Figure 2-2: Spins aligned in parallel and anti-parallel with $B_0$ are at a lower and higher energy level respectively. (courtesy of Martin Graves)*

In MRI, a radiofrequency (RF) pulse is therefore used to transfer energy to the spins so that their magnetization is rotated towards the transverse plane, where it can be detected.

The larger number of spins makes it possible to apply classical mechanics to the hydrogen nuclei; the spins are grouped together. Before application of an RF pulse, all protons are precessing out of phase, so that the net magnetization only has a z-component $M_z$, while its transverse components cancel out. The application of an RF

pulse then transfers energy to the spins and rotates the net magnetization from the longitudinal into or towards the transverse plane. The RF pulse is an electromagnetic wave, which oscillates at the radiofrequency part of the electromagnetic spectrum, more specifically it oscillates at the Larmor frequency. This is the resonant condition. It has a certain duration $T$ and magnetic field strength of magnitude $B_1$. The angle by which the net magnetization is rotated by a simple RF pulse, the flip angle, can be calculated by $\alpha = \gamma B_1 T$ (121,154–156). If chosen to be 90°, all of the magnetization in the z-direction (longitudinal direction), $M_z$, is flipped into the transverse plane to give $M_{xy}$ or the transverse magnetization. $M_{xy}$ can then be measured by the voltage it induces in a receiver that only detects the magnetization in the transverse plane (121,154–156).

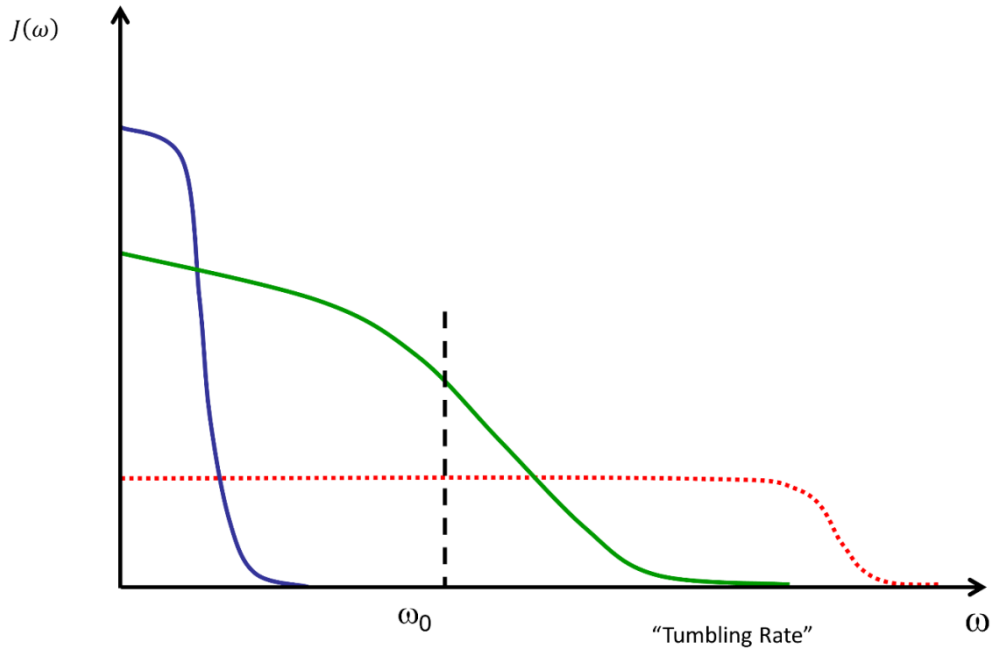


*Figure 2-3: The spectral density function $J(\omega)$ gives the probability at which a molecule rotates or tumbles at a given velocity. Here, the spectral density diagrams for three different tissue types are given. Blue indicates a tissue type, where the majority of molecules tumble at a lower frequency than the Larmor frequency, while the red curve shows a high abundance of molecules that tumble faster. Green indicates a tissue type where there is a high abundance of molecules tumbling at the Larmor frequency. (courtesy of Martin Graves)*

Besides classical mechanics, the rotation of the net magnetization can be described using an energy level model. The RF pulse has transferred energy to the spins. Through external stimulation, such as oscillating magnetic fields at the Larmor

frequency, they may release this energy and return to their initial state, i.e., they may "relax". In classical mechanics this would correspond to a regrowth back to their original orientation in the longitudinal plane. The return to the initial state is stimulated by the surrounding molecules, which tumble (rotate, translate, or vibrate), so that they generate oscillating magnetic fields. In different tissues there is a higher or lower abundance of fields oscillating at Larmor frequency. The abundance of molecules which tumble at a certain frequency is given by the spectral density function, as shown in Figure 2-3. In materials such as fat where many molecules tumble almost at Larmor frequency, the relaxation is faster than in materials where the molecules tumble much faster such as in free fluids or in materials where they tumble much slower since they are bound (121). The effect on $T_1$ is shown in Figure 2-4. The recovery of $M_z$ can be described by an exponential function and a time constant $T_1$: $M_z = M_0 \cdot \left(1 - \exp\left(-\frac{t}{T_1}\right)\right)$. The shorter the $T_1$, the faster the signal recovery (121,154–157).

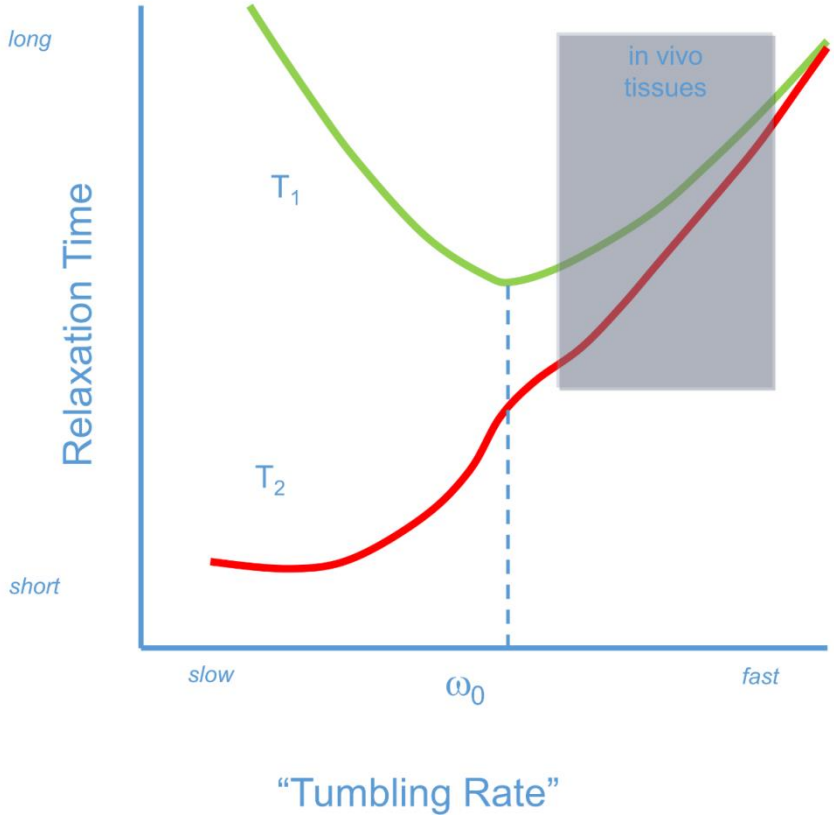


*Figure 2-4: Influence of the tumbling rate on $T_1$ and $T_2$ relaxation times (courtesy of Martin Graves)*

While $T_1$ relaxation describes the recovery of $M_z$, in biological tissues $M_{xy}$ decays much faster than $M_z$ recovers. Spins in the transverse plane within the net

magnetization precess at slightly different frequencies, so that they dephase eventually cancelling each other out. This decay is the free induction decay: it is characterized by the time constant $T_2^*$ (121,154–157). It consists of two components: first, there are spin-spin interactions: random movements of protons and molecules cause non-static changes in the local magnetic field that lead to a decay of the net magnetization. This decay is described by the time constant $T_2$. If the molecule is hardly moving, the dipolar field will be relatively static and will cause the dephasing of nearby spins, i.e. enhance relaxation and shorten $T_2$. If the tumbling rate is very fast, however, the field effects will average out, which results in a smaller dephasing effect, as shown in Figure 2-4 (121,154–157). Second, differences in local precession frequencies caused by static differences in the magnetic field $\Delta B$ cause a signal decay (121,154,155,157). This may be caused by local differences in magnetization, that arise from differences in material susceptibility or large-scale background inhomogeneities, which will be described in more detail later. This decay is described by the time constant $T_2'$. Therefore, $T_2^*$ can be described as:

$$\frac{1}{T_2^*} = \frac{1}{T_2'} + \frac{1}{T_2} \qquad 2\text{-}9$$

The signal decay of the transverse magnetization can be described as $M_{xy} \propto \exp\left(-\frac{t}{T_2^*}\right)$ (121,154,155,157). Effects, that may cause confusion on $T_2^*$w magnitude images are, for example chemical shift (158,159). Furthermore, the distribution of substances within a voxel on a microscopic level can cause differences in the estimation of the $T_2^*$. This may be a confounding factor when $T_2^*$ is estimated in order to draw conclusions about the concentration of certain susceptibility sources within the voxel (160–163).

### 2.1.2 MRI System

The MRI system typically consists of a large static magnetic field generated by a superconducting magnet. Transmit and receive radiofrequency coils, and gradient coils subsequently serve to generate, record, and spatially encode an electromagnetic signal from the tissue that is placed inside the magnet bore (121).

The static magnetic field is typically in either a horizontal or vertical orientation. In clinical systems, typically, a horizontal magnetic field is used and superconducting

magnets generate magnetic fields greater than approximately 0.6T. In a clinical setting 1.5T and 3.0T are used but higher field strengths such as 7.0T are used in research and certain clinical applications. The magnet windings comprise an alloy of Niobium/Titanium and are immersed in a bath of liquid helium in order to keep them at 4.2° K and maintain superconductivity (121,154,155,157).

In order to generate a detectable signal from the patient or tissue placed inside the magnet a radiofrequency transmit coil generates the RF pulse. The body transmit coil is located behind the external covers inside of the scanner bore. The MR signal, is spatially encoded via the gradient coils (121,154,155,157). The MR signal is then recorded by the receiver coils, as the precession of the nuclear magnetization induces a current in them. The raw MRI data are acquired with quadrature detection. Therefore, it is complex valued, which means that it has a real and imaginary part from which both a magnitude term, which is commonly used in clinical image analysis and a phase term, which is typically discarded, can be calculated. The receiver coils consist of either a single element or multiple elements, when they are called array coils. Surface receive-only coils for different anatomies are specifically designed so that they can be placed as closely as possible to the region of interest. The surface coils consist of multiple small coils, which produce high SNR in close proximity to the coil. The FOV for each loop is therefore small and excludes outside noise. Therefore, the signal from the region of interest will be high and the associated noise small, maximizing the signal-to-noise ratio (SNR) (121,154,155,157). In order to further

reduce the influence from external radiofrequency radiation, the magnet room is enclosed in an RF-shield, which serves as a Faraday cage and blocks out any outside electromagnetic interference (121). The gradient coils apply a linear variation in magnetic field in the three orthogonal directions that are superimposed onto the main

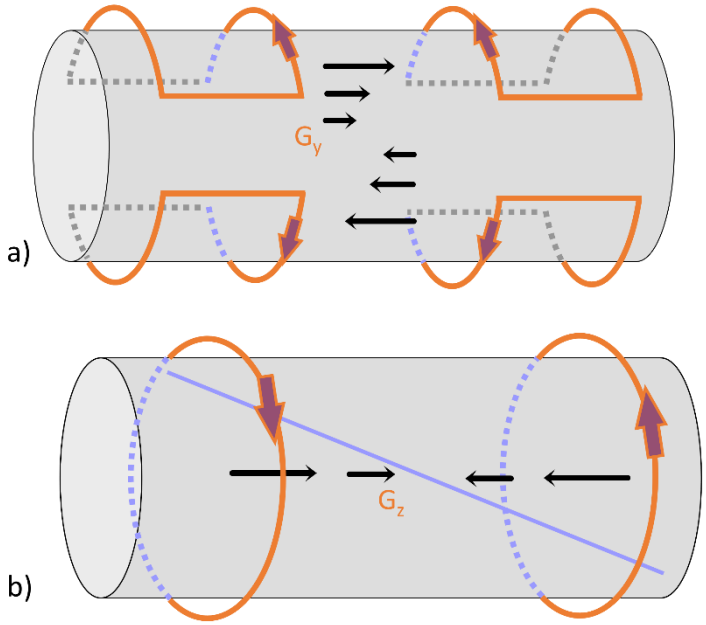


*Figure 2-5: Gradient coil configuration; Golay configuration (a), Maxwell pair (b) (Courtesy of Martin Graves)*

static magnetic field. The coils, as illustrated in Figure 2-5 a) in the x and y direction are oriented in the Golay configuration and the coils for the gradient in the z-direction (Figure 2-5 b) are a Maxwell pair. The coils cause small variations in the magnetic field along each orthogonal direction. The gradients are applied as short duration pulses. The spatial variation of the field leads to a variation of the precession frequency/Larmor frequency of protons at different locations (e.g. $\omega = \gamma(B_0 + \mathrm{zG_z})$). The resulting change in the signal phase and frequency can be used to spatially encode the signal recorded at any time. As the coils are switched on and off very rapidly a Lorentz force is generated, which causes the coils to flex, creating the loud noise inside the scanner (121,154,155,157).

### 2.1.3 Slice Selection

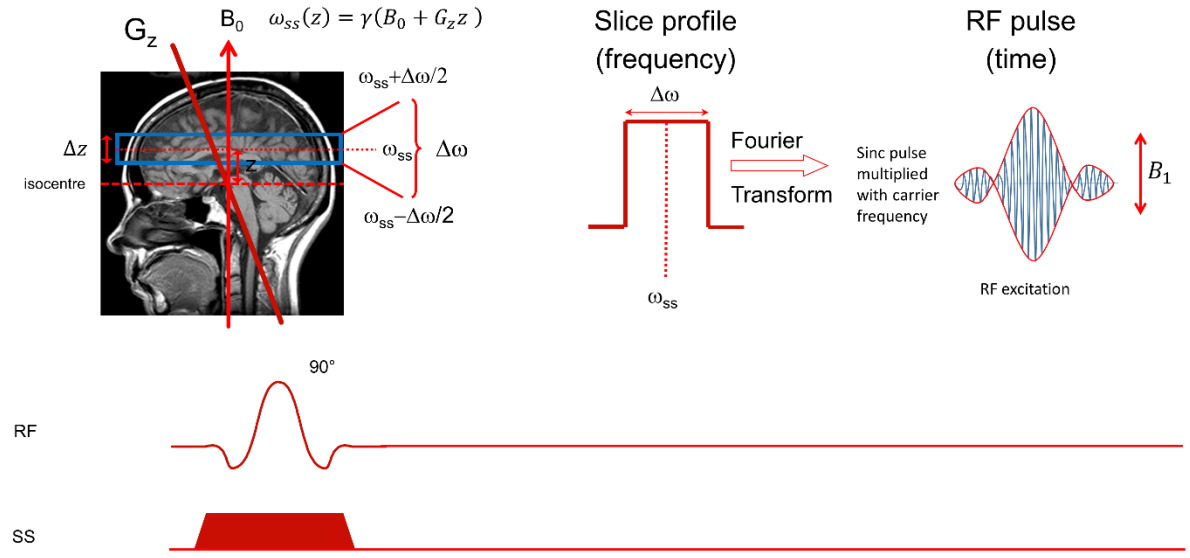


*Figure 2-6: Slice selection gradients are applied during application of an RF pulse to selectively excite a slice of tissue (courtesy of Martin Graves)*

In the following, the different steps involved in MR image generation are described. For simplicity, a 2D sequence with a Cartesian readout will be considered. As described in section 2.1.1, the detection of an MRI signal requires excitation with an RF pulse. As previously described, the pulse has a certain length and amplitude, which determine its flip angle. Furthermore, it has a carrier component, which oscillates at the carrier frequency $f_0$. In 2D MR imaging, a magnetic field gradient $G_{SS}$ is applied in the slice-encode direction. Now the $B_0$ varies linearly in the z-direction, as does the precession frequency of the local protons ($\omega = \gamma(B_0 + \mathrm{zG_{SS}})$). Therefore, the RF pulse will only excite a thin slice of protons that precess at the selected carrier frequency. The pulse also has an envelope that is multiplied with the carrier component. The envelope is typically an apodized sinc shaped pulse, so that the pulse's Fourier Transform is similar to a rect function with a finite bandwidth. Therefore, the RF pulse will excite nuclei precessing at range frequencies centred around the carrier frequency. The slice width depends on the range of frequencies or bandwidth $\Delta\omega$ around the centre frequency of the RF pulse as shown in Figure 2-6 (121,154,155,164).

### 2.1.4 Phase Encoding

After flipping $M_0$ into the transverse plane, another gradient, varying in a direction perpendicular to $G_{SS}$, is applied for a duration $\tau$. Here it will be assumed that it is the y-direction. As the magnetic field and therefore the precession frequency will vary according to the y-location of each proton, a different phase shift will be encoded into the signal according to the y-location. Therefore, this is called the phase-encode gradient $G_{PE}$. In fact, the magnetic field at a specific y-location has the magnitude of $G_{PE}y$ added onto $B_0$, so that the phase accumulation due to $G_{PE}$ at said location at time t will be $\gamma \int_0^t G_{PE}y\, dt$. Therefore, after the gradient has been applied for a time period $\tau_{PE}$, a specific, constant phase shift is applied to each location in the y-direction: $2\pi k_y(\tau_{G_{PE}})y = \gamma \int_0^{\tau_{G_{PE}}} G_{PE}y\, dt$ (121,154,155,164).

### 2.1.5 Frequency Encoding

Finally, another gradient in a direction perpendicular to both $G_{SS}$ and $G_{PE}$ is applied in this case assuming this is the x-direction. In conventional sequences such as spin echo or gradient echo, which will be described in more detail, later on, the gradient will be applied during the time an echo is generated, during which time the data will be read out. The readout gradient or frequency encoding gradient varies linearly along the x-direction and has a specific magnetic field strength at each location, $xG_{FE}$, which alters the precession frequency along the x-direction, so that at the time a data point is recorded, $\tau_{FE}$, the spins experience the following phase shift: $2\pi k_x(\tau_{FE})x = \gamma \int_0^{\tau_{FE}} G_{FE}x\, dt$ (121,154,155,164).

### 2.1.6 *k*-space

Therefore, the signal at every single data-point from every single 2D location can be rewritten as $S \propto S(x,y)e^{\,i2\pi k_y y}e^{i2\pi k_x x}$. The signals from all points in the field of view can be combined by an integration operation: $S \propto \int\int S(x,y)e^{\,i2\pi k_y y}e^{i2\pi k_x x}dxdy$, which corresponds to a 2D Fourier transform operation. Therefore the image can be recovered from the measured signal in k-space by applying an inverse 2D Fourier Transform, and the signal recorded at time t corresponds to a point in Fourier or *k*-space at location $(k_x, k_y)$ (121,154,155,164).

Following a single phase encode step, the echo signal is sampled $N_{FE}$ times at $N_{FE}$ different time points during signal readout. This means that for each phase encode step a series of $N_{FE}$ $k_x$ values are acquired, a line in *k*-space is filled. By repeating the acquisition and each time varying the amplitude $G_{PE}$, all of the points required to fill the entire *k*-space can be acquired. This is needed in order to apply an inverse 2D Fourier transform and reconstruct the image (121,154,155,164).

The following relationships hold between resolution ($\Delta x, \Delta y$), field of view ($FOV_{FE}, FOV_{PE}$), spatial frequencies (frequency resolution = $\Delta \mathrm{k}_x, \Delta \mathrm{k}_y$), and spatial frequency FOV ($FOV_{k_x}, FOV_{k_y}$), i.e. the range of spatial frequencies. The pixel size is calculated as (121,155,164):

$$\Delta x = \frac{1}{FOV_{k_x}}, \Delta y = \frac{1}{\mathrm{FOV_{k_y}}} \qquad \textit{2-10}$$

The field of view is given by multiplying the resolution by the number of phase encode or frequency encode steps respectively (121,155,164):

$$FOV_{FE} = \frac{1}{\Delta k_x}; FOV_{PE} = \frac{1}{\Delta k_y} \qquad \textit{2-11}$$

### 2.1.7 2D vs 3D Image Acquisition

Instead of exciting a thin slice with the slice select gradient, a thick volume can be excited. A second phase encode gradient is then applied in the slice select or third direction. This means that the signal can be recovered by applying a 3D instead of a 2D inverse Fourier transform to the acquired *k*-space (121,154,155,164).

### 2.1.8 Basic Pulse Sequences

#### *Spin Echo*

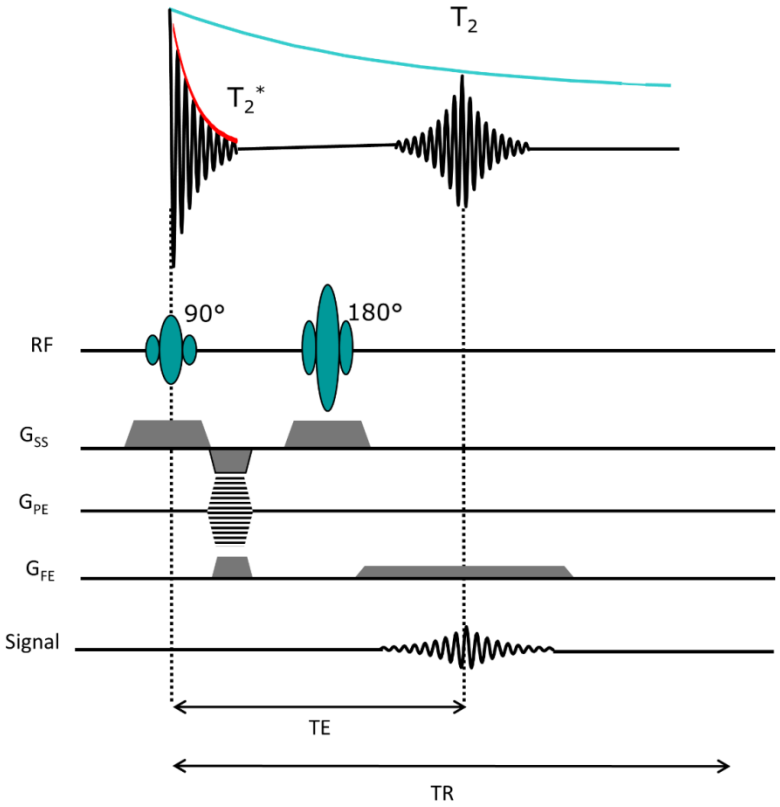


*Figure 2-7: Spin echo imaging sequence (courtesy of Martin Graves)*

Spin Echo is one of the basic sequences in MRI. After an initial excitation by a 90° RF pulse, the transverse magnetization will quickly decay with $T_2^*$. While the dephasing caused by spin-spin interactions is irreversible since it is random and time averaged, the static de-phasing, for example caused by magnetic susceptibility inhomogeneities, can be reversed. After a specific time TE/2, an additional 180° RF pulse is applied. This will now flip the spins through 180° about the axis onto which it is applied. The spins that precess faster will be placed behind those precessing at a lower frequency, so that after an additional TE/2, they will have reversed the de-phasing caused by the static field inhomogeneities alone, resulting in a spin echo signal. The only dephasing that will have occurred at time TE will be due to the spin-spin interactions, which is governed by $T_2$:

$$S \propto \left(1 - e^{-\frac{TR}{T_1}}\right) e^{-\frac{TE}{T_2}} \qquad 2\text{-}12$$

During the signal readout, the readout gradient is applied. In order to reverse the dephasing induced by the readout gradient and set the initial k-space position, a prewinder gradient applied. This is of the same polarity as the readout gradient as its effect is reversed by the 180° pulse (121,164).

After a repetition time, TR, the longitudinal signal will recover and another 90° excitation pulse will be applied to generate a new echo. By adjusting TE and TR, different types of contrast can be achieved. If TR is very long, $M_z$ will have completely recovered and the effect of differences in the $T_1$ relaxation time between different tissue types on the signal is negligible. If the TE is long, the effect of differences in between the $T_2$ values of different tissue types is enhanced. If the effects of both $T_1$ and $T_2$ are minimized by a long TR and short TE, the contrast in between different tissue types will depend on differences in the proton density.

$T_1$ weighting is therefore achieved with a short TE and short TR, while $T_2$ weighting is enhanced with a long TE and long TR. In proton density weighted images, the effects of both $T_1$ and $T_2$ are minimized, so that a PD weighting can be achieved with a long TR and short TE (121).

In order to speed up the acquisition time, Fast Spin Echo (FSE) acquires multiple lines of k-space within a single repetition time by employing a train of refocusing pulses. These lines in *k*-space are acquired at different echo times. The effective echo time is determined by the time at which lines around the centre of k-space are acquired, which dominate the image contrast (121,154,155,164).

***Gradient Echo***

In gradient echo imaging, an initial excitation is followed by a conventional free induction decay (FID). After initial excitation with an RF pulse with a flip angle typically smaller than 90° a smaller amount of longitudinal magnetization will be flipped into the transverse plane. This requires a smaller repetition time for full signal recovery. The maximum signal for a given TR and $T_1$ is given by the Ernst angle, which is defined as $\alpha_{Ernst} = \cos^{-1}\left[\exp\left(-\frac{TR}{T_1}\right)\right]$. Then the signal is read out at an echo time TE, during which the frequency encode gradient is applied. In order to avoid de-phasing due to

the frequency encode gradient and record the maximum signal in the middle of the frequency encode gradient, a pre-phasing gradient is applied in advance. The pre-phasing gradient is of opposite polarity to the readout gradient and has half the area of the readout gradient. Therefore, it will accelerate the signal dephasing by increasing the precession frequency. The readout gradient will reverse this effect due to its opposite polarity to create a gradient echo after half of its area. After signal readout, gradient spoiling is applied. In combination with RF spoiling, this removes any residual transverse magnetization before application of the next RF pulse.

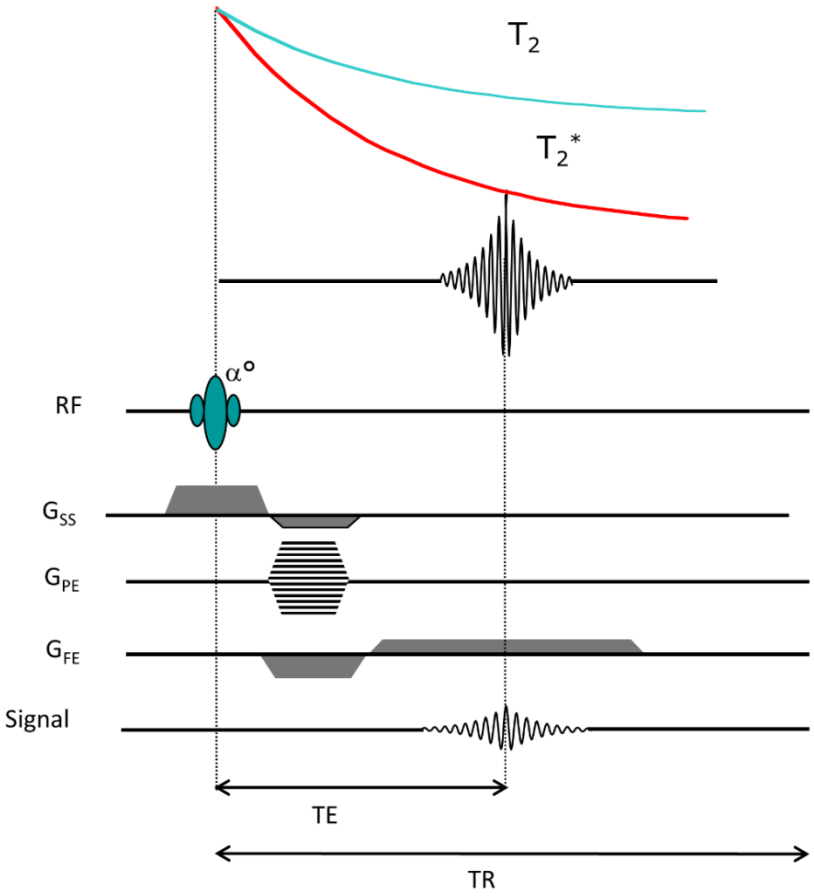


*Figure 2-8: Gradient echo imaging sequence (courtesy of Martin Graves)*

In spoiled gradient echo imaging, the steady state signal acquired at echo time TE can be calculated as (121,164):

$$S(TE) = S_0 \frac{\sin(\alpha)\left(1 - \exp\left(-\frac{TR}{T_1}\right)\right)}{1 - \cos(\alpha)\exp\left(-\frac{TR}{T_1}\right)} \exp\left(-\frac{TE}{T_2^*}\right) \qquad 2\text{-}13$$

A spoiled gradient echo sequence with a large flip angle $\alpha$ (>50°), will weigh the term $\frac{\sin(\alpha)\left(1-\exp\left(-\frac{TR}{T_1}\right)\right)}{1-\cos(\alpha)\exp\left(-\frac{TR}{T_1}\right)}$ more heavily so that the acquired image is said to be $T_1$-weighted. For a given TR, it is important to carefully select the flip angle in order to maximize $T_1$w contrast while maximizing SNR, as shown in Figure 2-9.

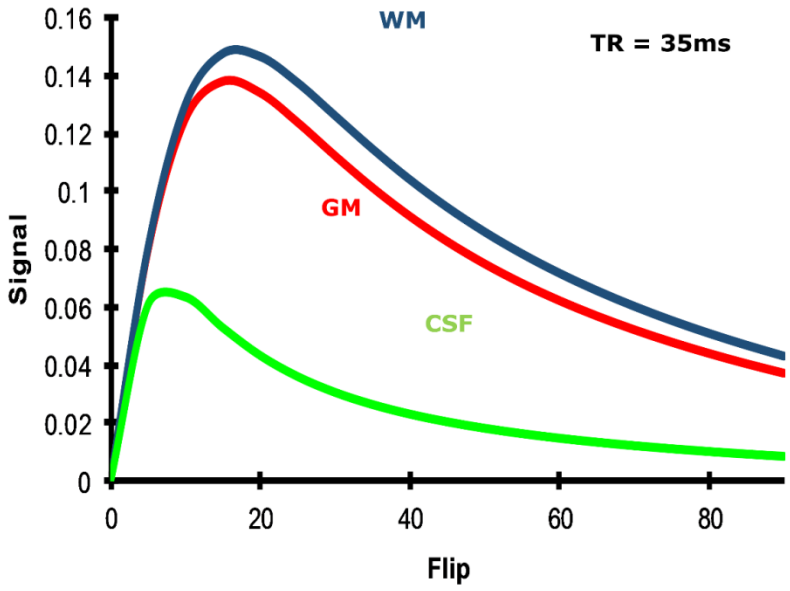


*Figure 2-9: Dependence of the signal magnitude on the applied flip angle (courtesy of Martin Graves)*

A short TE (<15 ms) is required in order to minimize the $T_2^*$ weighting which is given by the term $\exp\left(-\frac{TE}{T_2^*}\right)$, as this term then approaches unity.

If TE is large, the term $\exp\left(-\frac{TE}{T_2^*}\right)$ dominates the signal equation. For a $T_2^*$w image, TE should be as large as possible, while being short enough to maintain a high signal, while $\alpha$ is smaller to minimize $T_1$ weighting (121,154,155,164).

## 2.2 Magnetic Susceptibility in MRI

### 2.2.1 Magnetic Susceptibility

As previously described, the $T_2^*$-weighted imaging contrast arises from a variety of factors. On the one hand, the $T_2$ relaxation time characterises spin-spin interactions. Furthermore, $T_2'$ characterizes the de-phasing caused by static magnetic field inhomogeneities. These may originate from the MR system, affecting the external magnetic field ($B_0$), or instead from magnetic susceptibility effects within the subject.

Magnetic susceptibility ($\chi$) is a material property that describes the magnetizability of an object in response to an external magnetic field with a flux density $B_0$ and a magnetic field intensity $H$. Magnetization $M$ is defined as the magnetic dipole moment per unit volume and is proportional to the magnetic susceptibility: $M = \chi H$ (165,166).

This means that the magnetic moments generated from paramagnetic materials, which are of positive susceptibility, align in parallel with $H$ and $B_0$, while those within diamagnetic materials, of negative susceptibility, do so in the anti-parallel direction (165,166). Each magnetic dipole also has an associated magnetic field, which is of a characteristic shape that is shown in Figure 2-10. The field has two positive lobes in the direction of $B_0$ and negative values around the centre, perpendicular to the direction of $B_0$. It is zero-valued at an angle 54.7° to the direction of $B_0$, which is referred to as the magic angle.

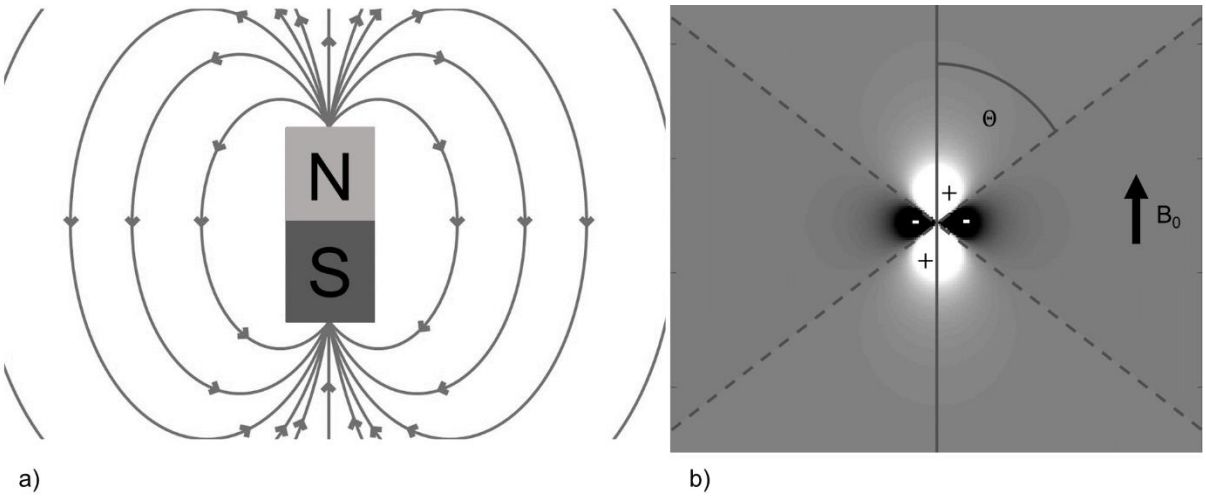


*Figure 2-10: A magnetic dipole can be visualized as a small bar magnet with the magnetic field lines given in (a). The magnitude of the unit dipole field in the direction of $B_0$ is shown in (b) (I published this illustration in* (153)*)*

The total field generated due to the susceptibility distribution $\Delta B$ can be described by a convolution operation, as represented by the convolution operator $\otimes$, between the susceptibility map and the unit dipole field or unit dipole kernel. This is scaled by the applied magnetic field strength of the scanner: $\Delta B(x,y,z) = B_0(\chi(x,y,z) \otimes d(x,y,z))$ (165–169). This can be simplified by applying a Fourier transform since a convolution in the image space corresponds to a multiplication in Fourier space, where k represents the spatial frequencies and $\Delta B(k_x,k_y,k_z)$, $\mathrm{X}(k_x,k_y,k_z)$, and $D(k_x,k_y,k_z)$ are the Fourier transforms of $\Delta B(x,y,z)$, $\chi(x,y,z)$, and $d(x,y,z)$: $\Delta B(k_x,k_y,k_z) = B_0(\mathrm{X}(k_x,k_y,k_z)D(k_x,k_y,k_z))$ (165–169). $\Delta B(x,y,z)$ can then be recovered by applying the inverse Fourier transform. This illustrates that the magnetic field distribution varies with the magnitude and shape of the underlying susceptibility distribution but also contains non-local effects due to the convolution operation. In chapter 3 these relationships will be illustrated further in numerical simulations.

### 2.2.2 Relationship Between Magnetic Susceptibility and the Magnitude of the Complex Signal in Gradient Echo MRI

As previously described, the field inhomogeneities created by the materials' susceptibility contribute to the exponential free induction decay, which is characterized by the time constant $T_2^*$.

$$S(t) = S_o e^{-\frac{t}{T_2^*}} \qquad 2\text{-}14$$

Gradient echo imaging acquires the signal of the free induction decay at a specific echo time and can therefore acquire $T_2^*$ weighted contrast, which shows qualitatively regions of interest with increased de-phasing. Multi-echo gradient echo acquires multiple signal readouts after an initial excitation pulse and therefore serves to sample the free induction decay at different time points. By fitting the signal model to the acquired samples, $T_2^*$ or its reciprocal $R_2^*$ ($R_2^* = \frac{1}{T_2^*}$) can be estimated to provide a quantitative measure of the amount of susceptibility induced dephasing. This has been demonstrated to be useful in a variety of applications, which will be explored in section 2.2.5, for example when estimating varying levels of iron or contrast agent concentration. However, the value of $T_2^*$ also contains $T_2$ influences and also effects from tissue microstructure (160–162).

### 2.2.3 Relationship Between Magnetic Susceptibility and the Phase of Gradient Echo MRI

While $R_2^*$-mapping is excellent at detecting and quantifying the presence of local dephasing it is not able to differentiate between sources of diamagnetism and paramagnetism as it only considers the signal magnitude. However, this may be necessary when the differentiation between the two is not immediately obvious, for example when dealing with diamagnetic calcification and paramagnetic haemorrhage.

The information about the sign of the susceptibility source is contained within the phase of the MR signal. Raw MRI data acquired with quadrature detection are complex valued, which means that it has a real and imaginary part from which both a magnitude term, which is commonly used in clinical image analysis and a phase term, which is typically discarded, can be calculated.

The $T_2^*$-weighted magnitude images do not only display local dephasing based on susceptibility differences alone but also contain information about $T_2$ effects arising from spin-spin interactions. But on the phase images, the $T_2$ effects are negligible (170). Instead the phase varies linearly with the echo time of the acquired signal. The slope of the phase variation with time is proportional to $\Delta B$.

$$\phi(t) = \phi_0 - 2\pi\not{\gamma}\Delta B t \qquad 2\text{-}15$$

Here $\phi_0$ is the initial phase offset and $\not{\gamma}$ the normalized gyromagnetic ratio. Therefore, the phase of a gradient echo signal is closely related to the distribution of field inhomogeneities. As diamagnetic and paramagnetic susceptibility sources create fields of opposite sign, this has allowed for the distinction between different types of materials using the signal phase (171–174). This is an advantage in comparison to gradient echo magnitude images, where sources of diamagnetism and paramagnetism appear as hypointensities.

SWI is a post-processing methodology that makes use of the information contained in the phase by combining the anatomical information contained in the magnitude with phase information:

Initially, so-called phase wraps are removed. While the term $\phi_0 - 2\pi\not{\gamma}\Delta B t$, may exceed the value $2\pi$, the measured signal phase is within the range $[-\pi\ \pi)$ and the displayed phase will become wrapped. Phase unwrapping algorithms may be employed to

remove these prior to background field removal. Subsequently background field effects need to be removed from the signal phase. Since the signal phase of a $T_2^*w$ gradient echo sequence does not only contain contributions of fields generated by susceptibility sources inside the region of interest but also from outside sources a background field removal technique is required. For example, when analysing the brain, the fields generated, for example, by local changes in iron concentration are obscured by background fields. These are typically large and slowly varying and are, for example, created by air tissue interfaces (170,175–177). Other contributions to the background field are shimming effects and inhomogeneities in the main magnetic field of the scanner (170,175–177).Therefore it is necessary to remove these confounding factors from the signal phase, which in SWI is often done by applying a high-pass filter as the background fields are usually large and varying at a low spatial frequency (178). This is frequently implemented by applying a low pass filter to the complex image and subsequently dividing the original complex image by the low-pass filtered image (178–181). The phase of the result is now high-pass filtered. As the large slowly varying frequency components have been removed a lot of phase wrapping artifacts have been removed simultaneously, so that an additional dedicated phase unwrapping algorithm may not be required (178–181). The resulting filtered phase information can be interpreted on its own or it can be used to generate a phase mask that selectively suppresses the signal where the phase shift is either positive or negative, as it is assumed that these phase shifts are generated by diamagnetic or paramagnetic susceptibility sources respectively (171–174,178,180–182). For example, in susceptibility weighted venography, it is assumed that deoxygenated blood is of a positive susceptibility and will present on the phase images with a negative phase shift. Therefore, the mask is set to unity wherever the phase shift is positive, and normalized to be between zero and one where it is negative:

$$Mask(x,y) = \begin{cases} \frac{\pi+\phi(x,y)}{\pi}; if\ \phi(x,y) \leq 0 \\ 1; if\ \phi > 0 \end{cases} \qquad 2\text{-}16$$

The mask is subsequently multiplied n times with the magnitude image:

$$SWI = Mag \times Mask^n \qquad 2\text{-}17$$

The number of multiplications n is typically varied in order to optimize the contrast-to-noise ratio (CNR) depending on the structure of interest and the echo time. A

commonly used value is n=4 (178,180,181). In addition to that, minimum intensity projections (miP) are applied frequently through the stack of slices to image the cerebral vasculature (178). This process is illustrated in Figure 2-11.

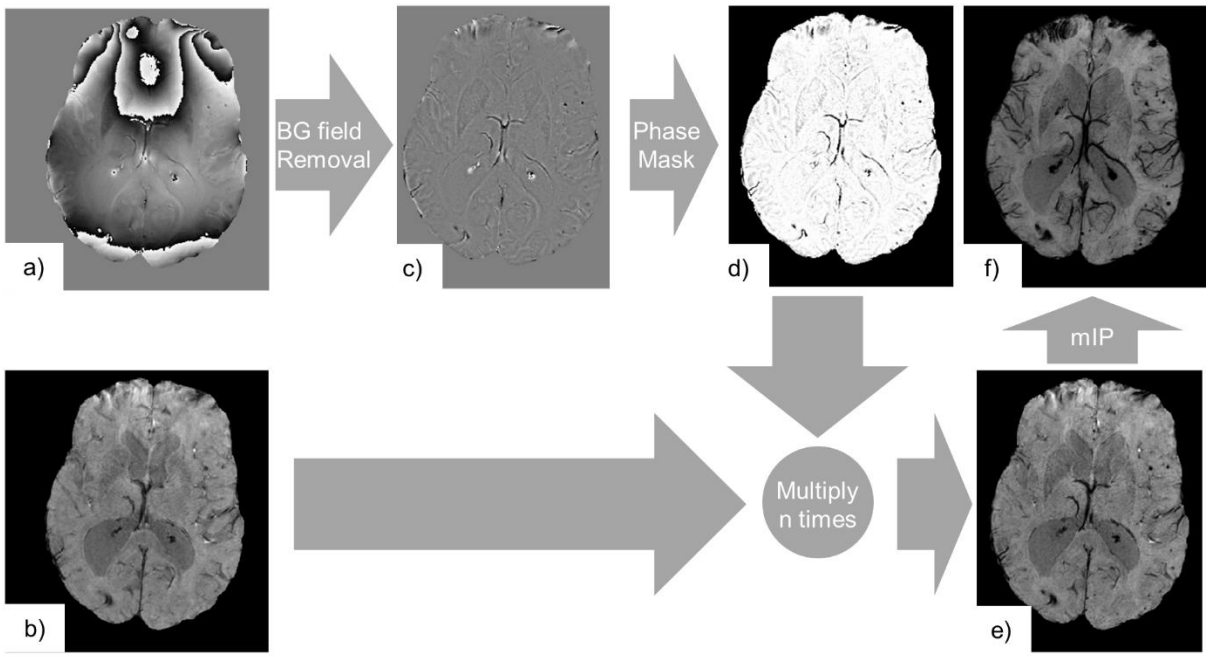


*Figure 2-11: Steps involved in SWI: The complex data consist of a phase (a) and magnitude image (b). In the first step, the phase is filtered (c) and subsequently turned into a phase mask (d). This mask is then multiplied n times with the magnitude image in order to acquire the susceptibility weighted image (e). An mIP can be applied for improved visualization of veins (f). (I published this illustration in* (153)*)*

However, just as for $T_2^*$-weighted imaging or $R_2^*$-mapping, SWI depicts the variation in the local field rather than the underlying susceptibility distribution. As previously explained the field is non-local and a downstream result of the susceptibility map and depends on the field strength and orientation. Furthermore, it extends beyond the local susceptibility changes. The relationship between field and susceptibility is further explored in chapter 3. By calculating the susceptibility distribution directly, Quantitative Susceptibility Mapping (QSM) is able to circumvent these effects and create a direct and quantitative map of the underlying material properties (166,170).

### 2.2.4 Quantitative Susceptibility Mapping

QSM calculates the distribution of susceptibility values within a volume of interest (VOI). Typically, the phase values from different echo times of a multi-echo gradient echo sequence are used to calculate a map of field inhomogeneities. Due to the non-locality of the fields generated by susceptibility variations, the measured field within

the VOI contains contributions that originate inside, $\Delta B_{int}$, and outside, $\Delta B_{ext}$, the selected volume. In order to calculate the susceptibility map inside the VOI, however, it is necessary to remove the background field $\Delta B_{ext}$ which is typically large and slowly varying; after the extraction of $\Delta B_{int}$ a mathematical operation called dipole field inversion can be applied in order to estimate the susceptibility map. This step involves the solution of an ill-posed problem so a variety of algorithms relying on several assumptions and regularisation parameters have been used to estimate the susceptibility map. QSM and the different algorithms used to implement it are described and illustrated in more detail in chapter 3.

### 2.2.5 Applications of Quantitative Susceptibility Mapping

In order to show the potential of both SWI and QSM, the following sections will illustrate the already existing applications of susceptibility-based contrast, which has proven to be a beneficial tool in many applications, such as neurodegenerative, oncological, and cardiovascular pathologies.

#### *Cerebral Imaging*

Susceptibility-based contrast has found many applications in brain imaging so that many of the initial QSM research has been applied in the brain. Varying myelin and iron concentrations—which are more diamagnetic and paramagnetic than water respectively—can be depicted on QSM, so that it can be used to provide highly detailed anatomical maps of the brain. QSM proved to be consistent with previously established techniques to measure iron concentrations in the brain. There was a high correlation with more established relaxation rate mapping MRI techniques and also post mortem iron values, X-ray fluorescence, inductively coupled plasma mass spectrometry, and QSM was consistent with histology (183–186). Simultaneously, QSM improved the CNR compared to SWI and $T_2^*$w imaging and $T_2^*$-mapping (187), so that it was able to detect structures which were consistent with histology, but might otherwise be missed (184,188,189). QSM directly quantified iron and myelin concentration without dependence of orientation or geometry of the ROI and non-local effects (186,189,190). These improvements suggest that QSM may be better in identifying targets in surgery planning for deep brain stimulation (DBS) (184,187,188) than conventionally used MRI techniques using susceptibility based contrast, which have previously been proved useful in this application (191).

Due to its quantitative nature, QSM can be used in longitudinal studies and track disease progress and structural changes over time that are caused by neurodegenerative diseases such as multiple sclerosis (MS), Parkinson's disease (PD), and Alzheimer's Disease (AD).

MS is associated with demyelination and cerebral iron accumulation, the latter of which has been shown using $T_2^*$-mapping (192) and SWI (193). However, demyelination, which prolongs the $T_2^*$ value and iron accumulation, which shortens it, have counteracting effects, that may lead to a lack of detection sensitivity for techniques using the $T_2^*$ effect to monitor early disease stages (190,194). Both disease developments increase tissue susceptibility, which can be depicted with QSM so that it is more sensitive to these disease developments than $T_2^*$ mapping (190) and is suitable to monitor the disease in its early stages (190,195,196). Due to its quantitative nature QSM is able to track the development and progression of the disease over different stages and compare these to healthy tissue quantitatively (195,197). This is very promising since demyelination- and iron-induced susceptibility effects detected on MRI have previously shown to correlate with disease duration and clinical disability (192,198).

AD and PD are also associated with elevated iron levels, which have been detected with susceptibility-based contrast (199–201) and with QSM (202–211). Susceptibility effects have served to monitor PD over time (212,213) and correlate iron levels with disease severity in terms of motor symptoms (214–216). This shows that QSM-identified changes in iron concentration may allow for longitudinal, quantitative tracking of disease progression.

***Cerebral Haemorrhage***

A common pathology that exhibits large susceptibility differences is haemorrhages. Different blood products contained in haemorrhages are deoxyhaemoglobin, methaemoglobin, and/or hemosiderin, which are paramagnetic (217,218). In various studies, susceptibility-based imaging improved detection of haemorrhages due to a better lesion contrast than with other magnitude based techniques and/or CT (219,220). As previously discussed QSM can improve on SWI in several aspects. Due to the removal of non-local effects and its quantitative nature QSM could more

accurately estimate blood product volume (221) and distinguish them from veins more easily (222).

This is advantageous in a variety of medical conditions where cerebral haemorrhages are present, such as stroke (223), cerebral cavernous malformations (224), and Traumatic Brain Injury (TBI) (222). QSM was not only able to provide excellent qualitative detection of lesions but was also able to quantitatively assess lesion size and iron content (221–224). This may allow for QSM to help understand disease developments in terms of progression but also treatment response and also determining disease severity (221–224). While suffering from several drawbacks in comparison to QSM, SWI has demonstrated the benefit of susceptibility based imaging since it was used to depict the occurrence and volume of microbleeds in order to assess their correlation with coma scores so that their importance as a marker of injury severity in patients with diffuse axonal injury could be evaluated (220).

***Blood Oxygenation and Venography***

Paramagnetic deoxyhaemoglobin is not only present in blood products but also in deoxygenated venous blood. Therefore cerebral venography is one of the most common applications of SWI (178) and QSM has shown potential to improve venogram image quality by removing non-local effects and sequence and scanner dependencies (225,226). For example, it has been demonstrated, that it can be assumed that veins in parallel to the magnetic field $B_0$ will produce a negative phase shift. The detection of veins perpendicular to the magnetic field with a negative phase shift on SWI, however relies on asymmetric voxel dimensions (178). Due to the lack of orientation dependence in QSM, all veins will appear as paramagnetic, unrelated to their physical location. Furthermore, QSM offers a quantitative assessment of the susceptibility measured inside each vein, which is linearly related to oxygen saturation and therefore deoxyhaemoglobin content. In combination with cerebral blood flow measurements, this allows QSM to calculate further measures such as oxygen extraction or cerebral metabolic rate of oxygen (225–228). It has therefore demonstrated to be feasible to use QSM to not only monitor normal deoxyhaemoglobin levels (226) but also changes induced by $CO_2$ inhalation (228) or caffeine administration (227). In addition to research settings, this technique has demonstrated promising potential in assessing stroke patients (229).

The mapping of cerebral oxygen levels can be extended even further in the temporal domain. Blood oxygen level dependent (BOLD) contrast uses the $T_2^*$ effect in functional MRI (fMRI) (230) to measure brain activity over time and in response to stimuli. It has subsequently been suggested that acquiring dynamic susceptibility maps at different time points eliminates non-local effects present on $T_2^*$ images and may provide a more direct measure of neuronal activity (231–233).

***Susceptibility-Based Contrast in Neuro-Oncology***

Blood products and haemorrhages play an important role in neuro-oncology, which is another field of frequent application of susceptibility-based contrast techniques.

SWI was not only able to improve tumour visibility (234), but also provide a morphological assessment through a high detection sensitivity of haemorrhages and venous vascular networks (235) and improved their distinction from calcifications, necrosis and artifacts when compared to conventional MRI protocols (236). The improved characterization of the tumours, could be used to grade tumours (235) and differentiate between different tumour types (237) and metastases (238), which found application in initial screening, and diagnosis, monitoring and treatment decisions (235–238). While more experimental, QSM has shown potential for improvement of existing techniques further by improving the differentiation between blood products and calcification (239).

***Susceptibility-Based Contrast outside the Brain***

The majority of applications for QSM have been developed for imaging the brain since other anatomies offer several difficulties, such as increased motion or the presence of fat. However, differences in susceptibility are present everywhere in the body and may provide vital medical information about a large number of pathologies.

As was shown in the brain, QSM and SWI were able to detect calcifications within breast tissue (240,241) and QSM detected calcifications in prostate cancer (242,243).

The imaging of neurodegenerative diseases has shown that susceptibility-based contrast may be an excellent tool for monitoring changing tissue iron concentrations. Similarly, changing iron levels in the liver are a characteristic of liver disease so that SWI has been used in staging liver fibrosis by detecting increased iron content and collagen deposition (244,245) and in liver cirrhosis for identifying iron in siderotic nodules (246). There are fewer applications of QSM in the liver due to its location and

the complications arising from the presence of fat, but QSM has shown promise in monitoring liver iron concentration and showed a good correlation with the measured $T_2^*$ values and biomagnetic liver susceptometry (247,248).

Susceptibility effects are not only limited to endogenous sources but may also originate from exogenous contrast agents, such as paramagnetic gadolinium-based contrast agents (GBCA) and (ultra)small superparamagnetic iron oxide nanoparticles (USPIO). Contrast agent concentration is linearly related to the measured susceptibility, so that QSM is able to quantify the amount of contrast agent present in the anatomy. GBCAs have been applied primarily as a blood pool contrast agent in cerebral perfusion imaging and to create dynamic three-dimensional susceptibility maps (249,250). USPIOs and SPIOs have also been used as a blood pool agent for detection of microvasculopathy, e.g. in cerebral amyloidosis, where they seemed to be more sensitive to vascular leakage than dynamic contrast enhanced (DCE)-MRI (251). Furthermore, these types of contrast agents can be taken up by macrophages so that they have found application in detecting inflammatory activity in the liver and spleen (252) and also detect inflammatory activity in carotid artery plaques as described in chapter 1.

# Chapter 3 Quantitative Susceptibility Mapping: Background and Numerical Simulations

Aspects of this work have been published in “Ruetten PPR, Gillard JH, Graves MJ. “Introduction to Quantitative Susceptibility Mapping and Susceptibility Weighted Imaging”. Br J Radiol. 2019;92(1101):20181016. doi:10.1259/bjr.20181016. (153)

## 3.1 Introduction

As discussed in the previous chapter, there are a wide variety of applications of susceptibility-based contrast in both the clinic and in research. To understand the challenges, scope for optimization, and potential in different anatomies and pathologies it is important to understand the underlying physical principles. These can subsequently be used in order to understand the different steps and algorithms involved in Quantitative Susceptibility Mapping (QSM). In the following, the theoretical underpinning of these algorithms will be explained and subsequently their application will be illustrated in numerical simulations and human brain imaging.

## 3.2 Theory

QSM consists of several steps: Initially, the complex images from a multi-echo gradient echo sequence are acquired. If multi-channel coils are used, the complex data from all channels need to be combined in a way that preserves the integrity of the phase information. Next, the map of magnetic field inhomogeneity is estimated by performing a fitting operation with the multi-echo data. During and after this process phase unwrapping may be required to eliminate unwanted aliasing effects. Subsequently background fields are removed and then a susceptibility map is generated from the internal field via dipole field inversion.

### 3.2.1 Relationship between Phase and Field

After acquisition of the complex multi-echo gradient echo data, before estimation of $\Delta B$, it is important to consider the issue of coil combination of the complex gradient echo signal which is important when the signal is acquired using a multi-channel array coil. The image from each channel carries a coil specific phase offset, which needs to be considered when combining the images as otherwise artifacts may arise in the composite phase image (170,253,254). One approach is called the phase difference method, where the offset is removed by subtracting the phase images at two different echo times through complex division from one another. The difference images do not carry any offset and can be added together in a weighted manner (170,253–255). Other methods estimate the coil specific phase offset and subtract it from each coil image before combination (253,254,256). Another example are parallel imaging approaches such as SENSE (257) which may be used for magnitude and phase reconstruction. These methods use an a priori acquired reference scan using a body coil to reconstruct the coil images (170,253,257).

As previously described, the phase $\phi(t)$ of the free induction decay signal varies linearly with time $t$, with an initial phase offset $\phi_0$. Its slope is proportional to the normalized gyromagnetic ratio $\not\gamma$, a constant, and the field inhomogeneity $\Delta B$ in the direction of $B_0$ (258,259):

$$\phi(t) = \phi_0 - 2\pi\not\gamma\Delta B t \qquad 3\text{-}1$$

Determining the slope of the phase variation for each voxel in order to estimate $\Delta B$ is frequently done using a least-squares algorithm (258–260). Other implementations have also estimated the phase from a single echo (217,258). While this description of the phase evolution over time holds true in the brain, in other parts of the body the presence of fat alters the signal model:

$$S \propto \left(W + Fe^{-i2\pi\Delta f_{chem}TE}\right)e^{-i2\pi\not\gamma\Delta BTE} \qquad 3\text{-}2$$

Fat differs in precession frequency from water by a frequency offset $\Delta f_{chem}$. Here W is the water image and F is the fat image. Ignoring this effect leads to a phase shift being added onto the $\Delta B$ estimate, which manifests as an artifact and can lead to artifacts in susceptibility mapping as will be shown in chapters 5 and 6. Water-fat separation techniques aim to estimate the fat fraction within each voxel and estimate how much

this alters the local precession frequency. This can be used to simultaneously correct $\Delta B$ within each voxel for QSM (166,241). An example for a water-fat separation technique, which will be discussed in more detail in chapters 5 and 6, is iterative decomposition of water and fat with echo asymmetry and least-squares estimation (IDEAL) (261,262). This algorithm uses the complex signal from a multi-echo gradient echo dataset and fits the signal model to this dataset. $\Delta B$, W, and F are iteratively determined. This has been used to remove chemical shift artifacts in several parts of the body. This methodology has been used in order to remove the chemical shift in the $\Delta B$ estimation in order to perform QSM in other parts of the body than the brain such as the liver (247,248,263–265), breast (241), spine (266), or ankle region (267).

When estimating $\Delta B$ it is important to consider that the phase of a complex number is bound to the range between $[-\pi\ \pi)$. However, $\phi_0 - 2\pi\gamma\Delta B$ may exceed these values so that the measured phase $\phi_w$ becomes wrapped into the range $[-\pi\ \pi)$. This is a form of aliasing that can be corrected by phase unwrapping algorithms, which give a corrected phase estimate by adding an integer multiple ($k$) of $2\pi$ onto the wrapped phase (258–260):

$$\phi_{uw} = \phi_w + k2\pi \qquad 3\text{-}3$$

In QSM these phase wraps may occur in both the temporal and spatial domains. Temporal phase unwrapping is performed when a phase wrap has occurred between subsequent echoes, so that the slope can be correctly estimated. This is illustrated in section 3.4.2, Figure 3-16. Then a scaled version of $\Delta B$, ($\Delta\phi = 2\pi\gamma\Delta TE\Delta B$) is estimated; this may contain phase wraps in the presence of large field inhomogeneities, which can be corrected with spatial phase unwrapping algorithms (166,268), such as graph-cut based approaches such as proposed and implemented in by Dong et al. (263) or using region growth phase unwrapping (269,270). Spatial phase unwrapping is illustrated in section 3.4.2, Figure 3-17.

### 3.2.2 Masking

A mask is typically applied in order to exclude regions of insufficient SNR from the analysis. Phase noise can lead to severe errors when estimating $\Delta B$, that may propagate into $B_{int}$ when removing the background field and also when estimating the susceptibility map (271). In the brain, the FSL's Brain Extraction Tool (272) is

frequently used to extract a mask of the brain from the magnitude images. However, this application is limited to application in the brain and in its performance by signal voids close to the brain surface, e.g. due to abnormal brain anatomy such as lesions close to the brain surface, or due to strong field inhomogeneity effects at ultra-high field strengths (273).

### 3.2.3 Background Field Removal

Before estimating the susceptibility map inside the selected region of interest (ROI), it is important to consider that the estimated map of field inhomogeneities consists of contributions from fields that were generated by differences in susceptibility outside the ROI, the external or background field ($B_{ext}$), and from differences in susceptibility inside the ROI ($B_{int}$). QSM only estimates the susceptibility distribution inside the ROI whilst the information about $B_{ext}$ and the outside susceptibility distribution is incomplete. Therefore it is important to remove these fields and extract $B_{int}$ before the final step of QSM, the dipole field inversion (175). Large susceptibility differences, for example those between air and soft tissue or air and cortical bone, can generate large, spatially slowly varying background fields that obscure $B_{int}$, which without removal would cause severe errors in the susceptibility estimation.

In phantom scans, the background field can be simply estimated by performing a reference scan (176,258,259,274). For example, if a sample, from which the susceptibility value is to be determined is placed within a water or gel bath, two scans are performed, one with the sample present and another one where it is absent (176,258,259,274). The susceptibility within the water or gel bath is relatively uniform so that the field measured in the absence of the high or low susceptibility sample can be assumed to be the background field, for example that generated by the air/water interface. However, this uniform background is typically impractical for *in vivo* scans.

Instead it is most practical to estimate $B_{ext}$ within a single scan and separate it from $B_{int}$ by making certain assumptions about the physical and mathematical properties of both fields. A simple approach is to assume that the spatial frequencies at which $B_{ext}$ varies are very low and that it can be removed by high pass filtering the total estimated $B_{total}$. This requires a careful selection of the filter size and whilst this removes a large part of $B_{ext}$, some residue may remain and in addition it may also remove slowly varying components of $B_{int}$ (166,175,178,225,275). Another approach

is geometry dependent artifact correction. By segmenting the magnitude image into regions of air and tissue, and assigning appropriate susceptibility values from the literature to the segments a so-called forward calculation can estimate the field induced by the air tissue interface (276). This technique however only achieves incomplete background field removal as it requires additional high pass filtering to remove residual fields (273,276).

Therefore, it is necessary to characterize $B_{ext}$ more accurately. It has been shown that $B_{ext}$ within the ROI can be better described as a harmonic function (167,176,277,278) and that fields generated from dipoles inside and outside the ROI are orthogonal to each other within the ROI (177).

A harmonic function $u$ is one that satisfies the Laplace equation so that $\nabla^2 u = 0$. The Sophisticated Harmonic Artifact Reduction (SHARP) algorithm makes use of the spherical mean value (SMV) property of harmonic functions to remove background fields (278). The mean value property holds for harmonic functions; this states that the harmonic function $u$, for example the background field, remains unchanged when convolved with a radially symmetric, non-negative, normalized function $\rho$: $u(r) = (\rho \otimes u)(r)$.

In the SHARP algorithm the total magnetic field $B_{total}$, which is the sum of $B_{int}$ and $B_{ext}$ is first convolved with a SMV kernel:

$$B' = \rho \otimes B_{total} = \rho \otimes B_{int} + B_{ext} \qquad 3\text{-}4$$

Therefore, a function of $B_{int}$ can be extracted by subtracting $B'$ from $B_{total}$, where $\delta$ is the unit impulse/Dirac function:

$$\begin{aligned} B'' &= B_{total} - B' = (B_{ext} + B_{int}) - (\rho \otimes B_{int} + \\ B_{ext}) &= B_{int} - \rho \otimes B_{int} \\ &= (\delta - \rho) \otimes B_{int} \end{aligned} \qquad 3\text{-}5$$

Since the convolution with $\rho$ has left $B_{ext}$ unaffected it is removed from $B''$. $B_{int}$ can subsequently be extracted from $B''$ by deconvolving it with the kernel $\delta - \rho$. The kernel is calculated by subtracting one from the central voxel of $\rho$ and then multiplying the result with -1 (278).

$$B_{int} = (\delta - \rho) \bigotimes^{-1} B'' \qquad 3\text{-}6$$

This method improves the separation of $B_{ext}$ and $B_{int}$ but results in a shrinking of the area of the ROI since the algorithm cannot be applied at the edges of the ROI. Other methods, based on the SMV property, that aim to improve the SHARP algorithm have also been proposed (279,280). The Regularized Enabled SHARP, for example, solves the deconvolution operation with a Tikhonov regularization (279).

As mentioned above, the defining mathematical property of harmonic functions, such as $B_{ext}$, is that they solve the Laplace equation within the region of interest: $\nabla^2 B_{ext} = 0$. This implies simultaneously that $B_{int}$ solves Poisson's equation: $\nabla^2 B_{int} = \nabla^2 B_{total}$. In the Laplacian Boundary Value (LBV) algorithm (176) it is assumed that both properties hold to be true within the regions of interest and can be used to set up a system of partial differential equations. These can be solved with the assumption that $B_{ext}$ is much larger within the boundary region than $B_{int}$. This means that the values at the boundary pixels can be defined as $B_{ext} = B_{total}$ and $B_{int} = 0$ (176).

Another background field removal technique is the Projection onto Dipole Fields (PDF) method (177). In brain acquisitions , it has been demonstrated that fields generated by dipoles inside and outside of the ROI are orthogonal to each other (177). The PDF method assumes that $B_{ext}$ can be calculated from a susceptibility distribution outside the ROI, but inside the FOV. In order to achieve this, a minimization problem is formulated based on the orthogonality assumption and the projection theorem in Hilbert space. This allows for the estimation of $B_{ext}$ and $B_{int}$ within the ROI. In the border region, i.e. the voxels close to the edge of the ROI the orthogonality assumption does not hold anymore and the estimation of $B_{ext}$ and $B_{int}$ will contain errors (177).

### 3.2.4 Dipole Field Inversion

After removing the background fields, the remaining field within the ROI, $B_{int}$, in the following also referred to as $\Delta B(x, y, z)$, with its Fourier transform being $\Delta B(k_x, k_y, k_z)$, is assumed to have been generated from the susceptibility variations within the ROI alone, $\chi(x, y, z)$, with its Fourier transform being $\mathrm{X}(k_x, k_y, k_z)$. As described in chapter 2 section 2.2.1, this relationship can be defined as $\Delta B(k_x, k_y, k_z) = B_0 \left(\mathrm{X}(k_x, k_y, k_z) D(k_x, k_y, k_z)\right)$. Here, $d(x, y, z)$ is the unit dipole kernel, and

$D(k_x, k_y, k_z)$ is its Fourier transform. As the map of field inhomogeneities $\Delta B(k_x, k_y, k_z)$, and the dipole kernel $D(k_x, k_y, k_z)$ are known, the susceptibility map $\mathrm{X}(k_x, k_y, k_z)$ can be extracted by dividing $\Delta B(k_x, k_y, k_z)$ by $D(k_x, k_y, k_z)$ in Fourier space: $\mathrm{X}(k_x, k_y, k_z) = \frac{1}{B_o}\left(\frac{\Delta B(k_x, k_y, k_z)}{D(k_x, k_y, k_z)}\right)$. This corresponds to a deconvolution operation in image space. Here, $D(k_x, k_y, k_z)$ is defined as $D(k_x, k_y, k_z) = \frac{1}{3} - \frac{k_z^2}{k_x^2 + k_y^2 + k_z^2}\ for\ k \neq 0$. Therefore, values of $D(k_x, k_y, k_z)$ are defined to be zero at spatial frequencies located on a cone surface at an angle $\beta = \pm 54.7°$ relative to the direction of $B_0$, also defined as the magic angle. The division by zero is an ill-posed problem as its result is undefined. Furthermore, small values of $D(k_x, k_y, k_z)$ in proximity to the zero-cone surface amplify noise (166,274,275).

Another problem arising from the deconvolution operation is that the solution at the *k*-space origin is either undefined (281) or defined to be zero (170), so that all susceptibility values are relative and not absolute. Several techniques have used different reference tissues, such as CSF, white matter, muscle tissue or urine (184).

One approach to fill in the values on the zero value cone surface is to measure these values by acquiring additional MRI data. The Calculation of Susceptibility through Multiple Orientation Sampling (COSMOS) method (274) relies on at least three acquisitions. For each acquisition, the subject is rotated with respect to the other acquisitions and with respect to the magnetic field. Therefore, at most two zero-value cones overlap at each location, so that there is always one acquisition that can fill in the missing values. In cerebral applications, the rotation of the ROI has been achieved by the subject tilting their head. However, the downsides of this method are that the rotation angle needs to be sufficiently large and the total acquisition time is increased by a factor of three. Therefore, while providing excellent performance in terms of SNR, image quality, and CNR, these factors have limited the clinical feasibility of this technique (274).

An ideal method should only require a single acquisition and the values within the zero value cone should be estimated. Several approaches have been proposed that use different types of regularization and solve the problem in *k*-space or in image space.

In order to perform the division in *k*-space, one set of approaches regularizes the dipole kernel. Replacing all values of $\frac{1}{D(k)}$, where |D(k)| is below a certain threshold $\alpha$, with zero (282) or a constant value $\frac{1}{sign(D(K))\alpha}$ (253,275,283) eliminates the problem of dividing by zero or very small values. The choice of $\alpha$ is crucial since a small regularization threshold will only replace values very close to the zero value cone. Noise in this region of *k*-space will be amplified and may obscure the susceptibility map. While increasing the threshold improves the image quality, it will also reduce contrast (275,282). An optimised solution has been proposed by Schweser et al. (283). Here, a large truncation threshold is used in order to minimize noise propagation. In order to account for the truncation induced underestimation, the Point Spread Function due to dipole modification is calculated. It is estimated that from this a constant scalar can be calculated, which can be used to correct for the underestimation. Furthermore, truncation of the dipole kernel also causes streaking artifacts, which primarily arise at the interfaces of two regions of homogeneous susceptibility (284,285). This inversion technique is highly computationally efficient but depending on quality of the underlying data quality may suffer in terms of image quality.

In comparison, image-space based approaches use regularization/minimization operations to estimate the susceptibility map that will produce a field map that resembles most closely the measured field map data. In addition to that, anatomical information can be used to regularize the deconvolution operation.

One example is the Morphology Enabled Dipole Inversion (MEDI) algorithm (281,286–288). The minimization operation estimates the susceptibility map which produces a field with the minimum difference to the estimated $B_{int}$. A regularization term is added onto this data fidelity term. The regularization is based on the assumption that the tissue compartments found on the magnitude images are of uniform susceptibility. Therefore, all edges that are present on the susceptibility map, but not on the magnitude image, should be removed or minimized. This approach particularly aims to reduce streaking artifacts. In order to determine the strength of the regularization, the data fidelity term is multiplied by a regularization parameter $\lambda$. Therefore, a smaller $\lambda$ will mean a stronger regularization and more strict removal of any gradients on the susceptibility map that are not present on the magnitude image. This means that the

map will be smoothed out accordingly, which can improve image quality but may also smooth out smaller details, that may be missed (281,286–288).

## 3.3 Numerical Simulations

### 3.3.1 Field Mapping

***Experimental Setup***

In order to illustrate the individual steps involved in QSM, synthetic field maps were generated based on a ground truth susceptibility map. These examples served to illustrate the relationship between the susceptibility distribution and field maps. In other cases, these maps underwent background field removal and dipole field inversion. The results are compared to the ground truth at each step.

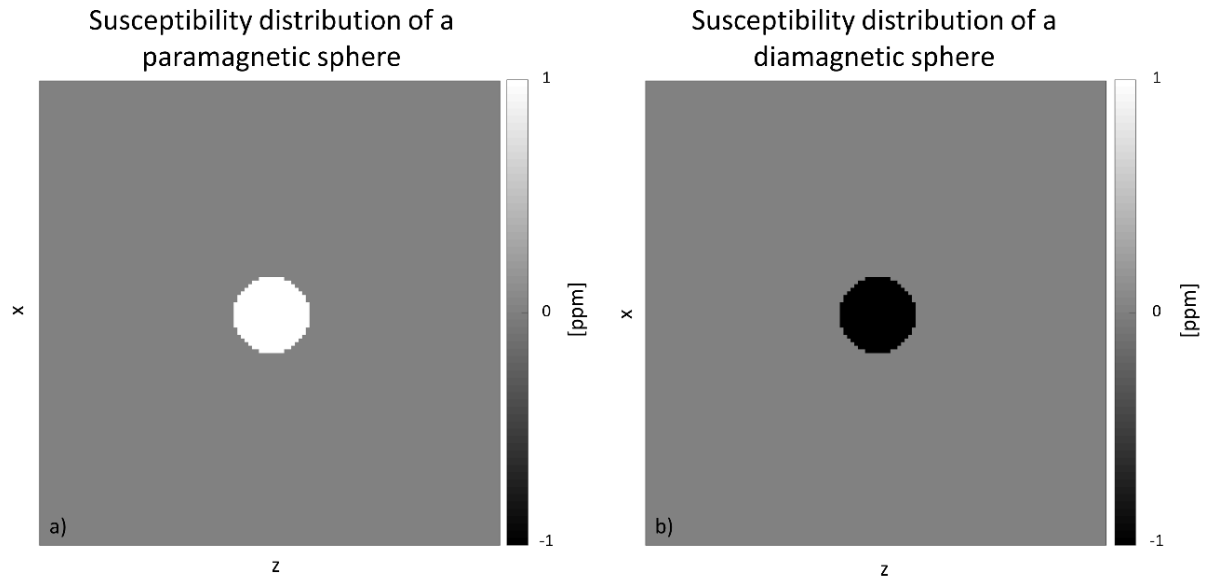


*Figure 3-1: Susceptibility distribution of a paramagnetic (a) and a diamagnetic (b) sphere*

To demonstrate the effects of geometry and orientation in the magnetic field inhomogeneity map, three paramagnetic phantoms were evaluated in numerical simulations. A sphere (Figure 3-1 a)), a cylinder oriented parallel to $B_0$ (Figure 3-2 a-c) and a cylinder perpendicular to $B_0$ (Figure 3-2 d-f), each of 1 ppm susceptibility, were placed in a background of 0 ppm susceptibility. Furthermore, a sphere of negative susceptibility was also analysed ($\chi$ = -1ppm) (Figure 3-1 b).

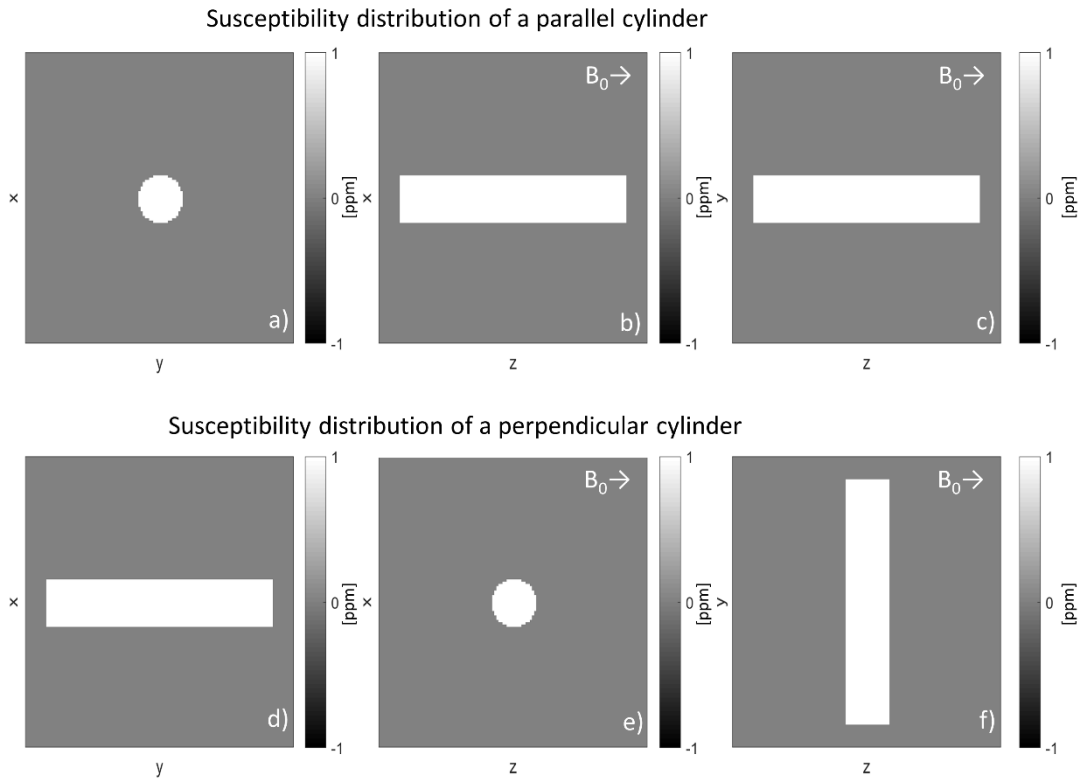


*Figure 3-2: Susceptibility distribution of a cylinder in parallel (a-c), and perpendicular to (d-f) $B_0$.The two cylinders are shown in the x-y (a, d), x-z (b, e), and y-z (c, f) planes.*

A forward calculation was performed to generate the field maps created by these susceptibility distributions. This corresponds to a convolution of the susceptibility map with the unit dipole kernel: $(d * \chi)(r)$ (165,168,289). The simulations were performed in Matlab (The MathWorks, Natick, MA). The Fourier transformed dipole kernel $D(k_x, k_y, k_z)$ was generated using the MEDI toolbox (http://pre.weill.cornell.edu/mri/pages/qsm.html and http://pre.weill.cornell.edu/mri/pages/qsmreview.html). The resulting field maps were compared to the unit dipole kernel, which was also generated using the MEDI toolbox. This set of forward calculations served to illustrate the differences in field distributions from susceptibility distributions that differed in sign, geometry, and orientation.

### *Results*

The field of a unit dipole, i.e. the field generated by an infinitely small susceptibility source, can be seen in Figure 3-3 from three different orientations. The main magnetic field is in the z-direction. The characteristic field has a positive lobe on either side of the dipole in parallel to the direction of the external magnetic field and there is a circular doughnut shaped negative field surrounding the dipole perpendicular to $B_0$.

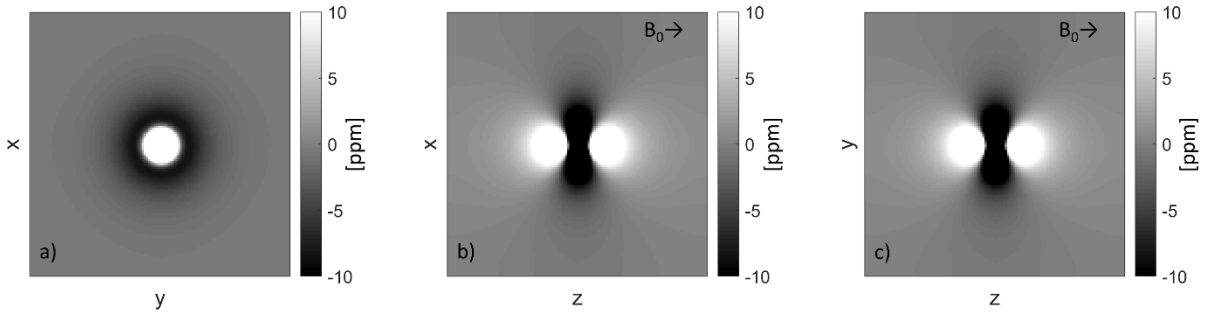


*Figure 3-3:Unit dipole field in the x-y (a), x-z (b), and y-z (c) planes. The main magnetic field is in the z-direction.*

The unit dipole is essentially an infinitely small spherical shape, which is why the field resembles that of the spherical phantom in Figure 3-4 a-c. When assessing the field generated by a negative sphere, it can be seen that it equals the field generated by the positive sphere, multiplied by a factor of -1 (Figure 3-4 d-f).

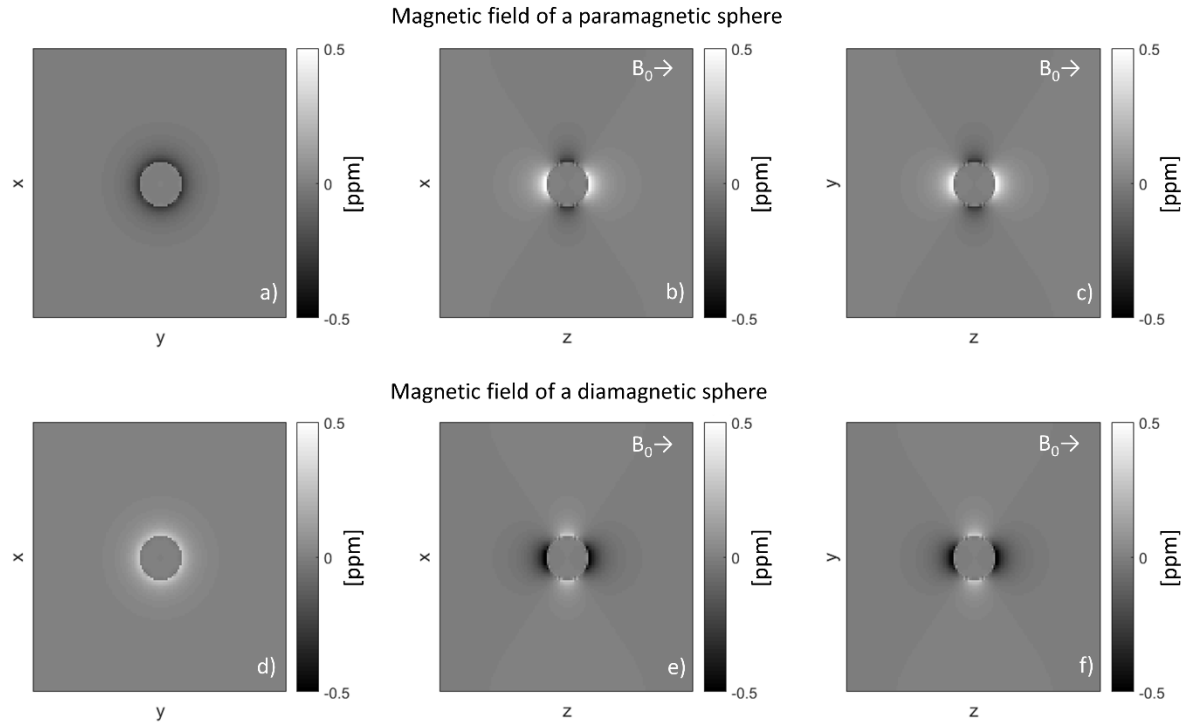


*Figure 3-4: Field generated by a paramagnetic (a-c) and diamagnetic sphere (d-f) in the x-y (a,d), x-z (b,e), and y-z (c,f) planes. $B_0$ is in the z-direction.*

When considering the cylinders, it can be seen that the induced field distribution has positive lobes in the direction of the external magnetic field and negative lobes perpendicular to the magnetic fields (Figure 3-5). As there will be fields induced within the cylinders, we can see that when in parallel to the magnetic field, positive fields will

dominate the field map inside the cylinder parallel to $B_0$ (Figure 3-5 a-c), and that when its orientation is perpendicular to the field, the negative fields will dominate (Figure 3-5 d-f). This is in keeping with observations made regarding SWI for venous imaging (178).

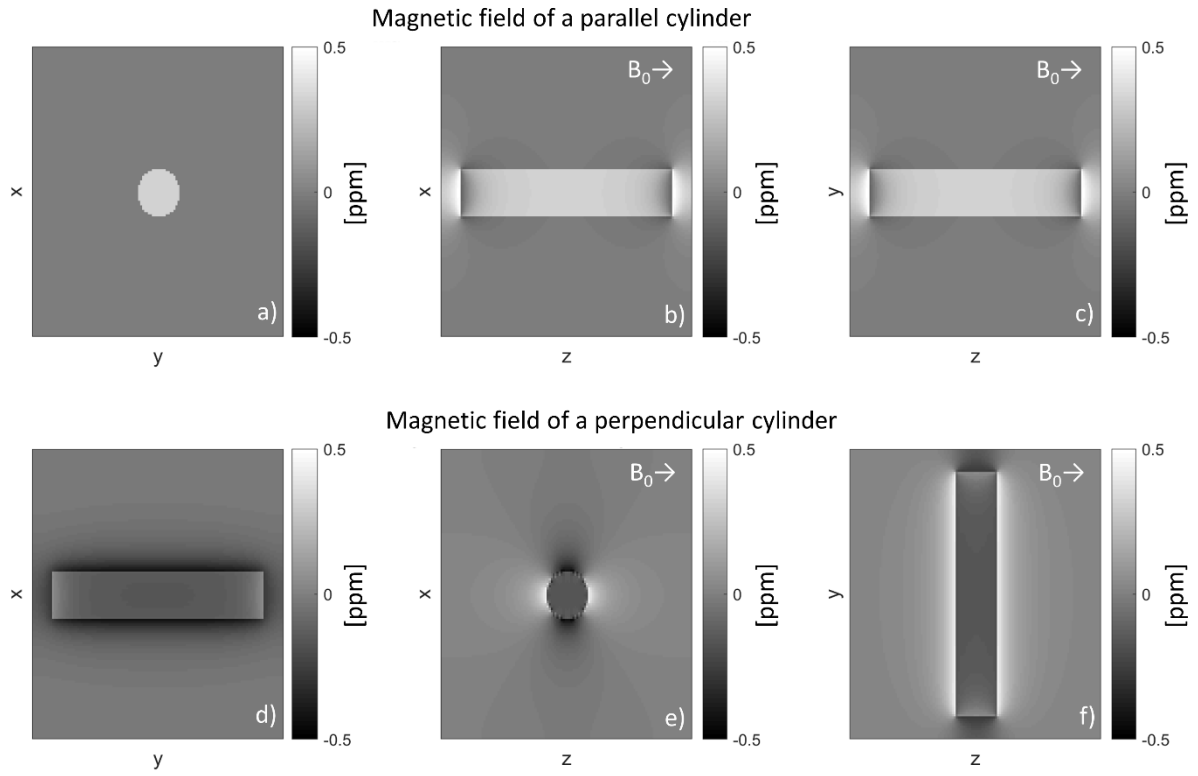


*Figure 3-5: Field generated by a paramagnetic cylinder oriented in parallel (a-c) and perpendicular to $B_0$, shown in the x-y (a,d), x-z (b,e), and y-z (c,f) planes. $B_0$ is in the z-direction*

### 3.3.2 Background Field Estimation

#### *Experimental Setup*

After exploring the differences in fields created by different susceptibility distributions, two background field removal algorithms, Projection onto Dipole Fields (PDF) and Laplacian Boundary Value (LBV), were evaluated using the following simulated arrangement. The codes for the background field removal algorithms were also obtained from the MEDI toolbox (http://pre.weill.cornell.edu/mri/pages/qsm.html and http://pre.weill.cornell.edu/mri/ pages/qsmreview.html). A field map was generated from six spherical phantoms (with susceptibilities in the range 0.5 ppm to 3 ppm, increasing in 0.5 ppm steps, which were chosen to simulate Gadolinium doped water phantoms with small variations in susceptibility that were biologically relevant) placed within a 'water tank' (a large cuboid volume with the susceptibility value set to 0 ppm

which is the susceptibility of water relative to air) in front of a background of 9.41 ppm susceptibility simulating air (290). The susceptibility distribution is shown in Figure 3-6.

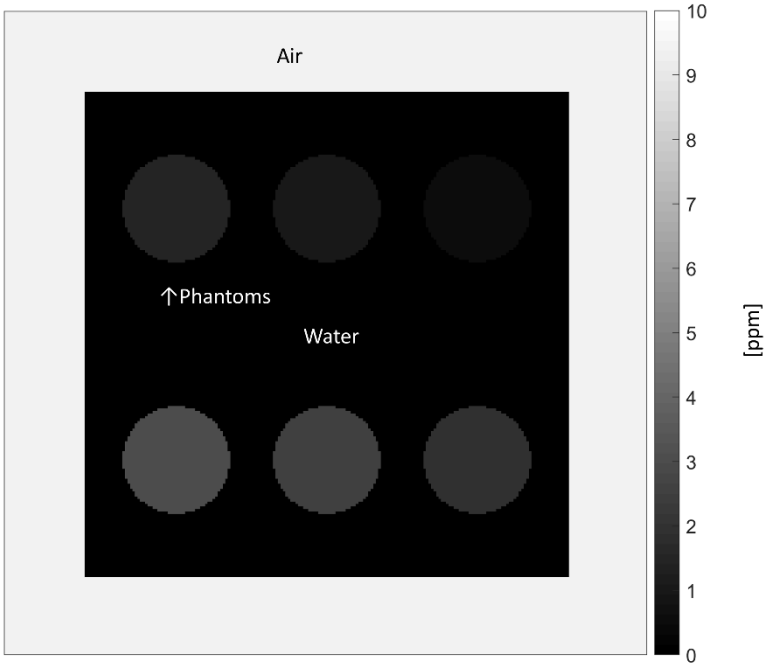


*Figure 3-6: Susceptibility distribution for the numerical phantom simulations*

$B_{int}$ for the cubic MRI-signal-generating volume, is generated considering only the susceptibility difference between water and the phantoms, while $B_{ext}$ originates from the susceptibility difference between air and water. The fields created from only a water tank placed within air without any phantoms present ($B_{ext}$) and the field generated by the set of paramagnetic spheres placed within a background of uniform susceptibility (0 ppm), with their susceptibility set to the same value as the difference between the phantoms and water ($B_{int}$) were calculated and served as ground truth estimates.

Subsequently, the simulations were repeated with the addition of noise. In order to add complex Gaussian noise to the field map, it was assumed that the magnitude $m$ of the signal was unity everywhere and noise was added to the signal to achieve different SNRs (10, 50, 100):

$$S_{noisy} = e^{-i2\pi\gamma B_{int}\Delta TE} + \frac{1}{SNR}(noise_{real} + i\, noise_{imaginary}) \qquad 3\text{-}7$$

In order to evaluate the performance of the algorithms, the $B_{int}$ estimates were visually compared to the ground truth with noise present. Difference images between the

ground truth without any noise present and the estimated $B_{int}$ were used to highlight errors. In order to analyse the error generated by the different background field removal algorithms with different noise levels in more detail, the field was divided into an inside region and a border region of 10 pixels. In the border region errors are most frequent. Subsequently the correlation between the estimated $B_{int}$ and the ground truth without any noise present was calculated in order to achieve a quality measure for the background field removal.

***Results***

When considering the ground truth of the simulation, it can be seen that the fields from the spherical phantoms inside the water tank are in fact the sum of the background field and the internal field as shown in Figure 3-7. The fields generated by the spheres overlap and decrease with distance. The background field is much larger and very slowly varying.

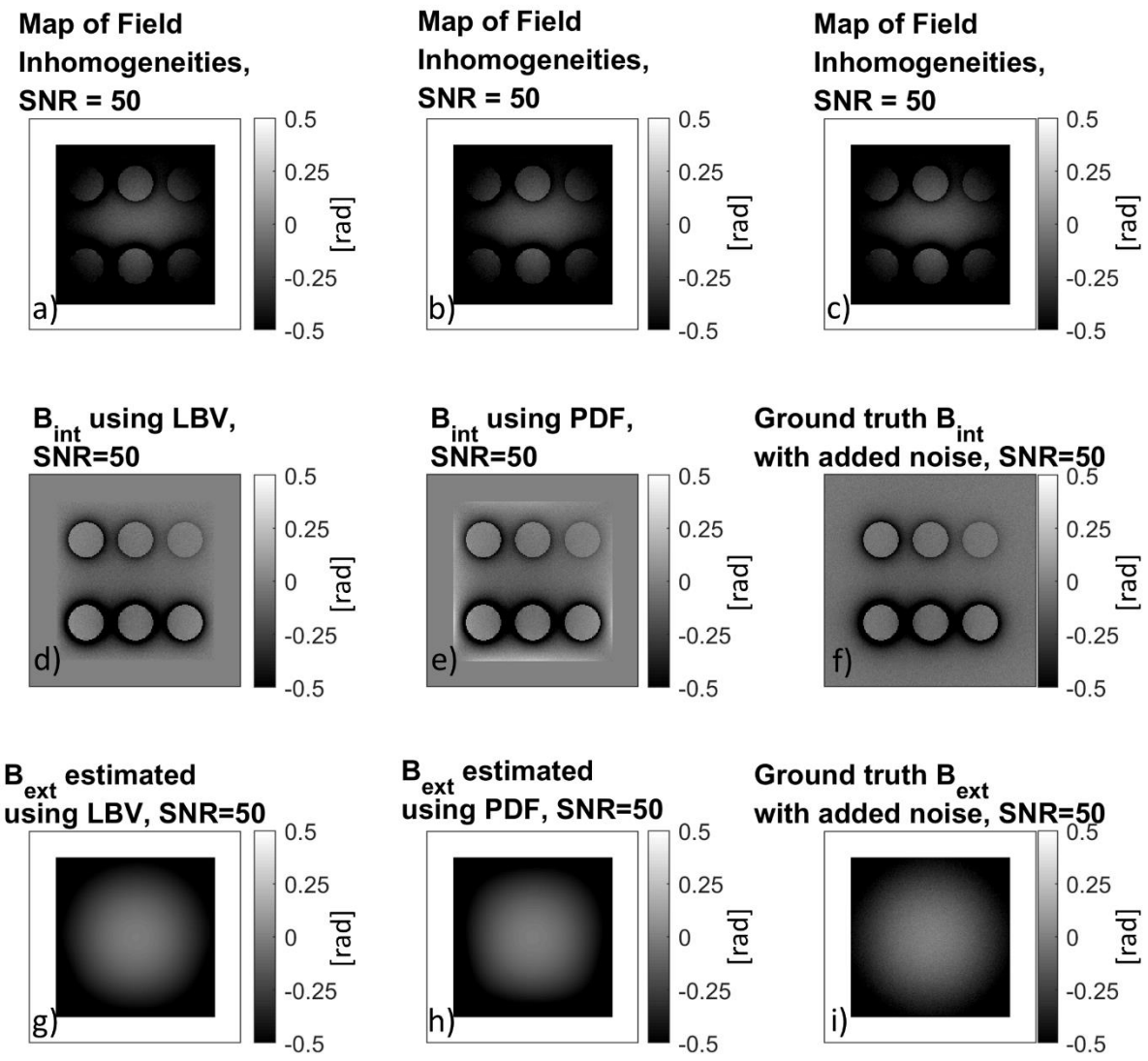


*Figure 3-7: The first row shows the total fields generated by the numerical phantoms (scaled to be given in radians) (a-c). The second row (d-f) show $B_{int}$ as estimated using LBV (d), PDF (e), and the ground truth calculated via forward calculation (f). The third row shows the corresponding $B_{ext}$ (g, h) and the ground truth calculated via forward calculation (i).*

The background field removal algorithms LBV and PDF estimated $B_{int}$ and $B_{ext}$, which largely corresponded in shape, size, and orientation to the ground truth as shown in Figure 3-7: $B_{int}$ as estimated with LBV (Figure 3-7 d) and PDF (Figure 3-7 e) corresponded to the field generated by the phantoms alone without any background fields present (Figure 3-7 f). The background fields estimated with LBV (Figure 3-7 g) and PDF (Figure 3-7 h) corresponded to the field generated by an air- water interface (Figure 3-7 i).

In Figure 3-7 d) and e) it can be observed that there are small errors in the estimation of $B_{int}$. To evaluate these further, the ground truth, i.e. the field generated by the phantoms in water alone without any noise present was subtracted from the $B_{int}$ estimates, which is shown in Figure 3-8. This was compared to the ground truth as calculated in the presence of noise from which the ground truth without any noise present was subtracted (Figure 3-8 c and f).

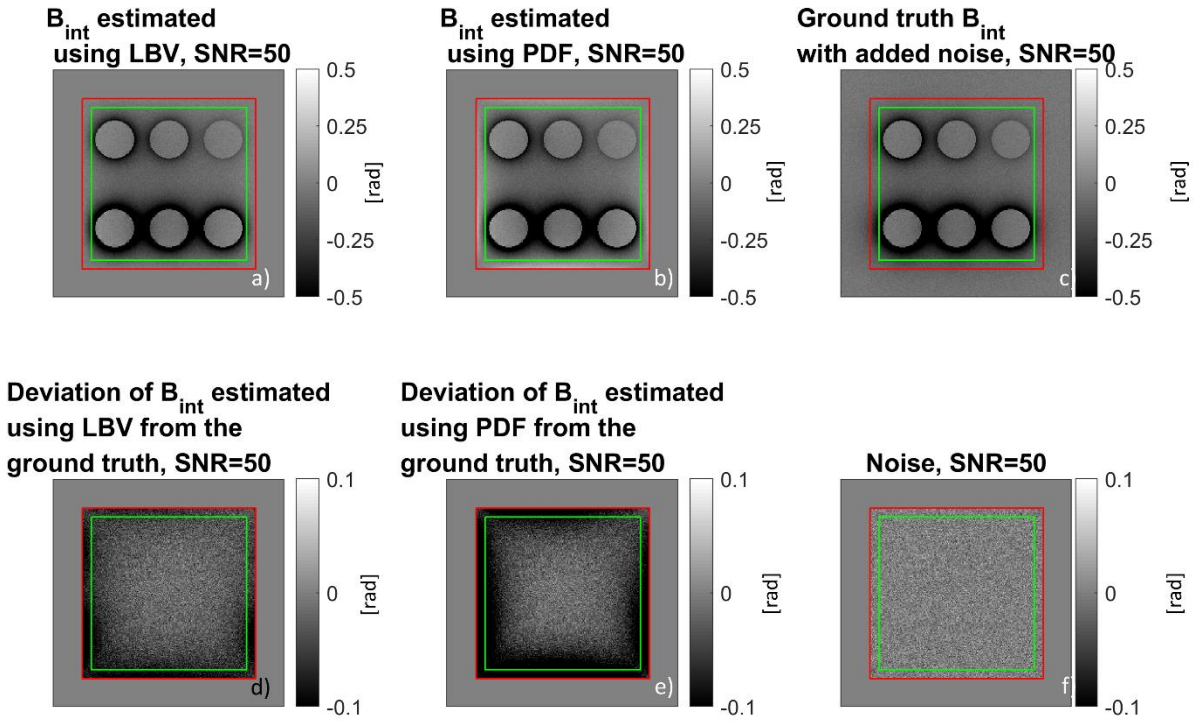


*Figure 3-8: The first row shows the internal fields estimated with LBV (a) and PDF (b) in comparison with the ground truth, which is the field generated in the absence of air (scaled to be given in radians) (c). The second row shows the deviation from all of those fields from the ground truth, as calculated in the absence of noise.*

In the border region, there are slight differences between the LBV (Figure 3-8 a, d) and PDF (Figure 3-8 b, e)) algorithms. The error in the border region is slightly larger for the PDF algorithm in comparison to LBV algorithm (Figure 3-8 d, e). In order to further classify the error in the boundary regions, the correlation between all voxels of the ground truth internal field without any noise present and the estimated internal fields at different noise levels was calculated. For reference, the correlation between the internal field with and without noise present was also calculated. Figure 3-9 shows two plots of Pearson's correlation coefficient against the applied noise level. In the low-noise case, the LBV algorithm more accurately estimates the field components

around the boundary as shown by its larger Pearson's correlation coefficient. While the overall correlation coefficient decreases with an increasing noise level, this may not be entirely due to errors in the background field estimation. In the boundary region, even the noisy ground truth estimate has a low correlation with the noiseless ground truth estimate (yellow line, Figure 3-9 a)). This is due to the overall small signal in the boundary region. As the noise level is increased, the performance of LBV reduced, as shown by the decreasing correlation coefficients. The results are worse than the ground truth but behave in a similar way. In contrast, the PDF algorithm had a low performance in the boundary region even at a high SNR and the correlation remained low.

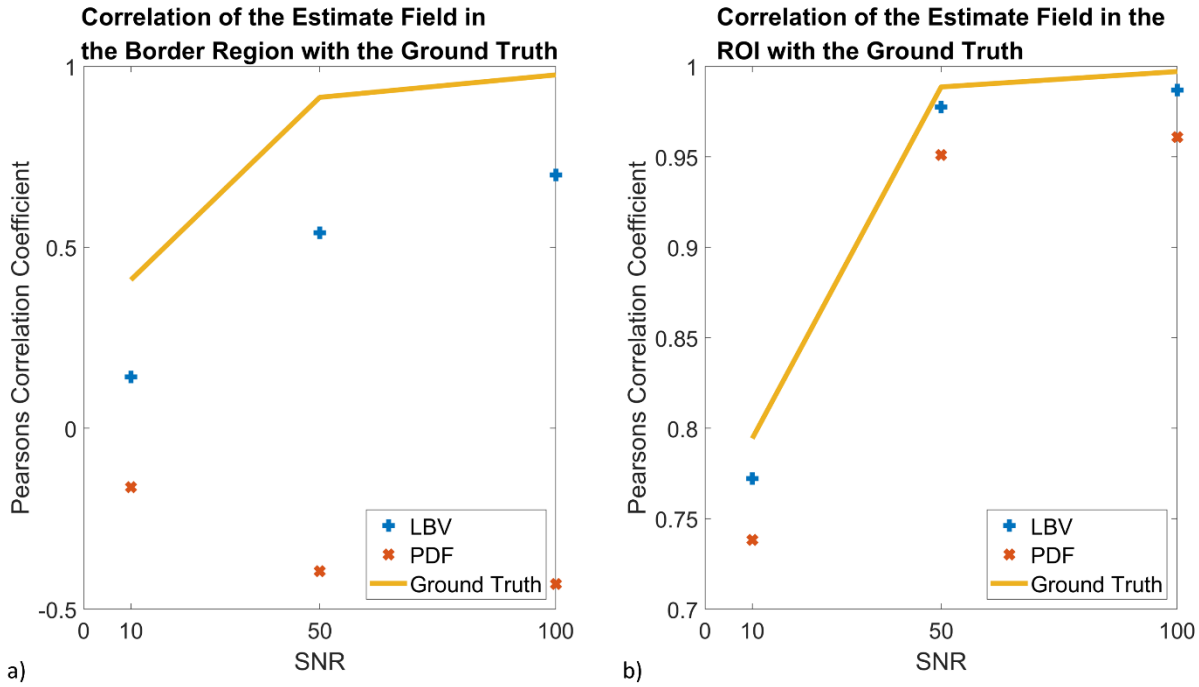


*Figure 3-9: Pearson's correlation coefficient between $B_{int}$ with added noise and as estimated with LBV and PDF and the ground truth internal field. A) shows the results in the border regions and b) inside the region of interest. The correlation coefficient is plotted against different noise levels*

For the internal field (Figure 3-9 b), both PDF and LBV had an excellent agreement with the ground truth. With increasing noise level, the correlation coefficient decreased. This was due to the increase in noise since the correlation between the ground truth with and without added noise decreased by a similar amount.

### 3.3.3 Dipole Field Inversion

***Experimental Setup***

In a third simulation, the effect of differences in SNR on the dipole field inversion was evaluated using two different methodologies: truncated k-space division (TKD) and Morphology Enabled Dipole Inversion (MEDI). The codes for the relevant algorithms were from the MEDI toolbox (http://pre.weill.cornell.edu/mri/pages/qsm.html and http://pre.weill.cornell.edu/mri/pages/qsmreview.html). The code for the corrected TKD algorithm was from the toolbox "MRI susceptibility calculation methods" (available at https://xip.uclb.com/i/software/mri_qsm_tkd.html (275,283)). A similar susceptibility distribution was used as in the background field removal section. In order to minimize the errors introduced by background field removal, $B_{int}$ as generated in the previous simulation from the spherical phantoms and water alone was used, without any air present. Furthermore, a point source of noise was added onto $\Delta B_{int}$ by assigning a single voxel the value 3.04 in order to illustrate the streaking artefact caused by these point sources of granular noise. Subsequently the MEDI algorithm and the TKD algorithm were evaluated with varying regularization parameters $\lambda$ (10, 100, 1000) and $\alpha$ (0.1, 0.2, 0.3). Furthermore, the TKD approach, which corrects for the underestimation, which was proposed by Schweser et al. (283) was employed. Here, a threshold value $\alpha$ of 2/3 was used and subsequently, the susceptibility map was corrected with a scaling factor in order to avoid underestimation.

***Results***

First, the TKD results were assessed. When varying the regularization parameter of the TKD algorithm the following was observed: With a small regularization parameter, the algorithm correctly estimated the paramagnetic susceptibility values within the spherical phantoms. As the regularization parameter increased, the algorithm slightly underestimated the susceptibility (Figure 3-10). This means the regularized region gets larger in the regularized *k*-space, which leads to greater underestimation. The PSF corrected implementation leads to an overestimation of the susceptibility values within the spheres. The overestimation is in part inherent to this methodology and in other parts due to the increased truncation induced streaking artefact surrounding the spheres, which is more pronounced in this method. However, as different noise levels were assessed, it can be seen that a stronger regularization reduced noise and the

streaking artefact from the point source in the susceptibility maps. A stronger regularization also leads to a more pronounced truncation induced artefact at the boundary of the high susceptibility spheres and the surrounding water. Figure 3-11 shows the shape of the streaking artifact by looking at Figure 3-10 from a different orientation and changing the range of voxel values.

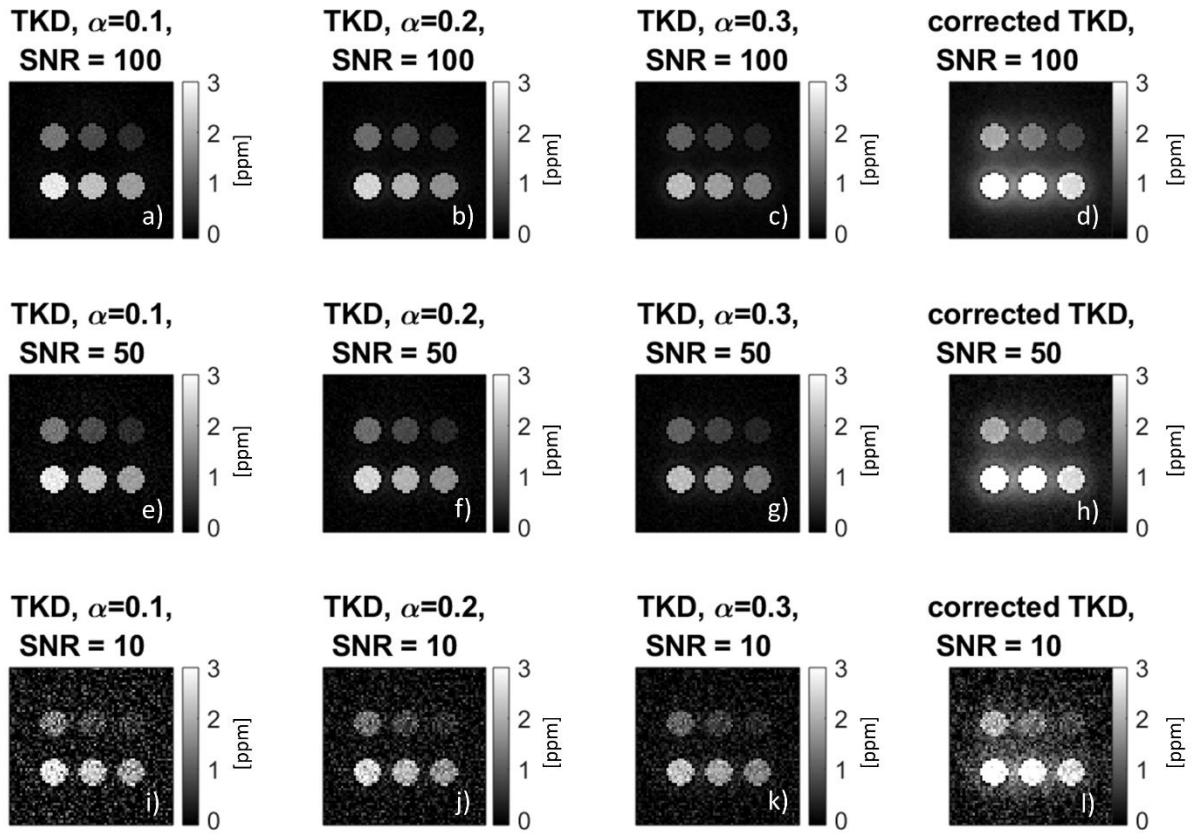


*Figure 3-10: QSM using TKD estimated with different noise levels (row 1(a-d): SNR = 100, row 2 (e-h): SNR = 50, row 3 (i-l): SNR = 10) and different regularization parameters (column 1 (a,e,i): α = 0.1, column 2 (b,f,j): α = 0.2, column 3 (c,g,k): α = 0.3), column 4 (d,h,l): corrected TKD)*

In order to illustrate the effect of varying the regularization parameters on the reduction in image contrast, Figure 3-12 a-c, show a plot of the estimated mean susceptibility values (y-axis) against the ground truth values (x-axis) within each phantom. To summarize Figure 3-12 d) shows the slope for each plot. A slope of 1 would signify a perfect estimation of the susceptibility values. A smaller slope indicates that the estimated susceptibility values are smaller than the ground truth.

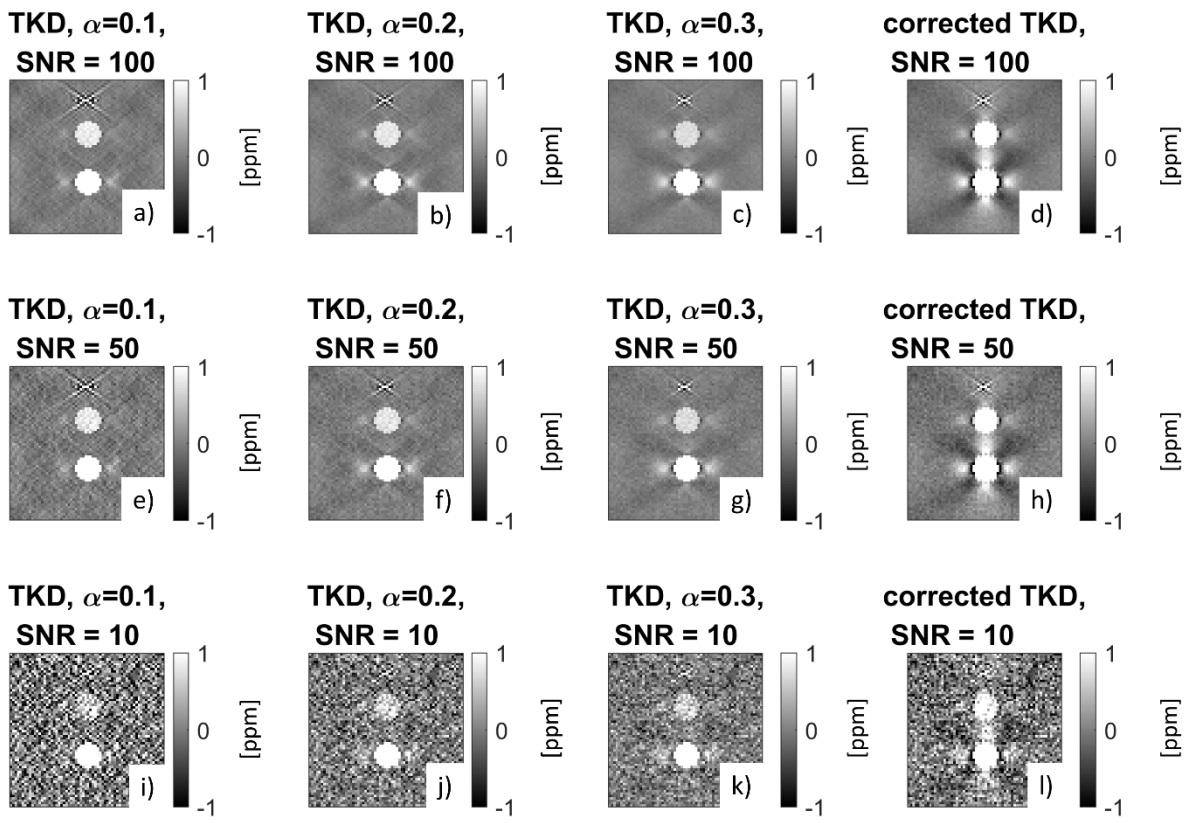


*Figure 3-11: TKD images displayed with a window level that shows the characteristic streaking artifact*

Here we can see that with increasing regularization parameter the slope is decreasing, which means that the TKD algorithm underestimates the true susceptibility values within the spheres. As described above, the corrected TKD algorithm lead to an overestimation of the susceptibility values. However, increasing noise did not have an effect on the relationship between susceptibility underestimation and regularization parameter. From Figure 3-10 and Figure 3-11 it can, however, be seen that a higher noise level may require stronger regularization to improve image quality.

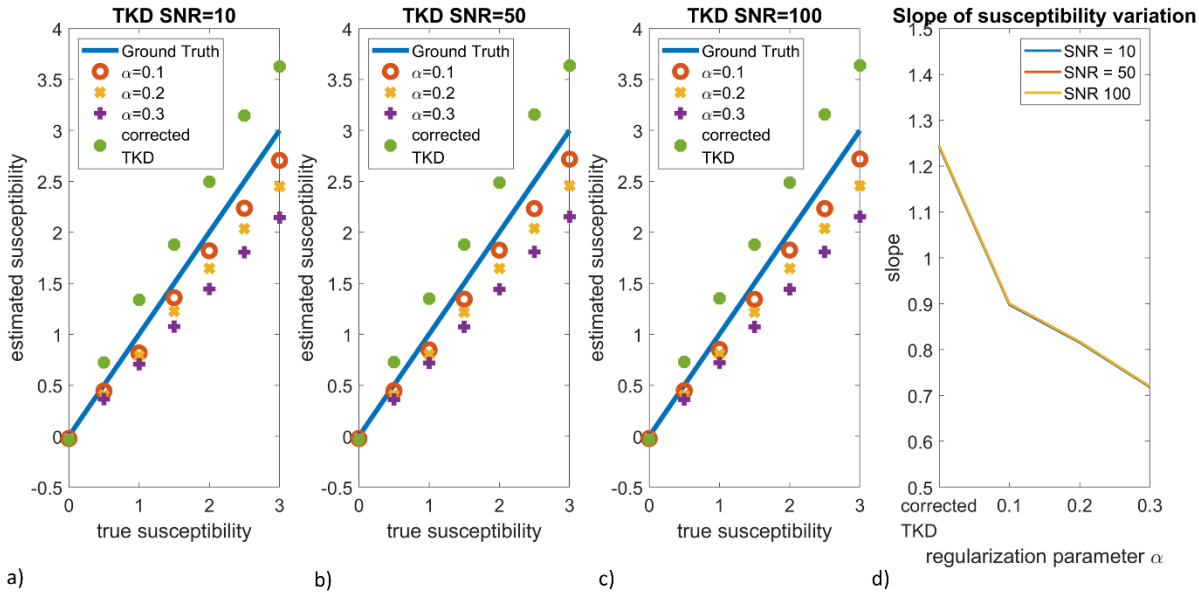


*Figure 3-12: These graphs plot the estimated against the true susceptibility values in ppm as estimated with TKD and varying regularization parameters (a-c). The noise conditions were varied from SNR = 10 (a), SNR = 50 (b), and SNR = 100 (c). D) summarizes the findings by plotting the slope for each graph against the applied regularization parameter.*

Subsequently, the MEDI algorithm was assessed. As described in section 3.3.2, it was assumed, that the magnitude of the images was unity everywhere, before noise was added. As the regularization parameter $\lambda$ decreased, the susceptibility differences between the spherical phantoms and the background were reduced as shown in Figure 3-13.

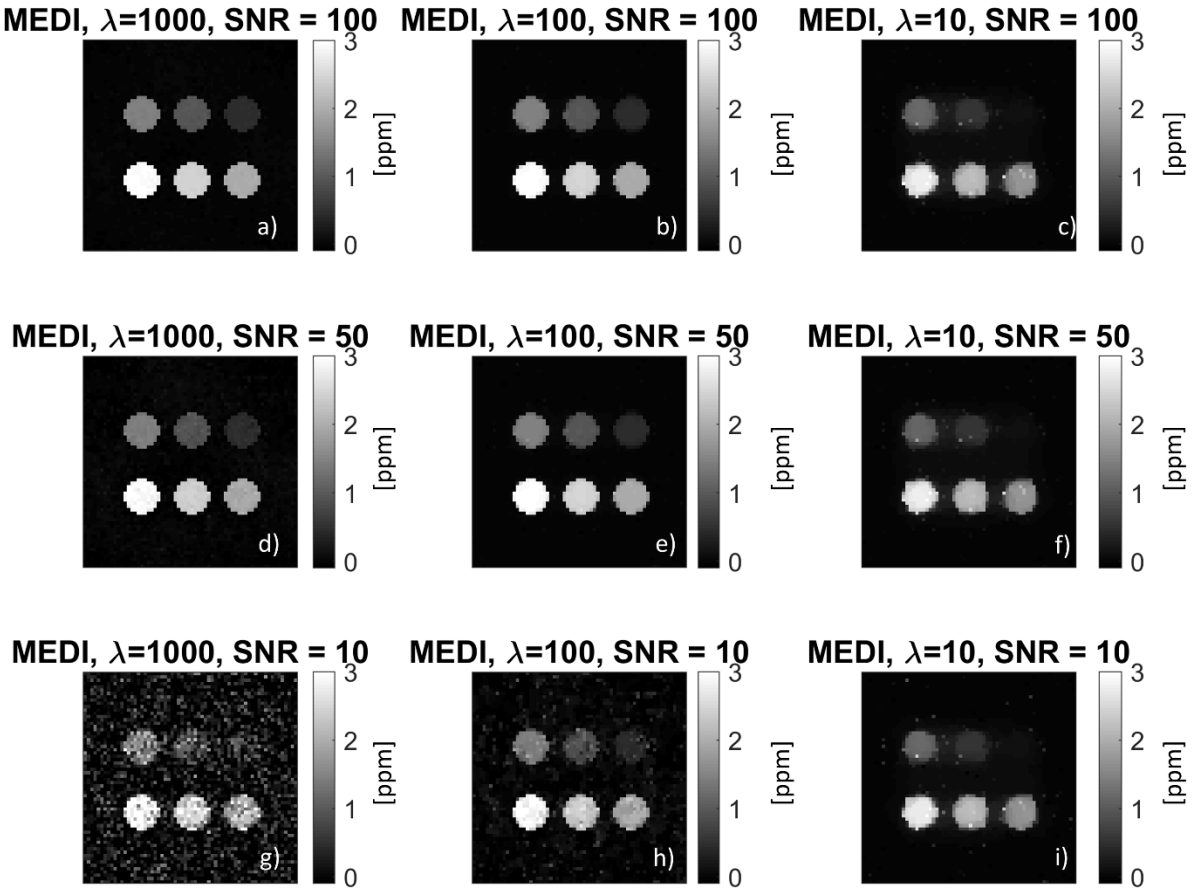


*Figure 3-13: QSM using MEDI estimated with different noise levels (row 1 (a-c): SNR = 100, row 2 (d-f): SNR = 50, row 3 (g-i): SNR = 10) and different regularization parameters (column 1 (a,d,g): λ = 1000, column 2 (b,e,h): λ = 100, column 3 (c,f,i): λ = 10)*

At the same time, noise and streaking artifacts were reduced (Figure 3-13 and Figure 3-14). Figure 3-14 shows the streaking artifact by looking at Figure 3-13 from a different orientation and changing the range of the grayscale. This illustrates that at different noise levels, the regularization parameters need to be carefully chosen. A very high regularization parameter might be acceptable when the SNR is high (Figure 3-14 a, b) but at a lower SNR, the image quality may be too low (Figure 3-14 g, h) and a much stronger regularization may be required (Figure 3-14 i). For all noise levels and regularization parameters, the granular noise was removed.

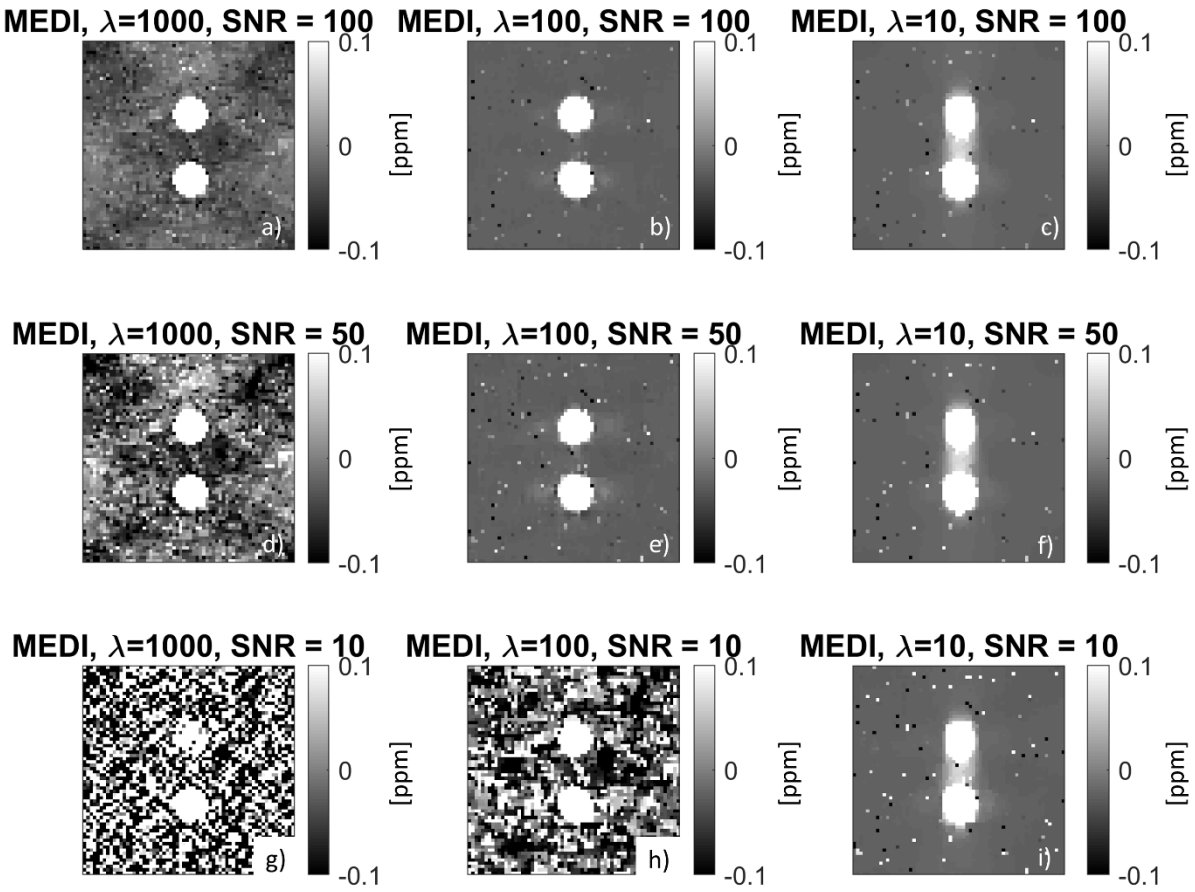


*Figure 3-14: MEDI images with a windowing that illustrates the shape of the characteristic streaking artifact*

In order to illustrate the effect of varying the regularization parameters on the reduction in image contrast, Figure 3-15 shows a plot of the estimated against the ground truth susceptibility values within each phantom. A plot of the slope against regularization parameter at the respective noise value summarizes these findings (Figure 3-15 d). The smaller the regularization parameter, the smaller the slope, i.e. the higher the underestimation of the susceptibility differences. Both, the choice of $\lambda$ and the noise level had an effect on the susceptibility underestimation. At relatively high SNRs of 50 and 100, a $\lambda$ of 100 and 1000 produced similar results. However, at a very low SNR of 10, the only a $\lambda$ of 100 did not lead to great underestimation. A $\lambda$ of 10 consistently led to a reduction of the slope for all SNRs. On Figure 3-14 (c, f, i) this can be seen by the blurring of the signal intensity around the edges of the phantoms.

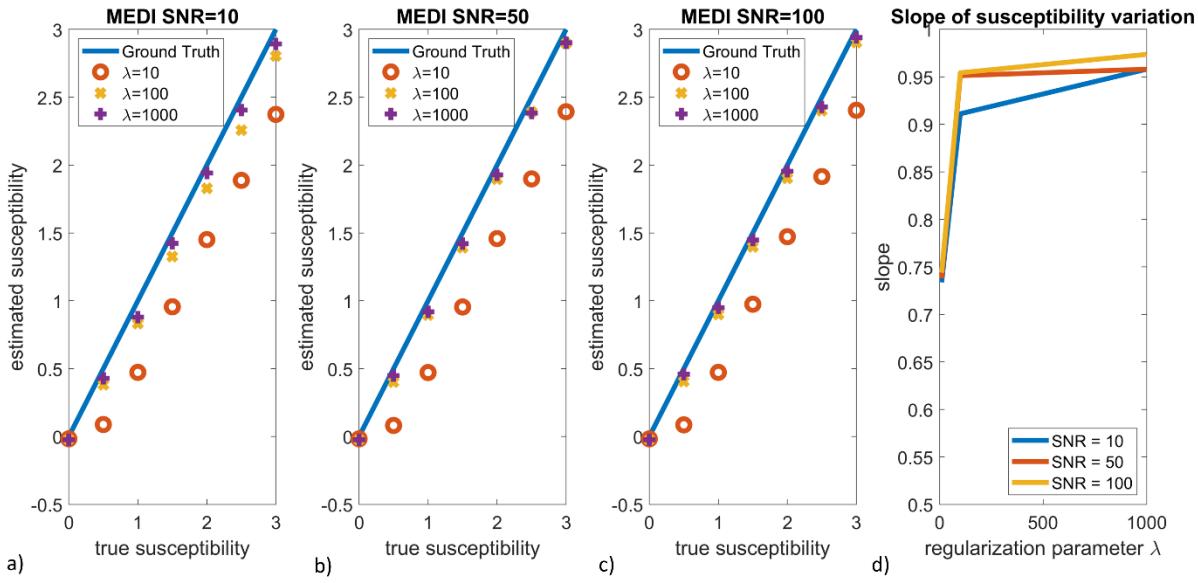


*Figure 3-15: These graphs plot the estimated against the true susceptibility values in ppm as estimated with MEDI and varying regularization parameters (a-c). The noise conditions were varied from SNR = 10 (a), SNR = 50 (b), and SNR = 100 (c). D) summarizes the findings by plotting the slope for each graph against the applied regularization parameter.*

## 3.4 Human Brain Imaging

### 3.4.1 Experimental Setup

In addition to the numerical simulations, images from a brain of a single subject in a patient study were processed. The data were acquired at 1.5T (MR 450, GE Healthcare, Waukesha, WI) with a multi-echo gradient echo sequence (Susceptibility-weighted Angiography (SWAN), GE Healthcare, Waukesha, WI). The data were acquired as part of the PEMA study, part of which has been published in (291). The data were provided by courtesy of Dr Andrew Priest. Magnitude and phase images were processed for QSM by estimating $\Delta B$ using a least squares algorithm (258–260), provided in the MEDI toolbox followed by background field removal and dipole field inversion.

In order to illustrate the different steps of the QSM algorithm, the background field was removed using both the LBV and PDF algorithms and the dipole field inversion was performed using MEDI (Regularization Parameter = 10, 320 & 1000) and TKD (Regularization Parameter = 0.07, 0.2 & 0.5; corrected TKD). The codes for $\Delta B$ estimation, phase unwrapping, background field removal, and dipole field inversion were from the Matlab MEDI toolbox (http://pre.weill.cornell.edu/mri/pages/qsm.html

and http://pre.weill.cornell.edu/mri/ pages/qsmreview.html). The code for the corrected TKD algorithm was from the toolbox “MRI susceptibility calculation methods” (available at https://xip.uclb.com/i/software/mri_qsm_tkd.html (275,283)).

### 3.4.2 Results

***Field Map Estimation and Phase Unwrapping***

The field map of the complex gradient echo images was acquired from the variation of the phase images with echo time. Figure 3-16 shows the phase images of a single slice acquired at the four different echo times (TE = 6.5,13.2,20.0,26.7 ms). It is assumed that the phase varies linearly with time and that its slope gives $\Delta B$ (as illustrated in Figure 3-16 b). This can be estimated by fitting on the complex data. During this process it is necessary to remove any phase wraps between subsequent echoes as demonstrated in Figure 3-16 b). The resulting temporally unwrapped map of $\Delta B$ (scaled by a factor of $\gamma 2\pi \Delta TE$) is shown in Figure 3-16 c). The code for the $\Delta B$ estimation stems from the MEDI toolbox (258–260).

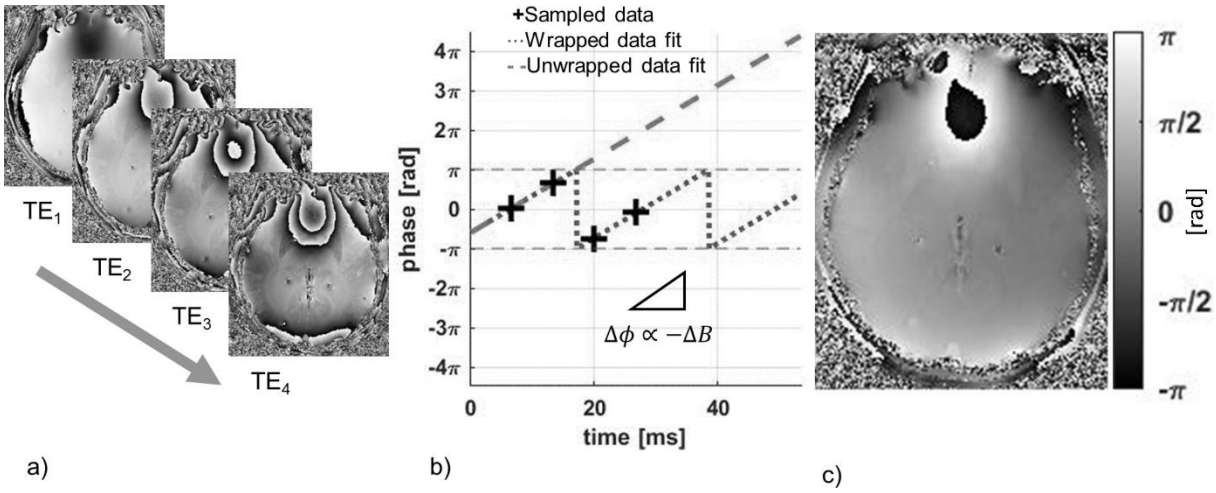


*Figure 3-16: A map of field inhomogeneities (scaled to be given in radians) (c) can be estimated from the linear phase variation with echo time (b) from gradient echo phase images acquired at different echo times (a). Phase wraps may occur in between subsequent, which need to be corrected as shown in b). (I published this illustration in* (153)*)*

The remaining phase wraps can be removed as demonstrated in Figure 3-17 with a graph-cut based spatial phase unwrapping algorithm as proposed in (263). The code for the phase unwrapping stems from the MEDI toolbox (263). Integer multiples of $2\pi$, $(k2\pi)$, are added onto the wrapped phase map in order to achieve a completely unwrapped map of $\Delta B$.

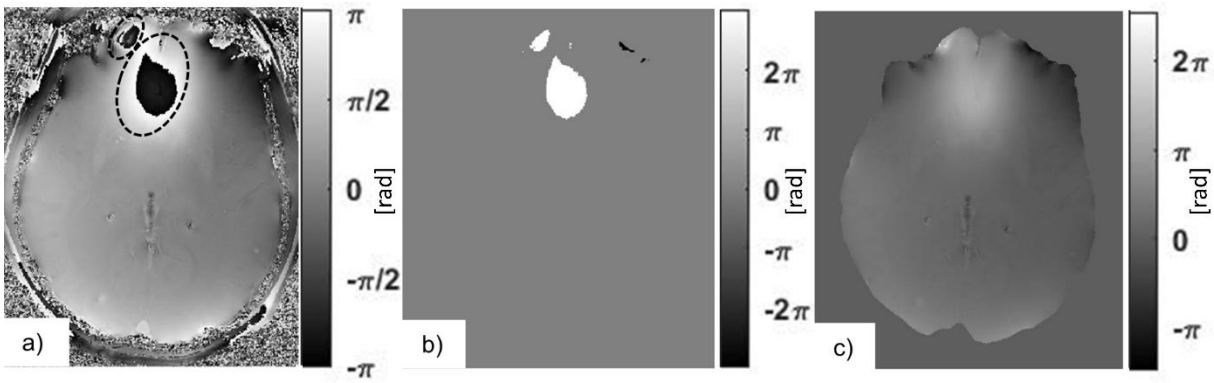


*Figure 3-17: Phase wraps may occur, in regions where the field inhomogeneity is too large (a). These can be identified by phase unwrapping algorithms, which add an integer multiple of 2π (b) onto the wrapped map of field inhomogeneities (scaled to be given in radians) (a) in order to calculate an unwrapped map of field inhomogeneities (c). (I published this illustration in* (153)*)*

### *Background Field Removal*

The unwrapped field map contains contributions from $B_{int}$ and $B_{ext}$. These can be separated using the two background field removal techniques that were demonstrated in the numerical simulation (LBV (176) and PDF (177)). The codes for the background field removal stems from the MEDI toolbox. As expected, the contributions from the background field and the internal field look similar when estimated with both techniques (LBV: Figure 3-18 a, PDF: Figure 3-18 b). $B_{ext}$ is large and slowly varying and dominates the image, obscuring $B_{int}$ (Figure 3-18 d, e). Here, these contributions originate from air tissue interfaces. Due to different assumptions for the boundary conditions, there are small differences between the two techniques near the boundary indicated by the black circles on the LBV and PDF images, and more clearly visible on their difference image (Figure 3-18 c)). However, these differences are limited to the boundary and are rather small compared to the overall magnitude of the background fields.

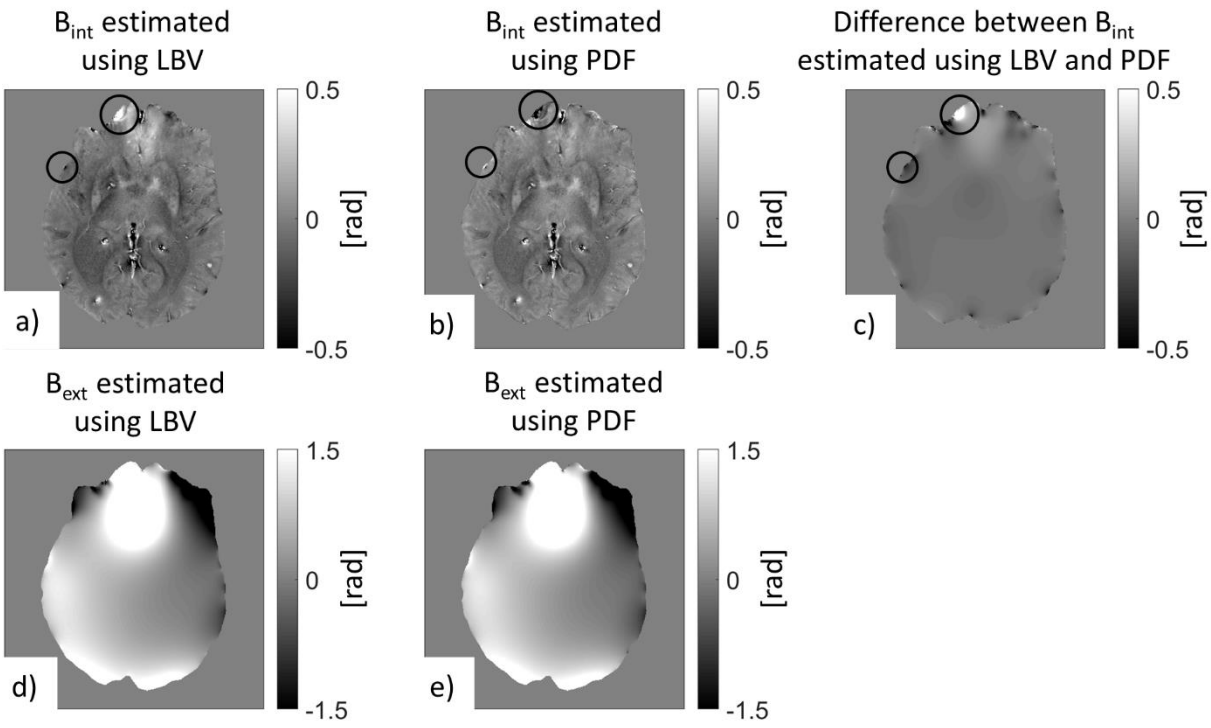


*Figure 3-18: $B_{int}$ (a, b) and $B_{ext}$ (d,e) (scaled to be given in radians) estimated using LBV (a, d), and PDF (b, e). The difference image between the two methods highlights the differences between the two approaches (c). (I published aspects of these results in* (153)*)*

### *Dipole Field Inversion*

The results estimated with the different dipole field inversion algorithms confirm the observations made in the numerical simulations. The susceptibility maps estimated using the TKD algorithm with a low threshold value (Figure 3-19 a), e), $\alpha = 0.07$) exhibits the characteristic streaking artifacts and noise. An increased threshold leads to an improvement in image quality and lower streaking artifacts and noise (Figure 3-19 b, f, $\alpha = 0.2$), but a simultaneous reduction in contrast (Figure 3-19 c, g, $\alpha = 0.5$). The reduction in contrast can be counteracted by using the corrected TKD method, which produced high image quality along with high contrast (Figure 3-19 d,h).

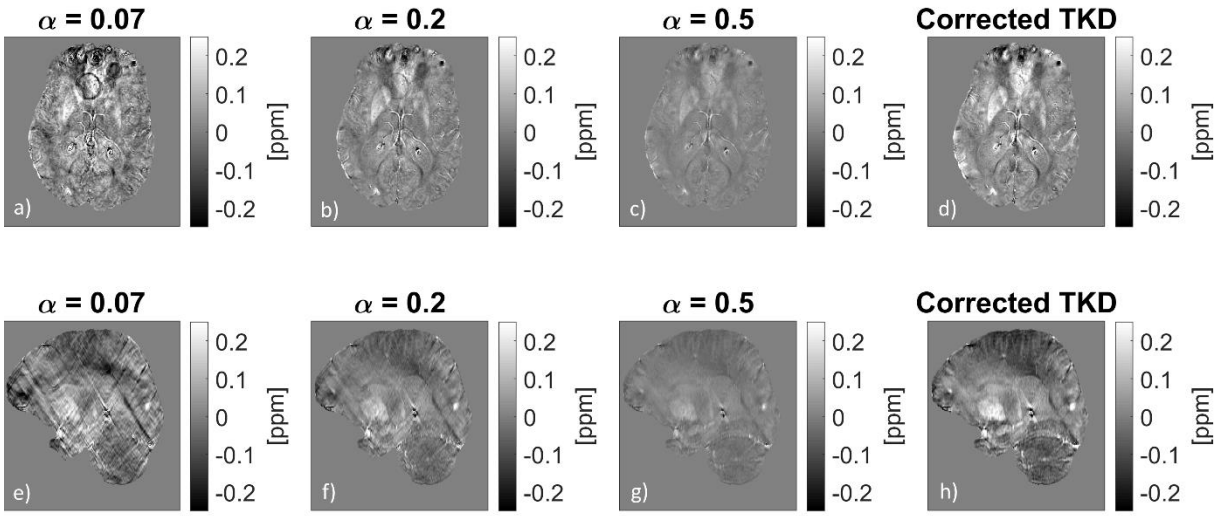


*Figure 3-19: Susceptibility maps estimated with TKD; The first row (a-d) shows the susceptibility maps in axial and the second row (e-h) in sagittal orientation. The values of the regularization parameter $\alpha$ are 0.07 (a, e), 0.2 (b, f) and 0.5 (c, g) in the first, second and third column respectively. The fourth column shows the results with the corrected TKD method. (I published aspects of these results in* (153)*)*

The MEDI algorithm improves the image quality and removes much of the streaking artifact. In comparison to a large regularization parameter $\lambda$ (Figure 3-20 c, f; $\lambda = 1000$), a reduction leads to a noticeable suppression of streaking artifacts (Figure 3-20 b, e; $\lambda = 320$). However, an overly small choice of $\lambda$ (Figure 3-20 a, d; $\lambda = 10$), can lead to over-smoothing of the data.

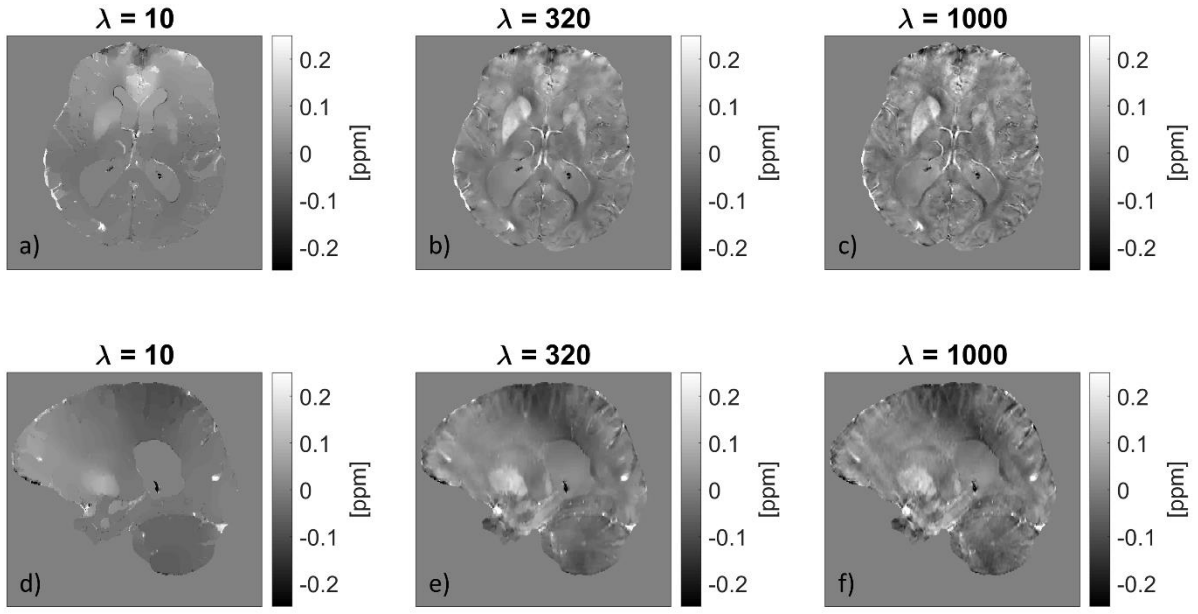


*Figure 3-20: Susceptibility Maps estimated with MEDI in axial (a-c) and in sagittal orientation (d-f). The values of the regularization parameter λ are 10 (a, d), 320 (b, e) and 1000 (c, f) in the first, second and third column respectively. (I published aspects of these results in* (153)*)*

## 3.5 Discussion

These simulations and the in vivo data illustrated the size and shape of different magnetic field inhomogeneities which depend on the geometry, orientation and susceptibility of the underlying susceptibility distribution. These non-local effects of different fields then overlap. This illustrates the advantages that QSM has over SWI that has been demonstrated in various studies. The elimination of the non-local effects and geometry dependence allows for a better differentiation between paramagnetic and diamagnetic substances (171) as has previously been shown in the brain and a more accurate assessment of their volumes as has been shown in cerebral hematoma volume assessment (221). The non-local effects also lead to the obscuring of internal fields by background fields. This leads to a requirement for background field removal techniques to extract the internal field generated within a certain ROI. Different algorithms vary in their performance. Errors and differences between different techniques primarily occur in the boundary region of the mask that is applied before the background field removal. It is important that these errors remain as small as possible as they may affect the susceptibility maps and cause errors in the quantitative assessment of local susceptibility differences and the qualitative assessment, as they may obscure the internal susceptibility map. While different noise levels degrade the overall performance of the algorithms, it was shown that the errors remain in the boundary region, so that the effects on the susceptibility distribution inside the region of interest remain small.

Furthermore, the application of different dipole field inversion techniques showed the importance of the regularization parameter. Under different noise conditions, a reduction in streaking artefact can be seen by choosing a stronger regularization but the improvement in image quality often comes at a cost. Stronger regularization led to an underestimation of susceptibility differences. Furthermore, when the regularization was too strong, the MEDI algorithm smoothed the susceptibility maps which lead to a loss of detail.

## 3.6 Conclusion

This chapter illustrates the different steps involved in QSM and illustrates the fields and effects of noise that are involved in each step. Understanding the principles and

steps involved in this post-processing technique is important in order to improve on the existing techniques, for example by including a water-fat separation technique into the post-processing and applying QSM in different anatomies as is done in chapter 5 and 6.

# Chapter 4 Susceptibility Weighted Imaging and $R_2^*$-Mapping for the Detection of Carotid Artery Plaque Calcification and USPIO Uptake

Aspects of this work were presented in Ruetten PPR, et al. “Calcification and USPIO detection in Carotid Artery Plaque using QSM and SWI”. In: Proceedings of the 27th Annual Meeting of ISMRM. ; 2019:2090 (292)

## 4.1 Introduction

As described in chapter 1 section 1.5, ultrasmall superparamagnetic iron oxide (USPIO) nanoparticles can serve as an MRI contrast agent. After intravenous injection, they are taken up by macrophages. Their detection may therefore serve to identify inflammation, which is helpful in carotid atherosclerotic plaques, where it is a marker of vulnerability to rupture.

Due to the USPIO’s strong paramagnetism the $R_2^*$-value is increased drastically in high-uptake regions (149). In the past USPIO-uptake has therefore been identified with two gradient echo acquisitions, that are acquired before and after contrast agent administration. The USPIO-uptake is then identified by a drop in $T_2^*$w signal intensity on the magnitude images or, if multiple echo times are acquired, an $R_2^*$ map can be generated and USPIO-uptake is identified by an increase in $R_2^*$-value (126,137,138,141–143).

A comparison of pre- and post-contrast scans is necessary in order to distinguish paramagnetic USPIO-uptake from other strong susceptibility sources within the plaque such as calcification or intraplaque haemorrhage. A wide variety of sequences have attempted to display USPIO-uptake with positive contrast, as was described in chapter 1 section 1.5.2, e.g. IRON (148,293) or GRASP (151).

Both $T_2^*$-weighted gradient echo contrast and positive contrast are generated from local field inhomogeneities created by changes in tissue susceptibility (149,294). In conventional gradient echo imaging, only the magnitude images are used while the important information contained within the phase from gradient echo acquisitions, which varies linearly with the field inhomogeneity, is discarded. However, the different effects caused by the field inhomogeneities are used in positive contrast techniques as described in chapter 1 section 1.5.2. Susceptibility weighted imaging (SWI) improves on $T_2^*$w gradient echo imaging by combining $T_2^*$w magnitude images with the phase information, which includes information about the magnitude and sign of the local field inhomogeneities in order to generate a new type of contrast (178). Furthermore, it does not require an additional, dedicated sequence like many positive contrast imaging techniques. The SWI phase images may also be analysed on their own. A detailed description of the implementation and applications of SWI can be found in chapter 2 section 2.2.3 and chapter 2 section 2.2.5.

A variety of studies have therefore used filtered phase images and SWI to image strongly paramagnetic materials, such as paramagnetic deoxygenated venous blood (178), haemorrhages (171–174), and iron oxide nanoparticles (295) or diamagnetic calcification (171–174,296–300). In particular, it has been suggested that due to the different signs of their susceptibilities, the fields generated by paramagnetic and diamagnetic materials may be distinguished with SWI and filtered phase images in several studies (171–174). It has been assumed that the fields generated by paramagnetic materials are positive while diamagnetic fields are negative. Therefore it is frequently assumed that the phase shifts from diamagnetic materials such as calcification and paramagnetic materials such as USPIO uptake are associated with positive and negative phase shifts in a right handed system respectively (173,174,301). In vascular imaging, SWI has been used to image carotid plaque calcification and distinguish the lumen from the more diamagnetic vessel wall (296,297,302).

Due to its ability to distinguish between paramagnetic and diamagnetic materials and the promise SWI has shown in previous studies, this study explores SWI and filtered phase images in imaging of carotid artery plaques. It was used to confirm that SWI and filtered phase images can image carotid plaque calcification and is proposed as a novel method for imaging USPIO-uptake in carotid artery plaques. The underlying

hypothesis is that SWI and filtered phase images are able to distinguish materials of different susceptibility in carotid artery plaques, i.e. calcification and USPIO-uptake. While previous “positive contrast” methods to image USPIO contrast rely on dedicated sequences, SWI is complementary to frequently used $R_2^*$-mapping imaging protocols.

In the following, a patient group with carotid artery disease underwent two MRI examinations before and after USPIO injection. The feasibility, benefits, and challenges of using SWI and filtered phase images in conjunction with a conventional MRI imaging protocol were subsequently explored.

## 4.2 Methods

### 4.2.1 Data Acquisition

Seven patients (1 woman and 6 men, mean age 70±7.28 years) with moderate to severe carotid artery disease (i.e. 50-99% luminal stenosis on carotid duplex imaging) were scanned at 1.5T (MR450w, GE Healthcare, Waukesha, WI). Four out of those patients are also analysed in Chapter 6. The patient recruitment was performed by Dr Ammara Usman. Prior to the study patients were screened to minimize potential contraindications of Ferumoxytol contrast agents. This included a review of their medical history, while screening and cross-checking at the time of recruitment and consent. The following exclusion criteria were used: History of atopy, asthma or allergic reaction to contrast media, iron or dextran or a known documented history of haemochromatosis. Furthermore, patients with immune inflammatory conditions, e.g. systemic lupus erythematosus, rheumatoid arthritis were excluded. All of the participants gave informed consent and the study had ethical approval from the East of England – Cambridge Central Research Ethics Committee. Two MRI examinations were performed per patient, one was performed before and the other one 48 hours after 5mg/kg USPIO-injection (Ferumoxytol, AMAG Pharmaceuticals, Lexington MA). The study protocol comprised: 3D Time-of-Flight (TOF) MRA; black-blood, fat suppressed $T_1$-w 3D fast spin echo (CUBE); and a black-blood, fat suppressed, 3D multi-echo gradient echo acquisition (Susceptibility Weighted Angiography, SWAN). For blood suppression DANTE (Delay alternating with nutation for tailored excitation) preparation pulses were used in both the CUBE and SWAN sequence (124). The sequence development for the black blood preparation was done by Dr Jianmin Yuan.

In four cases bright-blood SWAN without fat suppression was also acquired and the results were compared to the black-blood sequence. For bright blood SWI, the same sequence with the black blood preparation turned off was used but bipolar echo readouts were used. In the sequence, the number of echoes could be set manually. The $T_2^*$-weighted SWAN sequence was also used for $R_2^*$ mapping and SWI while the multi-contrast protocol was used for validation. The sequence parameters are given in Table 4-1.

| | **3D TOF** | **Black Blood Cube** | **Black Blood SWAN** | **Bright Blood SWAN** |
|---|---|---|---|---|
| TE1/ΔTE/ TR [ms] | 3.2/-/20 | 15.0/-/580 | 5.0/5.5/58.0 (6 echoes, unipolar acquisition) | 4.4/2.1/88.2 (6 echoes, bipolar acquisition) |
| FOV [$mm^3$] | 140×140×56 | 140×140×56 | 140×140×60 | 140×140×60 |
| Spatial Resolution [$mm^3$] | 0.625×0.625×1.4 | 0.625×0.625×1.4 | 0.625×0.625×1* | 0.625×0.625×1* |
| Receiver Bandwidth [kHz] | ±15.63 | ±31.25 | ±31.25 | ±83.3 |
| Acquisition Time [min:sec] | 3:07 | 5:47 | 7:24 | 7:38 |

*Table 4-1: MRI Sequence Parameters *the slice thickness is interpolated from the acquired 2 mm to 1 mm using zero-filling*

### 4.2.2 Data Processing

Both $T_2^*$w multi-echo gradient echo datasets were further processed to generate SWI and filtered phase images. For SWI, the raw MRI data were reconstructed using ASSET, which is similar to the SENSE technique (257) using a customised Matlab code written in GE's Orchestra framework, where Calibration scans were available. If the Calibration scans were not available the PULSAR toolbox was used for SENSE reconstruction (303). The SWI images were calculated for all of the echo times. The $T_2^*$w images for each individual echo, which were subsequently also used for $R_2^*$

mapping, were generated using the GE scanner recon as this had been done in previous studies using $T_2^*$w GRE images and $R_2^*$ maps.

$R_2^*$-mapping was performed with in-house-developed Matlab code provided by Dr Jianmin Yuan that fitted the formula $S \cdot exp(-R_2^* \cdot TE)$ to the acquired multi-echo gradient echo data using Levenberg-Marquardt on a voxel by voxel basis. This was done within the vessel wall and the plaque region, as outlined on the magnitude images. The DANTE CUBE and 3D TOF images were used as an aid to distinguish lumen from vessel wall, when necessary. On the filtered phase images and SWI, I outlined regions of calcification, normal plaque regions, and regions containing USPIO. Due to the poor SNR of the black blood images, the mean $R_2^*$ value was also calculated for each ROI on each slice. This was used later on for quantitative analysis.

For both SWI and filtered phase images, the phase images from the $T_2^*$w gradient echo acquisition were processed for all echo times. As previously described in chapters 2 and 3, it is important to consider only the field inhomogeneities that are generated within the region of interest, which are obscured by background fields, for example by air tissue interfaces. Therefore, the phase images were high-pass filtered. Therefore, a 2D 28×28 low pass Fermi filter with a full width half maximum of 18.7 pixels was applied to the complex data. The code for the low pass filter was provided by Dr Andrew Priest. The low pass filtered images served as an estimate for the background field and were then subtracted from the original phase images via complex division. The resulting high-pass filtered phase images could be interpreted by themselves and were also further processed to generate SWI. Since paramagnetic and diamagnetic susceptibility sources generate different kinds of fields it was assumed that the phase shifts from diamagnetic calcification and paramagnetic USPIO uptake were associated with positive and negative phase shifts in a right handed system respectively (173,174,301).

Two sets of phase masks were then generated to enhance negative (equation *4-1*) and positive phase (equation *4-2*) shifts respectively:

$$Mask(x,y) = \begin{cases} \dfrac{\pi + \phi(x,y)}{\pi}; if\ \phi(x,y) \leq 0 \\ 1; if\ \phi > 0 \end{cases} \qquad 4\text{-}1$$

$$Mask(x,y) = \begin{cases} \frac{\pi - \phi(x,y)}{\pi}; if\ \phi(x,y) \geq 0 \\ 1; if\ \phi < 0 \end{cases} \quad 4\text{-}2$$

The phase masks were subsequently multiplied four times with the magnitude data.

### 4.2.3 Data Analysis

In addition to SWI and filtered phase images, $R_2^*$ maps and normalized $T_2^*$w images were also generated from the gradient echo dataset. For normalization, I manually outlined a region of sternocleidomastoid muscle on the $T_2^*$w magnitude images and normalized the signal intensity within the carotid plaques with this value.

SWI, filtered phase images, $R_2^*$ maps, $T_2^*$w images and the remaining images from the multi-contrast protocol were subsequently centred on the carotid bifurcation to enable comparison of pre- and post-contrast images.

Each set of SWI showed darker regions for calcification or USPIO. On the high-pass filtered-phase image, calcification was identified by a positive phase shift and USPIO uptake by a negative one. Regions of USPIO uptake, calcification, and normal tissue were outlined based on the SWI and filtered phase images and the results were compared qualitatively to the multi-contrast protocol. Calcification was identified as dark regions on all acquisitions with an increased $R_2^*$ value. In three cases CT images were also available. USPIO-uptake was identified by comparing pre- and post-contrast images; uptake was identified by increased $R_2^*$ and hypointensity on $T_2^*$w images and as hyperintensities on $T_1$w images, if the USPIO-concentration was low. Besides increasing $R_2^*$, USPIOs shorten $T_2^*$ and $T_1$. In low concentrations the contrast agent therefore appears as hyperintensities on $T_1$ weighted images (127).

For quantitative analysis the images from the black blood gradient echo dataset were assessed. Regions of USPIO uptake, calcification, and normal tissue were outlined on filtered phase images and SWI. Within each ROI as outlined on SWI/filtered phase images the mean $R_2^*$-value was calculated and the mean $T_2^*$ signal intensity values from the third echo time (TE = 15.9 ms) relative to the sternocleidomastoid muscle (relative signal intensity is abbreviated to rSI) was measured. The mean values calculated for each patient were compared to each other in box-plot form.

### 4.2.4 Histological Analysis

In two patients, who underwent carotid endarterectomy after both MRI acquisitions, histological data were available, which served to validate the presence of either calcification or USPIO contrast agents. The specimens were decalcified, sliced at 3 mm intervals and subsequently embedded in paraffin wax. Thin sections, cut at 3 µm thickness, were stained with Haematoxylin and Eosin (H&E), Perl's Prussian Blue and Elastic Van Gieson Stain. The histopathological analysis was performed by the tissue bank team and Dr Alison Cluroe, the consultant histopathologist. The large spacing of the thin histology slides, compared to the tight spacing of thick MRI slices, limited the analysis, which simply served to confirm the presence of certain plaque features.

## 4.3 Results

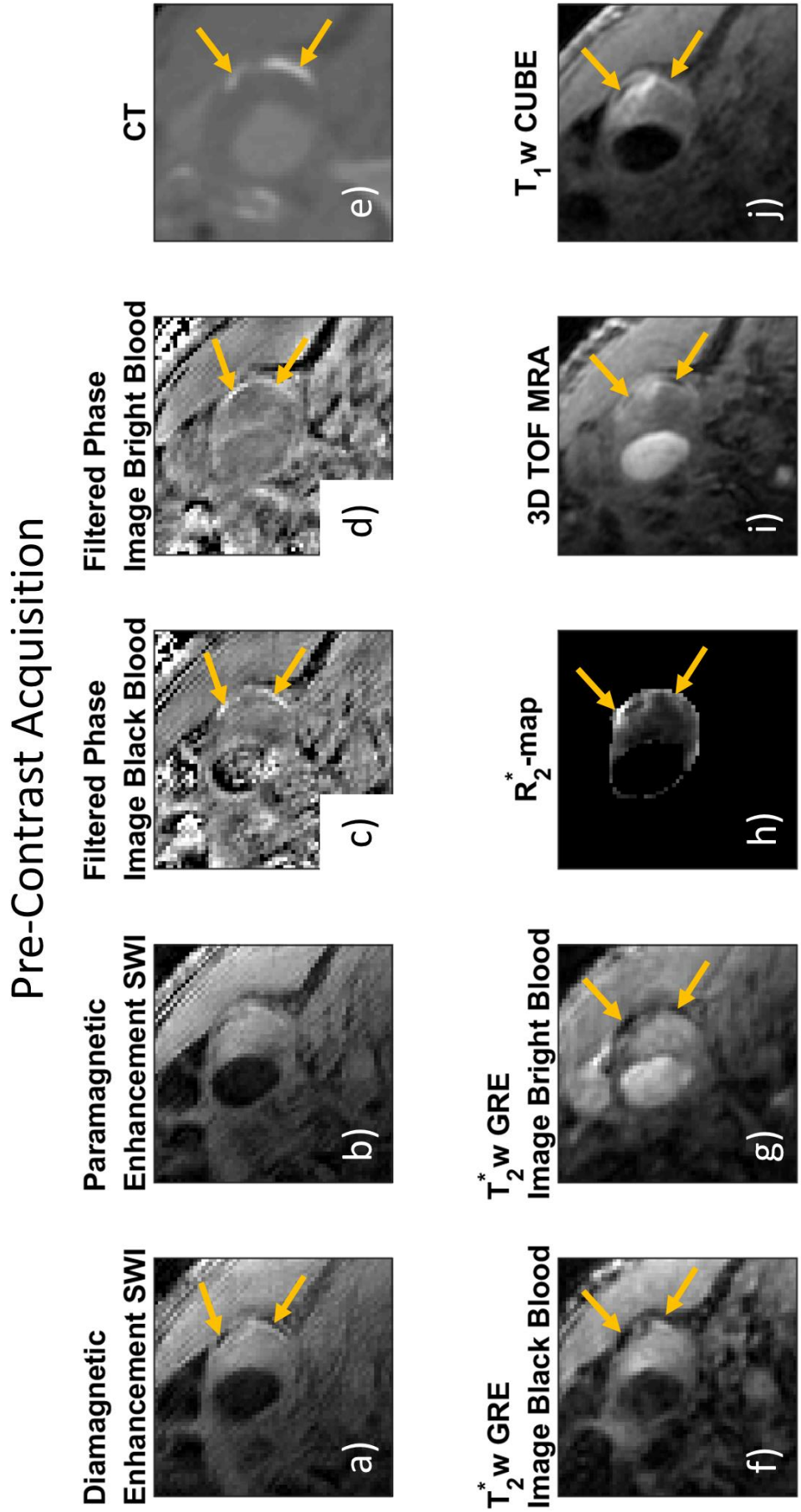
Pre-Contrast Acquisition
Diamagnetic Enhancement SWI
a)
Paramagnetic Enhancement SWI
b)
Filtered Phase Image Black Blood
c)
Filtered Phase Image Bright Blood
d)
CT
e)
T2*w GRE Image Black Blood
f)
T2*w GRE Image Bright Blood
g)
R2*-map
h)
3D TOF MRA
i)
T1w CUBE
j)

# Post-Contrast Acquisition

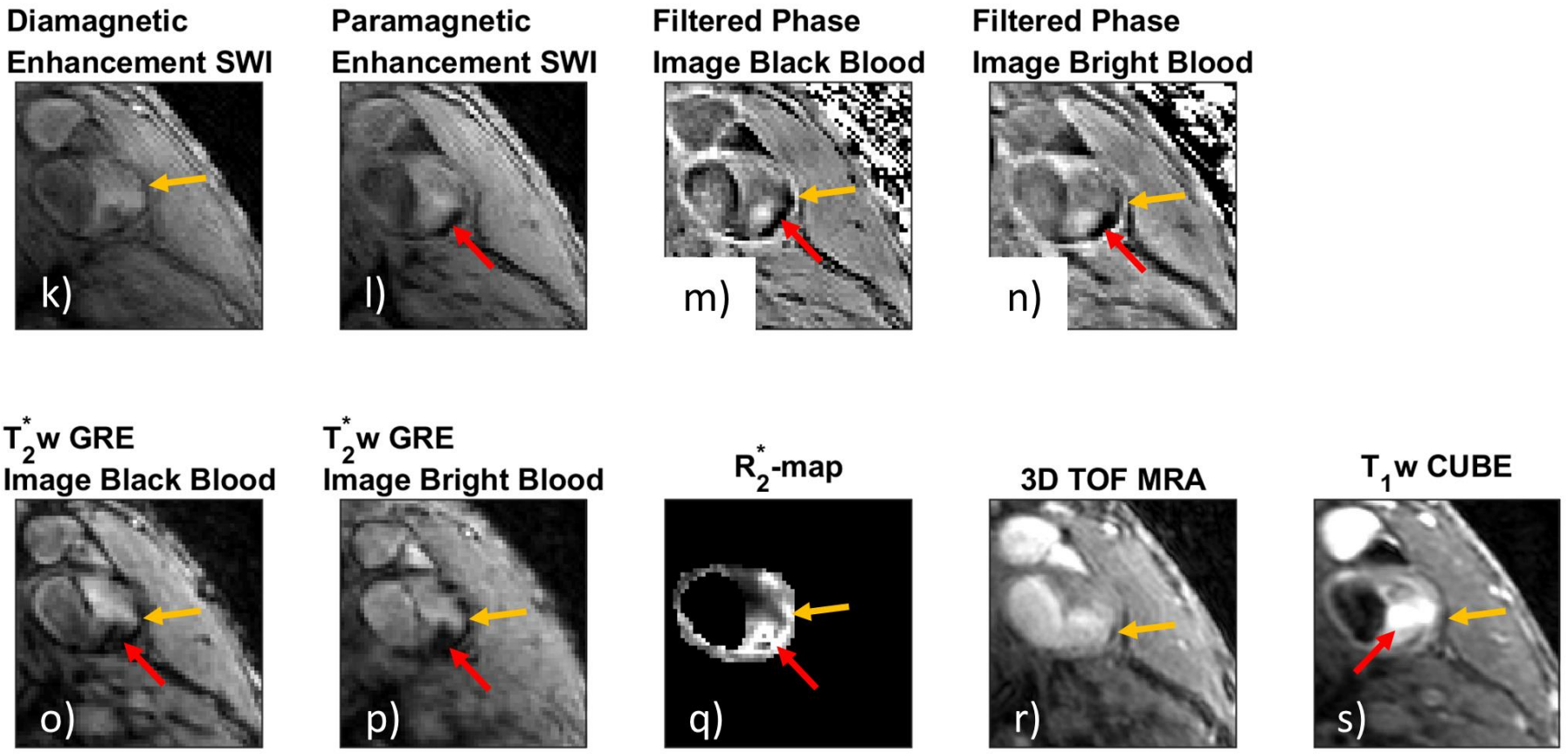

*Figure 4-1: Pre- (a-d, f-j) and post-contrast images (k-s) from the multi-contrast protocol. Calcification is identified by a positive phase shift on the filtered phase images of both bright (TE=4.4 ms) (d, n) and black blood (TE = 5 ms) (c, m) gradient echo filtered phase images as indicated by the yellow arrows. The signal in this region was selectively suppressed on the SWI specifically used to detect diamagnetic materials (a, k) but not on the SWI used for detection of paramagnetic materials (b, l). The SWI images are generated from the first echo time (TE = 5 ms). Correspondingly, calcification appeared hypointense on the $T_2^*$w bright (TE = 15.1 ms) (g, p) and black blood (15.9 ms) (f, o) images, 3D TOF (i, r) and $T_1$w CUBE (j, s). Calcification furthermore led to hyperintensities on $R_2$* maps. (h, q). CT showed increased Hounsfield units in the location of the calcification (e). USPIO-contrast agent uptake could be detected as hypointensities on the post-contrast filtered phase images (m, n) and selective signal suppression on the corresponding SWI (l) as indicated by the red arrow. This corresponded to a decrease in signal intensity on $T_2^*$w gradient echo (o, p), and a signal increase on the $R_2$* maps (q) and $T_1$w CUBE (s). (I presented aspects of these results at* (292)*)*

A comparison of the SWI pre-contrast images showed improved visualisation in all cases of the calcification on the diamagnetic SWI, due to a positive value on the filtered phase. On the “diamagnetic” SWI, the signal within regions of calcification was suppressed selectively. Figure 4-1 & Figure 4-2 show the images from the multi-contrast protocol before and after contrast-agent administration. The hyperintensities, identifying calcification on the filtered phase images (Figure 4-1 c, d, m, n; Figure 4-2 c, d, l, m), were consistent with the findings from the other sequences, i.e. an increase in $R_2^*$ (Figure 4-1 h, q; Figure 4-2 g, p) in comparison to “normal” plaque regions, that did not contain any susceptibility sources, and hypointensities detected on all other contrast weightings and an increase in Hounsfield Units as detected on CT images (Figure 4-1 e). The two examples on Figure 4-1 & Figure 4-2 are relatively lightly calcified plaques. Here, the paramagnetic SWI demonstrated USPIO-uptake (Figure 4-1 l, Figure 4-2 k), due to a negative value on the filtered phase image (Figure 4-1 m, n, Figure 4-2 l, m). This was consistent with an increase in $R_2^*$ value (Figure 4-1 q, Figure 4-2 p)/decrease in $T_2^*$w rSI (Figure 4-1 o, p; Figure 4-2 n, o) when comparing images acquired pre- and post-contrast administration. SWI processing allowed for a clear distinction between paramagnetism and diamagnetism on the post-contrast images alone.

# Pre-Contrast Acquisition

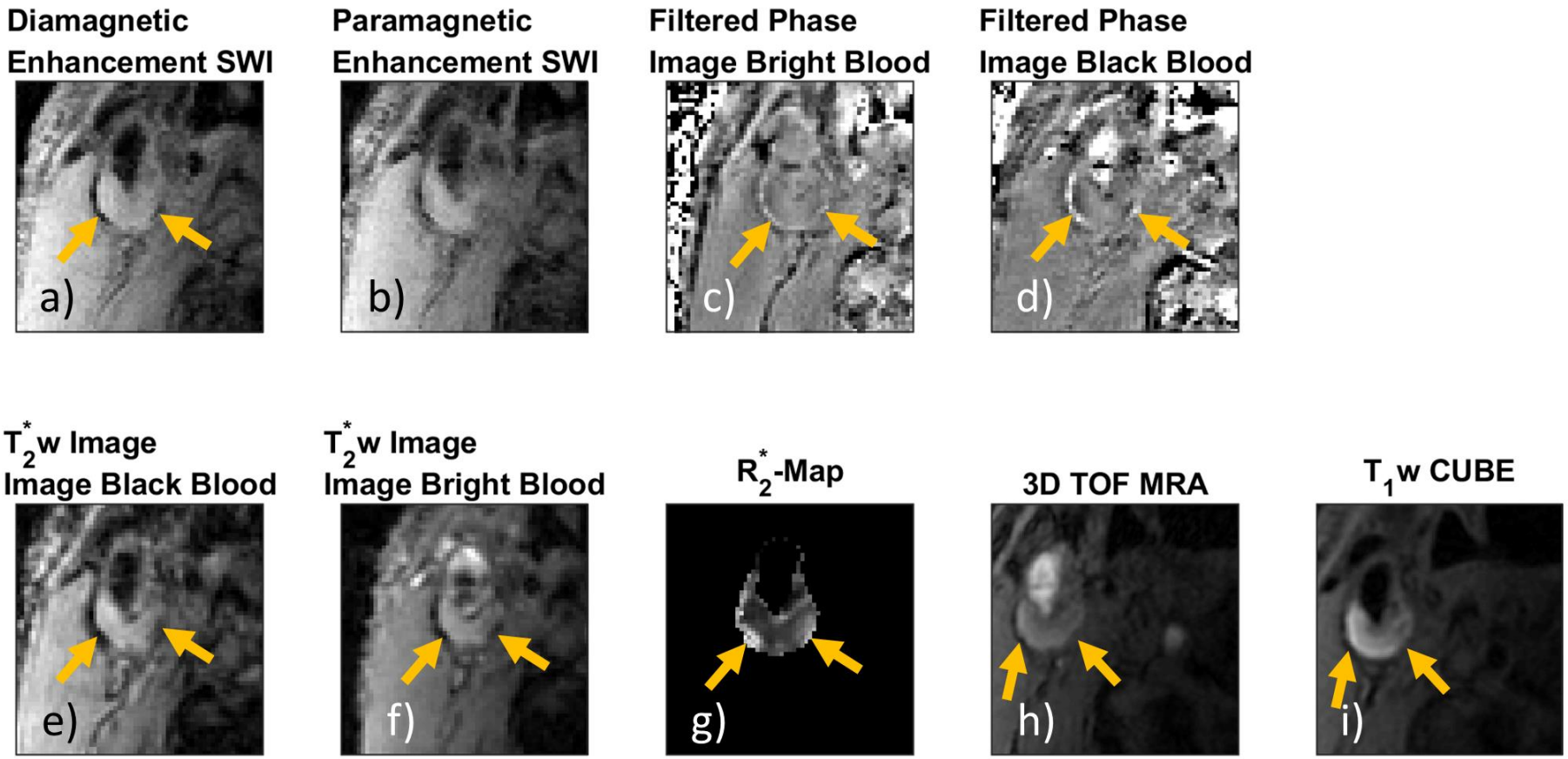

# Post-Contrast Acquisition

**Diamagnetic Enhancement SWI**

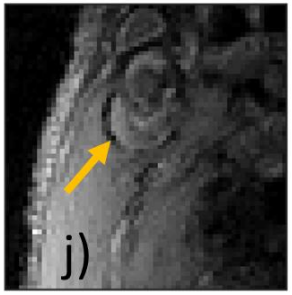


**Paramagnetic Enhancement SWI**

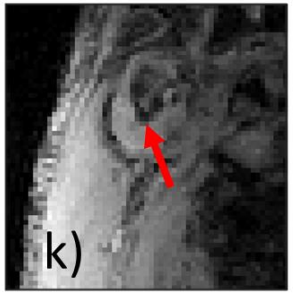


**Filtered Phase Image Bright Blood**

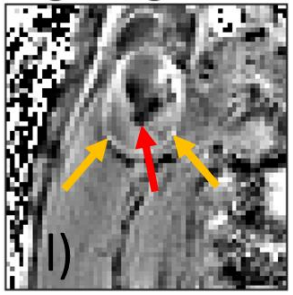


**Filtered Phase Image Black Blood**

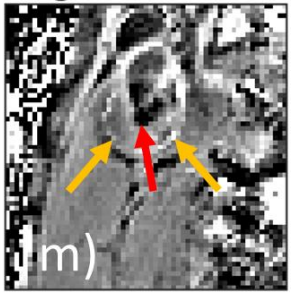


**$T_2^*$w Image Image Black Blood**

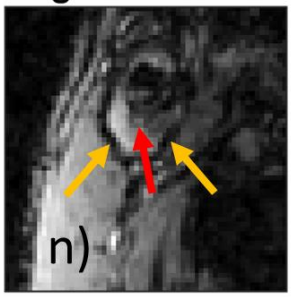


**$T_2^*$w Image Image Bright Blood**

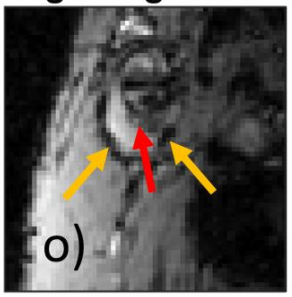


**$R_2^*$-Map**

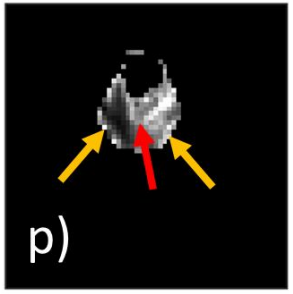


**3D TOF MRA**

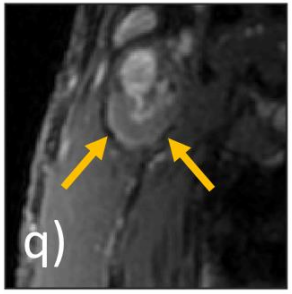


**$T_1$w CUBE**

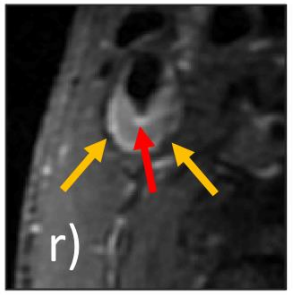

*Figure 4-2: Pre- (a-i) and post-contrast images (j-r) from the multi-contrast protocol. Calcification is identified by a positive phase shift on the filtered phase images of both bright (c, l) and black blood (d, m) gradient echo filtered phase images as indicated by the yellow arrows. The signal in this region was selectively suppressed on the SWI specifically used to detect diamagnetic materials (a, j) but not on the SWI used for detection of paramagnetic materials (b, k). Correspondingly, calcification appeared as hypointense on the $T_2^*$w bright (f, o) and black blood (e, n) images, 3D TOF (h, q) and T1w CUBE (i, r). It furthermore led to hyperintensities on R2* maps (g, p). USPIO-contrast agent uptake could be detected as hypointensities on the post-contrast filtered phase images (l, m) and selective signal suppression on the corresponding SWI (k) as indicated by the red arrow. This corresponded to a decrease in signal intensity on $T_2^*$w gradient echo (n, o), and a signal increase on the $R_2^*$ maps (p) and T1w CUBE (r). (I presented aspects of these results at* (292)*)*

In heavily calcified plaques, however, it was more difficult to clearly outline and distinguish between regions of USPIO uptake and calcification. Figure 4-3 shows a heavily calcified plaque. On the pre-contrast filtered phase image (Figure 4-3 c, d), plaques were hyperintense due to large regions of calcification, which was confirmed with a CT image (Figure 4-3 e). On the post-contrast images, however, the signal phase within the plaque was inhomogeneous (Figure 4-3 m, n) and there were regions of hyper- and hypointensity. Due to the non-local effects and geometry- and orientation-dependence of the magnetic field inhomogeneities, it is difficult to unambiguously distinguish calcification from USPIO-uptake.

Pre-Contrast Acquisition

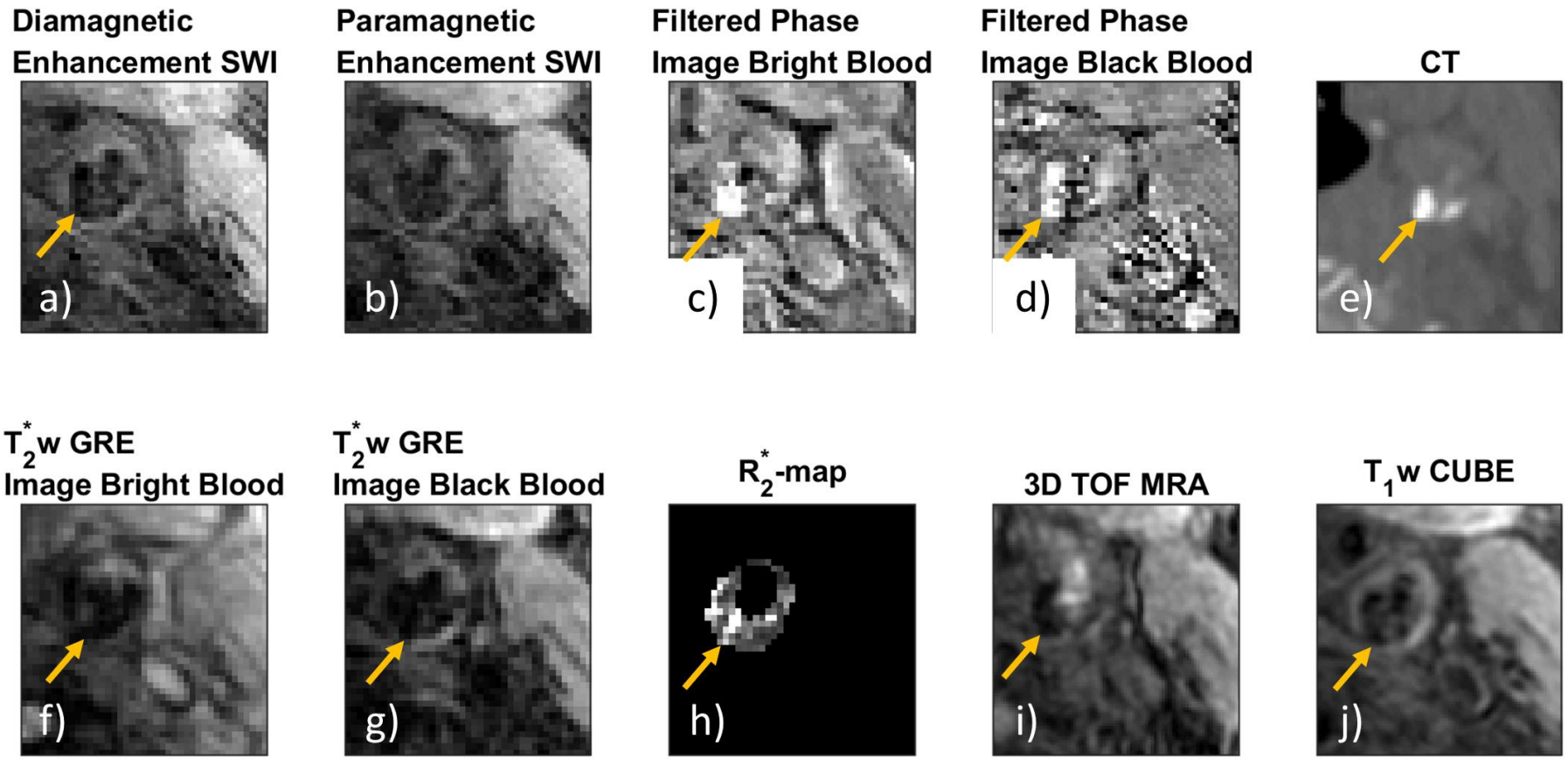

# Post-Contrast Acquisition

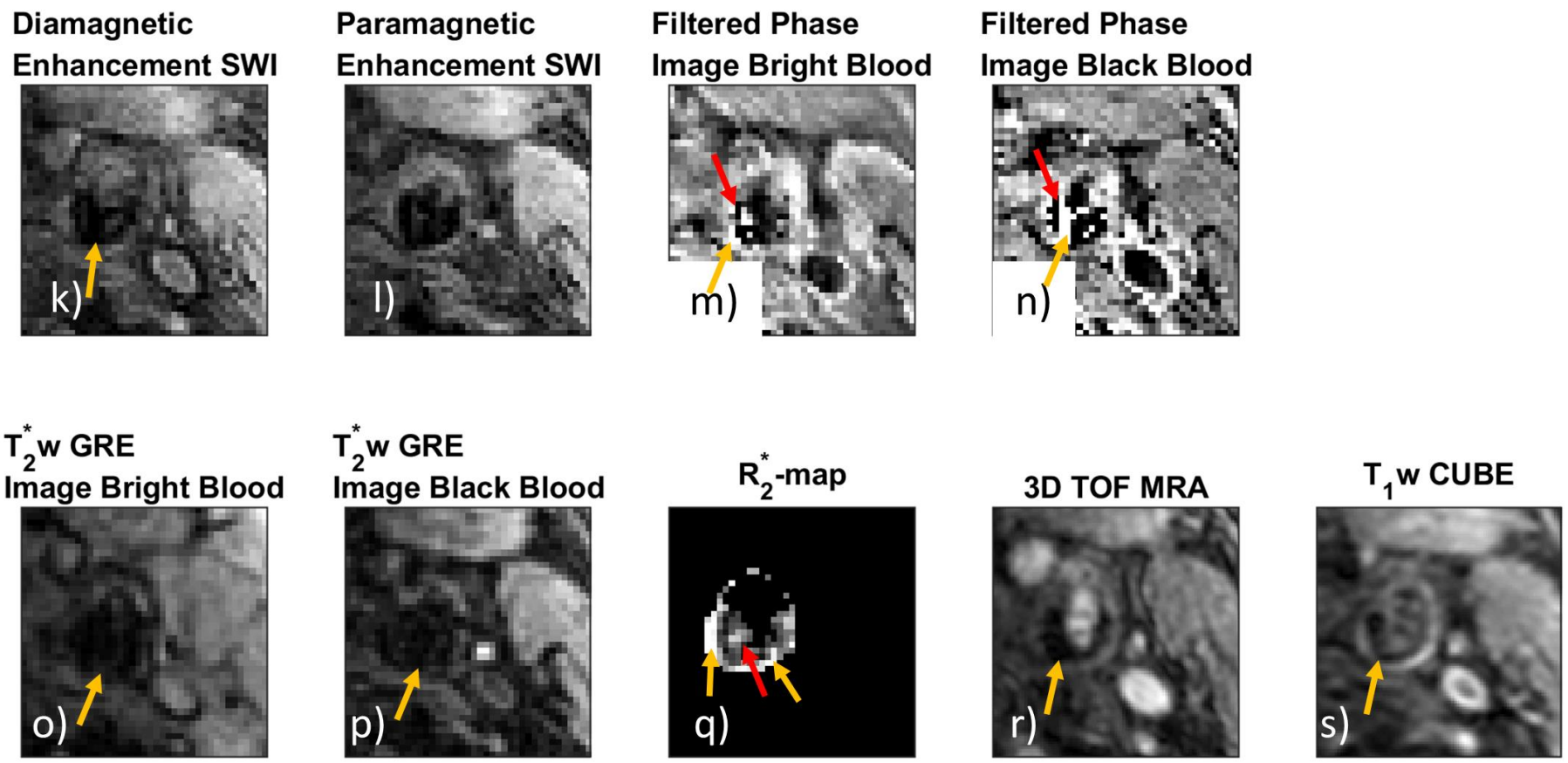

*Figure 4-3: Pre- (a-d, f-j) and post-contrast images (k-s) from the multi-contrast protocol. On the pre-contrast images calcification is identified by a positive phase shift on the filtered phase images of both bright (c) and black blood (d) gradient echo images as indicated by the yellow arrows. The signal in this region was selectively suppressed on the SWI specifically used to detect diamagnetic materials (a) but not on the SWI used for detection of paramagnetic materials (b). Correspondingly, calcification appeared as hypointense on the $T_2^*$w bright (f) and black blood (g) images, 3D TOF (i) and $T_1$w CUBE (j). It furthermore led to hyperintensities on $R_2^*$ maps (h) and CT (e). USPIO-contrast agent uptake rendered the signal in the post-contrast filtered phase images (m, n) inhomogeneous (red arrow). The plaques appeared hypointense on all the other contrast weightings and exhibited a high $R_2^*$ value.*

For quantitative analysis of these results, regions of calcification, USPIO uptake, and normal plaque tissue were outlined on the SWI images and filtered phase images on all patients and the mean $R_2^*$ values and $T_2^*$w rSI values were measured within those regions. For illustration purposes, Figure 4-4 shows the ROIs superimposed on a $T_2^*$w image.

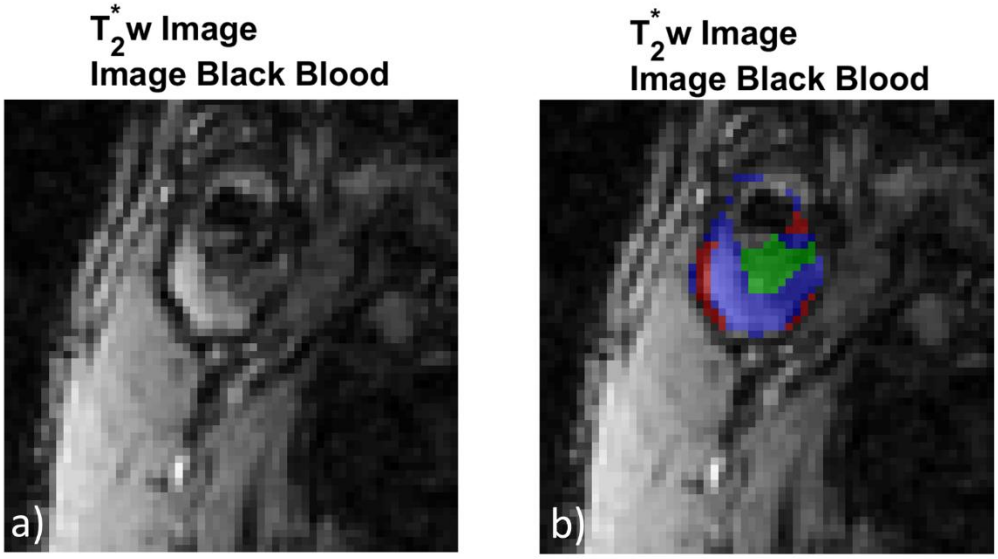


*Figure 4-4: ROIs for normal plaque tissue (blue), USPIO-contrast agent (green) and calcification (red) as outlined on SWI superimposed on a $T_2^*$w image*

In order to confirm the presence of susceptibility-induced de-phasing, the corresponding boxplots are shown in Figure 4-5. Here it can be seen that on the post-contrast images the normal tissues have increased $R_2^*$ values / decreased $T_2^*$ rSI in comparison to the pre-contrast analysis. This may be due to the increase in field inhomogeneities on the post-contrast images due to the presence of USPIO-contrast agents that are non-local and may increase the overall $R_2^*$. Both calcification and

USPIO uptake exhibited increased $R_2^*$ / decreased $T_2^*$ rSI values relative to normal tissue.

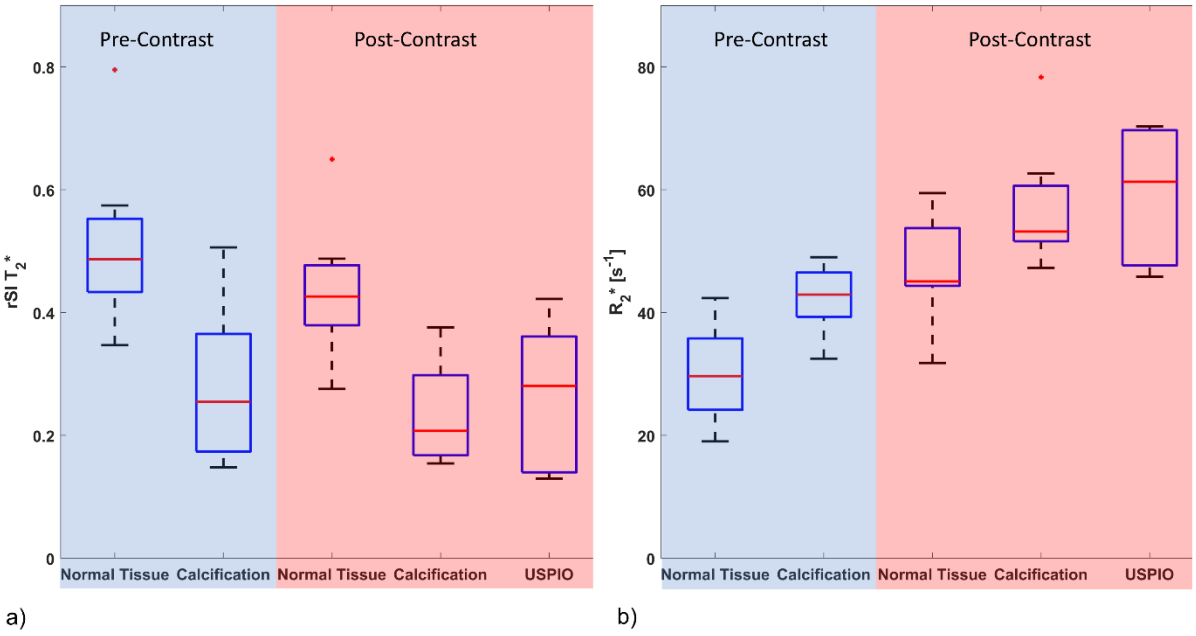


*Figure 4-5: SWI allows for the distinction between normal plaque regions and ROIs containing calcification and USPIO uptake. The $R_2^*$ and $T_2^*$ rSIs confirm that there is an increase in $R_2^*$ in regions of calcification and USPIO uptake relative to normal tissue. The overall $R_2^*$ on the post-contrast images is increased. (I presented aspects of these results at* (292))

When comparing black-blood and bright-blood SWI methodologies and filtered phase images, several differences could be noted. Figure 4-1 & Figure 4-2 show lightly calcified plaques (i.e. plaque region did not contain large amounts of hypointensities on $T_2^*$w GRE pre-contrast images). Figure 4-1 & Figure 4-2 show $T_2^*$w GRE magnitude images at a relatively long echo time, where the susceptibility induced dephasing is emphasized.

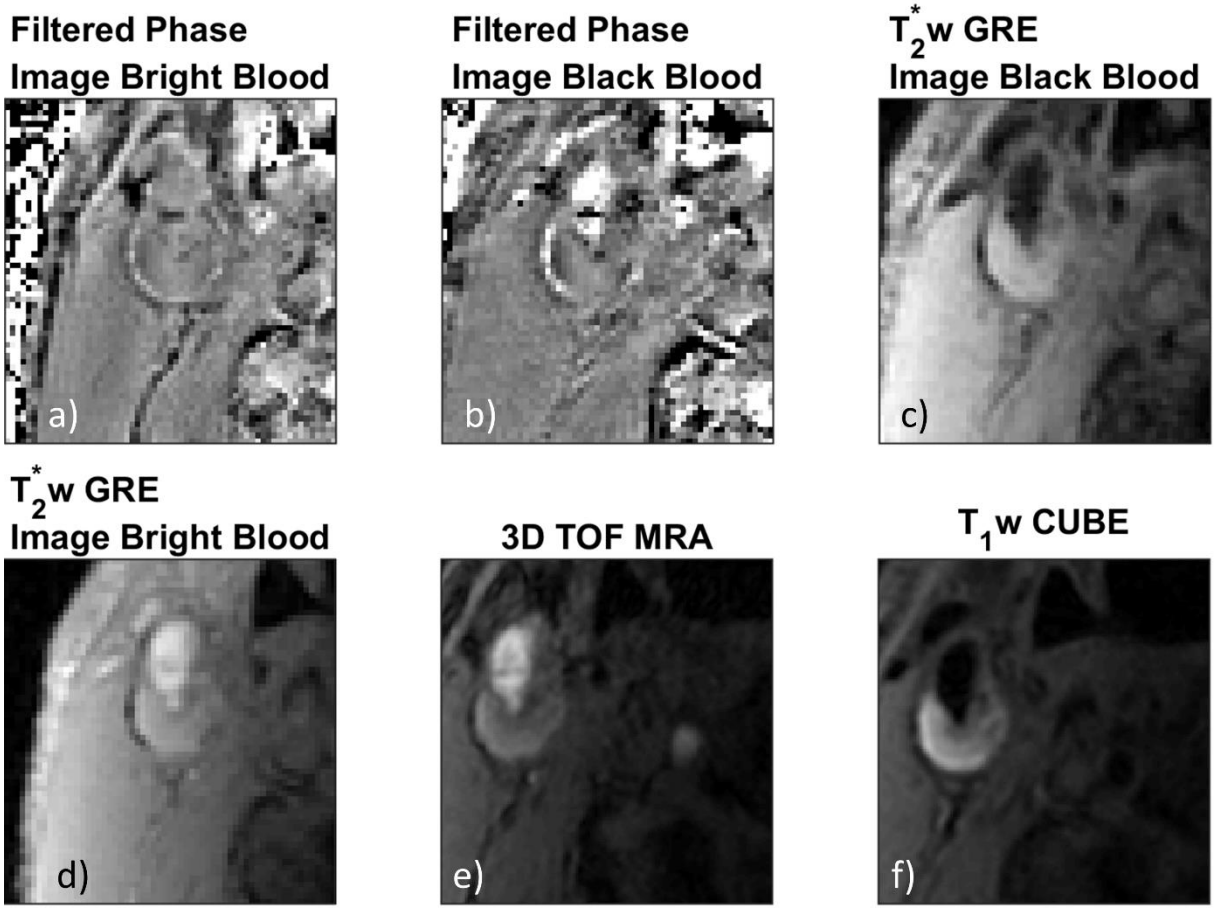


*Figure 4-6: Black blood imaging and bright blood imaging at early echo times allow for a clear delineation of the lumen in lightly calcified plaques*

In order to illustrate the distinction between lumen and vessel wall/plaque, Figure 4-6 & Figure 4-7 show the same imaging locations at an earlier echo time ($TE_{bright}$ = 4.4 ms; $TE_{black}$ = 5 ms) in order to achieve the highest amount of SNR. On Figure 4-6 the lumen and plaque region and vessel wall could be easily distinguished on the pre-contrast $T_2^*$w magnitude images using either black-blood or bright-blood imaging (Figure 4-6 c), d). The CNR is relatively high in both cases ($CNR_{bright}$ = 16.9, $CNR_{black}$ = 33.5). The same is true for Figure 4-7 but the CNR was lower ($CNR_{bright}$ = 5.3, $CNR_{black}$ = 24.3). The distinction between lumen and plaque region is much more difficult on the phase images. However, they allow for the identification of diamagnetic calcification.

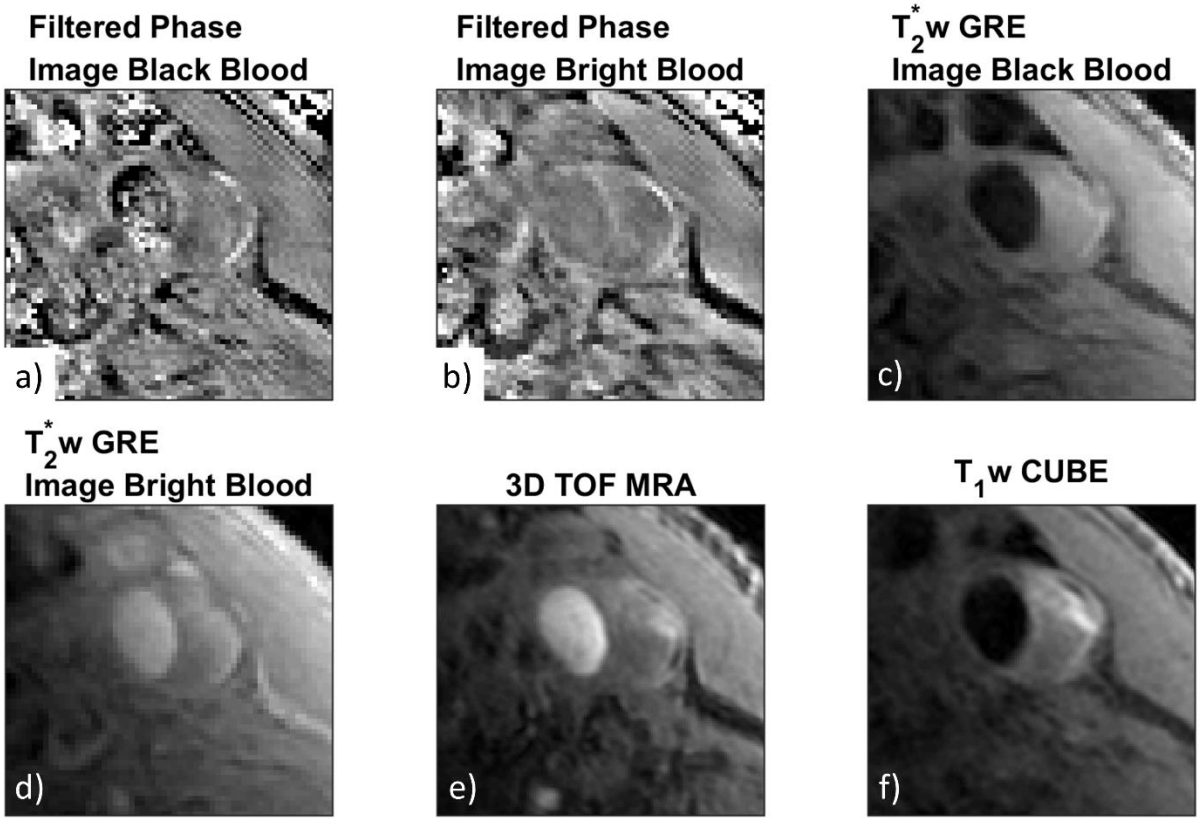


*Figure 4-7: Black blood imaging and bright blood imaging at early echo times allow for a clear delineation of the lumen in lightly calcified plaques*

However, when the plaque region is hypointense, for example due to juxtaluminal calcification, the distinction is rather difficult on the black-blood images, as shown in Figure 4-3. Figure 4-8 shows the corresponding magnitude images at the shorter echo times. Without the presence of additional MRI sequences, such as 3D TOF MRA (Figure 4-8 e), it is impossible to distinguish between calcified plaques or vessel wall and the lumen on black blood $T_2^*$w GRE (Figure 4-8 d). On the bright-blood magnitude images (Figure 4-8 c), in contrast, the bright blood can be clearly distinguished from the more hypointense plaque region and the calcification. On the simultaneously acquired phase images of the bright-blood images, the lumen stands in strong contrast to the hyperintense calcification. Therefore, the CNR is much higher on the bright blood images (($CNR_{bright}$ = 6.3, $CNR_{black}$ = 0.2). On the black-blood images, the low-SNR lumen produces phase noise and is more difficult to distinguish from the calcification.

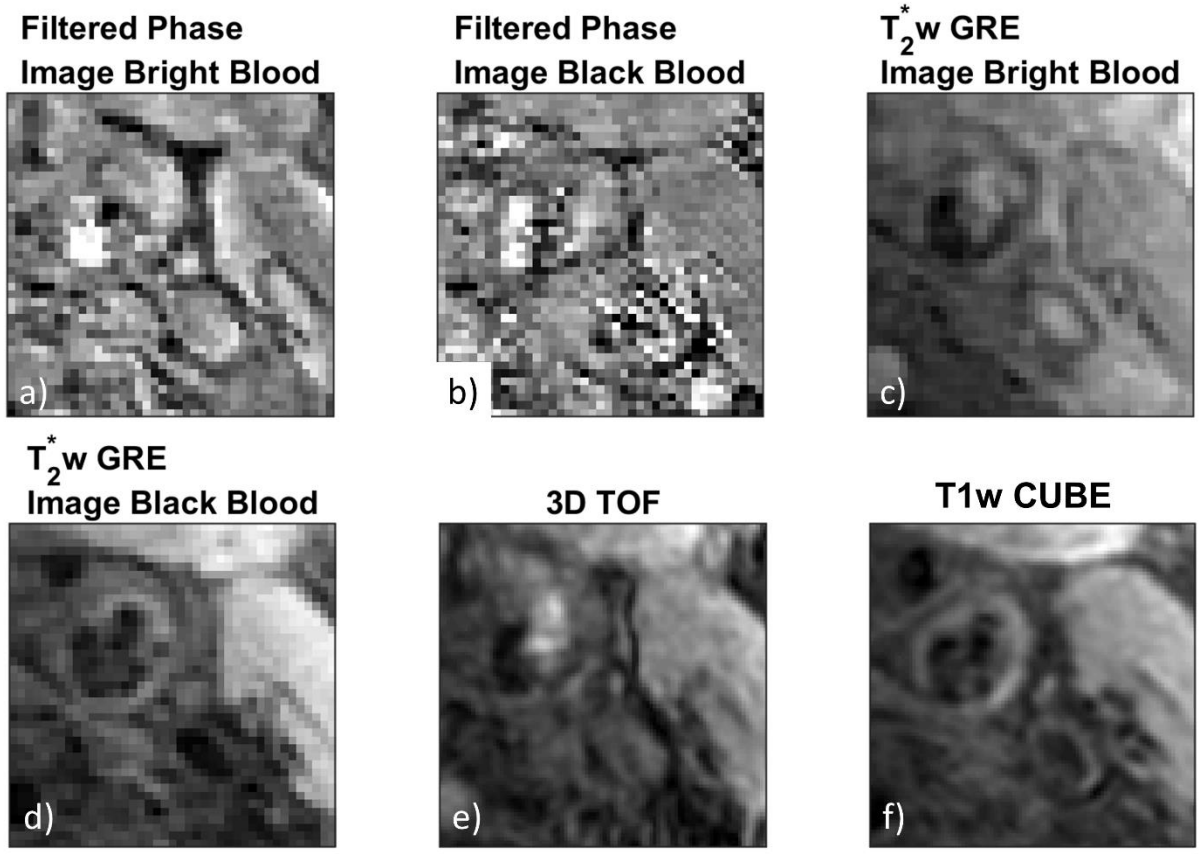


*Figure 4-8: Bright blood imaging improves a clear delineation of the lumen in heavily calcified plaques:*

Another example of juxtaluminal calcification is shown on Figure 4-9. On bright-blood gradient echo imaging and 3D TOF MRA, the calcified vessel wall region is clearly visible. However, it is difficult to distinguish hypointense calcification from the hypointense lumen on both black-blood FSE (DANTE CUBE), and black-blood gradient echo imaging. On the filtered phase image of the bright-blood gradient echo sequence, the hyperintense calcification is much easier to distinguish from the lumen than on the black-blood image, where there is a large amount of phase noise within the lumen due to insufficient SNR. The CNR between lumen and vessel wall is similar in both cases ($CNR_{bright}$ = 18.3, $CNR_{black}$ = 19.3) but the CNR between lumen and calcification is much lower in the case when black blood imaging is applied ($CNR_{bright}$=31.3, $CNR_{black}$=10.0). While CNR was recorded for all cases, it was a highly variable measure. In Figure 4-7, for example the lumen can be clearly delineated on the bright blood images, while on Figure 4-9, the calcification may be easily missed on the black blood images. However, both cases have a similar CNR value.

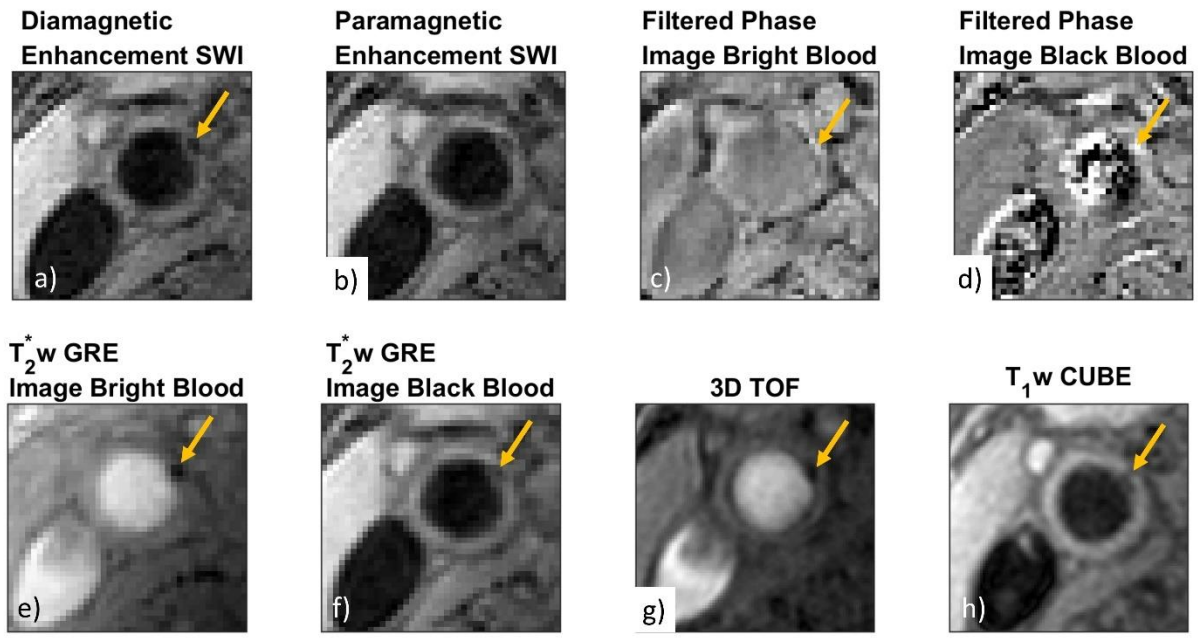


*Figure 4-9: Black blood imaging may lead to difficulties in identifying juxtaluminal calcification (yellow arrow)*

### 4.3.1 Histological Validation

The histological results that were available came from the patients shown in Figure 4-2 and Figure 4-3, which were lightly and heavily calcified plaques respectively. In the lightly calcified plaque, USPIO uptake as depicted on SWI and filtered phase images was confirmed by the multi-contrast protocol. Figure 4-10 shows the histological result for the same plaque. Due to Perl's Prussian Blue staining, the USPIO nanoparticles are stained blue and the calcification appears as pale regions on both Prussian Blue and Haematoxylin and Eosin staining due to decalcification. This confirms the depiction of USPIO uptake and calcification as seen on MRI. In the heavily calcified plaque shown in Figure 4-11, USPIO uptake could lead to a more inhomogeneous signal on the filtered phase image and ambiguous results on the corresponding SWI images. The corresponding histology slices show that there are widely dispersed iron particles in the overlying fibrotic tissue and the space between calcifications in keeping with USPIO uptake. Again, the iron particles are stained blue using a Perl's Prussian blue stain and the calcification appeared as pale nodules beneath the fibrotic area.

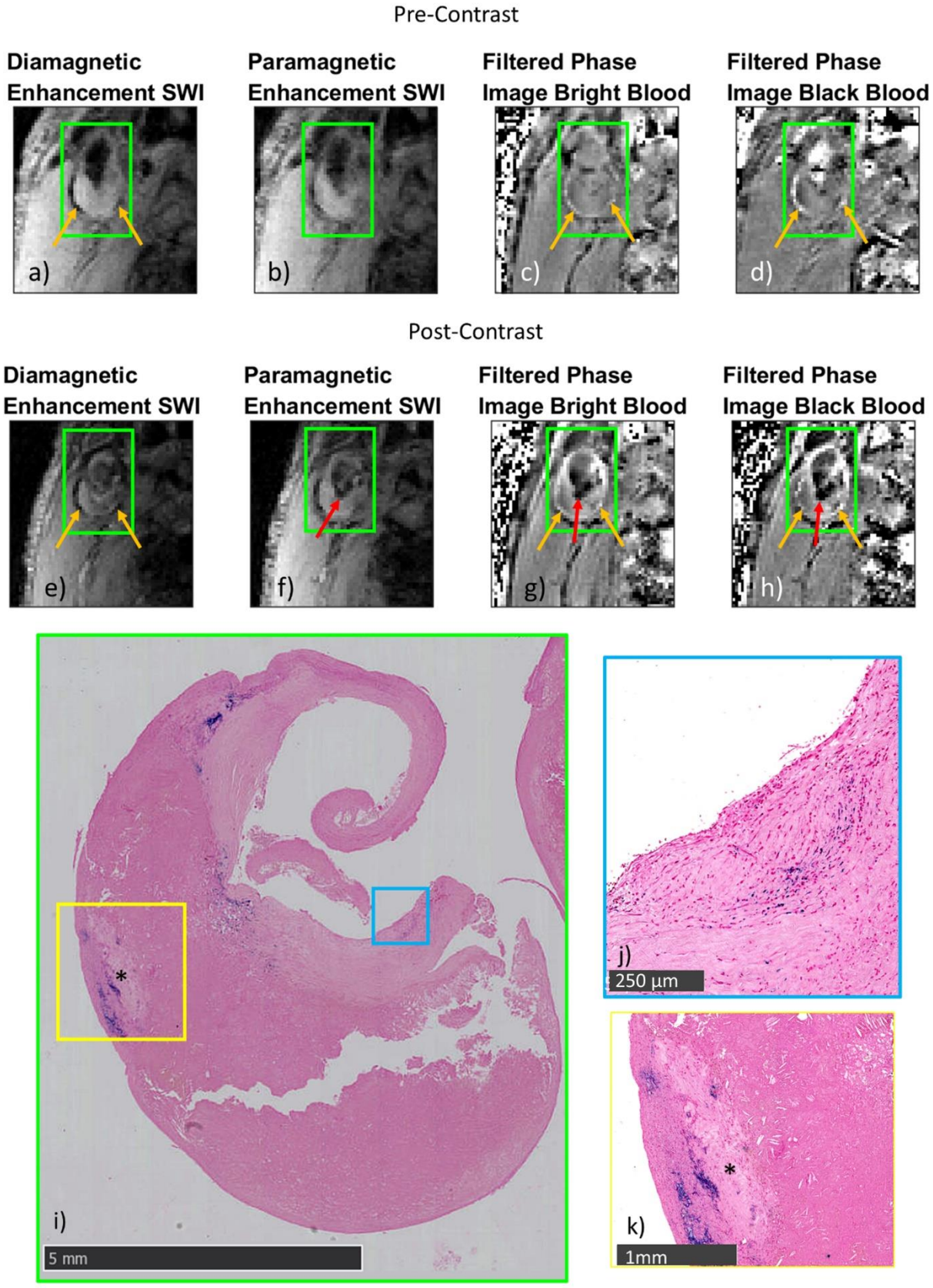


*Figure 4-10: The presence of calcification and USPIO-uptake identified on SWI and filtered phase images is confirmed by histology. Perl's staining has coloured iron particles next to the lumen blue and calcification can be identified by a pale island due to decalcification. The green box indicates the plaque location.*

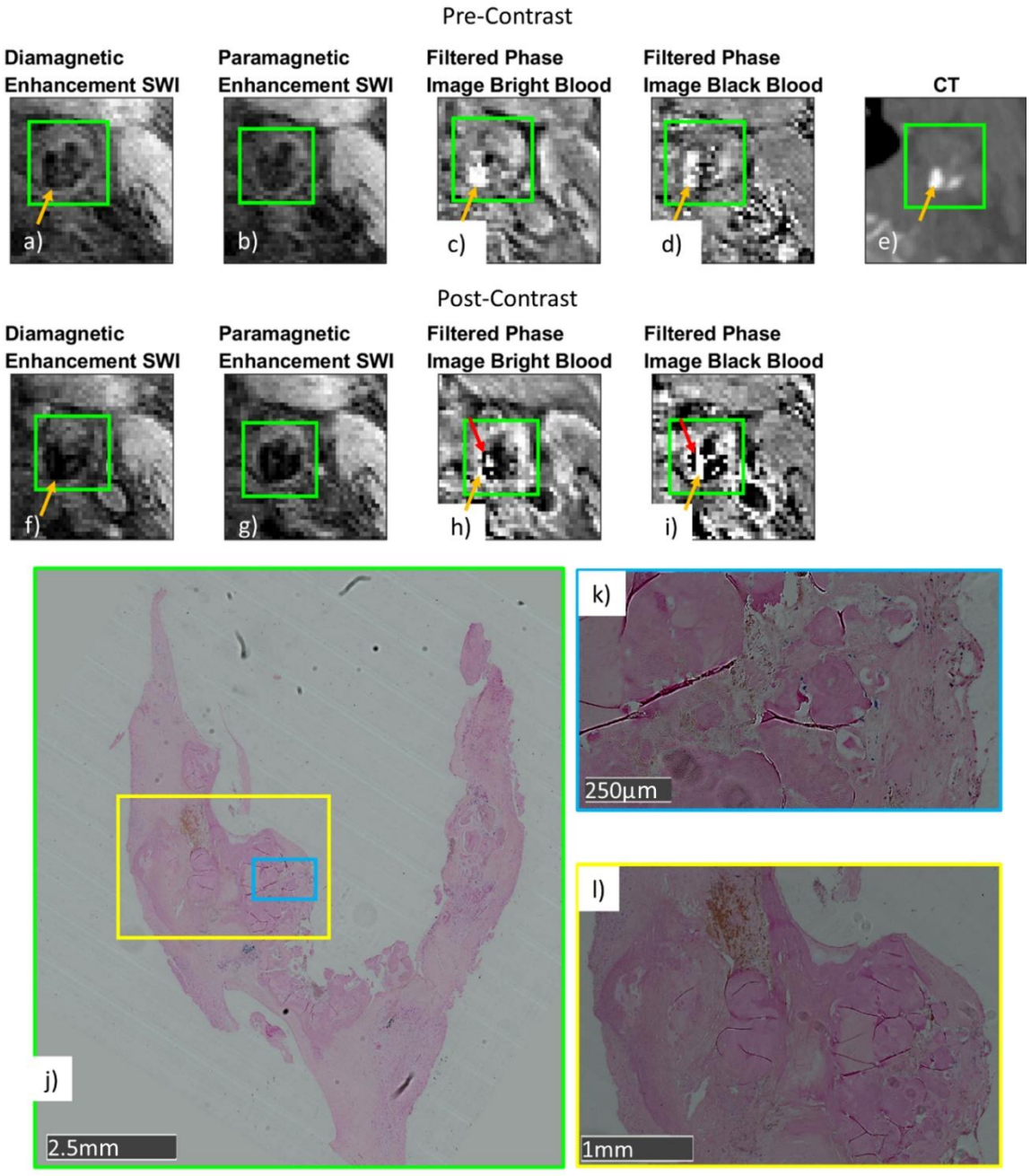


*Figure 4-11: USPIO uptake in a heavily calcified plaque rendered the phase more inhomogeneous on the post-contrast acquisition. This was confirmed in the histological analysis. The Perl's staining showed iron particles interspersed with calcified nodules. The green box indicates the plaque location.*

## 4.4 Discussion

This study evaluated SWI for the identification of plaque calcification and USPIO uptake. As discussed in previous studies, SWI can be used to identify plaque calcification and distinguish between lumen and vessel wall and plaque (296,297,302). Due to its diamagnetism, calcification is easily identifiable on the filtered phase images

and can enhance the contrast between calcification and the surrounding tissue selectively on the susceptibility weighted images. This is in accordance with previously presented results (171–174,296–300,302).

In lightly calcified plaques SWI and filtered phase images allowed for a clear delineation of the regions of calcification and of USPIO uptake. This simplifies USPIO-uptake detection in comparison to $T_2^*$w imaging or $R_2^*$ mapping. These techniques require a comparison of pre- and post-contrast images or quadrant analysis in order to detect USPIO-uptake (126,137,138,141–143). When there is little or no overlap between the calcification and USPIO uptake regions, SWI renders the need for a pre-contrast scan unnecessary. This is in accordance with studies where the different magnetic field inhomogeneities generated by paramagnetic and diamagnetic materials have been used to distinguish haemorrhage from calcification (171–174).

Several positive contrast techniques have been proposed to make use of the changes in local field inhomogeneities to selectively enhance the signal from the local field inhomogeneities. GRASP (151) and IRON (148,293) use the shifts in phase or local precession frequency caused by the local field inhomogeneities to suppress signal from other regions selectively. By acquiring the phase data along with the magnitude data, there is no need to use dedicated sequences such as GRASP or IRON. Instead, SWI provides phase information which has a linear relationship with the field inhomogeneity. In addition, SWI not only provides information about the local field inhomogeneities but also provides detailed high resolution anatomical information from the magnitude images. Furthermore, quantitative information can be extracted from $R_2^*$ mapping (which can be additionally generated from the same imaging sequence). SWI is therefore complementary to the conventionally used USPIO-imaging protocol but provides valuable positive contrast.

There has been research into using black-blood gradient echo imaging in order to improve the contrast between vessel wall and lumen (304). The work in this chapter has demonstrated the advantages of black-blood methods for evaluating lightly calcified plaques. However, for cases of juxtaluminal calcification, both plaque and lumen were hypointense so that the plaque border was difficult or impossible to distinguish from the lumen on the $T_2^*$w magnitude images. Therefore, it is proposed here that it is advantageous to use bright-blood gradient echo imaging.

In heavily calcified plaques, however, it was difficult to distinguish between calcification and USPIO-uptake on SWI and filtered phase images. The non-local effects of the local field inhomogeneities overlap, making it difficult to outline regions of USPIO-uptake and distinguish them from calcification, especially when USPIO nanoparticles are interspersed with calcification. This makes the analysis difficult and while there is a qualitative change in the post-contrast phase images in comparison to the pre-contrast images, it is difficult to identify regions of USPIO-uptake and calcification individually. The presented quantitative analysis is therefore limited in that for heavily calcified plaques the outlined USPIO-regions may accidentally include regions of calcification adjacent to the UPSIO-uptake regions and outlined calcification regions may include USPIO contrast agent. While it has been hypothesized that large regions of macrocalcification may counter macrophage activity (74,75), the frequency of co-localized calcification and USPIO-uptake was high in this study. Furthermore, non-local effects introduce errors in the estimation of areas of USPIO-uptake and calcification and are dependent on orientation and geometry of the underlying anatomy. It has been shown in cerebral applications that Quantitative Susceptibility Mapping may improve the distinction between diamagnetic and paramagnetic materials in comparison to SWI (171). Furthermore, QSM removes non-local effects and provides a quantitative estimate for the local susceptibility. The following chapters will therefore explore how quantitative susceptibility mapping can be performed in the neck and the additional benefits it offers when analysing carotid artery plaques with and without USPIO-contrast agent uptake.

## 4.5 Conclusion

This chapter shows that SWI can identify USPIO uptake and distinguish it from calcification. By displaying the differences in fields generated by paramagnetic and diamagnetic materials, SWI uses similar principles to positive contrast imaging methods but is a technique whose acquisition is identical to frequently used $T_2^*$w multi-echo gradient echo imaging. This may allow for an improved analysis of USPIO-contrast agent uptake to identify carotid plaque inflammation.

# Chapter 5 Joint Quantitative Susceptibility Mapping and Water-Fat Separation: Volunteer Study

Aspects of this work are published in the article Ruetten PPR, et al. “Simultaneous MRI water-fat separation and quantitative susceptibility mapping of carotid artery plaque pre- and post-ultrasmall superparamagnetic iron oxide-uptake”. Magn Reson Med. 2020;84(2):686–697. doi:10.1002/mrm.28151 (305). Other parts of this work have been presented at various conferences (Ruetten PPR, et al. “Quantitative Susceptibility Mapping of the Carotid Artery Wall using IDEAL”, Proc. 34th Ann. Sci. Meeting ESMRMB, 2017:20 (306); Ruetten PPR, et al. “Quantitative Susceptibility Mapping of the Carotid Artery Walls”, Proc. MRC Symposium, 2017 (307); Ruetten PPR, et al. “Phase Corrected Bipolar Acquisition for Simultaneous Water-Fat Separation and Quantitative Susceptibility Mapping of the Carotid Artery Wall”, Proc. 26th Ann. Meeting of ISMRM. ; 2018:2194 (308); Ruetten PPR, et al. “Simultaneous Water-Fat Separation and Quantitative Susceptibility Mapping of the Carotid Artery Wall: Sequence and Processing Considerations”, Proc. 30th Ann. Int. Conf. SMRA, 2018:A52 (309))

## 5.1 Introduction

Quantitative Susceptibility Mapping (QSM) was introduced in the previous chapters 2 and 3 as an MRI technique that can visualize and quantify the underlying susceptibility distributions which generate contrast in $T_2^*$w images and Susceptibility Weighted Imaging (SWI). QSM has been proposed for carotid plaque imaging (292,310–313) due to its ability to depict and distinguish between calcifications and haemorrhage (171) and also to quantify iron concentrations (248), which may play a role in the imaging of iron oxide based contrast agents in carotid plaques for imaging inflammation. Furthermore, QSM has often been cited to improve on existing techniques that generate contrast based on magnetic susceptibility differences (171): Both $T_2^*$w imaging and SWI generate contrast based on the distribution of magnetic field inhomogeneities. These are generated by the underlying susceptibility

distribution, but their signal variations are non-local, orientation- and geometry-dependent. Furthermore, SWI is non-quantitative and the quantification of $R_2^*$ values suffers from background field artifacts, which are typically not corrected in imaging of carotid plaques (137,144). QSM, on the other hand, directly quantifies the underlying susceptibility distribution. It has been shown to improve the distinction between paramagnetic and diamagnetic materials in comparison with gradient echo phase images used in SWI (171) and its quantitative nature has been used to measure ultrasmall superparamagnetic iron oxide (USPIO) contrast agent concentration (295).

QSM processes the complex data from a conventional multi-echo gradient echo sequence, which is typically used in $R_2^*$-mapping and is therefore complementary to conventional imaging protocols. QSM uses the phase data which are often discarded and estimates the distribution of underlying susceptibility via a series of post-processing steps.

After estimation of field inhomogeneities, the background field is removed, and then the dipole field inversion is performed. To estimate a map of the field inhomogeneities, in the brain where QSM has most widely been applied, it can be assumed that the phase varies linearly with time. However, in the neck this assumption does not hold. In the neck fat is present, which differs in precession frequency from water. This type of chemical shift artifact is problematic when estimating $\Delta B$ with the same methodology as is done in the brain. Previous studies performing QSM in the neck and of the carotid arteries have neglected this type of artifact (310,312) or used single echo phase data at an in-phase echo time (313). It has been acknowledged that this poses a limitation, since the artifact caused by the shift in precession frequency may propagate onto the susceptibility maps. Water-fat separation is a field in which complex multi-echo gradient echo data are processed to identify the fat-fraction within each voxel and correct the $\Delta B$ estimate accordingly. Water-fat separation has been widely explored in research but is also used clinically for fat suppression or quantitative fat fraction mapping in liver imaging. In this research a Dixon-based water fat separation technique, Iterative Decomposition of water and fat with Echo Asymmetric and Least-squares estimation (IDEAL), was used to quantify the fat fraction within each voxel and correct for the associated error on the resulting map of field inhomogeneities (261,262). IDEAL water fat separation has been used to correct chemical shift related artifacts during $\Delta B$ estimation in order to perform QSM in other parts of the body than

the brain such as the liver (247,248,263–265), breast (241), spine (266), or ankle region (267).

Furthermore, it is always important to exclude voxels of insufficient SNR with a tissue mask in QSM. In particular regions of bone and air do not produce sufficient signal, so that the phase values in those regions may take on any value in between $-\pi$ and $\pi$. In brain imaging a multi-channel head coil with relatively uniform coil sensitivity is typically used. Furthermore, the brain does not have any air or bone inclusions. A tissue mask for the brain can therefore typically be selected by threshold-based approaches or the brain extraction tool (272). In carotid imaging in our group, however, a dedicated four channel surface coil has been shown to produce the highest SNR. This type of coil however has an inhomogeneous coil sensitivity and therefore the masking process as used in the brain is unsuitable.

In the following chapter, susceptibility maps of the neck and the carotid artery wall were generated by using QSM in conjunction with water fat separation and taking into account the anatomy of the neck. The methodology was tested in a computational simulation, a phantom experiment, and a volunteer study.

### 5.1.1 Theory

In the initial $\Delta B$ estimation during QSM, typically, no chemical shift effects are considered and the complex gradient echo signal is modelled as $S(t) \propto e^{-i\cdot\gamma\cdot\Delta B\cdot TE}$. Therefore, the phase variation over time is linear ($\varphi = -\gamma \cdot \Delta B \cdot TE$) and its slope $\gamma \cdot \Delta B$ is proportional to $\Delta B$, as the gyromagnetic ratio $\gamma$ is a known constant. Typically a least squares algorithm which weights the data points according to their individual SNR can be used to estimate $\Delta B$ as implemented in the MEDI toolbox (258–260).

The presence of fat alters this behaviour. In this work, it is assumed that the precession frequency of fat varies by 3.4 ppm from that of water, which corresponds to $\Delta f_{chem}$ = -220 Hz at 1.5T and -440 Hz at 3.0 T. Therefore, the signal model needs to be adjusted to take into account the presence of fat:

$$S = \left(W + F \cdot e^{-i\cdot 2\pi\cdot\Delta f_{chem}\cdot TE}\right)e^{-i\cdot\gamma\cdot\Delta B\cdot TE} \qquad 5\text{-}1$$

This explains the errors caused when using a conventional $\Delta B$ estimation method. For example, in a voxel containing 100% fat, the estimated $\Delta B$ value would be offset by 220 Hz from the actual value.

Iterative decomposition of water and fat with echo asymmetry and least-squares estimation (IDEAL) is a water-fat separation method, which uses the complex signal from a multi-echo gradient echo sequence in order to fit the signal model to this data by determining $\Delta B$, the water image W, and the fat image F.

In this implementation the $T_2^*$ IDEAL algorithm was used (241,261,262), which includes $R_2^*$ estimation. Furthermore, the complex conjugate of the acquired signal (S*) was taken for estimation of water and fat fraction and $\Delta B$, so that the signal model could be written as:

$$S_i^* = (W + F\exp(2\pi i \Delta f_{chem} TE_i))\exp(2\pi i \psi_{estimate} TE_i) \qquad 5\text{-}2$$

Here $\psi$ is defined as $\psi = \gamma \cdot \Delta B + \frac{iR_2^*}{2\pi}$. From an initial estimate of $\Delta B$, $R_2^*$ and the recorded signal $S_i$ at each echo time $TE_i$, the water and fat image W and F can be estimated in step 1: In order to do this, $S_i^*$ is divided by $\exp(2\pi i \psi_{estimate} TE_i)$, which gives the following equation:

$$\frac{S_i^*}{\exp(2\pi i \psi_{estimate} TE_i)} = W + F\exp(2\pi i \Delta f_{chem} TE_i) \qquad 5\text{-}3$$

This can be written as a matrix multiplication to incorporate the information from all N echoes, with $\frac{S_i^*}{\exp(i2\pi \psi_{estimate} TE_i)} = \hat{s_i}$:

$$\hat{\mathbf{s}} = \mathbf{B}\boldsymbol{\rho} \qquad 5\text{-}4$$

With $\hat{\mathbf{s}} = [\hat{s}_1\ \hat{s}_2\ \hat{s}_3\ \ldots\ \hat{s}_N]^T$; $\mathbf{B} = \begin{bmatrix} 1 & \exp(2\pi i \Delta f_{chem} TE_1) \\ 1 & \exp(2\pi i \Delta f_{chem} TE_2) \\ & \ldots \\ 1 & \exp(2\pi i \Delta f_{chem} TE_N \end{bmatrix}$; $\boldsymbol{\rho} = \begin{bmatrix} w \\ f \end{bmatrix}$

W and F can now be calculated via least squares inversion. This concludes step 1. In step 2, a new system of equations is set up to iteratively update $\psi$, where W, F, and $\psi$ are rewritten as $W = W_{estimate} + \Delta W$, $F = F_{estimate} + \Delta F$, and $\psi = \psi_{estimate} + \Delta\psi$:

$$S_i^* = (W_{estimate} + \Delta W + (F_{estimate} + \Delta F)\exp(2\pi i \Delta f_{chem} TE_i)) \exp(2\pi i (\psi_{estimate} + \Delta\psi) TE_i) \qquad 5\text{-}5$$

So that:

$$\hat{s_i} = (W_{estimate} + \Delta W + (F_{estimate} + \Delta F)\exp(2\pi i \Delta f_{chem} TE_i))\exp(i2\pi \Delta\psi TE_i) \qquad 5\text{-}6$$

Via Taylor expansion, $\exp(i2\pi\Delta\psi TE)$, can be rewritten as $1 + i2\pi\Delta\psi TE$ this can be written as:

$$\hat{s_i} = (W_{estimate} + \Delta W + (F_{estimate} + \Delta F)\exp(2\pi i \Delta f_{chem} TE_i))(1 + i2\pi\Delta\psi TE_i) \quad 5\text{-}7$$

Subsequently it is assumed that the terms $i2\pi TE_i\Delta\psi\Delta W$ and $i2\pi TE_i\Delta\psi\Delta F exp(i2\pi\Delta f_{chem} TE_i)$ can be ignored. The formula is then simplified to:

$$\begin{gathered}\hat{s_i} = (W_{estimate} + F_{estimate}\exp(2\pi i \Delta f_{chem} TE_i)) + \\ \Delta W + \Delta F exp(i2\pi\Delta f_{chem} TE_i) + \\ (W_{estimate} + F_{estimate}\exp(2\pi i \Delta f_{chem} TE_i)) i2\pi\Delta\psi TE_i)\end{gathered} \quad 5\text{-}8$$

This can be rearranged as:

$$\begin{gathered}\hat{\hat{S}}_i = \hat{S}_i - (W_{estimate} + F_{estimate}\exp(i2\pi \Delta f_{chem} TE_i)) = \\ \Delta W + \Delta F exp(i2\pi\Delta f_{chem} TE_i) + \\ (W_{estimate} + F_{estimate}\exp(i2\pi \Delta f_{chem} TE_i)) j2\pi\Delta\psi TE_i)\end{gathered} \quad 5\text{-}9$$

In order to include the information from all TE, this is rewritten in matrix form as:

$$\hat{\hat{\boldsymbol{S}}} = \mathbf{A}\begin{bmatrix}\Delta\psi \\ \Delta W \\ \Delta F\end{bmatrix} \quad 5\text{-}10$$

With:

$$\hat{\hat{\boldsymbol{S}}} = \left[\hat{\hat{S}}_1\ \hat{\hat{S}}_2\ \hat{\hat{S}}_3 \ldots\ \hat{\hat{S}}_N\right]^T \quad 5\text{-}11$$

$$\mathbf{A} = \begin{bmatrix}(W + F + \exp(2\pi i \Delta f_{chem} TE_1)) i2\pi TE_1 & 1 & \exp(2\pi i \Delta f_{chem} TE_1) \\ (W + F + \exp(2\pi i \Delta f_{chem} TE_2)) i2\pi TE_2 & 1 & \exp(2\pi i \Delta f_{chem} TE_2) \\ \ldots & & \\ (W + F + \exp(2\pi i \Delta f_{chem} TE_N)) i2\pi TE_N & 1 & \exp(2\pi i \Delta f_{chem} TE_N)\end{bmatrix} \quad 5\text{-}12$$

$\Delta\psi$, $\Delta W$, and $\Delta F$ can be estimated via least squares inversion and $\psi$ is updated to $\psi + \Delta\psi$. This concludes step 2. Subsequently, a new iteration of the algorithm starts and continues with step 1. W and F are again estimated based on the updated value of $\Delta\psi$. Subsequently, each step is repeated and W, F, and $\Delta\psi$ are updated iteratively. This was repeated for 20 iterations. For the initial estimate of $R_2^*$, zero was chosen.

Based on an initial estimate of $\Delta B$, the $T_2^*$ IDEAL algorithm iteratively determines the water and fat image and then updates the $\Delta\psi$ and $\Delta B$ estimate accordingly. The robustness of the $T_2^*$ IDEAL algorithm depends on the accuracy of the initial estimate

of $\Delta B$ and the SNR and echo spacing of the acquired data. In this research, the background field serves as an initial estimate of $\Delta B$ for the water-fat separation. In chapter 3, it was shown that the background field in the brain is of a very high magnitude in comparison to the internal fields. The background field in the neck is even larger due to the presence of large susceptibility differences around air in the throat and bone in the vertebral column. It can be therefore assumed that it is the dominant field component in the neck. Furthermore, the fields are of the largest magnitude at the tissue interfaces, so that they have a stronger effect in the neck, which has typically a smaller diameter than the brain.

## 5.2 Methods

QSM in combination with $T_2^*$ IDEAL water-fat separation was performed in numerical simulations and phantom experiments. To ensure consistency in the experimental setup the numerical simulations were modelled after the phantom scan. The experimental setup consisted of a water tank into which a table tennis ball was suspended, which contained vegetable oil. Figure 5-1 a shows a magnitude image of the experimental set-up. The phantom was then scanned on a 1.5T GE system (MR450w, GE Healthcare, Waukesha, WI) using a multi-echo gradient echo sequence (Table 5-1).

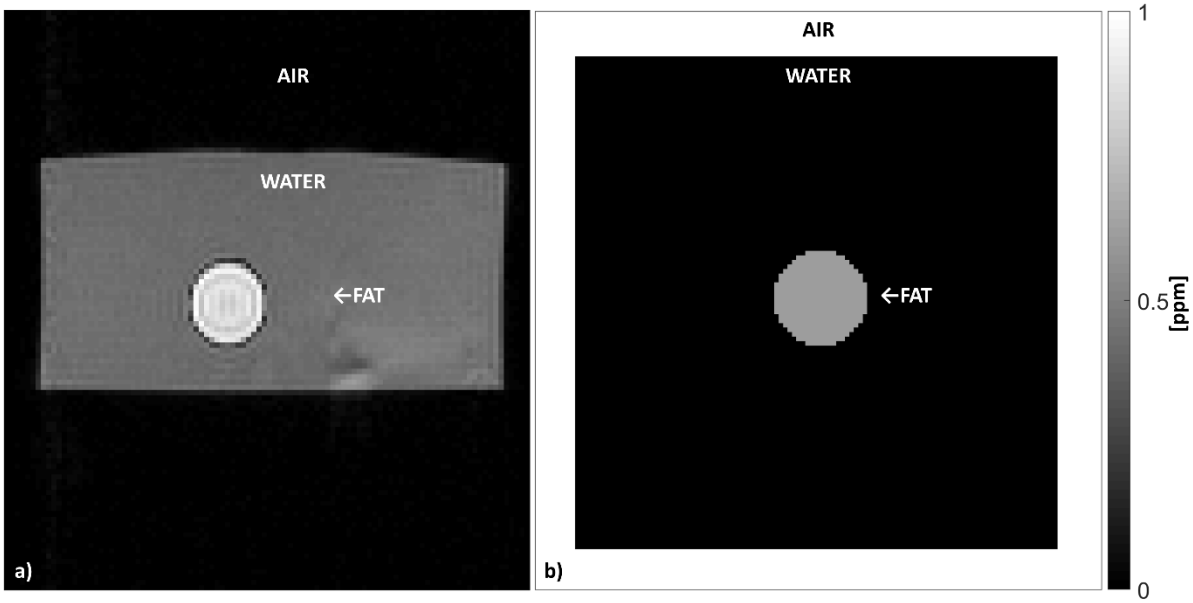


*Figure 5-1: Magnitude image of the Experimental Setup (a) and ground truth susceptibility distribution for the numerical simulation (b)*

For the numerical simulations a synthetic susceptibility distribution was designed as follows: The background was assigned a susceptibility of 9.41 ppm, which was supposed to simulate air relative to water. The susceptibility of water (0 ppm) was assigned to a cuboid shape to simulate the water tank. Within the cuboid a sphere of 0.61 ppm susceptibility was placed, which is a literature value found for the susceptibility of vegetable oil relative to water in order to simulate the oil phantom (314). The synthetic susceptibility map is shown in Figure 5-1 b. A forward calculation was performed that calculated $\Delta B$ at each voxel on the basis of the susceptibility map as described in chapter 3. For the calculation of the dipole kernel, the MEDI toolbox was used. Subsequently a chemical shift of -220 Hz was added onto the voxels within the fat phantom. Subsequently the expected phase values were calculated at each echo time.

After ethical approval and informed consent, ten healthy volunteers (3 women and 7 men aged 30.7±10.7 years, range 23-55 years) were scanned on a 1.5T MR system (MR450w, GE Healthcare, Waukesha, WI) using a similar 3D multi-echo gradient echo sequence to the phantom scans with different parameters due to changes in the field of view. The voxel size was chosen to be consistent with the resolution used for $T_2^*$w imaging and SWI in chapter 4. Dr Jianmin Yuan provided the multi-echo gradient echo sequence, where minor changes to the GE product sequence were made such as a modifiable number of echoes.

| | Phantom experiments | Volunteer Scans |
|---|---|---|
| $TE_1/\Delta TE$/TR [ms] | 1.72/1.58/50.3 | 4.4/4.1/88.2 (unipolar) |
| Number of echoes | 16 | 6 |
| Spatial Resolution [$mm^3$] | 2.2 × 2.0 × 2.0 | 0.625 × 0.625 × 1.0* |
| Field of View [$mm^3$] | 220 × 220 × 160 | 140 × 140 × 60 |
| Bandwidth [kHz] | ±83.3 | ±83.3 |
| Acquisition Time [m:s] | 5:10 | 7:38 |

*Table 5-1: Sequence Parameters *the slice thickness is interpolated from the acquired 2 mm to 1 mm using zero-filling*

In the volunteer scans, the raw MRI data were acquired and reconstructed using parallel imaging (ASSET, similar to the SENSE technique (257)) using customised Matlab code written within GE's orchestra framework, to produce both magnitude and phase images for each echo. For the phantom scan, ASSET coil combination was not

required since a single channel coil was used and the magnitude and phase images were reconstructed using a similar custom code written within the orchestra framework.

The reconstructed images from all scans were processed as follows. From the complex multi-echo datasets, $\Delta B_{uncorrected}$ was estimated without taking into account the errors caused by the chemical shift of fat (258–260). All images were inspected, and in some volunteer scans additional spatial phase unwrapping of the scaled $\Delta B$ was required and a graph-cut-based approach was used (263). The algorithm was chosen due to its robust performance in removing phase wraps and the code used was taken from the MEDI toolbox.

Subsequently a Mask was generated based on the magnitude images. This was straightforward in the phantom experiments and numerical simulations. In the numerical simulations, the area of the water tank was known. In the phantom experiments, the Mask could be extracted by applying a threshold to the magnitude images and extracting the cuboid shape of the water tank. Subsequently, I checked every slice to make sure that all voxels of insufficient signal intensity were excluded manually from the analysis. The Mask was adjusted accordingly. In the volunteer scans, I drew the Mask manually using the magnitude images of the first echo, which gave the maximal SNR, and using the uncorrected field maps for additional validation. A threshold-based approach was not feasible due to the large signal inhomogeneity of the surface coil. Care was taken when drawing the Mask in order to maximize the masked region while excluding voxels of insufficient SNR, which may cause artifacts during the subsequent processing steps. Furthermore, it was important to draw the mask in a way that minimized the presence of susceptibility variations within its boundary region since this may cause artifacts during the background field removal process. Therefore, the boundary was drawn through regions of relatively uniform susceptibility, i.e. muscle tissue, and the number of susceptibility variations inside the boundary region, i.e. caused by regions of fat was minimized. Furthermore, the boundary of the region of interest was placed as far away from the carotid artery wall as possible in order to minimize the errors caused by the background field removal, which primarily arise near the boundary of the masked region.

Subsequently the background field within the Masked region was estimated using the Laplacian Boundary Value algorithm (176), which I chose due to its robust performance in removing any background fields as demonstrated in previous publications (273), chapter 3, and the cases presented here. This served as an input to the $T_2^*$ IDEAL algorithm, which estimated the field map corrected for the chemical shift $\Delta B_{corrected}$ (241,261). Due to the large number of echoes, the $T_2^*$ IDEAL algorithm was performed twice in the phantom experiments. Initially $\Delta B$ was estimated using 4 echoes only, to maximize the bandwidth for unambiguous water-fat separation. This estimate of $\Delta B$ contained fewer artifacts in comparison to the estimate using all 16 echoes in the region where there were large field inhomogeneities for example due to air. Subsequently, the $T_2^*$ IDEAL algorithm was repeated using all 16 echo times, with the $\Delta B$ estimate as an initial estimate for $T_2^*$ IDEAL. This served to maximize SNR. For consistency, the same approach was used in the numerical simulations. A similar problem was not encountered in the volunteer scans, which is why all six echoes could be used for $T_2^*$ IDEAL estimation from the beginning.

In chapter 3, it was shown that errors may occur primarily at the boundary during background field removal. This did not affect the performance of the numerical simulations or the phantom experiments. However, in the volunteer scans, in regions, where muscle tissue and fat intersected the boundary, errors occurred, which lead to localized water fat swaps at the edge of the masked region. These could simply be excluded by manually adjusting the tissue mask after water fat separation.

Subsequently, the background field was removed from the corrected field map using the Laplacian Boundary Value algorithm (176). Finally, dipole field inversion was performed using the Morphology Enabled Dipole Inversion (MEDI) algorithm (260,281,286,287). A regularization parameter of $\lambda$ = 1000 was chosen in the volunteer cohort, since this provided a good trade-off between streaking minimization and only a limited amount of over-smoothing. In the phantom scans and numerical simulations, a stronger regularization was applied ($\lambda$ = 10) as there were only water, air and fat present in the scanned region.

For comparison and analysis, the algorithm was performed without $T_2^*$ IDEAL correction in the phantom experiments, the simulations, and a single volunteer case. Here, the background field from the uncorrected $\Delta B$ (258–260) was simply removed

using the Laplacian Boundary Algorithm and the susceptibility map was estimated using MEDI.

The acquired images in the phantom experiments suffered from several artifacts, in particular variations in signal intensity which were assumed to be due to flow induced by gradient vibrations. Furthermore, it was impossible to remove all air bubbles from the water tank and there was a small air inclusion at the top of the table tennis ball, which were difficult to process and caused artifacts. This may lead to incomplete removal of streaking artifacts using MEDI, which relies on the magnitude images for estimation of susceptibility maps. Since it was known that there would be only three materials present (air, water, fat), the fat fraction map, which simplified the segmentation of the fat phantom, in combination with the magnitude images were used in order to create an artificial magnitude image for the MEDI calculation. The MEDI algorithm was repeated using this magnitude image to improve streaking artifact correction. As explained in chapter 3, MEDI removes all streaking artifacts that correspond to edges not present on the magnitude image. Therefore, if the magnitude images only depict the table tennis ball and the air inclusion in water, most of the residual streaking artifact should be removed.

For each experiment, the outputs of the $T_2^*$ IDEAL algorithm, fat fraction, and $\Delta B_{corrected}$, were compared to the magnitude images and $\Delta B_{uncorrected}$. The susceptibility maps generated with $\Delta B_{corrected}$ and $\Delta B_{uncorrected}$ were compared. While the majority of susceptibility differences within the neck were small and the vessel wall is very thin in volunteers, the region of fat close to the carotid arteries was used in order to evaluate the quality of the susceptibility maps. Regions of fat and muscle tissue were outlined to measure the mean susceptibility values within each. These values were compared to values found in literature and the susceptibility noise level was measured in a way similar to (286). The noise estimate was defined as the standard deviation of the susceptibility within a water/muscle tissue region of interest.

Data processing and analysis were performed using MATLAB (R2017b, MathWorks, Natick, Mass). The code for the uncorrected $\Delta B$-estimation, phase unwrapping, background field removal and dipole field inversion were taken from the MEDI toolbox.

## 5.3 Results

In numerical simulations and the phantom experiments, $T_2^*$ IDEAL correctly identified regions containing fat. Figure 5-2 shows magnitude images (a-c) and fat fraction images (d-f) for the simulation (a, d), phantom experiment (b, e), and a volunteer scan (c, f). The regions containing fat exhibited a greater fat-fraction than the other areas. Within the sphere that was simulated to contain fat, the table-tennis ball fat phantom, and the fat in the volunteers, a high fat fraction was measured ($FF_{sim}$ = 99.38±0.32%, $FF_{experiment}$ = 94.61±1.5%, $FF_{volunteers}$ = 77.3%±6.75 (the latter values were the median and interquartile range calculated over all volunteers)).

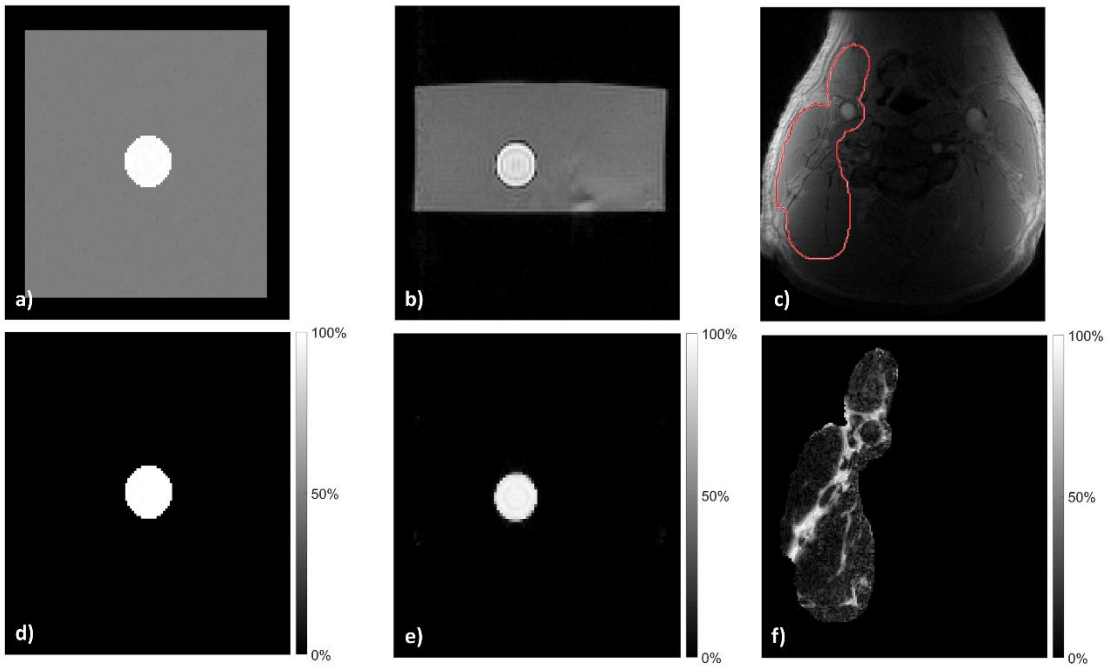


*Figure 5-2: Magnitude images (a-c) and fat fraction maps (d-f) for the numerical simulation (a, d), phantom experiment (b, e), and volunteer scan (c, f)*

Figure 5-3 compares the field maps $\Delta B_{corrected}$ to $\Delta B_{uncorrected}$, estimated with and without $T_2^*$ IDEAL correction respectively. It can be seen that the frequency value determined by scaling $\Delta B_{corrected}$ estimated with $T_2^*$ IDEAL was changed as expected (the difference between $\Delta B_{uncorrected} - \Delta B_{corrected}$ scaled to be given in Hz: $\Delta f_{sim}$=-220.00±0.00 Hz, $\Delta f_{phantom}$=-221.61±0.12 Hz, $\Delta f_{vols}$=-217.84±1.97 Hz (the latter values were the median and interquartile range calculated over all volunteers)).

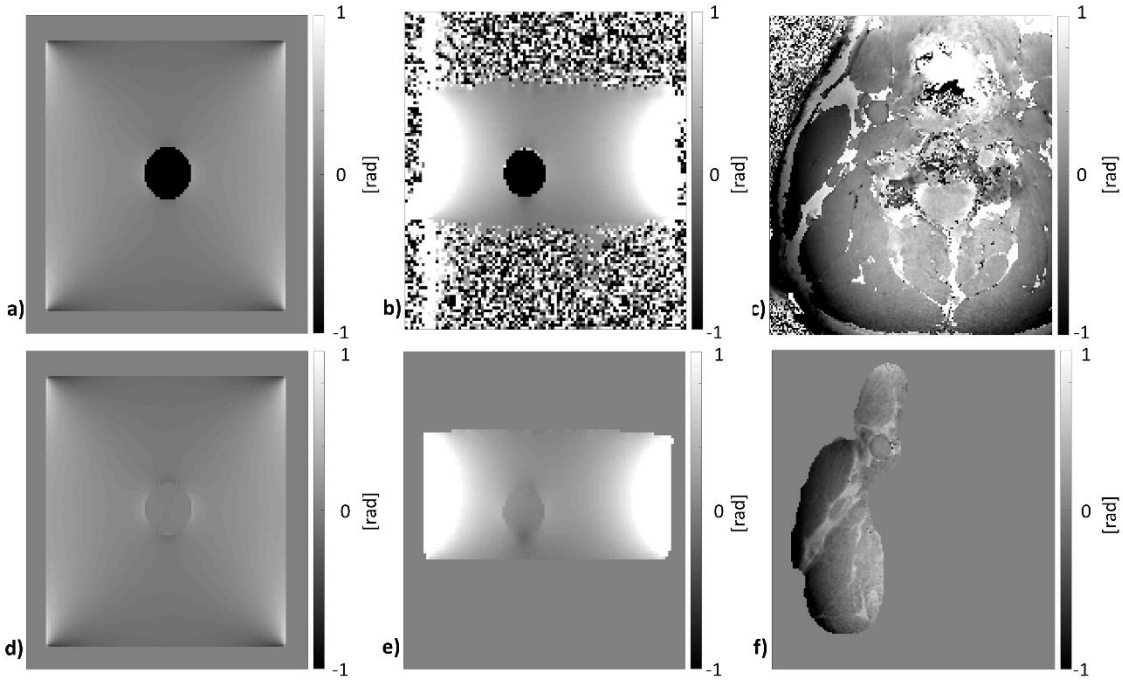


*Figure 5-3: Uncorrected (a-c) and $T_2^*$ IDEAL-corrected (d-f) field inhomogeneity maps (scaled to be given in radians) in the numerical simulation (a, d), phantom experiment (b,e), and volunteer scan (c, f)*

Figure 5-4 shows the magnitude images (a-c), as well as the susceptibility maps generated with (d-f) and without $T_2^*$ IDEAL correction (g-i). The first column shows the results from the numerical simulation, the second column shows the results from the phantom experiment, and the third column shows the results from the phantom experiment with a modified magnitude image. On the susceptibility maps calculated with $T_2^*$ IDEAL correction, the difference in mean susceptibility between fat and water and the standard deviation inside the fat phantom were measured to be 0.61±0.00 ppm in the simulations (Figure 5-4 d) which is in agreement with the ground truth value. For the phantom experiments the mean difference and standard deviation were 0.53±0.03 ppm (Figure 5-4 e), a relatively small deviation from the literature value of 0.61 ppm. The results were improved when the synthetic magnitude image was used as an input for the MEDI calculation, with a measured susceptibility difference of 0.56±0.02 ppm Figure 5-4 f. The improved quality of this susceptibility map was expected since flow related artifacts were removed on the synthetic magnitude images. The flow artifacts introduced edges on the original magnitude images, that were in reality not present within the water so that the removal of streaking artifacts by the MEDI algorithm was incomplete. The noise level as calculated by the standard deviation within water was relatively small, for the simulation $\sigma_{sim} = 0.0012\,ppm$, the

phantom experiments $\sigma_{phantom} = 0.05\,ppm$, and the phantom experiments with the synthetic magnitude images $\sigma_{phantom\_synth} = 0.05\,ppm$. Without $T_2^*$ IDEAL correction applied (Figure 5-4 g-i), the susceptibility differences differed greatly in both numerical simulations and phantom experiments from the expected values (Numerical Simulations: $\chi_{fat}$=-3.91±0.75 ppm; Phantom Experiments: $\chi_{fat}$=-3.88±1.49 ppm, Phantom experiments with modified magnitude image $\chi_{fat}$=-3.76±0.63). In addition, this large deviation from the ground truth worsened the image quality due to strong streaking artifacts. This means that, the noise level within water which was calculated as the standard deviation, is much larger ($\sigma_{sim} = 0.83\,ppm; \sigma_{phantom} = 0.96\,ppm$; $\sigma_{phantom\_synth} = 0.97\,ppm$).

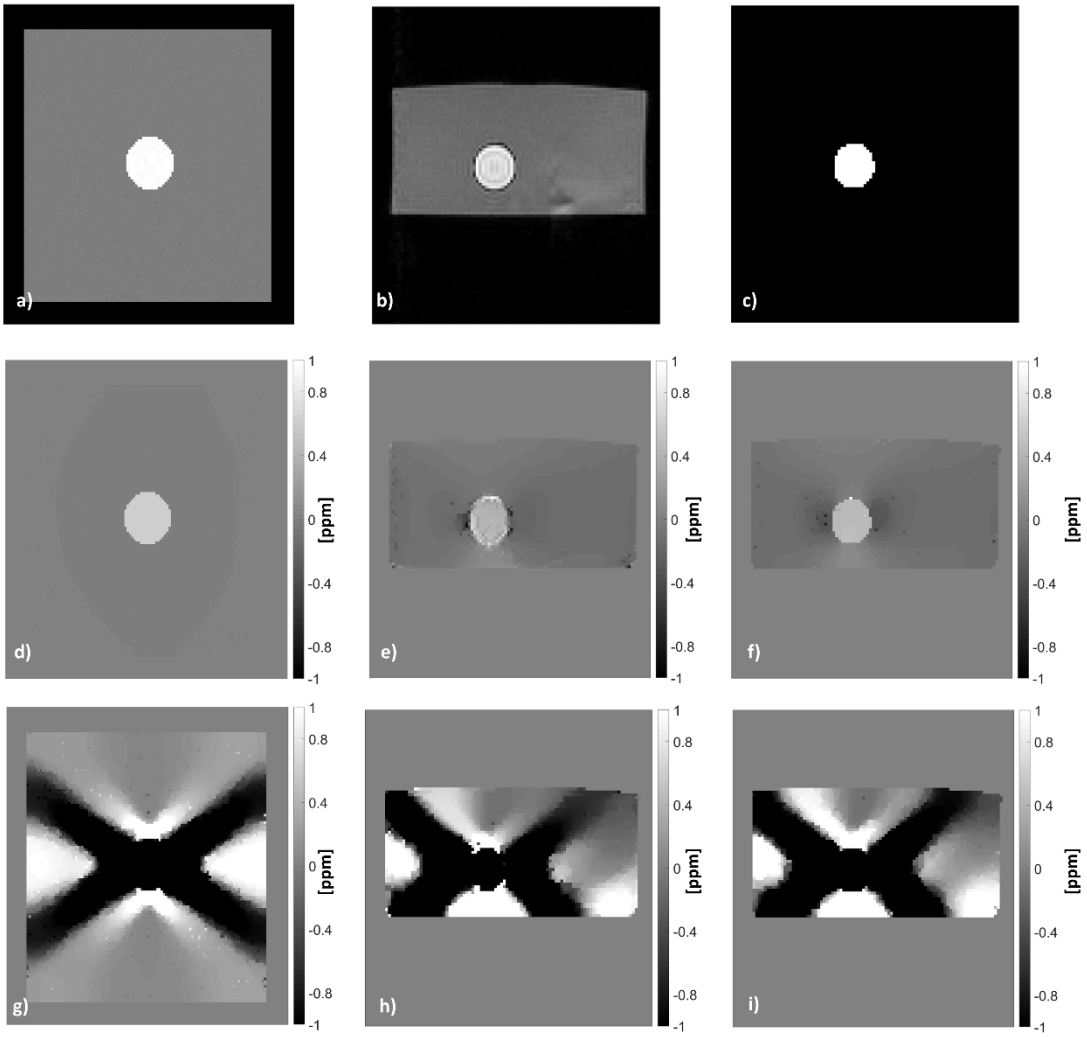


*Figure 5-4: Magnitude images (a-c), susceptibility maps generated with the $T_2^*$ IDEAL-corrected field inhomogeneity maps (d-f) and susceptibility maps generated with uncorrected field inhomogeneity maps (g-i) for the numerical simulation (a, d, g), phantom experiment (b, e, h), and the phantom experiments with a corrected magnitude image.*

In the volunteer study, high quality susceptibility maps could be produced after $T_2^*$ IDEAL correction (Figure 5-5). The median of the mean measured susceptibility values within regions of fat relative to muscle tissue, 0.64±0.13 ppm, in the volunteer scans corresponded to literature values (0.61-0.64 ppm). The vessel wall was identified as slightly more diamagnetic than blood and muscle tissue. While noisier than the magnitude images ($\sigma_{volunteers} = 0.09 \pm 0.04\ ppm$), the vessel wall and lumen could be identified. Without $T_2^*$ IDEAL correction, in the volunteer scans, a similar effect could be observed to the simulations and phantom experiments. Without $T_2^*$ IDEAL correction, the mean susceptibility value inside the fat relative to muscle tissue (1.9±0.67ppm) differed greatly from the expected literature values (0.61-0.64 ppm) and the susceptibility map suffered from streaking artifacts that obscured the entire region of interest ($\sigma_{sim} = 0.15\ ppm$). This made it very difficult to interpret. The susceptibility maps of the remaining volunteers are given in Appendix A.

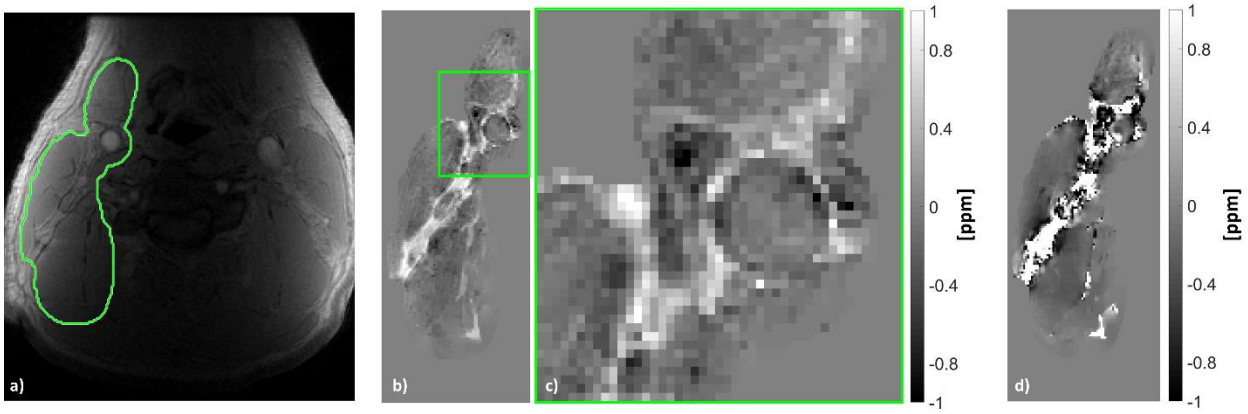


*Figure 5-5: This figure displays the magnitude image (a) for anatomical reference and the susceptibility map calculated where $\Delta B$ was $T_2^*$ IDEAL corrected (b,c). The entire slice is shown in b), while c) shows the area surrounding the carotid artery only for magnification purposes. The susceptibility map calculated from $\Delta B$, where no correction was applied is shown in (d).*

## 5.4 Discussion

This work shows the ability of the $T_2^*$ IDEAL algorithm to correctly and independently identify regions containing a large fat fraction and correct the $\Delta B$ estimate accordingly. This results in high quality susceptibility maps which were able to quantify the susceptibility of fat in the neck and identify the diamagnetic vessel wall. Without $T_2^*$ IDEAL correction, the fat introduced offset errors into the $\Delta B$ maps, which propagated

onto the susceptibility maps. This not only led to erroneous susceptibility estimates for fatty tissue but also severe streaking artifacts.

Due to the convolution operation that describes the relationship between the magnetic field and the susceptibility map, localized errors on $\Delta B$ lead to nonlocal errors on the susceptibility map—voxels where $\Delta B$ has been wrongly estimated, for example due to chemical shift artifacts or insufficient SNR, lead to nonlocal errors, for example streaking artifacts, on the resulting susceptibility map (284,285).

The reduction of streaking artifacts is important to correctly analyse the underlying anatomy. Without application of $T_2^*$ IDEAL a severe decrease in image quality could be observed. Streaking artifacts obscured the entire image and the carotid arteries and render either a qualitative or a quantitative analysis impossible.

It is acknowledged here that the chemical shift of fat in the neck may not be exactly 220 Hz and the susceptibility may not exactly be 0.61 ppm. The resulting inaccuracies in $\Delta B$ estimation may subsequently propagate onto the susceptibility maps. Despite this, the combination of $T_2^*$ IDEAL and QSM produced high quality susceptibility maps with these assumptions that were able to correctly estimate susceptibility in selected regions of interest and depict the anatomy of the neck. In order to further increase the accuracy, a more accurate estimation of the fat-spectrum within the fat could be achieved using MR spectroscopic imaging. However, when assessing carotid artery plaques, the exact susceptibility value of fat outside the carotid artery plaque is irrelevant and the streaking artifacts in the proposed methodology were not obscuring the carotid artery. An improved modelling of the fat spectrum therefore may or may not improve the image quality. Another effect of the frequency shift of lipids is chemical shift induced misregistration. During frequency encoding, the spatial information from which the image is reconstructed relies on the spatial variation of frequency. The chemical shift makes the signal from fat appear to be generated at a different location in the frequency encode direction. This results in band artifacts at water/fat interfaces (121). It was assumed that the chemical shift-induced misregistration was negligible, which was justified by the large bandwidth and low field strength.

Other methods attempting to perform QSM in the neck and of carotid arteries and carotid artery plaques have ignored chemical shift artifacts (310,312) or acquired the signal in-phase (313). It has even been acknowledged that neglecting these effects

leads to artifacts on the susceptibility maps (310). An alternative to minimize the chemical shift related artifacts would be to choose in-phase echoes only. This however limits the choice of echo times and therefore increases the echo spacing, which in turn decreases the SNR at later echoes. By using QSM in conjunction with $T_2^*$ IDEAL instead, it was possible to acquire echoes at arbitrary echo times. i.e. with a shorter echo spacing than would be required for in-phase imaging, with a conventional multi-echo gradient echo imaging sequence. This may be advantageous in patient scans at 1.5T imaging, particularly if the SNR and image quality is poor due to patient anatomy or patient movement.

## 5.5 Conclusion

The feasibility of acquiring susceptibility maps of the necks and carotid arteries of a volunteer cohort using a combination of QSM and $T_2^*$ IDEAL water fat separation has been demonstrated. In the next chapter this will be applied in a cohort of patients diagnosed with carotid artery disease. Carotid artery plaques frequently contain sources of high susceptibility differences relative to healthy muscle tissue – intraplaque haemorrhage and calcification – and plaques also contain a lipid core which may be identified using water-fat separation. Furthermore, QSM may offer a method of quantification and positive contrast in imaging paramagnetic contrast agents such as Ultrasmall Superparamagnetic Iron Oxide (USPIO) nanoparticles. Since the image quality is typically poorer in patients compared to volunteer studies, a further reduction in echo spacing will be achieved using bipolar readout gradients. A reduction in echo spacing leads to shorter echo times, which are of a higher SNR, and also renders the water-fat separation more robust.

# Chapter 6 Simultaneous MRI Water-Fat Separation and Quantitative Susceptibility Mapping of Carotid Artery Plaque Pre- and Post-USPIO

Aspects of this work are published in the article Ruetten PPR, et al. “Simultaneous MRI water-fat separation and quantitative susceptibility mapping of carotid artery plaque pre- and post-ultrasmall superparamagnetic iron oxide-uptake.”, Magn Reson Med. 2020;84(2):686–697. doi: 10.1002/mrm.28151 (305). Other parts of this work have been presented at various conferences (Ruetten PPR, et al. “Quantitative Susceptibility Mapping of the Carotid Artery Wall using IDEAL”, Proc. 34th Ann. Sci. Meeting ESMRMB, 2017:20 (306); Ruetten PPR, et al. “Quantitative Susceptibility Mapping of the Carotid Artery Walls”, Proc. MRC Symposium, 2017 (307); Ruetten PPR, et al. “Phase Corrected Bipolar Acquisition for Simultaneous Water-Fat Separation and Quantitative Susceptibility Mapping of the Carotid Artery Wall”, Proc. 26th Ann. Meeting of ISMRM. ; 2018:2194 (308); Ruetten PPR, et al. “Simultaneous Water-Fat Separation and Quantitative Susceptibility Mapping of the Carotid Artery Wall: Sequence and Processing Considerations”, Proc. 30th Ann. Int. Conf. SMRA, 2018:A52 (309); Ruetten PPR, et al. “Calcification and USPIO detection in Carotid Artery Plaque using QSM and SWI”, Proc. 27th Ann. Meeting of ISMRM 2019:2090 (292); Ruetten PPR, et al. “Plaque feature analysis using a joint method of QSM and water-fat separation”, Proc. 27th Ann. Meeting of ISMRM 2019:2091 (311); Ruetten PPR, et al. “Identification of USPIO-uptake in calcified Atherosclerotic Plaques”, Proc. 36th Ann. Sci. Meeting ESMRMB 2019:20 (315))

## 6.1 Introduction

As demonstrated in chapter 4, susceptibility effects play an important role in imaging carotid artery plaques. It has been demonstrated in particular that Susceptibility Weighted Imaging (SWI) may be used to identify large changes in tissue susceptibility

caused by plaque calcification and that SWI may be used in the detection of Ultrasmall Superparamagnetic Iron Oxide (USPIO) contrast agent uptake by macrophages in carotid plaques.

As previously described, USPIO nanoparticles are injected intravenously and can enter plaques from the lumen through a leaky endothelium, where they are taken up by macrophages, thus serving as a marker for plaque inflammation (126,137,138). In the past, USPIO-uptake has been detected by comparing two MRI scans, acquired before and after administration of the contrast agent. In regions containing the contrast agent, the signal intensity will decrease on $T_2^*$w gradient echo imaging and increase on $R_2^*$-maps (137,138,141–143). However, a pixel-wise comparison of images acquired before and after contrast agent administration requires complex co-registration so that the plaque is often divided into segments, which can be compared more easily (137,138,141,142). As an alternative, the use of positive contrast techniques to image USPIO uptake has been proposed to render pre-contrast scans obsolete and simplify USPIO-detection even in calcified plaques (144,148,151,152).

Many positive contrast techniques such as IRON (148) or GRASP (151) use the fact that USPIO-uptake leads to a severe increase in tissue susceptibility, thus creating field inhomogeneities. While the positive contrast techniques rely on dedicated sequences in order to image only the signal originating from regions containing certain field inhomogeneities, it was shown in chapter 4 that conventional (multi-echo) gradient echo phase images are linearly related to these field inhomogeneities. SWI and filtered phase images were used to distinguish between the fields from diamagnetic and paramagnetic materials, which are quite different. This allowed for a clear distinction between paramagnetic and diamagnetic materials in lightly calcified plaques. However, in chapter 3, it was shown that the fields are highly orientation and geometry dependent. By depicting the underlying susceptibility distribution instead, Quantitative Susceptibility Mapping (QSM) offers a more direct way to visualize the contrast agent uptake and distinguish it from calcification: The susceptibility distribution does not suffer from non-local effects, and also is not orientation dependent. These improvements that QSM offers over SWI have been discussed in previous studies in the brain, where QSM has improved the distinction between paramagnetic haemorrhage and diamagnetic calcification in comparison with SWI/filtered phase images (171).

Chapter 5 demonstrated the feasibility of imaging the carotid artery wall in a group of healthy volunteers using QSM in combination with water fat separation. The potential for QSM in imaging carotid atherosclerosis has been demonstrated in previous studies (292,308,310–313), but these studies either did not evaluate the errors caused by the presence of fat or required the acquisition at in-phase echo times (313) and also did not evaluate its potential for providing positive contrast in imaging USPIO contrast agent uptake in carotid atherosclerosis (310,312,313). In chapter 5 it was shown that the chemical shift from fat caused severe errors in the field map estimation, that propagated onto the susceptibility maps of the neck and the carotid arteries and obscured the region surrounding the carotid arteries. These errors were corrected through the inclusion of $T_2^*$ IDEAL water-fat separation in QSM processing. In addition to removing artifacts and improving the image quality of the resulting susceptibility maps, this may also offer a novel method of identifying the lipid rich necrotic core (LRNC), another feature of atherosclerotic plaques. A previous study has discussed the use of Dixon-based water-fat separation techniques in carotid artery plaques (not in combination with QSM) to identify the LRNC (316).

In chapter 5, it was shown feasible to generate susceptibility maps of the necks and carotid arteries of volunteers by performing QSM in combination with $T_2^*$-IDEAL water-fat separation, using a conventional multi-echo gradient echo MRI sequence (Susceptibility Weighted Angiography, SWAN). However, in patient studies, the signal-to-noise ratio (SNR) and image quality are often much lower than in volunteer scans as shown in Figure 6-1.

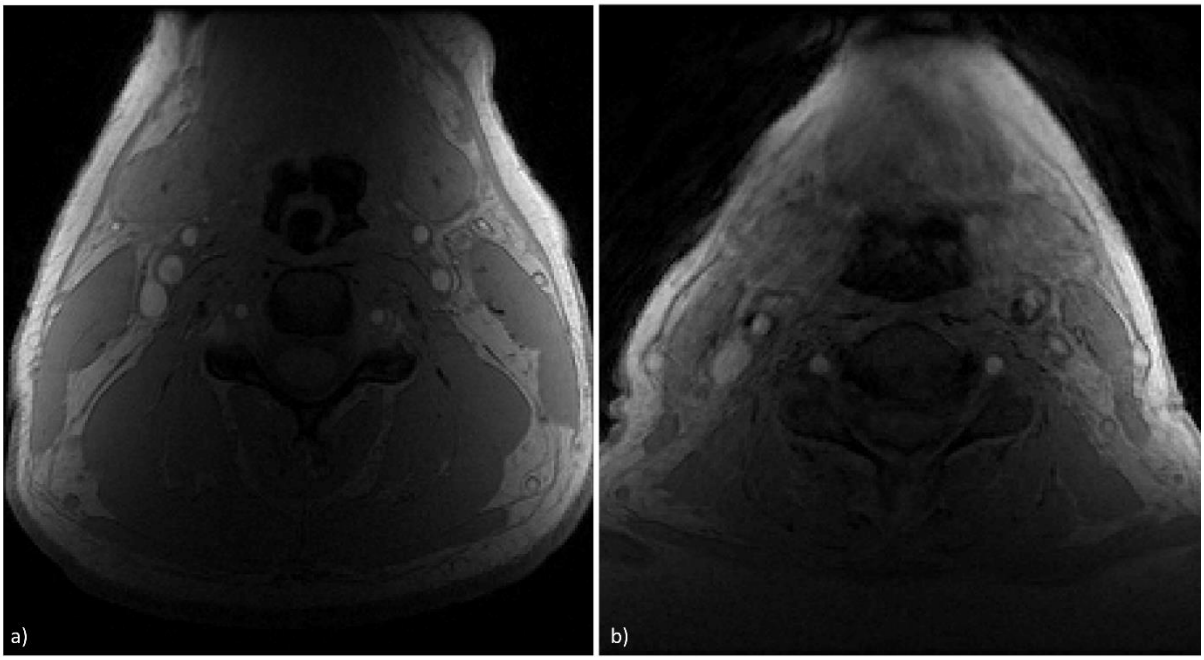


*Figure 6-1: The observed image quality is better in volunteer scans (a) in comparison to patient scans (b)*

This may be due to issues with coil positioning or patient movement. Within this study, it was therefore proposed to use bipolar readout gradients in order to shorten echo-spacing. This acquisition technique has shown in previous studies to improve SNR, acquisition efficiency and to reduce the number of phases wraps and to widen the spectral bandwidth in which water and fat can be separated (317,318). However, due to gradient delays and eddy currents, gradient-polarity-specific phase offsets are added onto the signal at each echo time. This means that phase discrepancies between even and odd numbered bipolar echoes are introduced, which require correction (317,318).

The hypothesis of this chapter is that using bipolar readout gradients would render $T_2^*$ IDEAL water-fat separation and QSM in the neck and of carotid arteries more robust and could be used in a patient cohort. Within the patient cohort $T_2^*$ IDEAL was evaluated as a means to identify the LRNC, and QSM served to identify and distinguish between USPIO-uptake and calcification.

## 6.2 Methods

### 6.2.1 Signal Processing:

***Phase Correction:***

In order to perform $\Delta B$ mapping of the bipolar multi-echo gradient echo dataset, it is necessary to remove the gradient-polarity-specific phase offsets, which are caused by gradient delays and eddy currents (317,318). Since unipolar echoes all have the same gradient polarity, as shown in Figure 6-2 a), the added phase-offset is constant and can be ignored. In bipolar echoes, the gradient polarity in even numbered echoes is reversed from the polarity in odd echoes (Figure 6-2 b).

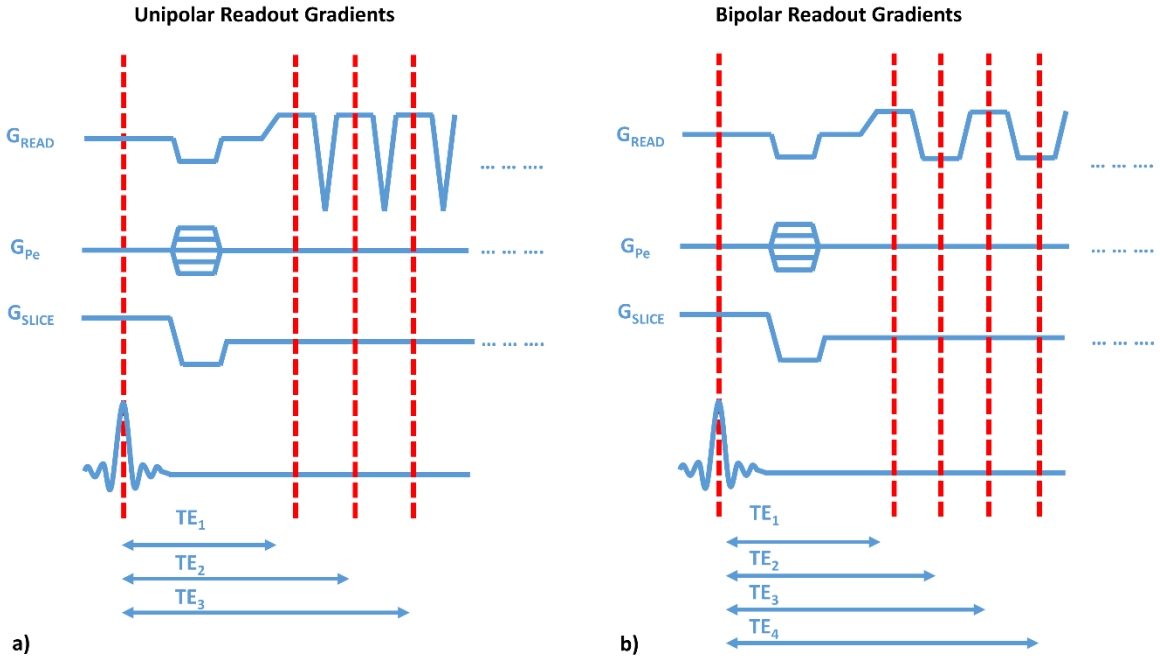


*Figure 6-2: Sequence Diagram of a gradient echo sequence using Unipolar (a) and Bipolar Readout Gradients (b)*

Therefore, even numbered echoes are offset in phase by $\Delta\theta$ from odd numbered echoes. Assuming a constant echo spacing, in voxels with a negligible fat-fraction, $\Delta\theta$ can be estimated from the phase of the first, second, and third echo: $\angle\left((S_2 \cdot S_1^*) \cdot (S_2 \cdot S_3^*)\right) = 2\Delta\theta$. Here, $S_1$, $S_2$, and $S_3$ are the complex signals acquired at the first, second, and third echo time respectively. In previously presented methods (317–319) to correct for this type of phase offset, the variation of $\Delta\theta$ with position was assumed to be linear—predominantly in the readout direction, but there have also

been cases where it was modelled in two or three dimensions (317,318). In this research the dataset was inspected and $\Delta\theta$ was assumed to vary linearly in 2D. A linear function was fit to the estimated $\Delta\theta$. Areas of insufficient SNR and areas of fat were excluded from the fitting process. The complex data were then corrected by removing the linearly modelled $\Delta\theta$ from the even echoes.

***Fat/Water Separation:***

As described previously in chapter 5, QSM in the neck requires correction of the chemical shift of fat. The $T_2^*$ IDEAL (241,261,262) algorithm was used in order to estimate the fat-fraction within each voxel and correct $\Delta B$ accordingly. In chapter 5, where unipolar readout gradients were used, the background field estimated with the Laplacian Boundary Value algorithm (176) was used as an initial $\Delta B$ estimate. In the current chapter, bipolar readout gradients were used to reduce the echo spacing and therefore a rougher initial estimate for the external field $B_{ext}$ could be used. This was achieved by estimating $\Delta B$ generated from the odd echoes only without any $T_2^*$ IDEAL correction applied (258–260); they were approximately at in-phase echo times, and therefore chemical shift artifacts that could potentially propagate onto $T_2^*$ IDEAL were minimized. To this $\Delta B$ estimate a low-pass filter was applied to extract its background field. If necessary, the background field estimate was then unwrapped using a graph-cut-based spatial phase unwrapping algorithm (263). Subsequently, the unwrapped background field served as an input to the $T_2^*$-IDEAL algorithm when estimating the corrected $\Delta B$ estimate. This $\Delta B$ estimate calculated with the $T_2^*$-IDEAL algorithm typically did not require additional phase unwrapping. Using a low-pass filter instead of the Laplacian Boundary Value algorithm (176) to estimate the background field has the advantage that there are fewer artifacts at the boundary of the ROI; these may lead to water fat swaps, which require the ROI to be adjusted after water-fat separation as described in chapter 5.

In order to illustrate the benefit of the bipolar echoes, the field maps in the volunteers were also estimated using an additional acquisition with unipolar readout gradients that was also analysed in chapter 5. The background field was estimated by low-pass filtering an initial $\Delta B$ estimate, which was calculated from the unipolar echo dataset without any $T_2^*$ IDEAL correction. This was used as an input for the $T_2^*$ IDEAL algorithm. The resulting fat-fraction maps and field maps were compared.

***Quantitative Susceptibility Mapping:***

From the $T_2^*$-IDEAL-corrected $\Delta B$-estimate of the bipolar readout gradient dataset, the background field was removed using the Laplacian Boundary Value algorithm (176). The internal field was then inverted using Morphologically Enabled Dipole Inversion (MEDI) (260,281,286,287). The 3D tissue mask for both background field removal and dipole field inversion was manually drawn slice-by-slice on magnitude images and $\Delta B$ maps by me. As described previously in Chapter 5 the mask was carefully drawn. This involved excluding voxels of insufficient SNR to avoid artifacts. Furthermore, the boundary of the mask was drawn through regions of relatively uniform susceptibility such as muscle tissue in order to minimize the presence of susceptibility variations within the boundary, which are the cause of artifacts during background field removal. The boundary was also placed as far away as possible from the carotid arteries in order to reduce the effect of errors that are caused by background field removal near the boundary of the tissue mask on the carotid artery wall.

### 6.2.2 Data Acquisition:

From 31/10/2017 to 10/01/2019, 15 participants were imaged after giving written informed consent. This prospective study had ethical approval.

| ***Parameter*** | ***3D SPGR (bipolar gradients)*** | ***3D SPGR (unipolar gradients)*** | ***3D TOF MRA*** | ***Black-blood fat-suppressed $T_1$w 3D FSE*** |
|---|---|---|---|---|
| ***TR [ms]*** | *88.2* | *88.2* | *20* | *580* |
| ***TE [ms]*** | *$TE_1$ = 4.4, $\Delta TE$ = 2.1* | *$TE_1$ = 4.4, $\Delta TE$ = 4.1* | *3.2* | *15.0* |
| ***Number of echoes*** | *6* | *6* | *-* | *24 (ETL)* |
| ***RBW [kHz]*** | *±83.3* | *±83.3* | *±15.63* | *±31.25* |
| ***FOV [$mm^3$]*** | *140×140×60* | *140×140×60* | *140×140×56* | *140×140×56* |
| ***Sp. res. [$mm^3$]*** | *0.625×0.625 ×1** | *0.625×0.625 ×1** | *0.625×0.625×1.4* | *0.625×0.625×1.4* |

| | | | | |
|---|---|---|---|---|
| ***Acq Time [m:s]*** | *7:38* | *7:38* | *3:07* | *5:47* |

*Table 6-1: Sequence Parameters * the slice thickness is interpolated from the acquired 2 mm to 1 mm using zero-filling.*

The ten healthy participants (3 women and 7 men aged 30.7±10.7 years, range 23-55 years) were scanned as described in chapter 5. In addition to the axial flow-compensated 3D multi-echo gradient-echo acquisition with unipolar readout gradients which was also analysed in chapter 5, an axial flow-compensated 3D multi-echo gradient-echo acquisition with bipolar readout gradients was also acquired at 1.5T (MR450w, GE Healthcare, Waukesha, WI) for QSM in the same scanning session. The repetition times (TR) of both sequences were chosen to be of equal length, so that they could be compared easily. This served to illustrate the benefit of the bipolar readout gradients in comparison to the unipolar readout gradients. The imaging parameters for the healthy volunteer study are given in Table 6-1.

The patient population consisted of five patients (1 woman and 4 men, mean age 71±7.5 years, range 63–81 years) with moderate to severe carotid artery disease (i.e. 50-99% luminal stenosis on carotid duplex imaging). Datasets from four out of the five patients were also analysed in chapter 4 for SWI analysis. The patient recruitment was done by Dr Ammara Usman. Prior to the study patients were screened to minimize potential contraindications of Ferumoxytol contrast agents. This included a review of their medical history, while screening and cross-checking at the time of recruitment and consent. The following exclusion criteria were used: History of atopy, asthma or allergic reaction to contrast media, iron or dextran or a known documented history of haemochromatosis. Furthermore, patients with immune inflammatory conditions, e.g. systemic lupus erythematosus, rheumatoid arthritis were excluded. All of the participants gave informed consent and the study, also presented in chapter 4, had ethical approval from the East of England – Cambridge Central Research Ethics Committee. The patients were scanned on the same MRI system as the volunteers. Two scans were performed, one was performed before and the other one 48 hours after 5 mg/kg USPIO-injection (Ferumoxytol, AMAG Pharmaceuticals, Lexington MA). The injection was performed under the supervision of Dr Usman by trained staff. For QSM, the axial 3D multi-echo gradient echo acquisition with bipolar gradients was used due to the benefits established in the volunteer study—which will be described

in the ‘Results’ and ‘Discussion’ sections of this chapter. The raw MRI data were reconstructed using ASSET, as in chapter 4 and 5. The $T_2^*$w images for each individual echo were generated using the GE scanner reconstruction. These magnitude images were also used for and $R_2^*$ mapping. An additional multi-contrast protocol was acquired during the same MRI exams in order to validate the QSM results. This included $T_2^*$w images and $R_2^*$-maps calculated from the same dataset, 3D time-of-flight MRA, and black-blood (DANTE) and fat-suppressed $T_1$w 3D fast-spin-echo (CUBE). $R_2^*$-mapping was performed with in-house-developed Matlab code provided by Dr Jianmin Yuan on a voxel-by-voxel basis. The black blood preparation CUBE was implemented by Dr Jianmin Yuan. He also provided the multi-echo gradient echo sequence, where minor changes to the GE product sequence were made such as a modifiable number of echoes. Through assessment of the multi-contrast protocol alone, plaque morphology could be evaluated. Plaque calcification appeared as hypointense on all sequences of the protocol and hyperintense on $R_2^*$-maps. Through comparison of the pre- and post-contrast images, USPIO-uptake could be identified. As described in the introduction, elevated concentrations of iron oxide nanoparticles lead to a decrease in signal intensity (SI) on $T_2^*$w images and an increase in $R_2^*$. Furthermore, at low concentrations, the contrast agent appeared hyperintense on $T_1$w imaging. As previously described, this stems from USPIOs also having a $T_1$ shortening effect (127). All of the imaging parameters for the patient study are given in Table 6-1.

In two patients, histology and in two patients computed tomography (CT) data were available. The CT scans were acquired on a Siemens Somatom Definition Flash system (100kV, 0.5×0.5×1 and 0.6×0.6×1 $mm^3$ resolution). The process of the histological analysis is described later.

### 6.2.3 Data Analysis:

#### *Healthy Volunteer Scans:*

To assess feasibility and benefits of bipolar acquisitions for generating susceptibility maps of the carotid arteries, the field maps and fat-fraction maps (generated with $T_2^*$ IDEAL) of bipolar and unipolar acquisitions were compared. On the magnitude images, I subsequently manually outlined fat and muscle tissue using ITK-SNAP (version 3.6.0; http://www.itksnap.org) (320). The mean values within these ROIs on the susceptibility maps, generated from the bipolar acquisition, were measured for all

volunteers to calculate the susceptibility differences and CNR. Noise was defined as the standard deviation within muscle tissue, which was of relatively uniform susceptibility similar to Liu et al. (286). Furthermore, the $T_2^*$ IDEAL corrected susceptibility map was compared to a susceptibility map calculated from an uncorrected $\Delta B$ estimate that was calculated by fitting the function $S(t) \propto e^{-i \cdot \gamma \cdot \Delta B \cdot TE}$ to the acquired data (258–260).

***Patient Scans:***

In order to evaluate the patient population, plaque features were identified on susceptibility maps. These findings were confirmed in comparison with the multi-contrast images. Therefore, all images acquired before and after contrast agent administration were centred on the bifurcation, so that slices could be compared. The susceptibility maps were referenced to the mean susceptibility within the sternocleidomastoid muscle, similar to the technique proposed in (242), where muscle tissue was used as a reference for QSM in the prostate. As susceptibility maps have an unknown offset, there has been a need to find suitable reference tissues that make susceptibility maps comparable across subjects (253,254,321). It is important that there is little variability in the susceptibility measured in these regions between patients. In the brain, cerebrospinal fluid and various white matter regions have been proposed as such reference regions (253,254,321). In other areas of the body urine and muscle tissue have been used (242). Regions of calcification were identified on both pre- and post-contrast susceptibility maps by their strong diamagnetism, i.e. negative susceptibility. USPIO-uptake was identified by its paramagnetic appearance, i.e. positive susceptibility, on the post-contrast susceptibility maps only. Furthermore, regions of “normal” plaque tissue were identified, where the susceptibility was close to zero. All of these regions were outlined on QSM and subsequently compared visually with the corresponding slices of the multi-contrast protocol. The presence of calcification was indicated by elevated $R_2^*$-values and Hounsfield units (CT) and appeared hypointense on all other images. USPIO-uptake was detected on the post-contrast images by identifying an increase in $R_2^*$ and a decrease in $T_2^*$w signal intensity in comparison with the pre-contrast images and also by an increase in signal intensity on some $T_1$w images, if the USPIO concentration was low.

Subsequently, the values measured within regions outlined to be normal plaque, calcification, and USPIO-uptake on QSM were compared quantitatively. QSM, $R_2^*$-

maps and $T_2^*$w gradient-echo magnitude images all stemmed from the same dataset and were therefore naturally co-registered. Susceptibility values and $R_2^*$-values are of a quantitative nature. However, a direct comparison of $T_2^*$w signal intensity in between patients and of pre-and post-contrast images is not very meaningful. This is primarily due to the non-quantitative nature of $T_2^*$w images and the inhomogeneous coil sensitivity of the carotid coil that was used. As the patient position changes between scans and the patients have differently shaped necks, the coil sensitivity around the carotid artery plaques will vary. Therefore, all of the signal intensities were relative signal intensities (rSI) to the sternocleidomastoid muscle. Voxels with insufficient SNR to calculate $R_2^*$ were excluded from the analysis by inspection of the $R_2^*$-maps and the $T_2^*$w magnitude images. After calculating the mean value within each region, the median and interquartile range over all patients were subsequently presented in box-plot form.

Subsequently, calcification volumes were outlined on 3D TOF and CT, so that their volumes could be calculated. These volumes were compared to the volumes of the calcified regions as outlined on QSM. Pearson's correlation coefficient was used to describe the relationship between the calcification regions measured on 3D TOF and QSM.

Furthermore, a lipid rich necrotic core was identified by an elevated value on the fat-fraction map generated using $T_2^*$ IDEAL from one pre-contrast scan, where histological validation was available. For comparison, a plaque region with a low fat fraction, unlikely to contain lipid core and a region of the sternocleidomastoid muscle were outlined. The fat fraction values measured within these ROIs were presented in box-plot form. Subsequently, the presence of the lipid core was confirmed through histology, as described below.

Data processing and analysis were performed using MATLAB (R2017b, MathWorks, Natick, Mass). The code for the uncorrected $\Delta B$-estimation, phase unwrapping, background field removal and dipole field inversion were taken from the MEDI toolbox.

***Histological Analysis:***

Two cases were available for histological analysis. These were already presented in chapter 4 for comparison with SWI. The specimens were decalcified and sliced at 3mm intervals. The tissue was embedded in paraffin wax; thin sections were cut at 3 µm

thickness and then stained with Haematoxylin and Eosin, Perl's Prussian Blue (for iron) and Elastic Van Gieson (elastic fibre stain). The histopathological analysis was performed by the tissue bank team and Dr Alison Cluroe, the consultant histopathologist. Slices of histology and MRI were approximately matched in location. This was presented as a method to validate the presence of plaque features such as USPIO uptake, calcification, and/or lipid core. However, it needs to be acknowledged that due to the differences in resolution and slice thickness between the two techniques, this comparison was limited by the resolution in the slice thickness.

## 6.3 Results:

The field maps and water-fat fraction images calculated from the bipolar readout acquisitions were visually similar to the results achieved with the unipolar readout as shown in Figure 6-3. In the border regions, the bipolar water-fat separation

outperformed the results achieved with the unipolar gradients, where there were more frequent water-fat swaps and $\Delta B$ also appeared noisier.

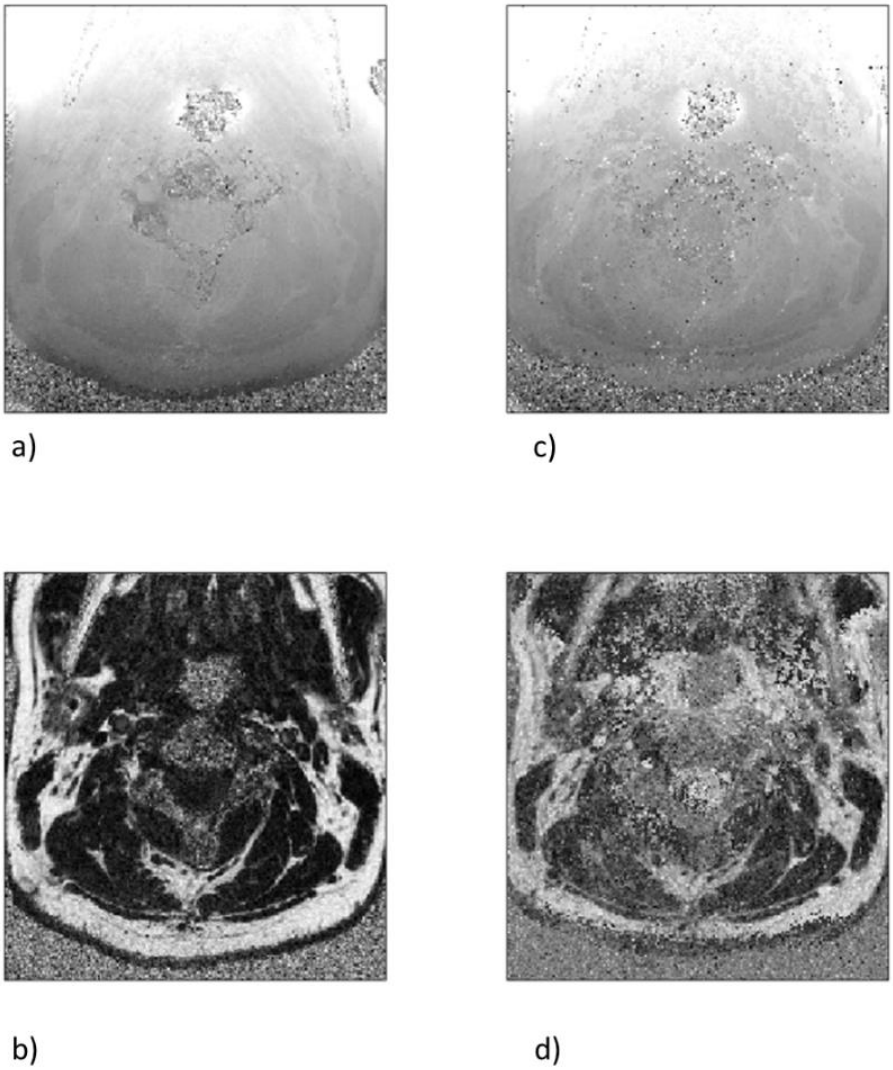


*Figure 6-3: $\Delta B$ (a,c) and Fat-Fraction maps (b,d) estimated with $T_2^*$ IDEAL bipolar (a,b) and unipolar readout gradient datasets (c,d) (I also presented the results in* (305)*)*

The $T_2^*$ IDEAL-corrected $\Delta B$ subsequently produced high-quality susceptibility maps. Figure 6-4 shows an axial slice of the neck of a healthy volunteer. Figure 6-4 a and b show the magnitude images for anatomical reference. The susceptibility map on Figure 6-4 c demonstrates high susceptibility differences between tissue and fat. The median of the mean susceptibility difference between fat and muscle tissue measured in all volunteers (median ± interquartile range (IQR) 0.56 ppm ± 0.12 ppm) agrees with previously published values for the susceptibility of fat (0.61-0.64 ppm) (241,314,322,323). The CNR calculated between fat and muscle was 6.95, with the

noise level estimated to be 0.08 ppm. The susceptibility maps of the remaining volunteers are given in Appendix B.

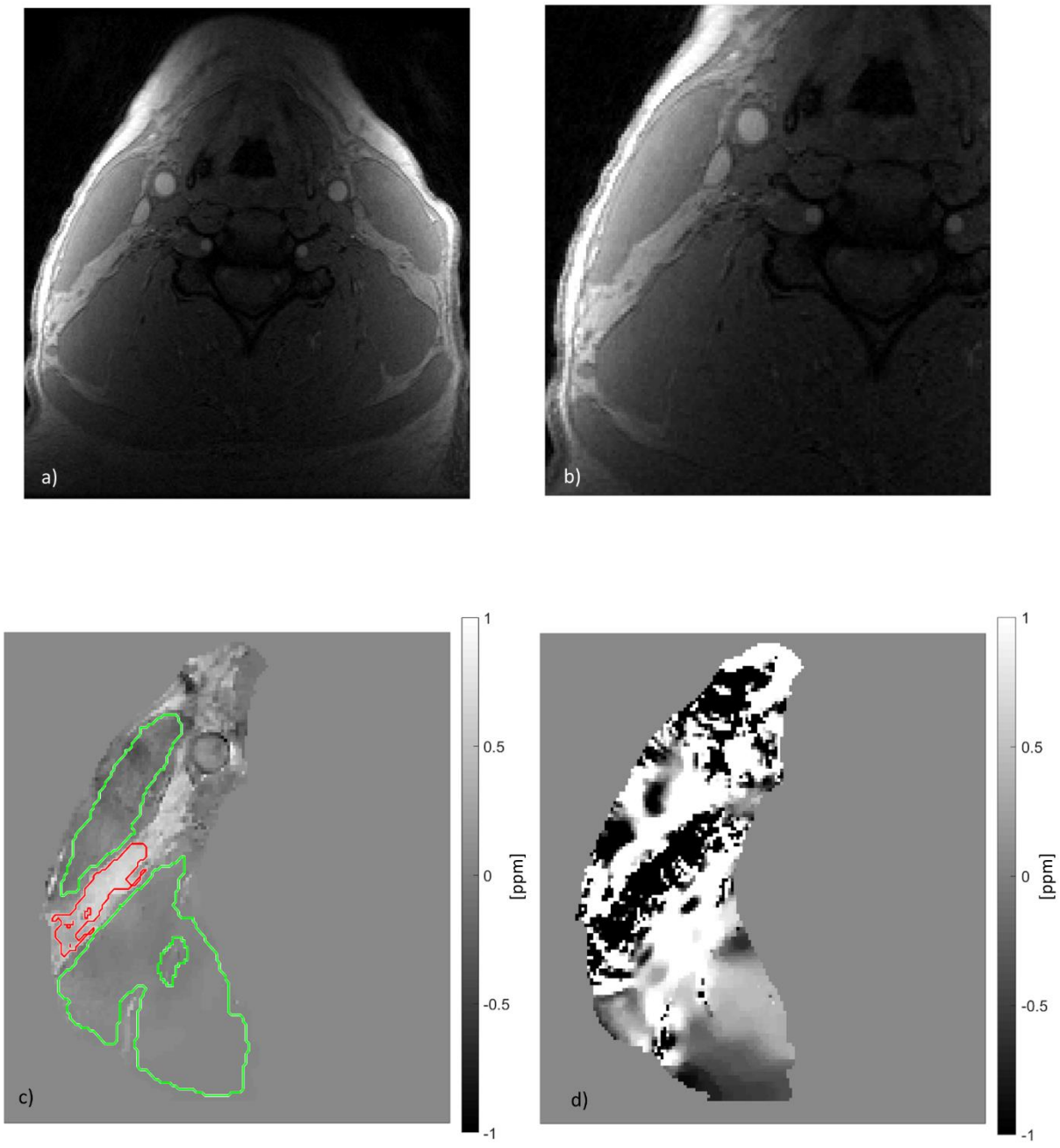


*Figure 6-4: The un-zoomed (a) and zoomed (b) magnitude images of a healthy volunteer scans are given as an anatomical reference for an $T_2^*$ IDEAL-corrected susceptibility map from a healthy volunteer (c) in comparison with an uncorrected susceptibility map from the same volunteer (d). On the $T_2^*$ IDEAL-corrected susceptibility map the ROI containing fat is outlined in red, and the muscle tissue in green. (I also presented these results in the publication* (305)*)*

In order to highlight the improvements achieved with this technique, the acquired susceptibility maps were again compared to a susceptibility map without $T_2^*$ IDEAL correction, which exhibited severe streaking artifacts and errors inside the regions containing fat (Figure 6-4 d). Therefore, the techniques could also be applied to the patient cohort. This way, it was possible to acquire high quality susceptibility maps in the patient study.

On all patient exams plaque calcification appeared much more diamagnetic on both pre-contrast (median ± IQR of -0.86±0.22 ppm) and post-contrast QSM (-1.27±0.71 ppm), than "normal plaque tissue" which had a susceptibility close to zero and did not seem to contain any calcification or USPIO-uptake (pre-contrast QSM: -0.1±0.04 ppm; post-contrast QSM: -0.16±0.07 ppm). USPIO uptake appeared as paramagnetic on the post-contrast QSM (1.32±0.61 ppm). Figure 6-5 & Figure 6-6 illustrate this in two patient cases, where the carotid plaque was lightly calcified.

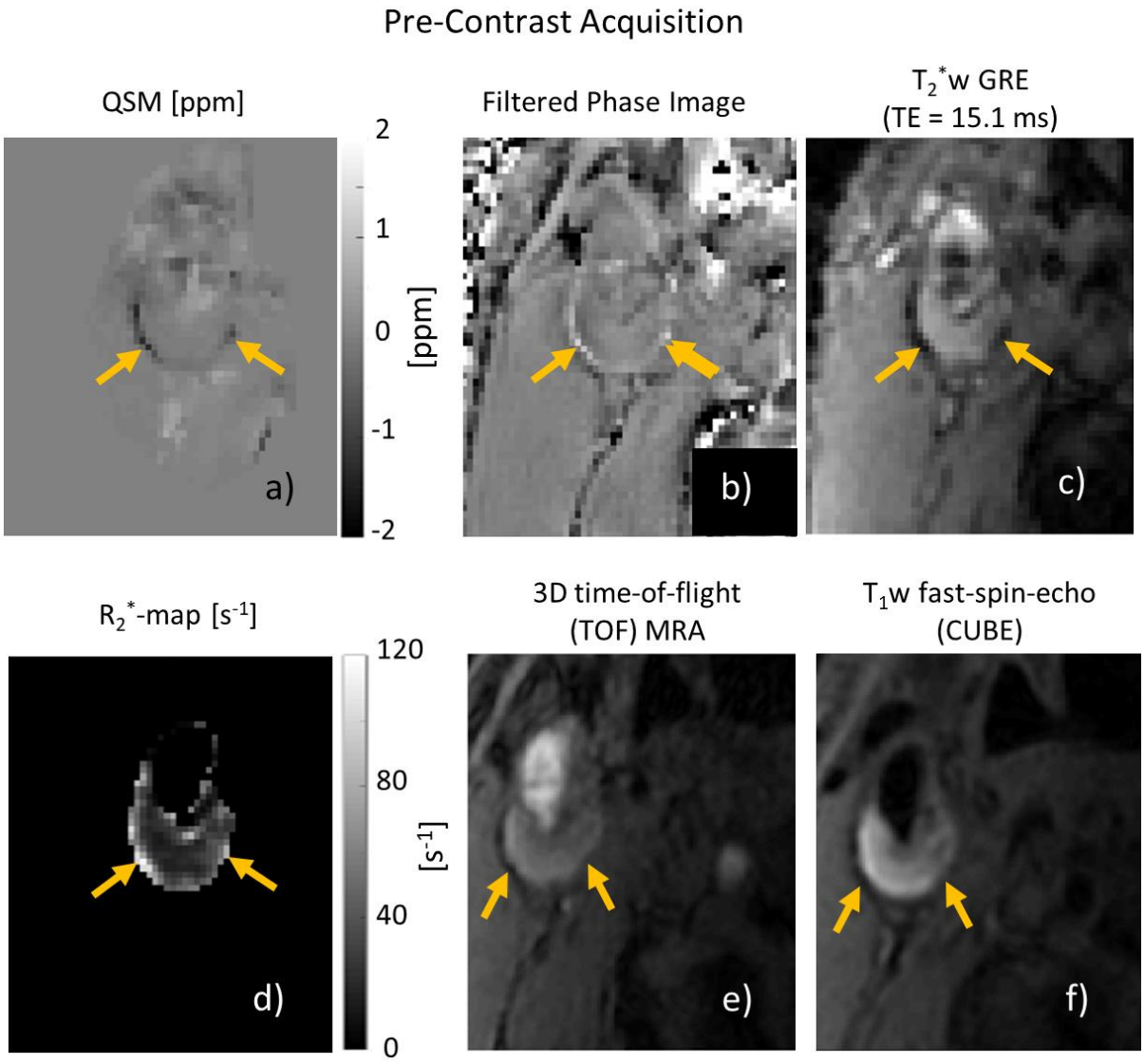

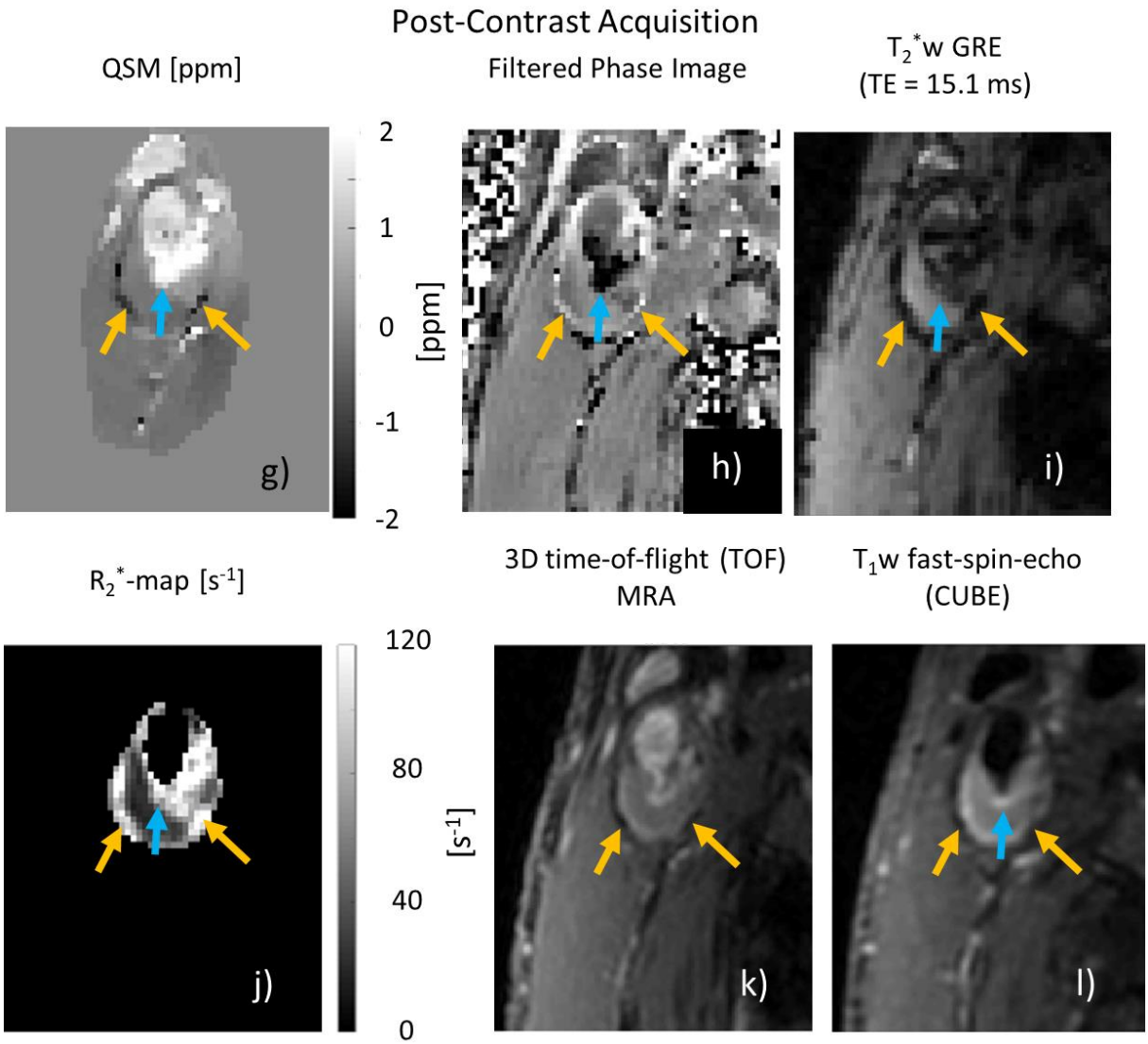


*Figure 6-5: A 70-year-old man was scanned before (a-f) and after (g-l) contrast agent administration. Calcified regions are indicated by a yellow arrow. They appear hypointense on QSM (a, g), $T_2^*$w GRE (c, i), 3D TOF MRA (e, k) and T1w FSE (f, l). They appear hyperintense on filtered phase images (b, h) and $R_2^*$-maps (d, j). USPIO uptake is indicated by the blue arrows on the post-contrast images. USPIO-uptake appears hyperintense on QSM (g), $R_2^*$-maps (j), and T1w FSE (l). It appears hypointense on filtered phase images (h) and $T_2^*$w GRE (i). (I also presented these results in the publication* (305)*)*

In both cases plaque calcification could again be easily identified by its strong diamagnetism on pre- and post-contrast susceptibility maps (yellow arrow). It could be distinguished from “normal plaque tissue”, and the strongly paramagnetic plaque regions, where USPIO contrast agents have been taken up, as indicated by the blue arrow. A comparison with the multi-contrast protocol, confirmed these results: regions of QSM-identified plaque calcification appeared as hypointense on 3D TOF, $T_1$w DANTE CUBE, and on $T_2^*$w gradient echo magnitude images. On $R_2^*$-maps, QSM-identified calcifications appeared hyperintense. This was the case for both pre- and

post-contrast images. On Figure 6-6 g) the presence of calcification was furthermore confirmed by an increase in Hounsfield Units on CT.

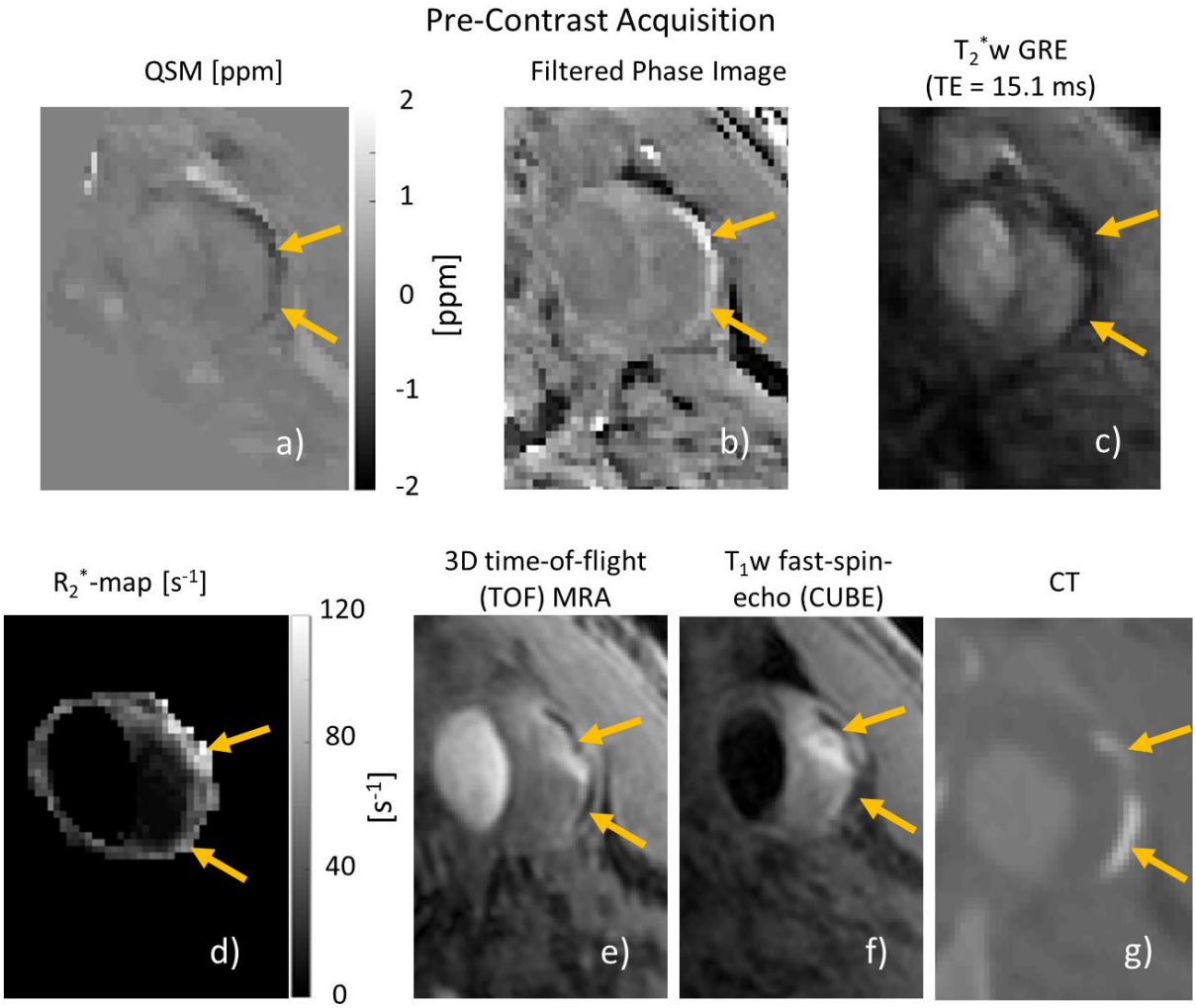

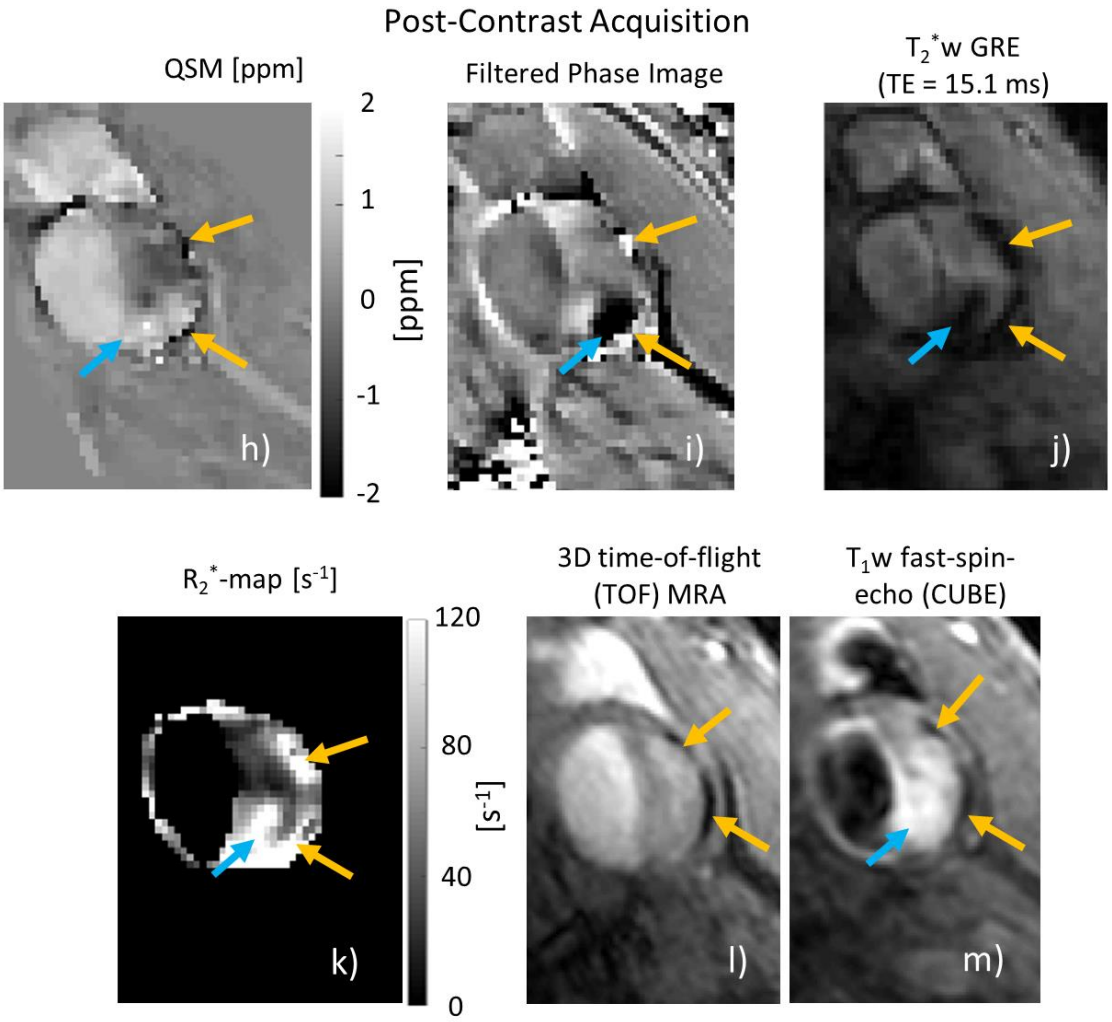


*Figure 6-6: A 65-year-old man was scanned before (a-f) and after (h-m) contrast agent administration. Calcified regions are indicated by a yellow arrow. They appear hypointense on QSM (a, h), $T_2^*$w GRE (c, j), 3D TOF MRA (e, l) and $T_1$w FSE (f, m). They appear hyperintense on filtered phase images (b, i), $R_2^*$-maps (d, k), and CT (g). USPIO uptake is indicated by the blue arrows on the post-contrast images. USPIO-uptake appears hyperintense on QSM (h), $R_2^*$-maps (k), and $T_1$w FSE (m). It appears hypointense on filtered phase images (i) and $T_2^*$w GRE (j). (I also presented these results in the publication* (305))

The presence of QSM-identified USPIO-uptake was confirmed by comparing the pre- and post-contrast images. Within these regions, a decrease in rSI on the $T_2^*$w gradient echo magnitude images (0.48 rSI units) and increase in $R_2^*$-values (75.8 $s^{-1}$) could be observed in comparison to the normal plaque tissue on the pre-contrast scans. While there was an overall decrease in $T_2^*$ rSI and increase in $R_2^*$ on the post-contrast images, the changes within regions of QSM-identified USPIO uptake were much stronger than within regions of QSM-identified calcification (0.14 rSI units / 43.4 $s^{-1}$) or normal plaque tissue (0.19 rSI units / 37.1 $s^{-1}$). In some cases, USPIO-uptake also coincided with an increase in $T_1$w SI.

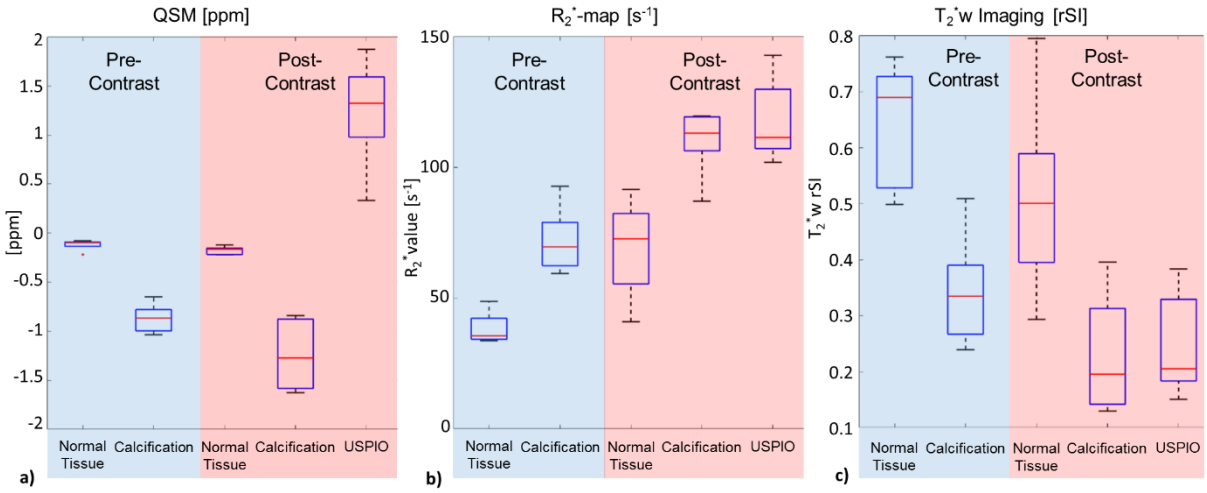


*Figure 6-7: To confirm the presence of calcification and USPIO uptake, the respective ROIs were outlined on QSM and the mean susceptibility values (a), $R_2^*$-values (b), and $T_2^*$w rSI values (c) were measured within each region. The box plots combine the mean ROI values measured in all volunteers. (I also presented these results in the publication* (305)*)*

These results were confirmed in box-plot form. Figure 6-7 shows the box-plots of the mean susceptibility values (Figure 6-7 a), $R_2^*$ values (Figure 6-7 b), and $T_2^*$w rSI values (Figure 6-7 c) measured within regions of calcification, USPIO-uptake and normal plaque tissue as outlined on QSM for all patients. QSM allowed for a clear distinction between calcification, USPIO-uptake, and normal plaque tissue, which had a strongly negative, positive and close to zero susceptibility value respectively (Figure 6-7 a). There is a slight difference in distribution between the susceptibility of calcified tissue on pre- and post-contrast scans. From inspection of the images, this may be due to the increase of streaking artifacts on the post-contrast dataset, which may lead to more extreme values within calcified regions, or it may be due to partial volume effects.

On both $R_2^*$ maps and $T_2^*$w images, USPIO-uptake and calcification caused high $R_2^*$/low $T_2^*$ values (Figure 6-7 b, c). This means that they confirm the results shown in QSM, i.e. increased de-phasing in regions of strong susceptibility sources but were unable to distinguish diamagnetic from paramagnetic materials. In contrast to the QSM dataset, the overall de-phasing increased on the $T_2^*$ rSI or $R_2^*$ datasets, which can be seen by an overall increase in $R_2^*$/decrease in $T_2^*$ rSI within normal plaque regions post-contrast. This highlights that it might be problematic to quantify the concentration of USPIO uptake from changes in $R_2^*$ alone due to the non-local field effects caused by the presence of USPIO contrast agents. The MRI results from the remaining patient cases are shown in Appendix C.

When assessing the volumes of calcification measured on QSM in comparison to 3D TOF, the measured volumes were of similar size and location and showed a high correlation (Pearson's Correlation Coefficient = 0.995). The QSM-identified volumes of calcification also agreed with CT validation, as shown in Figure 6-6, which was only available in a limited number of, i.e. two, cases.

### 6.3.1 Histology:

Histology was available in the same patients that were described in chapter 4 section 4.3.1. The first case is of a lightly calcified plaque (Figure 6-8), which was also described in Figure 6-5 and will also be analysed later in Figure 6-9. In chapter 4, this plaque was analysed in Figure 4-2 & Figure 4-10. Much like SWI, QSM was able to detect calcification and USPIO uptake within this plaque, which was initially confirmed by the multi-contrast protocol. When comparing the MRI results to the histological analysis, these results were confirmed. Perl's Prussian Blue stained the iron particles, i.e. the USPIO-nanoparticles blue. Due to decalcification, plaque calcification appeared as pale areas on both Perl's Prussian Blue and Haematoxylin and Eosin staining. There is a small area of blue staining next to the plaque calcification, which may be due to USPIO particles but could also stem from haemorrhage, hemosiderin or methaemoglobin. This does not show on the MR images which may be due to partial volume effects.

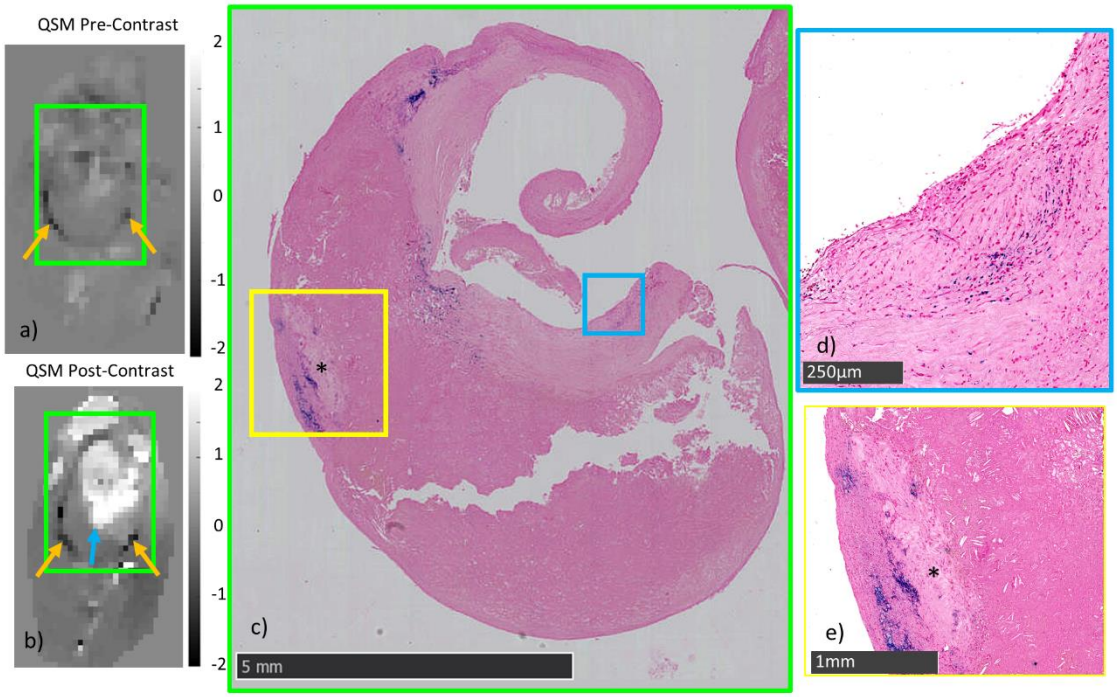


*Figure 6-8: This is a case of a 70-year-old man in which USPIO uptake and calcification were identified on pre- (a) and post-contrast (b) QSM, which was confirmed by histology (c). On this histology slide (c), which is decalcified and uses a Perl's Prussian Blue Stain, the calcification appears as a pale island and the iron particles are stained blue. Calcification can be seen in the yellow box (*) (e) and the iron particles, stained blue, are in the blue box (d). These results confirm the presence of the QSM-detected juxtaluminal USPIO-uptake on the post-contrast susceptibility map (b) (blue arrow). Calcification can be seen at the border of the plaque on both pre- and post-contrast QSM (yellow arrow, a, b). The tissue section was slightly ripped, which commonly occurs during carotid endarterectomy surgery or during sectioning. (I also presented these results in the publication* (305))

Analysis of the fat-fraction map of the same plaque showed an elevated fat-fraction, indicating the presence of a lipid rich necrotic core (Figure 6-9). The analysis used was similar to Koppal et al. (316), who used an elevated fat-fraction on Dixon-based water fat separation, but not $T_2^*$ IDEAL, to identify the lipid core. Figure 6-9 shows that the fat-fraction was heightened in the region identified as the lipid core when compared to "normal" plaque region and the sternocleidomastoid muscle. This was confirmed when considering the Elastic Van Gieson histochemical stain, on which the LRNC could be identified by a yellow/pink colouring and the presence of cholesterol crystals. This is in contrast to the purple staining which is due to the elastic fibres.

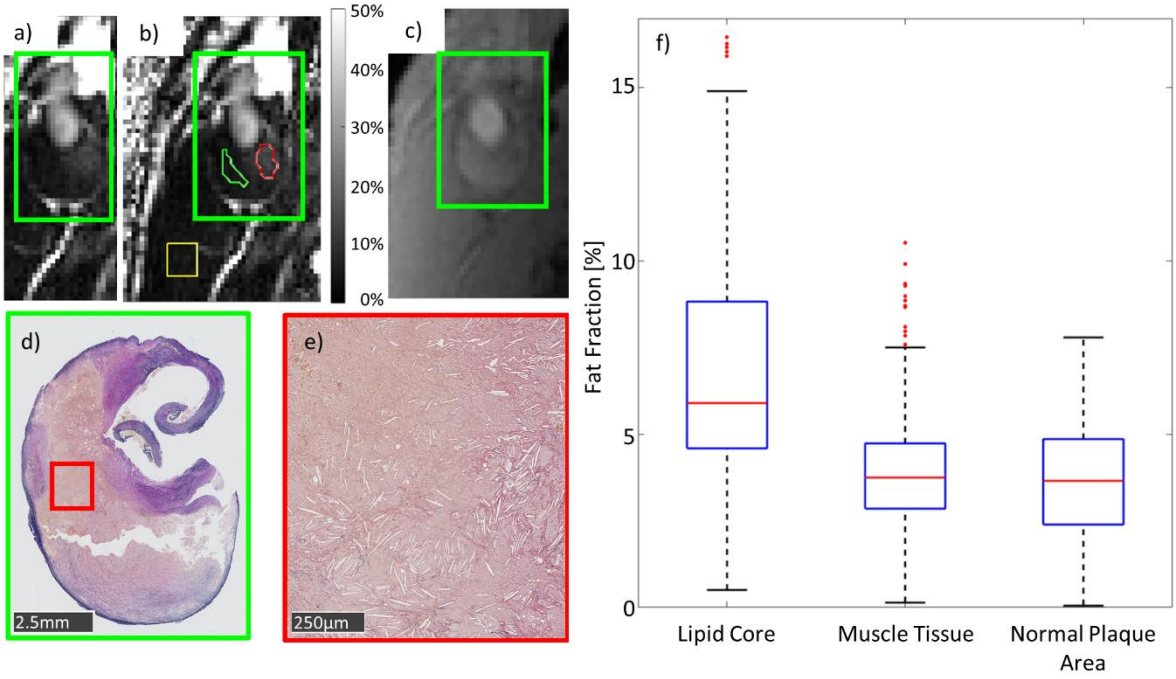


*Figure 6-9: This case shows the plaque of a 70-year-old man. The fat-fraction map (a, b) with (b) and without (a) the ROIs outlined is positioned next to a gradient-echo magnitude image (TE = 4.4 ms) for anatomical reference (c). The carotid artery plaque is inside the green box. On the fat fraction map, the lipid rich necrotic core is identifiable by hyperintensity (b, outlined in red), while the plaque area containing low to no lipid content is outlined in green. A region of sternocleidomastoid muscle tissue was outlined in yellow for reference. The fat fractions measured within all regions of interest are presented in boxplot form (f). The histological analysis with the Elastic Van Gieson histochemical stain, depicted the presence of the lipid core clearly. This was made visible due to the yellow/pink colouring (d, e) and the presence of cholesterol crystals (e). (I also presented these results in the publication* (305))

The second plaque that underwent histological analysis was more heavily calcified (Figure 6-10). This plaque was also analysed in chapter 4, and is shown in Figure 4-3 and Figure 4-11. On pre-contrast QSM, it appeared strongly hypointense. On the post-contrast QSM, the overall signal intensity changed to hyperintense. This suggests that there was UPSIO uptake within the plaque and USPIO-particles were interspersed with calcification. The histological analysis confirmed these results. The calcification was located beneath the lining of the vessel. Iron particles stained in blue on the Perl's Prussian Blue stain were located within the overlying fibrotic tissue and widely dispersed in the space between large areas/nodules of macrocalcification, which appear as pale islands beneath the fibrotic area.

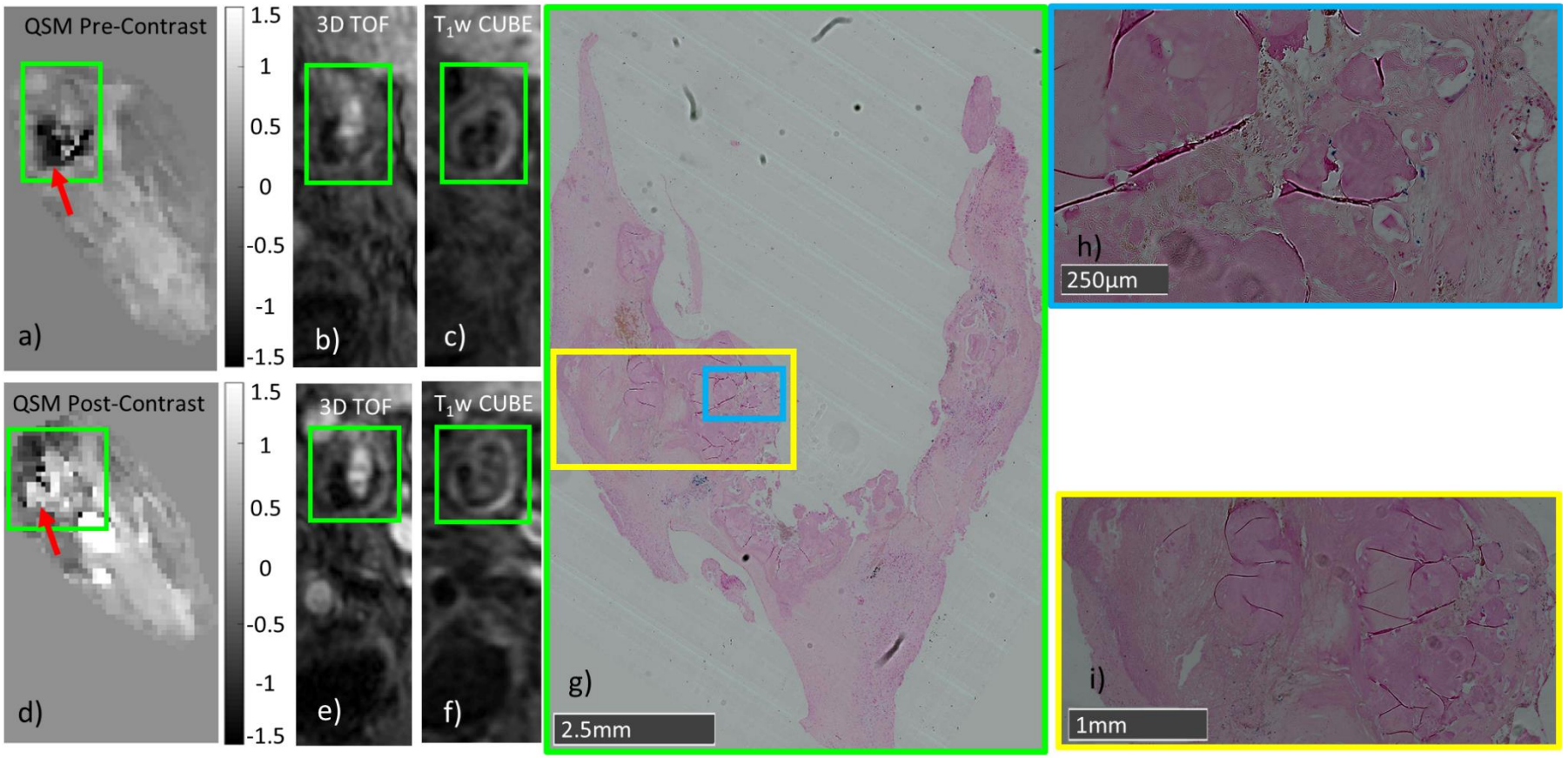


*Figure 6-10: The plaque of this 81-year old woman, is heavily calcified and also took up USPIO-contrast agents. Pre-contrast QSM shows a heavily calcified plaque (a). 3D TOF (b) and black blood FSE (c) are given for anatomical reference. On the post-contrast QSM (d), the plaque appears hyperintense, indicating the presence of USPIO uptake. The red arrow indicates the location of the contrast change. 3D TOF (e) and black blood FSE (f) were again given for anatomical reference. On the MR images, the carotid plaque location is indicated by the green box. The histological analysis (g) shows a plaque containing heavy calcification located just beneath the lining of the vessel, which manifested as pale pink nodules. This was magnified in the yellow box (i). The USPIO-contrast agent appeared blue due to the Perl's Prussian Blue stain for iron. The iron particles appear to be widely dispersed within the overlying fibrotic tissue and in the space between the calcified nodules, as indicated by the blue box and magnified in (h). This confirms the presence of USPIO-uptake within a heavily calcified plaque. (I also presented these results in the publication* (305))

## 6.4 Discussion

Within this chapter the feasibility and benefit of performing simultaneous QSM and $T_2^*$ IDEAL water fat-separation in the neck and of carotid arteries using bipolar readout gradients was demonstrated. In chapter 5, it was shown that an accurate estimate of the fat-fraction and correction of the $\Delta B$ map improved image quality of the susceptibility maps of the neck and carotid arteries by reducing streaking artifacts and also corrects the susceptibility value measured inside regions of fat. In this chapter, bipolar instead of unipolar readout gradients were used. This improves the SNR of the echoes following the first echo, which is important for $\Delta B$ estimation. Furthermore, minimum spaced echoes improved water-fat separation. This improvement can be explained by considering the cost-function of the $T_2^*$ IDEAL algorithm. The algorithm searches for the value of ΔB which minimizes the difference between the signal model and the measured signal. A larger echo spacing leads to a smaller frequency range (bandwidth) within which the signal can be correctly determined. The initial $\Delta B$-estimate is required to be within this frequency range and therefore needs to be sufficiently accurate. If it is outside the frequency range, the algorithm may converge to a different solution, producing water-fat swaps and errors in $\Delta B$. The reduced minimum echo spacing achieved by the bipolar echoes therefore maximized SNR and simultaneously widened the bandwidth within which water and fat could be unambiguously determined. The effect of echo spacing on the convergence of the IDEAL algorithm has been demonstrated in previous studies (324–326).

After evaluating the feasibility and performance of this technique for generating susceptibility maps of the neck and the carotid artery wall in a volunteer study, this technique was subsequently applied within a patient cohort. QSM was able to assess atherosclerotic plaques in vivo, to detect features such as calcification and also provide a novel method for positive contrast of USPIO-uptake, a marker for carotid plaque inflammation. In addition to this, QSM may also be able to identify intra-plaque haemorrhage (IPH). IPH was not detected in our patient cohort, but other research studies have shown the ability of QSM to detect it due to its high paramagnetism (310,327). In the brain, haemorrhage has been one of the features that has been widely detected and distinguished from calcification using QSM (171). This allows for the hypothesis that although not present in our study, IPH could be detected using this

methodology. Furthermore, $T_2^*$ IDEAL water-fat separation detected a LRNC in one patient, where its presence was confirmed using histology. While this is only a single case, it was believed to be worth inclusion in our results as another study employed another Dixon-based water fat separation technique in a larger patient cohort in comparison with histology (316). All of this was achieved within a single sequence, which can be used as part of a conventional multi-contrast protocol that already involves $R_2^*$-mapping, and therefore does not require any additional scanning time.

Particular interest is granted to QSM's ability to detect USPIO-uptake. In previous research, USPIO-uptake is commonly detected by a decrease in signal intensity on $T_2^*$w imaging and increase in $R_2^*$-value on $R_2^*$ mapping, when comparing post-contrast images to images acquired before contrast agent administration. The comparison with the set of pre-contrast images is required since the USPIO-uptake regions are indistinguishable from other strong sources of susceptibility such as calcification. In previously published techniques pre- and post-contrast images were matched on the carotid bifurcation and the plaque was divided into segments (quadrants (126,141,143) or octants (137)). Subsequently, the mean $R_2^*$ value or $T_2^*$ signal intensity relative to the sternocleidomastoid muscle within each segment could be compared. A large change in signal then indicated that there was USPIO-uptake (137,138,141–143). Therefore, USPIO-uptake is only detected with a coarse resolution (e.g. four plaque regions if quadrant analysis is used (126,141,143) or eight if octant analysis is used (137)) and USPIO-uptake may be underestimated or missed due to partial volume effects. Furthermore, background field effects increase the overall de-phasing on post-contrast images, which may lead to errors in estimating the amount of contrast agent uptake. In chapter 4 SWI has been proposed as a potential technique that improves on some of these issues. While the images provided meaningful and improved results, SWI suffered from non-local effects, which played an especially serious role in heavily calcified plaques.

Within this study, QSM has shown the potential to identify USPIO-uptake qualitatively within a single post-contrast scan with positive contrast, which can potentially eliminate the need for a pre-contrast scan (144,148,151,152), typically performed two or three days before the post-contrast scan (137,138,141–143). This is particularly evident in lightly calcified plaques, where regions of USPIO-uptake and calcification do not overlap. QSM distinguished between regions of paramagnetism and diamagnetism on

the post-contrast images, rendering the pre-contrast acquisition superfluous (Figure 6-5 & Figure 6-6). In heavily calcified plaques (e.g. Figure 6-10), partial volume effects lead to a hyperintense appearance of the USPIO-uptake post-contrast even when it is interspersed with calcified nodules. Although partial volume effects decreased the signal intensity in those regions, USPIO-uptake dominated the contrast, rendering the plaques hyperintense rather than hypointense, as they had appeared on the pre-contrast scan. The calcification may be identified by comparison of the multi-contrast protocol, for example on 3D TOF MRA or $T_1$w sequences, where it appeared hypointense. Besides eliminating the need for an additional costly and time-consuming pre-contrast scan, QSM allows for an analysis of the USPIO-uptake regions in much higher detail. In contrast to quadrant analysis which simply evaluates the signal intensity within four segments, QSM allows for high resolution depiction of USPIO-uptake.

While this illustrates the benefit of QSM for qualitative analysis of USPIO-uptake, it also allows for improvements of the quantitative analysis of USPIO uptake. In the past, $R_2^*$-mapping and relative $T_2^*$w measurements have been used (137,138,141–143). As described above, this may require complex co-registration, which is why segment analysis is used. In addition to that insufficient SNR may lead to failing of $R_2^*$ mapping in individual voxels. Also $R_2^*$ may overestimate USPIO-uptake due to background field and non-local USPIO-field effects increasing the overall $R_2^*$ value on post-contrast scans (137,143,144). Furthermore, both $T_2^*$w imaging and $R_2^*$-mapping suffer from non-local artifacts which lead to an overestimation of the volumes containing USPIO-uptake. By contrast, QSM displays the underlying susceptibility distribution, which minimizes non-local artifacts and background field effects due to the QSM processing. In addition, the relationship between UPSIO-content and susceptibility has been demonstrated to be linear (295). For Ferumoxytol a scaling factor of 59.6 ppm ml/mg at 1.5T (295) has been previously established, so that it can be estimated that the plaques scanned within this study contain a concentration of 22±10 µg/ml of Ferumoxytol. This is calculated by dividing the median of the mean susceptibility values measured in regions of USPIO (1.32 ppm) by the scaling factor. For quantitative analysis, a pre-contrast scan may still be necessary to determine the change from the baseline susceptibility within regions of USPIO-uptake.

Due to these benefits, it is important to compare QSM to other positive contrast techniques. These are typically dedicated sequences such as IRON and GRASP. These techniques rely on detecting phase shifts caused by USPIO-contrast agents, not the underlying susceptibility distribution (148,151,152,293). As described in chapter 1, both IRON and GRASP use the effects of susceptibility induced fields generated by USPIO-contrast agents to selectively suppress signal from all other tissue. Therefore, these techniques image the field distribution rather than the underlying susceptibility. Furthermore, both IRON (148) and GRASP (151) are non-quantitative and are dedicated sequences which require prior knowledge about the amount of dephasing due to USPIO-contrast agents (148,151,293). QSM therefore provides positive contrast and can simply be acquired with a conventional gradient echo sequence. It only requires consideration of how to minimize the chemical shift artifacts and maximize SNR. Furthermore, it provides a method to quantitatively assess USPIO uptake as described above and does not suffer from non-local effects.

This study demonstrated that simultaneous $T_2^*$ IDEAL water fat separation and QSM using bipolar readout gradients could be applied in the neck in 10 healthy volunteers and 5 patients (10 scans) and produced high quality susceptibility maps. Here the benefits of QSM in imaging carotid plaques over previously established techniques were made clear. However, the study was limited by the relatively small sample size. There was an even smaller subset of patients who underwent surgery and on which histological analysis could be performed. Since the patients did not undergo a dedicated CT scan, the CT validation was also limited. However, the QSM results were confirmed by a previously established multi-contrast MRI protocol and, where available, QSM agreed with histology and also with CT. There was no IPH identified in any of these patients. However, QSM was able to detect paramagnetic substances, i.e. USPIO-uptake, and previous studies in the brain have shown that it can detect haemorrhage and distinguish it from calcification. A pilot study that used QSM in the carotid arteries detected calcification and intraplaque haemorrhage, thus confirming our hypothesis (310). When imaging USPIO-contrast agents in the presence of intraplaque haemorrhage, a dedicated pre-contrast scan may be necessary. Alternatively, an additional sequence to selectively image IPH such as MR Direct Thrombus Imaging (which can be used to image fresh thrombus) (MR DTI) could be used to distinguish USPIO-uptake from IPH on QSM (125). As low concentrations of

USPIO-uptake also have a $T_1$ shortening effect, future studies could investigate whether a combination of QSM and MR DTI could be used to distinguish IPH from USPIO-uptake.

Another limitation of QSM of the carotid artery plaque was a reduced image quality due to streaking artifacts, noise, and artifacts, which may originate from imperfect background field removal. For anatomical imaging of the carotid plaques, QSM should be combined with an additional sequence for anatomical imaging such as 3D TOF or black blood FSE. Furthermore, the proposed algorithm ignored chemical-shift-induced misregistration errors associated with bipolar readout gradients, which were assumed to be negligible due to the large bandwidth, relatively large pixel size and low magnetic field strengths. At smaller pixel sizes or at stronger field strengths, this may become an issue and may be addressed using different methods. For instance Lu et al. generated water and fat images by addressing the chemical shift induced misregistration issues in k-space (319). However, this study only solves the issue for water and fat images and may require further work for a solution for the field map.

## 6.5 Conclusion

In conclusion, the work in this chapter demonstrated that QSM in combination with $T_2^*$ IDEAL water-fat separation was able to identify the lipid rich necrotic core, calcification, and USPIO uptake within a single sequence. This is complementary to the conventional protocol and provides a novel positive contrast methodology for the identification and quantification of USPIO-uptake in carotid plaques, which simplifies and improves the detection of USPIO-contrast agent uptake even in calcified plaques. Therefore, it may be used in the future to assess carotid plaque inflammation in vivo in a larger patient cohort.

# Chapter 7 Summary and Future Developments

In this work it was hypothesized that susceptibility effects can help in characterizing carotid artery plaques and provide a positive contrast mechanism for imaging inflammation using USPIO contrast agents. Susceptibility Weighted Imaging showed promising results and was further improved upon using Quantitative Susceptibility Mapping in combination with $T_2^*$ IDEAL water-fat separation.

$T_2^*$w imaging and $R_2^*$-mapping have frequently been used to image paramagnetic haemorrhage and diamagnetic calcification (294), which are features of atherosclerotic plaques. However, both features shorten $T_2^*$ relaxation time and therefore they can typically only be identified in post-acquisition analysis of the multi-contrast images. Both techniques have also been used to image USPIO-uptake by macrophages in inflamed atherosclerotic plaques (137,138,141–143). The highly paramagnetic USPIO nanoparticles cause an increase in $R_2^*$. In order to differentiate this change, from diamagnetic calcification, it is necessary to measure the changes in $R_2^*$ or $T_2^*$w SI between two MRI examinations acquired before and after USPIO contrast-agent administration. Therefore, it has been suggested that positive contrast imaging techniques could be used to identify susceptibility changes induced by uptake of the USPIO to depict the presence of the contrast agent as signal hyperintensities (144,148,151,152). SWI and QSM have been shown to reflect changes in local field inhomogeneity and susceptibility respectively which are unique to paramagnetic and diamagnetic substances. This can simplify and improve the post-contrast acquisition analysis. The applications where this has been demonstrated were reviewed extensively in chapter 2 section 2.2.5.

The results in chapter 4 show that SWI and filtered phase images were able to identify calcification and distinguish it from USPIO-uptake within a single scan under certain conditions: The acquired information was complementary to $R_2^*$ mapping and $T_2^*$w GRE and simplified the post-acquisition analysis. This allowed for unambiguous identification of calcification on pre-contrast images and also for a distinction between paramagnetic USPIO-particles and diamagnetic materials on the post-contrast scan

alone, if their locations did not overlap. In previous studies which employed $R_2^*$-mapping and/or $T_2^*$w imaging, a distinction between the two substances always required the comparison of pre- and post-contrast scans, due to their identical appearance in terms of signal intensity within these techniques. However, in heavily calcified plaques the unambiguous identification of USPIO-nanoparticles and calcification was difficult as this technique suffered from non-local effects, i.e., the geometry, sequence-, and orientation dependence associated with SWI. This limitation was addressed in the following chapters by more extensively processing the GRE data to produce susceptibility maps. In chapters 5 and 6 QSM was performed in numerical simulations, phantom scans, a volunteer cohort and a patient study to both identify atherosclerotic plaque calcification and USPIO contrast agent uptake. The susceptibility maps could be generated from a conventional $T_2^*$w multi-echo gradient echo sequence as is used for $R_2^*$-mapping. In addition to the conventionally applied post-processing steps used for QSM in the brain, a water-fat separation method was used in order to account for the presence of fat in the neck near the location of the carotid artery bifurcation. In this study $T_2^*$ IDEAL water-fat separation was implemented to correct for the chemical shift artifacts stemming from fat present in the neck that lead to severe streaking artifacts which obscured the carotid arteries and erroneous susceptibility values on the susceptibility maps. In other studies that have attempted to perform QSM to image the carotid artery wall and/or carotid artery plaques these artifacts have been acknowledged however they have always been neglected (310,312) or the data were required to be acquired at an in-phase echo time (313).

In $T_2^*$ IDEAL water-fat separation a shorter echo spacing is beneficial and it is not necessary to acquire echoes at specific echo times, for example in or out of phase. In this study minimally spaced echoes were essential due to the reduced image quality in patient scans and at a relatively low field strength of 1.5T. Using bipolar echoes reduces the echo spacing in comparison to conventionally used unipolar readout multi-echo gradient echo acquisitions used in QSM. Multi-shot multi-echo gradient echo could be used to further reduce echo spacing, but at the proposed resolution this would have led to unnecessarily long and not clinically feasible imaging times. The proposed method manages to reduce echo spacing while not at the same scale as the multi-shot techniques in a clinically feasible acquisition time.

QSM was able to identify USPIO-uptake in heavily and lightly calcified plaques and carotid plaque calcification, allowing for a quantitative analysis of carotid artery plaques in a patient cohort. Due to its quantitative nature, it may also be used to evaluate the concentration of USPIO nanoparticles taken up in the plaques. QSM required more complex post-acquisition processing. However, it was able to address the shortcomings of SWI. QSM and $T_2^*$ IDEAL water-fat separation can be performed with the complex data from a conventional multi-echo gradient echo MRI sequence using a minimum echo spacing, that maximizes signal to noise ratio and is acquired for conventional $R_2^*$-mapping. In addition, water-fat separation also served to identify a lipid rich necrotic core, which agreed with results from another previous study (316), that used a Dixon-based water-fat separation method to detect the lipid core. Overall this is a very important additional advantage since it means that QSM in combination with $T_2^*$ IDEAL water fat separation can serve to identify plaque features such lipid rich necrotic core and calcification within a single sequence as well as providing a positive contrast mechanism for imaging USPIO-uptake. Furthermore, other studies have demonstrated the ability of QSM to identify intraplaque haemorrhage (310,327).

There are several limitations to this study. First of all, the sample size was limited. For a statistical comparison of this methodology to other methods a larger sample size would be required. It should be noted that Ferumoxytol is no longer commercially available in the UK (328) and must be obtained via a specialist unlicensed medicines importer (Mawdsleys, Salford, UK) . This had the consequence of having a small study population. No intraplaque haemorrhage and only one lipid core could be unambiguously detected. As discussed in chapter 6, it is important to assess if and how USPIO-uptake can be detected in a single scan using QSM in plaques containing haemorrhage. In future implementations, it is therefore necessary to include additional sequences into the MRI protocol: The current study was designed to detect calcification and USPIO-uptake with the multi-contrast protocol, which could therefore be used as a confirmation of the results from QSM. A dedicated sequence to image intraplaque haemorrhage, such as MR direct thrombus imaging (125) could serve as a comparative measure with QSM to confirm the presence of intraplaque haemorrhage. The feasibility of detecting intraplaque haemorrhage and calcification has been shown in a pilot study applying QSM to a patient cohort in the neck (310). Similarly, the presence of a lipid rich necrotic core as identified with water-fat

separation should be confirmed with dedicated sequences, such as diffusion weighted imaging (329) or using contrast enhanced MRI (330). These would be the additions necessary if the study was designed again today.

An additional reason why the study population for QSM was limited, was due to the fact that the study was initially designed to detect USPIO-uptake using $R_2^*$-mapping and $T_2^*$w imaging using a fat-suppressed, black-blood multi-echo gradient echo dataset. As was shown in chapter 4, it is possible to perform SWI on this dataset, but the benefits of improved vessel wall detection in volunteers do not always translate to the detection of carotid artery plaques, which may be hypointense, for example in the presence of calcification. When considering the phase images for performing QSM of the carotid artery wall, the suppression of signal from blood and fat is also counterproductive, as this will leave the regions of fat and the lumen to contain phase noise only. Therefore, the resulting susceptibility maps would contain strong artifacts. If the study was redesigned today, it would therefore not only include the relevant sequence to image a lipid core and intraplaque haemorrhage, but also would only contain a bright blood, multi-echo gradient echo sequence in all patient scans.

This study has also shown the capability of QSM to identify calcification. Typically, this has been detected by using the multi-contrast protocol and was identified by hypointensities on all contrast-weightings. In our research group, zero-echo time (ZTE) imaging has demonstrated the ability to detect carotid artery calcification (331). On PDw ZTE images, calcification appear as hypointensities or after intensity correction on inverse log-scale ZTE images as hyperintensities (331,332). Due to the short acquisition time, it would be a useful sequence to add to the imaging protocol and compare its performance against that of QSM. Furthermore, it would be interesting to evaluate how QSM may detect smaller calcifications, or regions of microcalcification, that are below a certain resolution. Since microcalcifications in carotid arteries have been shown to be a feature of plaque vulnerability and are associated with plaque inflammation (75), it would be interesting to investigate the limits of detection of QSM for certain small calcifications. This could be done, for example, in a phantom by imaging different concentrations of hydroxyapatite.

Improvements can also be made to the post-processing methodology: The current implementation of the water-fat separation to correct for chemical shift artifacts

assumes that there is a fixed chemical shift of -220 Hz at 1.5T for all types of fat. However, it is acknowledged that the chemical shift of fat in the neck and the lipid core are different. More accurate modelling of the fat spectrum within the fat in the neck close to the carotid arteries would potentially allow for improved correction of the $\Delta B$ estimate and a further reduction in artifacts. A multi-peak modelling of the fat spectrum can be included in the $T_2^*$ IDEAL algorithm, as has been demonstrated by Yu et al. (333). More accurate modelling of the fat spectrum within the lipid core would possibly allow for the improved detection of elevated fat fraction within the lipid core. The currently proposed technique, like the one proposed by Koppal et al. (316), shows only a slight elevation in the region, where a lipid rich necrotic core was identified. Validation of this method would require a spectroscopic analysis of the fat in the neck and the lipid rich necrotic core. The fat in the neck close to the carotid arteries could be analysed in volunteer scans, while the lipid core could be analysed in ex-vivo scans.

In addition, several assumptions were made when modelling the effects of bipolar gradient echo readouts. A more accurate modelling of phase and amplitude modulation of bipolar echoes may improve the accuracy of the technique (334). An additional assumption was that the chemical shift induced misregistration between echoes was negligible due to the high bandwidth and the relatively low scanner field strength. This may be included in future algorithmic implementations, particularly when using higher field strengths.

I have shown consistently that QSM was able to provide high quality susceptibility maps of the carotid artery wall in healthy volunteers and patients with carotid artery atherosclerosis. Therefore, it is suited for larger scale studies to detect the presence of macrophages in plaques with high levels of USPIO-uptake. QSM is more specific than $R_2^*$-mapping or $T_2^*$ weighted imaging in the identification of regions of USPIO-uptake and therefore allows regions of USPIO-uptake to be manually outlined. In contrast, $R_2^*$-mapping or $T_2^*$ weighted images are unable to differentiate between diamagnetic and paramagnetic substances and frequently required the use of segment/quadrant analysis to compare pre- and post-contrast administration scans to identify and analyse regions of USPIO-uptake in previous studies (126,137,141,143). QSM-identified USPIO-uptake may be analysed like any other feature identified with high-resolution MRI, so that for example, the more detailed volume measurements of USPIO-uptake could be analysed as well as the morphology of USPIO-uptake regions.

While $R_2^*$-mapping displays a quantifiable increase with USPIO-contrast agent concentration, it is hampered by background field effects and it is difficult to make a direct estimation of USPIO contrast agent concentration from $R_2^*$-values alone. The susceptibility measured with QSM has a direct linear relationship with USPIO-concentration. All these novel features can be evaluated in terms of their correlation with different stages of disease, monitoring disease progression or assessing plaque vulnerability. QSM may also allow the identification of USPIO-uptake within a single scan, eliminating the need for a pre-contrast acquisition. This simplifies study design, eliminates the need for image co-registration, reduces cost due to the additional MRI examinations, and improves patient acceptance.

Therefore, QSM of carotid atherosclerosis offers a wide variety of applications in assessing plaque features and also improves the analysis of carotid artery plaque inflammation through the detection of USPIO uptake making its inclusion in future studies beneficial.

# References


1. Benjamin EJ, Muntner P, Alonso A, et al. Heart Disease and Stroke Statistics-2019 Update: A Report From the American Heart Association. *Circulation*. 2019;139(10):e56-e528. doi:10.1161/CIR.0000000000000659.

2. Mozaffarian D, Benjamin EJ, Go AS, et al. Heart disease and stroke statistics--2015 update: a report from the American Heart Association. *Circulation*. 2015;131(4):e29-322. doi:10.1161/CIR.0000000000000152.

3. Lee S, Shafe ACE, Cowie MR. UK stroke incidence, mortality and cardiovascular risk management 1999-2008: time-trend analysis from the General Practice Research Database. *BMJ Open*. 2011;1(2):e000269. doi:10.1136/bmjopen-2011-000269.

4. Vangen-Lønne AM, Wilsgaard T, Johnsen SH, Løchen M-L, Njølstad I, Mathiesen EB. Declining Incidence of Ischemic Stroke: What Is the Impact of Changing Risk Factors? The Tromsø Study 1995 to 2012. *Stroke*. 2017;48(3):544-550. doi:10.1161/STROKEAHA.116.014377.

5. Lackland DT, Roccella EJ, Deutsch AF, et al. Factors influencing the decline in stroke mortality: a statement from the American Heart Association/American Stroke Association. *Stroke*. 2014;45(1):315-353. doi:10.1161/01.str.0000437068.30550.cf.

6. Saka Ö, McGuire A, Wolfe C. Cost of stroke in the United Kingdom. *Age Ageing*. 2009;38(1):27-32. doi:10.1093/ageing/afn281.

7. Naylor AR. Why is the management of asymptomatic carotid disease so controversial? *Surgeon*. 2015;13(1):34-43. doi:10.1016/j.surge.2014.08.004.

8. NHS. Carotid endarterectomy. https://www.nhs.uk/conditions/carotid-endarterectomy/. Published 2018.

9. Warlow C. MRC European Carotid Surgery Trial: interim results for symptomatic patients with severe (70-99%) or with mild (0-29%) carotid stenosis. *Lancet*. 1991;337(8752):1235-1243. doi:10.1016/0140-6736(91)92916-P.

10. North American Symptomatic Carotid Endarterectomy Trial Collaborators, Barnett HJM, Taylor DW, et al. Beneficial effect of carotid endarterectomy in symptomatic patients with high-grade carotid stenosis. *N Engl J Med*. 1991;325(7):445-453. doi:10.1056/NEJM199108153250701.

11. Gaba K, Ringleb PA, Halliday A. Asymptomatic Carotid Stenosis: Intervention or Best Medical Therapy? *Curr Neurol Neurosci Rep*. 2018;18(11):80. doi:10.1007/s11910-018-0888-5.

12. Douglas G, Channon KM. The pathogenesis of atherosclerosis. *Medicine*. 2010;38(8):397-402. doi:10.1016/j.mpmed.2010.05.002.

13. Saam T, Yuan C, Chu B, et al. Predictors of carotid atherosclerotic plaque progression as measured by noninvasive magnetic resonance imaging. *Atherosclerosis*. 2007;194(2):e34-e42. doi:10.1016/j.atherosclerosis.2006.08.016.

14. Yuan C, Hatsukami T. MR plaque imaging. In: Gillard J, Graves M, Hatsukami T, Yuan C, eds. *Carotid Disease: The Role of Imaging in Diagnosis and Management*. Cambridge, UK: Cambridge University Press; 2006:180-190. doi:10.1017/CBO9780511544941.015.

15. Spagnoli LG, Mauriello A, Sangiorgi G, et al. Extracranial thrombotically active carotid plaque as a risk factor for ischemic stroke. *JAMA*. 2004;292(15):1845-1852. doi:10.1001/jama.292.15.1845.

16. Goikuria H, Vandenbroeck K, Alloza I. Inflammation in human carotid atheroma plaques. *Cytokine Growth Factor Rev*. 2018;39:62-70. doi:10.1016/j.cytogfr.2018.01.006.

17. Libby P. Atherosclerosis: The New View. *Sci Am*. 2002;286(5):46-55. doi:10.1038/scientificamerican0502-46.

18. Sakakura K, Nakano M, Otsuka F, Ladich E, Kolodgie FD, Virmani R. Pathophysiology of Atherosclerosis Plaque Progression. *Hear Lung Circ*. 2013;22(6):399-411. doi:10.1016/j.hlc.2013.03.001.

19. Gimbrone MA, García-Cardeña G. Vascular endothelium, hemodynamics, and the pathobiology of atherosclerosis. *Cardiovasc Pathol*. 2013;22(1):9-15.

doi:10.1016/j.carpath.2012.06.006.

20. Wang T, Palucci D, Law K, Yanagawa B, Yam J, Butany J. Atherosclerosis: pathogenesis and pathology. *Diagn Histopathol (Oxf)*. 2012;18(11):461-467. doi:10.1016/j.mpdhp.2012.09.004.

21. Tsimikas S, I. Miller Y. Oxidative Modification of Lipoproteins: Mechanisms, Role in Inflammation and Potential Clinical Applications in Cardiovascular Disease. *Curr Pharm Des*. 2011;17(1):27-37. doi:10.2174/138161211795049831.

22. Witztum J, Steinberg D. The Oxidative Modification Hypothesis of Atherosclerosis: Does It Hold for Humans? *Trends Cardiovasc Med*. 2001;11(3-4):93-102. doi:10.1016/S1050-1738(01)00111-6.

23. Wang T, Butany J. Pathogenesis of atherosclerosis. *Diagn Histopathol (Oxf)*. 2017;23(11):473-478. doi:10.1016/j.mpdhp.2017.11.009.

24. Hurtubise J, McLellan K, Durr K, Onasanya O, Nwabuko D, Ndisang JF. The Different Facets of Dyslipidemia and Hypertension in Atherosclerosis. *Curr Atheroscler Rep*. 2016;18(12):82. doi:10.1007/s11883-016-0632-z.

25. Libby P, Ridker PM, Maseri A. Inflammation and atherosclerosis. *Circulation*. 2002;105(9):1135-1143. doi:10.1161/hc0902.104353.

26. Boisvert WA, Santiago R, Curtiss LK, Terkeltaub RA. A leukocyte homologue of the IL-8 receptor CXCR-2 mediates the accumulation of macrophages in atherosclerotic lesions of LDL receptor-deficient mice. *J Clin Invest*. 1998;101(2):353-363. doi:10.1172/JCI1195.

27. Boring L, Gosling J, Chensue SW, et al. Impaired monocyte migration and reduced type 1 (Th1) cytokine responses in C-C chemokine receptor 2 knockout mice. *J Clin Invest*. 1997;100(10):2552-2561. doi:10.1172/JCI119798.

28. Cybulsky MI, Iiyama K, Li H, et al. A major role for VCAM-1, but not ICAM-1, in early atherosclerosis. *J Clin Invest*. 2001;107(10):1255-1262. doi:10.1172/JCI11871.

29. Smith JD, Trogan E, Ginsberg M, Grigaux C, Tian J, Miyata M. Decreased

atherosclerosis in mice deficient in both macrophage colony-stimulating factor (op) and apolipoprotein E. *Proc Natl Acad Sci USA*. 1995;92(18):8264-8268. doi:10.1073/pnas.92.18.8264.

30. Fatkhullina AR, Peshkova IO, Koltsova EK. The role of cytokines in the development of atherosclerosis. *Biochemistry (Mosc)*. 2016;81(11):1358-1370. doi:10.1134/S0006297916110134.

31. Libby P. Inflammation in Atherosclerosis. *Arterioscler Thromb Vasc Biol*. 2012;32(9):2045-2051. doi:10.1161/ATVBAHA.108.179705.

32. Badimon L, Vilahur G. Thrombosis formation on atherosclerotic lesions and plaque rupture. *J Intern Med*. 2014;276(6):618-632. doi:10.1111/joim.12296.

33. Raggi P, Genest J, Giles JT, et al. Role of inflammation in the pathogenesis of atherosclerosis and therapeutic interventions. *Atherosclerosis*. 2018;276:98-108. doi:10.1016/j.atherosclerosis.2018.07.014.

34. Insull W. The Pathology of Atherosclerosis: Plaque Development and Plaque Responses to Medical Treatment. *Am J Med*. 2009;122(1):S3-S14. doi:10.1016/j.amjmed.2008.10.013.

35. Doran AC, Meller N, McNamara CA. Role of Smooth Muscle Cells in the Initiation and Early Progression of Atherosclerosis. *Arterioscler Thromb Vasc Biol*. 2008;28(5):812-819. doi:10.1161/ATVBAHA.107.159327.

36. Camejo G, Fager G, Rosengren B, Hurt-Camejo E, Bondjers G. Binding of low density lipoproteins by proteoglycans synthesized by proliferating and quiescent human arterial smooth muscle cells. *J Biol Chem*. 1993;268(19):14131-7. http://www.ncbi.nlm.nih.gov/pubmed/8314779.

37. Bennett MR, Sinha S, Owens GK. Vascular Smooth Muscle Cells in Atherosclerosis. *Circ Res*. 2016;118(4):692-702. doi:10.1161/CIRCRESAHA.115.306361.

38. Dubland JA, Francis GA. So Much Cholesterol: the unrecognized importance of smooth muscle cells in atherosclerotic foam cell formation. *Curr Opin Lipidol*. 2016;27(2):155-161. doi:10.1097/MOL.0000000000000279.

39. Rong JX, Shapiro M, Trogan E, Fisher EA. Transdifferentiation of mouse aortic

smooth muscle cells to a macrophage-like state after cholesterol loading. *Proc Natl Acad Sci USA*. 2003;100(23):13531-13536. doi:10.1073/pnas.1735526100.

40. Allahverdian S, Chehroudi AC, McManus BM, Abraham T, Francis GA. Contribution of Intimal Smooth Muscle Cells to Cholesterol Accumulation and Macrophage-Like Cells in Human Atherosclerosis. *Circulation*. 2014;129(15):1551-1559. doi:10.1161/CIRCULATIONAHA.113.005015.

41. Clarke MCH, Figg N, Maguire JJ, et al. Apoptosis of vascular smooth muscle cells induces features of plaque vulnerability in atherosclerosis. *Nat Med*. 2006;12(9):1075-1080. doi:10.1038/nm1459.

42. Sima A V., Stancu CS, Simionescu M. Vascular endothelium in atherosclerosis. *Cell Tissue Res*. 2009;335(1):191-203. doi:10.1007/s00441-008-0678-5.

43. Napoli C, Ignarro LJ. Nitric Oxide and Atherosclerosis. *Nitric Oxide*. 2001;5(2):88-97. doi:10.1006/niox.2001.0337.

44. Takaya N, Yuan C, Chu B, et al. Association between carotid plaque characteristics and subsequent ischemic cerebrovascular events: A prospective assessment with MRI - Initial results. *Stroke*. 2006;37(3):818-823. doi:10.1161/01.STR.0000204638.91099.91.

45. Newby A, Zaltsman AB. Fibrous cap formation or destruction — the critical importance of vascular smooth muscle cell proliferation, migration and matrix formation. *Cardiovasc Res*. 1999;41(2):345-360. doi:10.1016/S0008-6363(98)00286-7.

46. Chistiakov DA, Sobenin IA, Orekhov AN. Vascular Extracellular Matrix in Atherosclerosis. *Cardiol Rev*. 2013;21(6):270-288. doi:10.1097/CRD.0b013e31828c5ced.

47. Underhill HR, Yuan C, Yarnykh VL, et al. Predictors of Surface Disruption with MR Imaging in Asymptomatic Carotid Artery Stenosis. *AJNR Am J Neuroradiol*. 2010;31(3):487-493. doi:10.3174/ajnr.A1842.

48. Arbustini E, Grasso M, Diegoli M, et al. Coronary atherosclerotic plaques with

and without thrombus in ischemic heart syndromes: A morphologic, immunohistochemical, and biochemical study. *Am J Cardiol*. 1991;68(7):B36-B50. doi:10.1016/0002-9149(91)90383-V.

49. Burke AP, Kolodgie FD, Farb A, et al. Healed Plaque Ruptures and Sudden Coronary Death: Evidence That Subclinical Rupture Has a Role in Plaque Progression. *Circulation*. 2001;103(7):934-940. doi:10.1161/01.CIR.103.7.934.

50. Heo SH, Cho C-H, Kim HO, et al. Plaque Rupture is a Determinant of Vascular Events in Carotid Artery Atherosclerotic Disease: Involvement of Matrix Metalloproteinases 2 and 9. *J Clin Neurol*. 2011;7(2):69. doi:10.3988/jcn.2011.7.2.69.

51. Molloy KJ, Thompson MM, Jones JL, et al. Unstable Carotid Plaques Exhibit Raised Matrix Metalloproteinase-8 Activity. *Circulation*. 2004;110(3):337-343. doi:10.1161/01.CIR.0000135588.65188.14.

52. Galis ZS, Sukhova GK, Lark MW, Libby P. Increased expression of matrix metalloproteinases and matrix degrading activity in vulnerable regions of human atherosclerotic plaques. *J Clin Invest*. 1994;94(6):2493-2503. doi:10.1172/JCI117619.

53. Jia H, Abtahian F, Aguirre AD, et al. In Vivo Diagnosis of Plaque Erosion and Calcified Nodule in Patients With Acute Coronary Syndrome by Intravascular Optical Coherence Tomography. *J Am Coll Cardiol*. 2013;62(19):1748-1758. doi:10.1016/j.jacc.2013.05.071.

54. Prati F, Uemura S, Souteyrand G, et al. OCT-Based Diagnosis and Management of STEMI Associated With Intact Fibrous Cap. *JACC Cardiovasc Imaging*. 2013;6(3):283-287. doi:10.1016/j.jcmg.2012.12.007.

55. van der Wal AC, Becker AE, van der Loos CM, Das PK. Site of intimal rupture or erosion of thrombosed coronary atherosclerotic plaques is characterized by an inflammatory process irrespective of the dominant plaque morphology. *Circulation*. 1994;89(1):36-44. doi:10.1161/01.CIR.89.1.36.

56. Kramer MCA, Rittersma SZH, de Winter RJ, et al. Relationship of Thrombus Healing to Underlying Plaque Morphology in Sudden Coronary Death. *J Am*

*Coll Cardiol*. 2010;55(2):122-132. doi:10.1016/j.jacc.2009.09.007.

57. Virmani R, Burke A, Ladich E, Kolodgie FD. Pathology of carotid artery atherosclerotic disease. In: Gillard J, Graves M, Hatsukami T, Yuan C, eds. *Carotid Disease: The Role of Imaging in Diagnosis and Management*. Cambridge, UK: Cambridge University Press; 2006:1-21. doi:10.1017/CBO9780511544941.002.

58. Kolodgie FD, Yahagi K, Mori H, et al. High-risk carotid plaque: lessons learned from histopathology. *Semin Vasc Surg*. 2017;30(1):31-43. doi:10.1053/j.semvascsurg.2017.04.008.

59. Finn A V., Narula J. Intraplaque Hemorrhage: Most Dangerous Is the Wound That Bleedeth Inwardly…. *JACC Cardiovasc Imaging*. 2012;5(8):856-858. doi:10.1016/j.jcmg.2012.07.003.

60. Xu J, Lu X, Shi G-P. Vasa Vasorum in Atherosclerosis and Clinical Significance. *Int J Mol Sci*. 2015;16(12):11574-11608. doi:10.3390/ijms160511574.

61. Williams JK, Heistad DD. Structure and function of vasa vasorum. *Trends Cardiovasc Med*. 1996;6(2):53-57. doi:10.1016/1050-1738(96)00008-4.

62. Moreno PR, Purushothaman KR, Sirol M, Levy AP, Fuster V. Neovascularization in human atherosclerosis. *Circulation*. 2006;113(18):2245-2252. doi:10.1161/CIRCULATIONAHA.105.578955.

63. Kockx MM, Cromheeke KM, Knaapen MWM, et al. Phagocytosis and Macrophage Activation Associated With Hemorrhagic Microvessels in Human Atherosclerosis. *Arterioscler Thromb Vasc Biol*. 2003;23(3):440-446. doi:10.1161/01.ATV.0000057807.28754.7F.

64. Kolodgie FD, Gold HK, Burke AP, et al. Intraplaque Hemorrhage and Progression of Coronary Atheroma. *N Engl J Med*. 2003;349(24):2316-2325. doi:10.1056/NEJMoa035655.

65. Takaya N, Yuan C, Chu B, et al. Presence of Intraplaque Hemorrhage Stimulates Progression of Carotid Atherosclerotic Plaques. *Circulation*. 2005;111(21):2768-2775. doi:10.1161/CIRCULATIONAHA.104.504167.

66. Virmani R, Kolodgie FD, Burke AP, et al. Atherosclerotic Plaque Progression and Vulnerability to Rupture: Angiogenesis as a Source of Intraplaque Hemorrhage. *Arterioscler Thromb Vasc Biol*. 2005;25(10):2054-2061. doi:10.1161/01.ATV.0000178991.71605.18.

67. Zemplenyi T, Crawford DW, Cole MA. Adaptation to arterial wall hypoxia demonstrated in vivo with oxygen microcathodes. *Atherosclerosis*. 1989;76(2-3):173-179. doi:10.1016/0021-9150(89)90101-9.

68. Sun J, Balu N, Hippe DS, et al. Subclinical Carotid Atherosclerosis: Short-term Natural History of Lipid-rich Necrotic Core—A Multicenter Study with MR Imaging. *Radiology*. 2013;268(1):61-68. doi:10.1148/radiol.13121702.

69. Sun J, Underhill HR, Hippe DS, Xue Y, Yuan C, Hatsukami TS. Sustained acceleration in carotid atherosclerotic plaque progression with intraplaque hemorrhage: A long-term time course study. *JACC Cardiovasc Imaging*. 2012;5(8):798-804. doi:10.1016/j.jcmg.2012.03.014.

70. Underhill HR, Yuan C, Yarnykh VL, et al. Arterial Remodeling in the Subclinical Carotid Artery Disease. *JACC Cardiovasc Imaging*. 2009;2(12):1381-1389. doi:10.1016/j.jcmg.2009.08.007.

71. Ota H, Yu W, Underhill HR, et al. Hemorrhage and large lipid-rich necrotic cores are independently associated with thin or ruptured fibrous caps: An in vivo 3T MRI study. *Arterioscler Thromb Vasc Biol*. 2009;29(10):1696-1701. doi:10.1161/ATVBAHA.109.192179.

72. Bentzon JF, Otsuka F, Virmani R, Falk E. Mechanisms of plaque formation and rupture. *Circ Res*. 2014;114(12):1852-1866. doi:10.1161/CIRCRESAHA.114.302721.

73. Speer MY, Yang H-Y, Brabb T, et al. Smooth Muscle Cells Give Rise to Osteochondrogenic Precursors and Chondrocytes in Calcifying Arteries. *Circ Res*. 2009;104(6):733-741. doi:10.1161/CIRCRESAHA.108.183053.

74. Shanahan CM. Inflammation ushers in calcification: A cycle of damage and protection? *Circulation*. 2007;116(24):2782-2785. doi:10.1161/CIRCULATIONAHA.107.749655.

75. Pugliese G, Iacobini C, Fantauzzi CB, Menini S. The dark and bright side of atherosclerotic calcification. *Atherosclerosis*. 2015;238(2):220-230. doi:10.1016/j.atherosclerosis.2014.12.011.

76. Otsuka F, Sakakura K, Yahagi K, Joner M, Virmani R. Has Our Understanding of Calcification in Human Coronary Atherosclerosis Progressed? *Arterioscler Thromb Vasc Biol*. 2014;34(4):724-736. doi:10.1161/ATVBAHA.113.302642.

77. Basatemur GL, Jørgensen HF, Clarke MCH, Bennett MR, Mallat Z. Vascular smooth muscle cells in atherosclerosis. *Nat Rev Cardiol*. 2019;16(12):727-744. doi:10.1038/s41569-019-0227-9.

78. Aikawa E, Nahrendorf M, Figueiredo J-L, et al. Osteogenesis Associates With Inflammation in Early-Stage Atherosclerosis Evaluated by Molecular Imaging In Vivo. *Circulation*. 2007;116(24):2841-2850. doi:10.1161/CIRCULATIONAHA.107.732867.

79. Hutcheson JD, Goettsch C, Bertazzo S, et al. Genesis and growth of extracellular-vesicle-derived microcalcification in atherosclerotic plaques. *Nat Mater*. 2016;15(3):335-343. doi:10.1038/nmat4519.

80. Otsuka F, Yasuda S, Noguchi T, Ishibashi-Ueda H. Pathology of coronary atherosclerosis and thrombosis. *Cardiovasc Diagn Ther*. 2016;6(4):396-408. doi:10.21037/cdt.2016.06.01.

81. Nandalur KR, Hardie AD, Raghavan P, Schipper MJ, Baskurt E, Kramer CM. Composition of the Stable Carotid Plaque: Insights From a Multidetector Computed Tomography Study of Plaque Volume. *Stroke*. 2007;38(3):935-940. doi:10.1161/01.STR.0000257995.74834.92.

82. Petty GW, Brown RD, Whisnant JP, Sicks JD, O'Fallon WM, Wiebers DO. Ischemic Stroke Subtypes: A Population-Based Study of Functional Outcome, Survival, and Recurrence. *Stroke*. 2000;31(5):1062-1068. doi:10.1161/01.STR.31.5.1062.

83. Rothwell P, Eliasziw M, Gutnikov S, Warlow C, Barnett H. Endarterectomy for symptomatic carotid stenosis in relation to clinical subgroups and timing of surgery. *Lancet*. 2004;363(9413):915-924. doi:10.1016/S0140-6736(04)15785-

1.

84. Reznik M, Kamel H, Gialdini G, Pandya A, Navi BB, Gupta A. Timing of Carotid Revascularization Procedures After Ischemic Stroke. *Stroke*. 2017;48(1):225-228. doi:10.1161/STROKEAHA.116.015766.

85. de Weerd M, Greving JP, de Jong AWF, Buskens E, Bots ML. Prevalence of Asymptomatic Carotid Artery Stenosis According to Age and Sex. *Stroke*. 2009;40(4):1105-1113. doi:10.1161/STROKEAHA.108.532218.

86. de Weerd M, Greving JP, Hedblad B, et al. Prevalence of Asymptomatic Carotid Artery Stenosis in the General Population: An Individual Participant Data Meta-Analysis. *Stroke*. 2010;41(6):1294-1297. doi:10.1161/STROKEAHA.110.581058.

87. LeFevre ML. Screening for Asymptomatic Carotid Artery Stenosis: U.S. Preventive Services Task Force Recommendation Statement. *Ann Intern Med*. 2014;161(5):356. doi:10.7326/M14-1333.

88. Inzitari D, Eliasziw M, Gates P, et al. The Causes and Risk of Stroke in Patients with Asymptomatic Internal-Carotid-Artery Stenosis. *N Engl J Med*. 2000;342(23):1693-1701. doi:10.1056/NEJM200006083422302.

89. Brott TG, Halperin JL, Abbara S, et al. 2011 ASA/ACCF/AHA/AANN/AANS/ACR/ASNR/CNS/SAIP/SCAI/SIR/SNIS/SVM/SVS guideline on the management of patients with extracranial carotid and vertebral artery disease: executive summary: a report of the American College of Cardiology Foundation/American Heart Association Task Force on Practice Guidelines, and the American Stroke Association, American Association of Neuroscience Nurses, American Association of Neurological Surgeons, American College of Radiology, American Society of Neuroradiology, Congress of Neurological Surgeons, Society of Atherosclerosis Imaging and Prevention, Society for Cardiovascular Angiography and Interventions, Society of Interventional Radiology, Society of NeuroInterventional Surgery, Society for Vascular Medicine, and Society for Vascular Surgery Developed in Collaboration With the American Academy of Neurology and Society of Cardiovascular Computed Tomography. *J Am Coll Cardiol*. 2011;57(8):1002-

1044. doi:10.1016/j.jacc.2010.11.005.

90. Brott TG, Halperin JL, Abbara S, et al. 2011 ASA/ACCF/AHA/AANN/AANS/ACR/ASNR/CNS/SAIP/SCAI/SIR/SNIS/SVM/SVS guideline on the management of patients with extracranial carotid and vertebral artery disease: a report of the American College of Cardiology Foundation/American Heart Association Task F orce on Practice Guidelines, and the American Stroke Association, American Association of Neuroscience Nurses, American Association of Neurological Surgeons, American College of Radiology, American Society of Neuroradiology, Congress of Neurological Surgeons, Society of Atherosclerosis Imaging and Prevention, Society for Cardiovascular Angiography and Interventions, Society of Interventional Radiology, Society of NeuroInterventional Surgery, Society for Vascular Medicine, and Society for Vascular Surgery Developed in Collaboration With the American Academy of Neurology and Society of Cardiovascular Computed Tomography. *J Am Coll Cardiol*. 2011;57(8):e16-e94. doi:10.1016/j.jacc.2010.11.006.

91. Warlow C, Farrell B, Fraser A, Sandercock P, Slattery J. Randomised trial of endarterectomy for recently symptomatic carotid stenosis: final results of the MRC European Carotid Surgery Trial (ECST). *Lancet*. 1998;351(9113):1379-1387. doi:10.1016/S0140-6736(97)09292-1.

92. Gokaldas R, Singh M, Lal S, Benenstein RJ, Sahni R. Carotid Stenosis: From Diagnosis to Management, Where Do We Stand? *Curr Atheroscler Rep*. 2015;17(2):1. doi:10.1007/s11883-014-0480-7.

93. Grant EG, Benson CB, Moneta GL, et al. Carotid Artery Stenosis: Gray-Scale and Doppler US Diagnosis—Society of Radiologists in Ultrasound Consensus Conference. *Radiology*. 2003;229(2):340-346. doi:10.1148/radiol.2292030516.

94. Canadian Cooperative Study Group. A randomized trial of aspirin and sulfinpyrazone in threatened stroke. *N Engl J Med*. 1978;299(2):53-59. doi:10.1056/NEJM197807132990201.

95. Ettehad D, Emdin CA, Kiran A, et al. Blood pressure lowering for prevention of cardiovascular disease and death: a systematic review and meta-analysis.

*Lancet*. 2016;387(10022):957-967. doi:10.1016/S0140-6736(15)01225-8.

96. Sillesen H, Amarenco P, Hennerici MG, et al. Atorvastatin Reduces the Risk of Cardiovascular Events in Patients With Carotid Atherosclerosis: A Secondary Analysis of the Stroke Prevention by Aggressive Reduction in Cholesterol Levels (SPARCL) Trial. *Stroke*. 2008;39(12):3297-3302. doi:10.1161/STROKEAHA.108.516450.

97. Barnett HJM, Taylor DW, Eliasziw M, et al. Benefit of Carotid Endarterectomy in Patients with Symptomatic Moderate or Severe Stenosis. *N Engl J Med*. 1998;339(20):1415-1425. doi:10.1056/NEJM199811123392002.

98. Rothwell PM, Gutnikov SA, Warlow CP. Reanalysis of the final results of the European Carotid Surgery Trial. *Stroke*. 2003;34(2):514-523. doi:10.1161/01.STR.0000054671.71777.C7.

99. Noiphithak R, Liengudom A. Recent Update on Carotid Endarterectomy versus Carotid Artery Stenting. *Cerebrovasc Dis*. 2017;43(1-2):68-75. doi:10.1159/000453282.

100. Song HK, Wolf RL, Schneiderman J, Wilensky RL. Magnetic resonance imaging and intravascular magnetic resonance imaging. In: Virmani R, Narula J, Leon MB, Willerson JT, eds. *The Vulnerable Atherosclerotic Plaque: Strategies for Diagnosis and Management*. Oxford, UK: Blackwell Publishing; 2006:230-246. doi:10.1002/9780470987575.ch14.

101. Cai JM, Hatsukami TS, Ferguson MS, Small R, Polissar NL, Yuan C. Classification of human carotid atherosclerotic lesions with in vivo multicontrast magnetic resonance imaging. *Circulation*. 2002;106(11):1368-1373. doi:10.1161/01.CIR.0000028591.44554.F9.

102. Chu B, Kampschulte A, Ferguson MS, et al. Hemorrhage in the atherosclerotic carotid plaque: A high-resolution MRI study. *Stroke*. 2004;35(5):1079-1084. doi:10.1161/01.STR.0000125856.25309.86.

103. Yuan C, Mitsumori LM, Ferguson MS, et al. In vivo accuracy of multispectral magnetic resonance imaging for identifying lipid-rich necrotic cores and intraplaque hemorrhage in advanced human carotid plaques. *Circulation*.

2001;104(17):2051-2056. doi:10.1161/hc4201.097839.

104. Saam T, Ferguson MS, Yarnykh VL, et al. Quantitative evaluation of carotid plaque composition by in vivo MRI. *Arterioscler Thromb Vasc Biol*. 2005;25(1):234-239. doi:10.1161/01.ATV.0000149867.61851.31.

105. Mitsumori LM, Hatsukami TS, Ferguson MS, Kerwin WS, Cai J, Yuan C. In vivo accuracy of multisequence MR imaging for identifying unstable fibrous caps in advanced human carotid plaques. *J Magn Reson Imaging*. 2003;17(4):410-420. doi:10.1002/jmri.10264.

106. Touzé E, Toussaint JF, Coste J, et al. Reproducibility of high-resolution MRI for the identification and the quantification of carotid atherosclerotic plaque components: Consequences for prognosis studies and therapeutic trials. *Stroke*. 2007;38(6):1812-1819. doi:10.1161/STROKEAHA.106.479139.

107. Trivedi RA, U-King-Im J, Graves MJ, et al. Multi-sequence in vivo MRI can quantify fibrous cap and lipid core components in human carotid atherosclerotic plaques. *Eur J Vasc Endovasc Surg*. 2004;28(2):207-213. doi:10.1016/j.ejvs.2004.05.001.

108. Ota H, Yarnykh VL, Ferguson MS, et al. Carotid intraplaque hemorrhage imaging at 3.0-T MR imaging: comparison of the diagnostic performance of three T1-weighted sequences. *Radiology*. 2010;254(2):551-563. doi:10.1148/radiol.09090535.

109. Yarnykh VL, Terashima M, Hayes CE, et al. Multicontrast black-blood MRI of carotid arteries: Comparison between 1.5 and 3 Tesla magnetic field strengths. *J Magn Reson Imaging*. 2006;23(5):691-698. doi:10.1002/jmri.20562.

110. Underhill HR, Yarnykh VL, Hatsukami TS, et al. Carotid plaque morphology and composition: initial comparison between 1.5- and 3.0-T magnetic field strengths. *Radiology*. 2008;248(2):550-560. doi:10.1148/radiol.2482071114.

111. Young VE, Patterson AJ, Tunnicliffe EM, et al. Signal-to-noise ratio increase in carotid atheroma MRI: A comparison of 1.5 and 3 T. *Br J Radiol*. 2012;85(1015):937-944. doi:10.1259/bjr/70496948.

112. Koktzoglou I, Chung YC, Mani V, et al. Multislice dark-blood carotid artery wall

imaging: A 1.5 T and 3.0 T comparison. *J Magn Reson Imaging*. 2006;23(5):699-705. doi:10.1002/jmri.20563.

113. Saam T, Raya JG, Cyran CC, et al. High resolution carotid black-blood 3T MR with parallel imaging and dedicated 4-channel surface coils. *J Cardiovasc Magn Reson*. 2009;11(1):41. doi:10.1186/1532-429X-11-41.

114. Treiman GS, McNally JS, Kim S-E, Parker DL. Correlation of Carotid Intraplaque Hemorrhage and Stroke Using 1.5 T and 3 T Mri. *Magn Reson Insights*. 2015;8s1(1):MRI.S23560. doi:10.4137/MRI.S23560.

115. de Rotte AAJ, Koning W, Truijman MTB, et al. Seven-Tesla Magnetic Resonance Imaging of Atherosclerotic Plaque in the Significantly Stenosed Carotid Artery: A Feasibility Study. *Invest Radiol*. 2014;49(11):749-757. doi:10.1097/RLI.0000000000000079.

116. Koning W, de Rotte AAJ, Bluemink JJ, et al. MRI of the carotid artery at 7 Tesla: Quantitative comparison with 3 Tesla. *J Magn Reson Imaging*. 2015;41(3):773-780. doi:10.1002/jmri.24601.

117. Majidi S, Sein J, Watanabe M, et al. Intracranial-derived atherosclerosis assessment: An in vitro comparison between virtual histology by intravascular ultrasonography, 7T MRI, and histopathologic findings. *AJNR Am J Neuroradiol*. 2013;34(12):2259-2264. doi:10.3174/ajnr.A3631.

118. Kröner ESJ, van Schinkel LD, Versluis MJ, et al. Ultrahigh-field 7-T magnetic resonance carotid vessel wall imaging: initial experience in comparison with 3-T field strength. *Invest Radiol*. 2012;47(12):697-704. doi:10.1097/RLI.0b013e31826dc174.

119. Zhu C, Sadat U, Patterson AJ, Teng Z, Gillard JH, Graves MJ. 3D high-resolution contrast enhanced MRI of carotid atheroma - a technical update. *Magn Reson Imaging*. 2014;32(5):594-597. doi:10.1016/j.mri.2014.01.019.

120. Balu N, Chu B, Hatsukami TS, Yuan C, Yarnykh VL. Comparison between 2D and 3D high-resolution black-blood techniques for carotid artery wall imaging in clinically significant atherosclerosis. *J Magn Reson Imaging*. 2008;27(4):918-924. doi:10.1002/jmri.21282.

121. McRobbie DW, Moore EA, Graves MJ, Prince MR. *MRI: From Picture to Proton*. 2nd ed. Cambridge, UK: Cambridge University Press; 2006. doi:10.1017/CBO9780511545405.

122. Mani V, Itskovich V V., Szimtenings M, et al. Rapid Extended Coverage Simultaneous Multisection Black-Blood Vessel Wall MR Imaging. *Radiology*. 2004;232(1):281-288. doi:10.1148/radiol.2321031022.

123. Mani V, Itskovich V V., Aguiar SH, et al. Comparison of gated and nongated fast multislice black-blood carotid imaging using rapid extended coverage and inflow/outflow saturation techniques. *J Magn Reson Imaging*. 2005;22(5):628-633. doi:10.1002/jmri.20428.

124. Li L, Miller KL, Jezzard P. DANTE-prepared pulse trains: A novel approach to motion-sensitized and motion-suppressed quantitative magnetic resonance imaging. *Magn Reson Med*. 2012;68(5):1423-1438. doi:10.1002/mrm.24142.

125. Moody AR, Murphy RE, Morgan PS, et al. Characterization of complicated carotid plaque with magnetic resonance direct thrombus imaging in patients with cerebral ischemia. *Circulation*. 2003;107(24):3047-3052. doi:10.1161/01.CIR.0000074222.61572.44.

126. Tang TY, Muller KH, Graves MJ, et al. Iron Oxide Particles for Atheroma Imaging. *Arterioscler Thromb Vasc Biol*. 2009;29(7):1001-1008. doi:10.1161/ATVBAHA.108.165514.

127. Alam SR, Stirrat C, Richards J, et al. Vascular and plaque imaging with ultrasmall superparamagnetic particles of iron oxide. *J Cardiovasc Magn Reson*. 2015;17(1):83. doi:10.1186/s12968-015-0183-4.

128. Li W, Tutton S, Vu AT, et al. First-pass contrast-enhanced magnetic resonance angiography in humans using ferumoxytol, a novel ultrasmall superparamagnetic iron oxide (USPIO)-based blood pool agent. *J Magn Reson Imaging*. 2005;21(1):46-52. doi:10.1002/jmri.20235.

129. Prince MR, Zhang HL, Chabra SG, Jacobs P, Wang Y. A pilot investigation of new superparamagnetic iron oxide (ferumoxytol) as a contrast agent for cardiovascular MRI. *J Xray Sci Technol*. 2003;11(4):231-240.

http://www.ncbi.nlm.nih.gov/pubmed/22388293.

130. Neuwelt EA, Várallyay CG, Manninger S, et al. The Potential of Ferumoxytol Nanoparticle Magnetic Resonance Imaging, Perfusion, and Angiography in Central Nervous System Malignancy: A Pilot Study. *Neurosurgery*. 2007;60(4):601-612. doi:10.1227/01.NEU.0000255350.71700.37.

131. Dosa E, Guillaume DJ, Haluska M, et al. Magnetic resonance imaging of intracranial tumors: intra-patient comparison of gadoteridol and ferumoxytol. *Neuro Oncol*. 2011;13(2):251-260. doi:10.1093/neuonc/noq172.

132. Weissleder R, Elizondo G, Wittenberg J, Lee AS, Josephson L, Brady TJ. Ultrasmall superparamagnetic iron oxide: an intravenous contrast agent for assessing lymph nodes with MR imaging. *Radiology*. 1990;175(2):494-498. doi:10.1148/radiology.175.2.2326475.

133. Richards JMJ, Semple SI, MacGillivray TJ, et al. Abdominal Aortic Aneurysm Growth Predicted by Uptake of Ultrasmall Superparamagnetic Particles of Iron Oxide: A Pilot Study. *Circ Cardiovasc Imaging*. 2011;4(3):274-281. doi:10.1161/CIRCIMAGING.110.959866.

134. Sadat U, Taviani V, Patterson AJ, et al. Ultrasmall Superparamagnetic Iron Oxide-enhanced Magnetic Resonance Imaging of Abdominal Aortic Aneurysms–A Feasibility Study. *Eur J Vasc Endovasc Surg*. 2011;41(2):167-174. doi:10.1016/j.ejvs.2010.08.022.

135. Rausch M, Sauter A, Fröhlich J, Neubacher U, Radü EW, Rudin M. Dynamic patterns of USPIO enhancement can be observed in macrophages after ischemic brain damage. *Magn Reson Med*. 2001;46(5):1018-1022. doi:10.1002/mrm.1290.

136. Alam SR, Shah ASV, Richards J, et al. Ultrasmall Superparamagnetic Particles of Iron Oxide in Patients With Acute Myocardial Infarction: Early Clinical Experience. *Circ Cardiovasc Imaging*. 2012;5(5):559-565. doi:10.1161/CIRCIMAGING.112.974907.

137. Smits LP, Tiessens F, Zheng KH, Stroes ES, Nederveen AJ, Coolen BF. Evaluation of ultrasmall superparamagnetic iron-oxide (USPIO) enhanced MRI

with ferumoxytol to quantify arterial wall inflammation. *Atherosclerosis*. 2017;263:211-218. doi:10.1016/j.atherosclerosis.2017.06.020.

138. Trivedi RA, U-King-Im J-M, Graves MJ, et al. In vivo detection of macrophages in human carotid atheroma: temporal dependence of ultrasmall superparamagnetic particles of iron oxide-enhanced MRI. *Stroke*. 2004;35(7):1631-1635. doi:10.1161/01.STR.0000131268.50418.b7.

139. Hope MD, Hope TA, Zhu C, et al. Vascular Imaging With Ferumoxytol as a Contrast Agent. *AJR Am J Roentgenol*. 2015;205(3):W366-W373. doi:10.2214/AJR.15.14534.

140. Hasan DM, Mahaney KB, Magnotta VA, et al. Macrophage Imaging Within Human Cerebral Aneurysms Wall Using Ferumoxytol-Enhanced MRI: A Pilot Study. *Arterioscler Thromb Vasc Biol*. 2012;32(4):1032-1038. doi:10.1161/ATVBAHA.111.239871.

141. Kooi ME, Cappendijk VC, Cleutjens KBJM, et al. Accumulation of Ultrasmall Superparamagnetic Particles of Iron Oxide in Human Atherosclerotic Plaques Can Be Detected by In Vivo Magnetic Resonance Imaging. *Circulation*. 2003;107(19):2453-2458. doi:10.1161/01.CIR.0000068315.98705.CC.

142. Trivedi RA, Mallawarachi C, U-King-Im J-M, et al. Identifying Inflamed Carotid Plaques Using In Vivo USPIO-Enhanced MR Imaging to Label Plaque Macrophages. *Arterioscler Thromb Vasc Biol*. 2006;26(7):1601-1606. doi:10.1161/01.ATV.0000222920.59760.df.

143. Patterson AJ, Tang TY, Graves MJ, Müller KH, Gillard JH. In vivo carotid plaque MRI using quantitative T2* measurements with ultrasmall superparamagnetic iron oxide particles: a dose-response study to statin therapy. *NMR Biomed*. 2011;24(1):89-95. doi:10.1002/nbm.1560.

144. Howarth SPS, Tang T, Graves MJ, Trivedi R, Harle J, Gillard JH. USPIO – enhanced magnetic resonance imaging of carotid atheroma. In: Gillard J, Graves M, Hatsukami T, Yuan C, eds. *Carotid Disease: The Role of Imaging in Diagnosis and Management*. Cambridge, UK: Cambridge University Press; :272-287. doi:10.1017/CBO9780511544941.021.

145. Howarth SPS, Tang TY, Trivedi R, et al. Utility of USPIO-enhanced MR imaging to identify inflammation and the fibrous cap: A comparison of symptomatic and asymptomatic individuals. *Eur J Radiol*. 2009;70(3):555-560. doi:10.1016/j.ejrad.2008.01.047.

146. Vasanawala SS, Nguyen K-L, Hope MD, et al. Safety and technique of ferumoxytol administration for MRI. *Magn Reson Med*. 2016;75(5):2107-2111. doi:10.1002/mrm.26151.

147. U.S. Food & Drug Administration. FDA Drug Safety Communication: FDA strengthens warnings and changes prescribing instructions to decrease the risk of serious allergic reactions with anemia drug Feraheme (ferumoxytol). http://www.fda.gov/Drugs/DrugSafety/ucm440138.htm. Published 2015.

148. Stuber M, Gilson WD, Schaer M, Bulte JW, Kraitchman DL. Shedding light on the dark spot with IRON - A method that generates positive contrast in the presence of superparamagnetic nanoparticles. In: *Proceedings of the 13th Annual Meeting of ISMRM*. ; 2005:2608.

149. Lin C, Cai S, Feng J. Positive contrast imaging of SPIO Nanoparticles. *J Nanomater*. 2012;2012(Article ID 734842):1-9. doi:10.1155/2012/734842.

150. Graves MJ. Pulse sequences for contrast-enhanced magnetic resonance imaging. *Radiography*. 2007;13:e20-e30. doi:10.1016/j.radi.2006.10.002.

151. Mani V, Briley-Saebo KC, Itskovich V V., Samber DD, Fayad ZA. GRadient echo Acquisition for Superparamagnetic particles with Positive contrast (GRASP): Sequence characterization in membrane and glass superparamagnetic iron oxide phantoms at 1.5T and 3T. *Magn Reson Med*. 2006;55(1):126-135. doi:10.1002/mrm.20739.

152. Dahnke H, Liu W, Herzka D, Frank JA, Schaeffter T. Susceptibility gradient mapping (SGM): A new postprocessing method for positive contrast generation applied to superparamagnetic iron oxide particle (SPIO)-labeled cells. *Magn Reson Med*. 2008;60(3):595-603. doi:10.1002/mrm.21478.

153. Ruetten PPR, Gillard JH, Graves MJ. Introduction to Quantitative Susceptibility Mapping and Susceptibility Weighted Imaging. *Br J Radiol*.

2019;92(1101):20181016. doi:10.1259/bjr.20181016.

154. Brown RW, Cheng YCN, Haacke EM, Thompson MR, Venkatesan R. *Magnetic Resonance Imaging : Physical Principles and Sequence Design*. 2nd ed. Hoboken, USA: John Wiley & Sons, Incorporated; 2014. doi:10.1002/9781118633953.

155. Ansorge R, Graves MJ. *The Physics and Mathematics of MRI*. San Rafael, USA: Morgan & Claypool Publishers; 2016. doi:10.1088/978-1-6817-4068-3.

156. Hore P. *Nuclear Magnetic Resonance*. 2nd ed. Oxford, UK: Oxford University Press; 2015.

157. Buonincontri G, Kaggie J, Graves M. *Fast Quantitative Magnetic Resonance Imaging*. Synthesis Lectures on Biomedical Engineering: Morgan & Claypool Publishers; 2020. doi:10.2200/S00959ED1V01Y201910BME059.

158. Hernando D, Vigen KK, Shimakawa A, Reeder SB. R 2* mapping in the presence of macroscopic B0 field variations. *Magn Reson Med*. 2012;68(3):830-840. doi:10.1002/mrm.23306.

159. Hernando D, Levin YS, Sirlin CB, Reeder SB. Quantification of liver iron with MRI: State of the art and remaining challenges. *J Magn Reson Imaging*. 2014;40(5):1003-1021. doi:10.1002/jmri.24584.

160. Yablonskiy DA, Haacke EM. Theory of NMR signal behavior in magnetically inhomogeneous tissues: The static dephasing regime. *Magn Reson Med*. 1994;32(6):749-763. doi:10.1002/mrm.1910320610.

161. Duyn JH, Schenck J. Contributions to magnetic susceptibility of brain tissue. *NMR Biomed*. 2017;30(4):e3546. doi:10.1002/nbm.3546.

162. Duyn JH. Studying brain microstructure with magnetic susceptibility contrast at high-field. *Neuroimage*. 2018;168:152-161. doi:10.1016/j.neuroimage.2017.02.046.

163. Colgan TJ, Knobloch G, Reeder SB, Hernando D. Sensitivity of quantitative relaxometry and susceptibility mapping to microscopic iron distribution. *Magn Reson Med*. 2020;83(2):673-680. doi:10.1002/mrm.27946.

164. Bernstein MA, King KF, Zhou XJ. *Handbook of MRI Pulse Sequences*. Burlington, USA: Elsevier Academic Press; 2004. doi:10.1016/B978-0-12-092861-3.X5000-6.

165. Marques JP, Bowtell R. Application of a fourier-based method for rapid calculation of field inhomogeneity due to spatial variation of magnetic susceptibility. *Concepts Magn Reson Part B Magn Reson Eng*. 2005;25B(1):65-78. doi:10.1002/cmr.b.20034.

166. Wang Y, Liu T. Quantitative susceptibility mapping (QSM): Decoding MRI data for a tissue magnetic biomarker. *Magn Reson Med*. 2015;73(1):82-101. doi:10.1002/mrm.25358.

167. Li L, Leigh JS. Quantifying Arbitrary Magnetic Susceptibility Distributions with MR. *Magn Reson Med*. 2004;51(5):1077-1082. doi:10.1002/mrm.20054.

168. Salomir R, De Senneville BD, Moonen CTW. A fast calculation method for magnetic field inhomogeneity due to an arbitrary distribution of bulk susceptibility. *Concepts Magn Reson Part B Magn Reson Eng*. 2003;19B(1):26-34. doi:10.1002/cmr.b.10083.

169. Deville G, Bernier M, Delrieux JM. NMR multiple echoes observed in solid He3. *Phys Rev B*. 1979;19(11):5666-5688. doi:10.1103/PhysRevB.19.5666.

170. Schweser F, Deistung A, Reichenbach JR. Foundations of MRI phase imaging and processing for Quantitative Susceptibility Mapping (QSM). *Z Med Phys*. 2016;26(1):6-34. doi:10.1016/j.zemedi.2015.10.002.

171. Chen W, Zhu W, Kovanlikaya I, et al. Intracranial Calcifications and Hemorrhages: Characterization with Quantitative Susceptibility Mapping. *Radiology*. 2014;270(2):496-505. doi:10.1148/radiol.13122640.

172. ZHU W, QI J, ZHAN C, et al. Magnetic resonance susceptibility weighted imaging in detecting intracranial calcification and hemorrhage. *Chin Med J (Engl)*. 2008;121(20):2021-2025. doi:10.1097/00029330-200810020-00014.

173. Yamada N, Imakita S, Sakuma T, Takamiya M. Intracranial calcification on gradient-echo phase image: depiction of diamagnetic susceptibility. *Radiology*. 1996;198(1):171-178. doi:10.1148/radiology.198.1.8539373.

174. Barbosa JHO, Santos AC, Salmon CEG. Susceptibility weighted imaging: differentiating between calcification and hemosiderin. *Radiol Bras*. 2015;48(2):93-100. doi:10.1590/0100-3984.2014.0010.

175. Li L. Magnetic susceptibility quantification for arbitrarily shaped objects in inhomogeneous fields. *Magn Reson Med*. 2001;46(5):907-916. doi:10.1002/mrm.1276.

176. Zhou D, Liu T, Spincemaille P, Wang Y. Background field removal by solving the Laplacian boundary value problem. *NMR Biomed*. 2014;27(3):312-319. doi:10.1002/nbm.3064.

177. Liu T, Khalidov I, de Rochefort L, et al. A novel background field removal method for MRI using projection onto dipole fields (PDF). *NMR Biomed*. 2011;24(9):1129-1136. doi:10.1002/nbm.1670.

178. Haacke EM, Xu Y, Cheng Y-CN, Reichenbach JR. Susceptibility weighted imaging (SWI). *Magn Reson Med*. 2004;52(3):612-618. doi:10.1002/mrm.20198.

179. Li N, Wang W-T, Pham DL, Butman JA. Artifactual microhemorrhage generated by susceptibility weighted image processing. *J Magn Reson Imaging*. 2015;41(6):1695-1700. doi:10.1002/jmri.24728.

180. Haacke EM, Mittal S, Wu Z, Neelavalli J, Cheng Y-CN. Susceptibility-Weighted Imaging: Technical Aspects and Clinical Applications, Part 1. *AJNR Am J Neuroradiol*. 2009;30(1):19-30. doi:10.3174/ajnr.A1400.

181. Wang Y, Yu Y, Li D, et al. Artery and vein separation using susceptibility-dependent phase in contrast-enhanced MRA. *J Magn Reson Imaging*. 2000;12(5):661-670. doi:10.1002/1522-2586(200011)12:5<661::AID-JMRI2>3.0.CO;2-L.

182. Hagberg GE, Welch EB, Greiser A. The sign convention for phase values on different vendor systems: definition and implications for susceptibility-weighted imaging. *Magn Reson Imaging*. 2010;28(2):297-300. doi:10.1016/j.mri.2009.06.001.

183. Langkammer C, Schweser F, Krebs N, et al. Quantitative susceptibility

mapping (QSM) as a means to measure brain iron? A post mortem validation study. *Neuroimage*. 2012;62(3):1593-1599. doi:10.1016/j.neuroimage.2012.05.049.

184. Deistung A, Schäfer A, Schweser F, Biedermann U, Turner R, Reichenbach JR. Toward in vivo histology: A comparison of quantitative susceptibility mapping (QSM) with magnitude-, phase-, and R2*-imaging at ultra-high magnetic field strength. *Neuroimage*. 2013;65:299-314. doi:10.1016/j.neuroimage.2012.09.055.

185. Bilgic B, Pfefferbaum A, Rohlfing T, Sullivan E V., Adalsteinsson E. MRI estimates of brain iron concentration in normal aging using quantitative susceptibility mapping. *Neuroimage*. 2012;59(3):2625-2635. doi:10.1016/j.neuroimage.2011.08.077.

186. Zheng W, Nichol H, Liu S, Cheng Y-CN, Haacke EM. Measuring iron in the brain using quantitative susceptibility mapping and X-ray fluorescence imaging. *Neuroimage*. 2013;78:68-74. doi:10.1016/j.neuroimage.2013.04.022.

187. Liu T, Eskreis-Winkler S, Schweitzer AAD, et al. Improved Subthalamic Nucleus Depiction with Quantitative Susceptibility Mapping. *Radiology*. 2013;269(1):216-223. doi:10.1148/radiol.13121991.

188. Deistung A, Schäfer A, Schweser F, et al. High-Resolution MR Imaging of the Human Brainstem In vivo at 7 Tesla. *Front Hum Neurosci*. 2013;7(October):710. doi:10.3389/fnhum.2013.00710.

189. Schäfer A, Forstmann BU, Neumann J, et al. Direct visualization of the subthalamic nucleus and its iron distribution using high-resolution susceptibility mapping. *Hum Brain Mapp*. 2012;33(12):2831-2842. doi:10.1002/hbm.21404.

190. Langkammer C, Liu T, Khalil M, et al. Quantitative susceptibility mapping in multiple sclerosis. *Radiology*. 2013;267(2):551-559. doi:10.1148/radiol.12120707.

191. Abosch A, Yacoub E, Ugurbil K, Harel N. An assessment of current brain targets for deep brain stimulation surgery with susceptibility-weighted imaging at 7 tesla. *Neurosurgery*. 2010;67(6):1745-1756.

doi:10.1227/NEU.0b013e3181f74105.

192. Khalil M, Langkammer C, Ropele S, et al. Determinants of brain iron in multiple sclerosis: A quantitative 3T MRI study. *Neurology*. 2011;77(18):1691-1697. doi:10.1212/WNL.0b013e318236ef0e.

193. Haacke EM, Makki M, Ge Y, et al. Characterizing iron deposition in multiple sclerosis lesions using susceptibility weighted imaging. *J Magn Reson Imaging*. 2009;29(3):537-544. doi:10.1002/jmri.21676.

194. Langkammer C, Krebs N, Goessler W, et al. Susceptibility induced gray-white matter MRI contrast in the human brain. *Neuroimage*. 2012;59(2):1413-1419. doi:10.1016/j.neuroimage.2011.08.045.

195. Al-Radaideh AM, Wharton SJ, Lim S-Y, et al. Increased iron accumulation occurs in the earliest stages of demyelinating disease: an ultra-high field susceptibility mapping study in Clinically Isolated Syndrome. *Mult Scler J*. 2013;19(7):896-903. doi:10.1177/1352458512465135.

196. Blazejewska AI, Al-Radaideh AM, Wharton S, et al. Increase in the iron content of the substantia nigra and red nucleus in multiple sclerosis and clinically isolated syndrome: A 7 Tesla MRI study. *J Magn Reson Imaging*. 2015;41(4):1065-1070. doi:10.1002/jmri.24644.

197. Chen W, Gauthier SA, Gupta A, et al. Quantitative susceptibility mapping of multiple sclerosis lesions at various ages. *Radiology*. 2014;271(1):183-192. doi:10.1148/radiol.13130353.

198. Rudko DA, Solovey I, Gati JS, Kremenchutzky M, Menon RS. Multiple Sclerosis: Improved Identification of Disease-relevant Changes in Gray and White Matter by Using Susceptibility-based MR Imaging. *Radiology*. 2014;272(3):851-864. doi:10.1148/radiol.14132475.

199. Gorell J, Ordidge R, Brown G, Deniau J, Buderer N, Helpern J. Increased iron-related MRI contrast in the substantia nigra in Parkinson's disease. *Neurology*. 1995;45(6):1138-1143. doi:10.1212/WNL.45.6.1138.

200. Zhang W, Sun S-G, Jiang Y-H, Qiao X, Sun X, Wu Y. Determination of brain iron content in patients with Parkinson's disease using magnetic susceptibility

imaging. *Neurosci Bull*. 2009;25(6):353-360. doi:10.1007/s12264-009-0225-8.

201. Zhu W-Z, Zhong W, Wang W, et al. Quantitative MR phase-corrected imaging to investigate increased brain iron deposition of patients with Alzheimer disease. *Radiology*. 2009;253(2):497-504. doi:10.1148/radiol.2532082324.

202. Lotfipour AK, Wharton S, Schwarz ST, et al. High resolution magnetic susceptibility mapping of the substantia nigra in Parkinson's disease. *J Magn Reson Imaging*. 2012;35(1):48-55. doi:10.1002/jmri.22752.

203. Barbosa JHO, Santos AC, Tumas V, et al. Quantifying brain iron deposition in patients with Parkinson's disease using quantitative susceptibility mapping, R2 and R2*. *Magn Reson Imaging*. 2015;33(5):559-565. doi:10.1016/j.mri.2015.02.021.

204. Murakami Y, Kakeda S, Watanabe K, et al. Usefulness of Quantitative Susceptibility Mapping for the Diagnosis of Parkinson Disease. *AJNR Am J Neuroradiol*. 2015;36(6):1102-1108. doi:10.3174/ajnr.A4260.

205. Acosta-Cabronero J, Williams GB, Cardenas-Blanco A, Arnold RJ, Lupson V, Nestor PJ. In vivo quantitative susceptibility mapping (QSM) in Alzheimer's disease. *PLoS One*. 2013;8(11):e81093. doi:10.1371/journal.pone.0081093.

206. Moon Y, Han S-H, Moon W-J. Patterns of Brain Iron Accumulation in Vascular Dementia and Alzheimer's Dementia Using Quantitative Susceptibility Mapping Imaging. *J Alzheimers Dis*. 2016;51(3):737-745. doi:10.3233/JAD-151037.

207. Ayton S, Fazlollahi A, Bourgeat P, et al. Cerebral quantitative susceptibility mapping predicts amyloid-β-related cognitive decline. *Brain*. 2017;140(8):2112-2119. doi:10.1093/brain/awx137.

208. van Bergen JMG, Li X, Quevenco FC, et al. Simultaneous quantitative susceptibility mapping and Flutemetamol-PET suggests local correlation of iron and β-amyloid as an indicator of cognitive performance at high age. *Neuroimage*. 2018;174:308-316. doi:10.1016/j.neuroimage.2018.03.021.

209. Du G, Liu T, Lewis MM, et al. Quantitative susceptibility mapping of the midbrain in Parkinson's disease. *Mov Disord*. 2016;31(3):317-324. doi:10.1002/mds.26417.

210. Sjöström H, Granberg T, Westman E, Svenningsson P. Quantitative susceptibility mapping differentiates between parkinsonian disorders. *Parkinsonism Relat Disord*. 2017;44:51-57. doi:10.1016/j.parkreldis.2017.08.029.

211. Langkammer C, Pirpamer L, Seiler S, et al. Quantitative Susceptibility Mapping in Parkinson's Disease. *PLoS One*. 2016;11(9):e0162460. doi:10.1371/journal.pone.0162460.

212. Ulla M, Bonny JM, Ouchchane L, Rieu I, Claise B, Durif F. Is R2* a New MRI Biomarker for the Progression of Parkinson's Disease? A Longitudinal Follow-Up. *PLoS One*. 2013;8(3):e57904. doi:10.1371/journal.pone.0057904.

213. Bartzokis G, Cummings JL, Markham CH, et al. MRI evaluation of brain iron in earlier- and later-onset Parkinson's disease and normal subjects. *Magn Reson Imaging*. 1999;17(2):213-222. doi:10.1016/S0730-725X(98)00155-6.

214. Wallis LI, Paley MNJ, Graham JM, et al. MRI assessment of basal ganglia iron deposition in Parkinson's disease. *J Magn Reson Imaging*. 2008;28(5):1061-1067. doi:10.1002/jmri.21563.

215. Zhang J, Zhang Y, Wang J, et al. Characterizing iron deposition in Parkinson's disease using susceptibility-weighted imaging: An in vivo MR study. *Brain Res*. 2010;1330:124-130. doi:10.1016/j.brainres.2010.03.036.

216. Jin L, Wang J, Zhao L, et al. Decreased serum ceruloplasmin levels characteristically aggravate nigral iron deposition in Parkinson's disease. *Brain*. 2011;134(1):50-58. doi:10.1093/brain/awq319.

217. Schweser F, Deistung A, Lehr BW, Reichenbach JR. Differentiation between diamagnetic and paramagnetic cerebral lesions based on magnetic susceptibility mapping. *Med Phys*. 2010;37(10):5165-5178. doi:10.1118/1.3481505.

218. Bradley WG. MR appearance of hemorrhage in the brain. *Radiology*. 1993;189(1):15-26. doi:10.1148/radiology.189.1.8372185.

219. Nandigam RNK, Viswanathan A, Delgado P, et al. MR imaging detection of cerebral microbleeds: Effect of susceptibility-weighted imaging, section

thickness, and field strength. *AJNR Am J Neuroradiol*. 2009;30(2):338-343. doi:10.3174/ajnr.A1355.

220. Tong KA, Ashwal S, Holshouser BA, et al. Diffuse axonal injury in children: Clinical correlation with hemorrhagic lesions. *Ann Neurol*. 2004;56(1):36-50. doi:10.1002/ana.20123.

221. Wang S, Lou M, Liu T, Cui D, Chen X, Wang Y. Hematoma Volume Measurement in Gradient Echo MRI Using Quantitative Susceptibility Mapping. *Stroke*. 2013;44(8):2315-2317. doi:10.1161/STROKEAHA.113.001638.

222. Liu J, Xia S, Hanks RA, et al. Susceptibility Weighted Imaging and Mapping of Micro-hemorrhages and Major Deep Veins after Traumatic Brain Injury. *J Neurotrauma*. 2016;33(1):10-21. doi:10.1089/neu.2014.3856.

223. Liu T, Surapaneni K, Lou M, Cheng L, Spincemaille P, Wang Y. Cerebral microbleeds: burden assessment by using quantitative susceptibility mapping. *Radiology*. 2012;262(1):269-278. doi:10.1148/radiol.11110251.

224. Tan H, Liu T, Wu Y, et al. Evaluation of iron content in human cerebral cavernous malformation using quantitative susceptibility mapping. *Invest Radiol*. 2014;49(7):498-504. doi:10.1097/RLI.0000000000000043.

225. Haacke EM, Tang J, Neelavalli J, Cheng YCN. Susceptibility mapping as a means to visualize veins and quantify oxygen saturation. *J Magn Reson Imaging*. 2010;32(3):663-676. doi:10.1002/jmri.22276.

226. Fan AP, Bilgic B, Gagnon L, et al. Quantitative oxygenation venography from MRI phase. *Magn Reson Med*. 2014;72(1):149-159. doi:10.1002/mrm.24918.

227. Zhang J, Liu T, Gupta A, Spincemaille P, Nguyen TD, Wang Y. Quantitative mapping of cerebral metabolic rate of oxygen (CMRO2 ) using quantitative susceptibility mapping (QSM). *Magn Reson Med*. 2015;74(4):945-952. doi:10.1002/mrm.25463.

228. Fan AP, Evans KC, Stout JN, Rosen BR, Adalsteinsson E. Regional quantification of cerebral venous oxygenation from MRI susceptibility during hypercapnia. *Neuroimage*. 2015;104:146-155. doi:10.1016/j.neuroimage.2014.09.068.

229. Xia S, Utriainen D, Tang J, et al. Decreased oxygen saturation in asymmetrically prominent cortical veins in patients with cerebral ischemic stroke. *Magn Reson Imaging*. 2014;32(10):1272-1276. doi:10.1016/j.mri.2014.08.012.

230. Ogawa S, Lee TM, Kay AR, Tank DW. Brain magnetic resonance imaging with contrast dependent on blood oxygenation. *Proc Natl Acad Sci USA*. 1990;87(24):9868-9872. doi:10.1073/pnas.87.24.9868.

231. Balla DZ, Sanchez-Panchuelo RM, Wharton SJ, et al. Functional quantitative susceptibility mapping (fQSM). *Neuroimage*. 2014;100:112-124. doi:10.1016/j.neuroimage.2014.06.011.

232. Chen Z, Liu J, Calhoun VD. Susceptibility-based functional brain mapping by 3D deconvolution of an MR-phase activation map. *J Neurosci Methods*. 2013;216(1):33-42. doi:10.1016/j.jneumeth.2013.03.003.

233. Chen Z, Calhoun V. Intrinsic functional brain mapping in reconstructed 4D magnetic susceptibility (χ) data space. *J Neurosci Methods*. 2015;241:85-93. doi:10.1016/j.jneumeth.2014.12.014.

234. Sehgal V, Delproposto Z, Haddar D, et al. Susceptibility-weighted imaging to visualize blood products and improve tumor contrast in the study of brain masses. *J Magn Reson Imaging*. 2006;24(1):41-51. doi:10.1002/jmri.20598.

235. Li C, Ai B, Li Y, Qi H, Wu L. Susceptibility-weighted imaging in grading brain astrocytomas. *Eur J Radiol*. 2010;75(1):e81-e85. doi:10.1016/j.ejrad.2009.08.003.

236. Löbel U, Sedlacik J, Sabin ND, et al. Three-dimensional susceptibility-weighted imaging and two-dimensional T2*-weighted gradient-echo imaging of intratumoral hemorrhages in pediatric diffuse intrinsic pontine glioma. *Neuroradiology*. 2010;52(12):1167-1177. doi:10.1007/s00234-010-0771-9.

237. Radbruch A, Wiestler B, Kramp L, et al. Differentiation of glioblastoma and primary CNS lymphomas using susceptibility weighted imaging. *Eur J Radiol*. 2013;82(3):552-556. doi:10.1016/j.ejrad.2012.11.002.

238. Radbruch A, Graf M, Kramp L, et al. Differentiation of brain metastases by

percentagewise quantification of intratumoral-susceptibility-signals at 3 Tesla. *Eur J Radiol*. 2012;81(12):4064-4068. doi:10.1016/j.ejrad.2012.06.016.

239. Deistung A, Schweser F, Wiestler B, et al. Quantitative Susceptibility Mapping Differentiates between Blood Depositions and Calcifications in Patients with Glioblastoma. *PLoS One*. 2013;8(3):e57924. doi:10.1371/journal.pone.0057924.

240. Fatemi-Ardekani A, Boylan C, Noseworthy MD. Identification of breast calcification using magnetic resonance imaging. *Med Phys*. 2009;36(12):5429-5436. doi:10.1118/1.3250860.

241. Dimov A V., Liu T, Spincemaille P, et al. Joint estimation of chemical shift and quantitative susceptibility mapping (chemical QSM). *Magn Reson Med*. 2015;73(6):2100-2110. doi:10.1002/mrm.25328.

242. Straub S, Laun FB, Emmerich J, et al. Potential of quantitative susceptibility mapping for detection of prostatic calcifications. *J Magn Reson Imaging*. 2017;45(3):889-898. doi:10.1002/jmri.25385.

243. Straub S, Emmerich J, Schlemmer HP, et al. Mask-Adapted Background Field Removal for Artifact Reduction in Quantitative Susceptibility Mapping of the Prostate. *TOMOGRAPHY*. 2017;3(2):96-100. doi:10.18383/j.tom.2017.00005.

244. Feier D, Balassy C, Bastati N, Fragner R, Wrba F, Ba-Ssalamah A. The diagnostic efficacy of quantitative liver MR imaging with diffusion-weighted, SWI, and hepato-specific contrast-enhanced sequences in staging liver fibrosis—a multiparametric approach. *Eur Radiol*. 2016;26(2):539-546. doi:10.1007/s00330-015-3830-0.

245. Balassy C, Feier D, Peck-Radosavljevic M, et al. Susceptibility-weighted MR imaging in the grading of liver fibrosis: a feasibility study. *Radiology*. 2014;270(1):149-158. doi:10.1148/radiol.13122440.

246. Dai Y, Zeng M, Li R, et al. Improving detection of siderotic nodules in cirrhotic liver with a multi-breath-hold susceptibility-weighted imaging technique. *J Magn Reson Imaging*. 2011;34(2):318-325. doi:10.1002/jmri.22607.

247. Sharma SD, Hernando D, Horng DE, Reeder SB. Quantitative susceptibility

mapping in the abdomen as an imaging biomarker of hepatic iron overload. *Magn Reson Med*. 2015;74(3):673-683. doi:10.1002/mrm.25448.

248. Sharma SD, Fischer R, Schoennagel BP, et al. MRI-based quantitative susceptibility mapping (QSM) and R2* mapping of liver iron overload: Comparison with SQUID-based biomagnetic liver susceptometry. *Magn Reson Med*. 2017;78(1):264-270. doi:10.1002/mrm.26358.

249. Bonekamp D, Barker PB, Leigh R, Van Zijl PCM, Li X. Susceptibility-based analysis of dynamic gadolinium bolus perfusion MRI. *Magn Reson Med*. 2015;73(2):544-554. doi:10.1002/mrm.25144.

250. Xu B, Spincemaille P, Liu T, et al. Quantification of cerebral perfusion using dynamic quantitative susceptibility mapping. *Magn Reson Med*. 2015;73(4):1540-1548. doi:10.1002/mrm.25257.

251. Klohs J, Deistung A, Ielacqua GD, et al. Quantitative assessment of microvasculopathy in arcAβ mice with USPIO-enhanced gradient echo MRI. *J Cereb Blood Flow Metab*. 2016;36(9):1614-1624. doi:10.1177/0271678X15621500.

252. Wong R, Chen X, Wang Y, Hu X, Jin MM. Visualizing and quantifying acute inflammation using ICAM-1 specific nanoparticles and MRI quantitative susceptibility mapping. *Ann Biomed Eng*. 2012;40(6):1328-1338. doi:10.1007/s10439-011-0482-3.

253. Deistung A, Schweser F, Reichenbach JR. Overview of quantitative susceptibility mapping. *NMR Biomed*. 2017;30(4):e3569. doi:10.1002/nbm.3569.

254. Haacke EM, Liu S, Buch S, Zheng W, Wu D, Ye Y. Quantitative susceptibility mapping: Current status and future directions. *Magn Reson Imaging*. 2015;33(1):1-25. doi:10.1016/j.mri.2014.09.004.

255. Bernstein MA, Grgic M, Brosnan TJ, Pelc NJ. Reconstructions of phase contrast, phased array multicoil data. *Magn Reson Med*. 1994;32(3):330-334. doi:10.1002/mrm.1910320308.

256. Hammond KE, Lupo JM, Xu D, et al. Development of a robust method for

generating 7.0 T multichannel phase images of the brain with application to normal volunteers and patients with neurological diseases. *Neuroimage*. 2008;39(4):1682-1692. doi:10.1016/j.neuroimage.2007.10.037.

257. Pruessmann KP, Weiger M, Scheidegger MB, Boesiger P. SENSE: Sensitivity encoding for fast MRI. *Magn Reson Med*. 1999;42(5):952-962. doi:10.1002/(SICI)1522-2594(199911)42:5<952::AID-MRM16>3.0.CO;2-S.

258. Kressler B, de Rochefort L, Tian Liu, Spincemaille P, Quan Jiang, Yi Wang. Nonlinear Regularization for Per Voxel Estimation of Magnetic Susceptibility Distributions From MRI Field Maps. *IEEE Trans Med Imaging*. 2010;29(2):273-281. doi:10.1109/TMI.2009.2023787.

259. De Rochefort L, Brown R, Prince MR, Wang Y. Quantitative MR susceptibility mapping using piece-wise constant regularized inversion of the magnetic field. *Magn Reson Med*. 2008;60(4):1003-1009. doi:10.1002/mrm.21710.

260. Liu T, Wisnieff C, Lou M, Chen W, Spincemaille P, Wang Y. Nonlinear formulation of the magnetic field to source relationship for robust quantitative susceptibility mapping. *Magn Reson Med*. 2013;69(2):467-476. doi:10.1002/mrm.24272.

261. Reeder SB, Wen Z, Yu H, et al. Multicoil Dixon chemical species separation with an iterative least-squares estimation method. *Magn Reson Med*. 2004;51(1):35-45. doi:10.1002/mrm.10675.

262. Yu H, McKenzie CA, Shimakawa A, et al. Multiecho reconstruction for simultaneous water-fat decomposition and T2* estimation. *J Magn Reson Imaging*. 2007;26(4):1153-1161. doi:10.1002/jmri.21090.

263. Dong J, Liu T, Chen F, et al. Simultaneous phase unwrapping and removal of chemical shift (SPURS) using graph cuts: Application in quantitative susceptibility mapping. *IEEE Trans Med Imaging*. 2015;34(2):531-540. doi:10.1109/TMI.2014.2361764.

264. Simchick G, Liu Z, Nagy T, Xiong M, Zhao Q. Assessment of MR-based R2* and quantitative susceptibility mapping for the quantification of liver iron concentration in a mouse model at 7T. *Magn Reson Med*. 2018;80(5):2081-

2093. doi:10.1002/mrm.27173.

265. Lin H, Wei H, He N, et al. Quantitative susceptibility mapping in combination with water-fat separation for simultaneous liver iron and fat fraction quantification. *Eur Radiol*. 2018;28(8):3494-3504. doi:10.1007/s00330-017-5263-4.

266. Guo Y, Liu Z, Wen Y, et al. Quantitative susceptibility mapping of the spine using in-phase echoes to initialize inhomogeneous field and R2* for the nonconvex optimization problem of fat-water separation. *NMR Biomed*. 2019;32(11):e4156. doi:10.1002/nbm.4156.

267. Diefenbach MN, Meineke J, Ruschke S, Baum T, Gersing A, Karampinos DC. On the sensitivity of quantitative susceptibility mapping for measuring trabecular bone density. *Magn Reson Med*. 2019;81(3):1739-1754. doi:10.1002/mrm.27531.

268. Robinson SD, Bredies K, Khabipova D, Dymerska B, Marques JP, Schweser F. An illustrated comparison of processing methods for MR phase imaging and QSM: combining array coil signals and phase unwrapping. *NMR Biomed*. 2017;30(4):e3601. doi:10.1002/nbm.3601.

269. Wei Xu, Cumming I. A region-growing algorithm for InSAR phase unwrapping. *IEEE Trans Geosci Remote Sens*. 1999;37(1):124-134. doi:10.1109/36.739143.

270. Witoszynskyj S, Rauscher A, Reichenbach JR, Barth M. Phase unwrapping of MR images using ΦUN – A fast and robust region growing algorithm. *Med Image Anal*. 2009;13(2):257-268. doi:10.1016/j.media.2008.10.004.

271. Sun H, Kate M, Gioia LC, Emery DJ, Butcher K, Wilman AH. Quantitative susceptibility mapping using a superposed dipole inversion method: Application to intracranial hemorrhage. *Magn Reson Med*. 2016;76(3):781-791. doi:10.1002/mrm.25919.

272. Smith SM. Fast robust automated brain extraction. *Hum Brain Mapp*. 2002;17(3):143-155. doi:10.1002/hbm.10062.

273. Schweser F, Robinson SD, de Rochefort L, Li W, Bredies K. An illustrated

comparison of processing methods for phase MRI and QSM: removal of background field contributions from sources outside the region of interest. *NMR Biomed*. 2017;30(4):e3604. doi:10.1002/nbm.3604.

274. Liu T, Spincemaille P, De Rochefort L, Kressler B, Wang Y. Calculation of susceptibility through multiple orientation sampling (COSMOS): A method for conditioning the inverse problem from measured magnetic field map to susceptibility source image in MRI. *Magn Reson Med*. 2009;61(1):196-204. doi:10.1002/mrm.21828.

275. Shmueli K, de Zwart JA, van Gelderen P, Li T-Q, Dodd SJ, Duyn JH. Magnetic susceptibility mapping of brain tissue in vivo using MRI phase data. *Magn Reson Med*. 2009;62(6):1510-1522. doi:10.1002/mrm.22135.

276. Neelavalli J, Cheng YCN, Jiang J, Haacke EM. Removing background phase variations in susceptibility-weighted imaging using a fast, forward-field calculation. *J Magn Reson Imaging*. 2009;29(4):937-948. doi:10.1002/jmri.21693.

277. Li L, Leigh JS. High-precision mapping of the magnetic field utilizing the harmonic function mean value property. *J Magn Reson*. 2001;148(2):442-448. doi:10.1006/jmre.2000.2267.

278. Schweser F, Deistung A, Lehr BW, Reichenbach JR. Quantitative imaging of intrinsic magnetic tissue properties using MRI signal phase: An approach to in vivo brain iron metabolism? *Neuroimage*. 2011;54(4):2789-2807. doi:10.1016/j.neuroimage.2010.10.070.

279. Sun H, Wilman AH. Background field removal using spherical mean value filtering and Tikhonov regularization. *Magn Reson Med*. 2014;71(3):1151-1157. doi:10.1002/mrm.24765.

280. Wu B, Li W, Guidon A, Liu C. Whole brain susceptibility mapping using compressed sensing. *Magn Reson Med*. 2012;67(1):137-147. doi:10.1002/mrm.23000.

281. De Rochefort L, Liu T, Kressler B, et al. Quantitative susceptibility map reconstruction from MR phase data using bayesian regularization: Validation

and application to brain imaging. *Magn Reson Med*. 2010;63(1):194-206. doi:10.1002/mrm.22187.

282. Wharton S, Schäfer A, Bowtell R. Susceptibility mapping in the human brain using threshold-based k-space division. *Magn Reson Med*. 2010;63(5):1292-1304. doi:10.1002/mrm.22334.

283. Schweser F, Deistung A, Sommer K, Reichenbach JR. Toward online reconstruction of quantitative susceptibility maps: Superfast dipole inversion. *Magn Reson Med*. 2013;69(6):1582-1594. doi:10.1002/mrm.24405.

284. Kee Y, Liu Z, Zhou L, et al. Quantitative Susceptibility Mapping (QSM) Algorithms: Mathematical Rationale and Computational Implementations. *IEEE Trans Biomed Eng*. 2017;64(11):2531-2545. doi:10.1109/TBME.2017.2749298.

285. Zhou L, Choi JK, Kee Y, Wang Y, Seo JK. Dipole Incompatibility Related Artifacts in Quantitative Susceptibility Mapping. *arXiv [Preprint] arXiv:1701.05457*. January 2017. http://arxiv.org/abs/1701.05457.

286. Liu T, Liu J, De Rochefort L, et al. Morphology enabled dipole inversion (MEDI) from a single-angle acquisition: Comparison with COSMOS in human brain imaging. *Magn Reson Med*. 2011;66(3):777-783. doi:10.1002/mrm.22816.

287. Liu J, Liu T, De Rochefort L, et al. Morphology enabled dipole inversion for quantitative susceptibility mapping using structural consistency between the magnitude image and the susceptibility map. *Neuroimage*. 2012;59(3):2560-2568. doi:10.1016/j.neuroimage.2011.08.082.

288. Liu T, Xu W, Spincemaille P, Avestimehr AS, Wang Y. Accuracy of the morphology enabled dipole inversion (MEDI) algorithm for quantitative susceptibility mapping in MRI. *IEEE Trans Med Imaging*. 2012;31(3):816-824. doi:10.1109/TMI.2011.2182523.

289. Koch KM, Papademetris X, Rothman DL, Graaf RA de. Rapid calculations of susceptibility-induced magnetostatic field perturbations for in vivo magnetic resonance. *Phys Med Biol*. 2006;51(24):6381-6402. doi:10.1088/0031-9155/51/24/007.

290. Jordan CD, Daniel BL, Koch KM, Yu H, Conolly S, Hargreaves BA. Subject-specific models of susceptibility-induced B 0 field variations in breast MRI. *J Magn Reson Imaging*. 2013;37(1):227-232. doi:10.1002/jmri.23762.

291. Sheikh-Bahaei N, Manavaki R, Sajjadi SA, Priest AN, O'Brien JT, Gillard JH. Correlation of Lobar Cerebral Microbleeds with Amyloid, Perfusion, and Metabolism in Alzheimer's Disease. *J Alzheimer's Dis*. 2019;68(4):1489-1497. doi:10.3233/JAD-180443.

292. Ruetten PPR, Usman A, Priest AN, Gillard JH, Graves MJ. Calcification and USPIO detection in Carotid Artery Plaque using QSM and SWI. In: *Proceedings of the 27th Annual Meeting of ISMRM*. ; 2019:2090.

293. Howarth SPS, Li Z-Y, Tang TY, Graves MJ, U-King-Im JM, Gillard JH. In Vivo Positive Contrast IRON Sequence and Quantitative T2* Measurement Confirms Inflammatory Burden in a Patient with Asymptomatic Carotid Atheroma after USPIO-enhanced MR Imaging. *J Vasc Interv Radiol*. 2008;19(3):446-448. doi:10.1016/j.jvir.2007.11.019.

294. Chavhan GB, Babyn PS, Thomas B, Shroff MM, Haacke EM. Principles, Techniques, and Applications of T2*-based MR Imaging and Its Special Applications. *RadioGraphics*. 2009;29(5):1433-1449. doi:10.1148/rg.295095034.

295. Liu S, Brisset J-C, Hu J, Haacke EM, Ge Y. Susceptibility weighted imaging and quantitative susceptibility mapping of the cerebral vasculature using ferumoxytol. *J Magn Reson Imaging*. 2018;47(3):621-633. doi:10.1002/jmri.25809.

296. Yang Q, Liu J, Li K, Dai Y, Haacke M, Jerecic R. Visualization of carotid plaque calcification - a novel approach using susceptibility weighted MR imaging. *J Cardiovasc Magn Reson*. 2010;12(Suppl 1):O66. doi:10.1186/1532-429X-12-S1-O66.

297. Yang Q, Liu J, Barnes SRS, et al. Imaging the vessel wall in major peripheral arteries using susceptibility-weighted imaging. *J Magn Reson Imaging*. 2009;30(2):357-365. doi:10.1002/jmri.21859.

298. Nörenberg D, Ebersberger HU, Walter T, et al. Diagnosis of Calcific Tendonitis of the Rotator Cuff by Using Susceptibility-weighted MR Imaging. *Radiology*. 2016;278(2):475-484. doi:10.1148/radiol.2015150034.

299. Adams LC, Böker SM, Bender YY, et al. Detection of vessel wall calcifications in vertebral arteries using susceptibility weighted imaging. *Neuroradiology*. 2017;59(9):861-872. doi:10.1007/s00234-017-1878-z.

300. Bender YY, Böker SM, Diederichs G, et al. MRI for the detection of calcific features of vertebral haemangioma. *Clin Radiol*. 2017;72(8):692.e1-692.e7. doi:10.1016/j.crad.2017.02.018.

301. Borrelli P, Palma G, Tedeschi E, et al. Improving Signal-to-Noise Ratio in Susceptibility Weighted Imaging: A Novel Multicomponent Non-Local Approach. *PLoS One*. 2015;10(6):e0126835. doi:10.1371/journal.pone.0126835.

302. Liu Q, Fan Z, Yang Q, Li D. Peripheral Arterial Wall Imaging Using Contrast-Enhanced, Susceptibility-Weighted Phase Imaging. *J Comput Assist Tomogr*. 2012;36(1):77-82. doi:10.1097/RCT.0b013e3182388cdf.

303. Ji JX, Son JB, Rane SD. PULSAR: A Matlab toolbox for parallel magnetic resonance imaging using array coils and multiple channel receivers. *Concepts Magn Reson Part B Magn Reson Eng*. 2007;31B(1):24-36. doi:10.1002/cmr.b.20081.

304. Yuan J, Graves MJ, Patterson AJ, et al. The development and optimisation of 3D black-blood R2* mapping of the carotid artery wall. *Magn Reson Imaging*. 2017;44:104-110. doi:10.1016/j.mri.2017.08.006.

305. Ruetten PPR, Cluroe AD, Usman A, Priest AN, Gillard JH, Graves MJ. Simultaneous MRI water-fat separation and quantitative susceptibility mapping of carotid artery plaque pre- and post-ultrasmall superparamagnetic iron oxide-uptake. *Magn Reson Med*. 2020;84(2):686-697. doi:10.1002/mrm.28151.

306. Ruetten PPR, Graves MJ, Yuan J, Gillard JH. Quantitative Susceptibility Mapping of the Carotid Artery Wall using IDEAL. In: *Proceedings of the 34th Annual Scientific Meeting of ESMRMB*. ; 2017:20.

307. Ruetten PPR, Graves MJ, Yuan J, Gillard JH. Quantitative Susceptibility Mapping of the Carotid Artery Walls. In: *Proceedings of the MRC Symposium*. ; 2017.

308. Ruetten PPR, Priest AN, Yuan J, Usman A, Gillard JH, Graves MJ. Phase Corrected Bipolar Acquisition for Simultaneous Water-Fat Separation and Quantitative Susceptibility Mapping of the Carotid Artery Wall. In: *Proceedings of the 26th Annual Meeting of ISMRM*. ; 2018:2194.

309. Ruetten PPR, Gillard JH, Graves MJ. Simultaneous Water-Fat Separation and Quantitative Susceptibility Mapping of the Carotid Artery Wall: Sequence and Processing Considerations. In: *Proceedings of the 30th Annual International Conference SMRA*. ; 2018:A52.

310. Ikebe Y, Ishimaru H, Imai H, et al. Quantitative Susceptibility Mapping for Carotid Atherosclerotic Plaques: A Pilot Study. *Magn Reson Med Sci*. 2020;19(2):135-140. doi:10.2463/mrms.mp.2018-0077.

311. Ruetten PPR, Cluroe AD, Usman A, Gillard JH, Graves MJ. Plaque feature analysis using a joint method of QSM and water-fat separation. In: *Proceedings of the 27th Annual Meeting of ISMRM*. ; 2019:2091.

312. Wang C, Liu S, Buch S, et al. Quantitative Susceptibility Mapping of Atherosclerosis in Carotid Arteries. In: *Proceedings of the 24th Annual Meeting of ISMRM*. ; 2016:2552.

313. Wang C. Quantitative susceptibility mapping of atherosclerosis in carotid arteries. Master's thesis, McMaster University. 2017.

314. Szczepaniak LS, Dobbins RL, Stein DT, McGarry JD. Bulk magnetic susceptibility effects on the assessment of intra- and extramyocellular lipids in vivo. *Magn Reson Med*. 2002;47(3):607-610. doi:10.1002/mrm.10086.

315. Ruetten PPR, Cluroe AD, Usman A, Gillard JH, Graves MJ. Identification of USPIO-uptake in calcified Atherosclerotic Plaques. In: *Proceedings of the 36th Annual Scientific Meeting of ESMRMB*. ; 2019:S13.04.

316. Koppal S, Warntjes M, Swann J, et al. Quantitative fat and R2* mapping in vivo to measure lipid-rich necrotic core and intraplaque hemorrhage in carotid

atherosclerosis. *Magn Reson Med*. 2017;78(1):285-296. doi:10.1002/mrm.26359.

317. Li J, Chang S, Liu T, et al. Phase-corrected bipolar gradients in multi-echo gradient-echo sequences for quantitative susceptibility mapping. *Magn Reson Mater Physics, Biol Med*. 2015;28(4):347-355. doi:10.1007/s10334-014-0470-3.

318. Liu J, Christiansen SD, Drangova M. Single multi-echo GRE acquisition with short and long echo spacing for simultaneous quantitative mapping of fat fraction, B0 inhomogeneity, and susceptibility. *Neuroimage*. 2018;172:703-717. doi:10.1016/j.neuroimage.2018.02.012.

319. Lu W, Yu H, Shimakawa A, Alley M, Reeder SB, Hargreaves BA. Water-fat separation with bipolar multiecho sequences. *Magn Reson Med*. 2008;60(1):198-209. doi:10.1002/mrm.21583.

320. Yushkevich PA, Piven J, Hazlett HC, et al. User-guided 3D active contour segmentation of anatomical structures: Significantly improved efficiency and reliability. *Neuroimage*. 2006;31(3):1116-1128. doi:10.1016/j.neuroimage.2006.01.015.

321. Straub S, Schneider TM, Emmerich J, et al. Suitable reference tissues for quantitative susceptibility mapping of the brain. *Magn Reson Med*. 2017;78(1):204-214. doi:10.1002/mrm.26369.

322. Liu Z, Kee Y, Zhou D, Wang Y, Spincemaille P. Preconditioned total field inversion (TFI) method for quantitative susceptibility mapping. *Magn Reson Med*. 2017;78(1):303-315. doi:10.1002/mrm.26331.

323. Karampinos DC, Yu H, Shimakawa A, Link TM, Majumdar S. Chemical shift-based water/fat separation in the presence of susceptibility-induced fat resonance shift. *Magn Reson Med*. 2012;68(5):1495-1505. doi:10.1002/mrm.24157.

324. Yu H, Reeder SB, Shimakawa A, McKenzie CA, Brittain JH. Robust multipoint water-fat separation using fat likelihood analysis. *Magn Reson Med*. 2012;67(4):1065-1076. doi:10.1002/mrm.23087.

325. Yu H, Reeder SB, Shimakawa A, Brittain JH, Pelc NJ. Field map estimation with a region growing scheme for iterative 3-point water-fat decomposition. *Magn Reson Med*. 2005;54(4):1032-1039. doi:10.1002/mrm.20654.

326. Yu H, Shimakawa A, McKenzie CA, et al. A multi-echo acquisition method with reduced echo spacing for robust IDEAL water-fat decomposition at 3T. In: *Proceedings of the 15th Annual Meeting of ISMRM*. ; 2007:3353.

327. Azuma M, Maekawa K, Yamashita A, et al. Characterization of Carotid Plaque Components by Quantitative Susceptibility Mapping. *AJNR Am J Neuroradiol*. 2020;41(2):310-317. doi:10.3174/ajnr.A6374.

328. UK government. Ferumoxytol (Rienso) intravenous iron no longer available for use. https://www.gov.uk/drug-safety-update/ferumoxytol-rienso-intravenous-iron-no-longer-available-for-use. Published 2015.

329. Clarke SE, Hammond RR, Mitchell JR, Rutt BK. Quantitative assessment of carotid plaque composition using multicontrast MRI and registered histology. *Magn Reson Med*. 2003;50(6):1199-1208. doi:10.1002/mrm.10618.

330. Cai J, Hatsukami TS, Ferguson MS, et al. In vivo quantitative measurement of intact fibrous cap and lipid-rich necrotic core size in atherosclerotic carotid plaque: Comparison of high-resolution, contrast-enhanced magnetic resonance imaging and histology. *Circulation*. 2005;112(22):3437-3444. doi:10.1161/CIRCULATIONAHA.104.528174.

331. Yuan J, Wiesinger F, Ruetten P, et al. Head and Neck Vascular Calcification Imaging using Zero Echo Time. In: *Proceedings of the 26th Annual Meeting of ISMRM*. ; 2018:3467.

332. Wiesinger F, Sacolick LI, Menini A, et al. Zero TE MR Bone Imaging in the Head. *Magn Reson Med*. 2016;75(1):107-114. doi:10.1002/mrm.25545.

333. Yu H, Shimakawa A, McKenzie CA, Brodsky E, Brittain JH, Reeder SB. Multi-Echo water-fat separation and simultaneous R 2* estimation with multifrequency fat spectrum modeling. *Magn Reson Med*. 2008;60(5):1122-1134. doi:10.1002/mrm.21737.

334. Yu H, Shimakawa A, McKenzie CA, et al. Phase and amplitude correction for

multi-echo water-fat separation with bipolar acquisitions. *J Magn Reson Imaging*. 2010;31(5):1264-1271. doi:10.1002/jmri.22111.

# Appendix A

The remaining susceptibility maps from the volunteer scans presented in chapter 5.

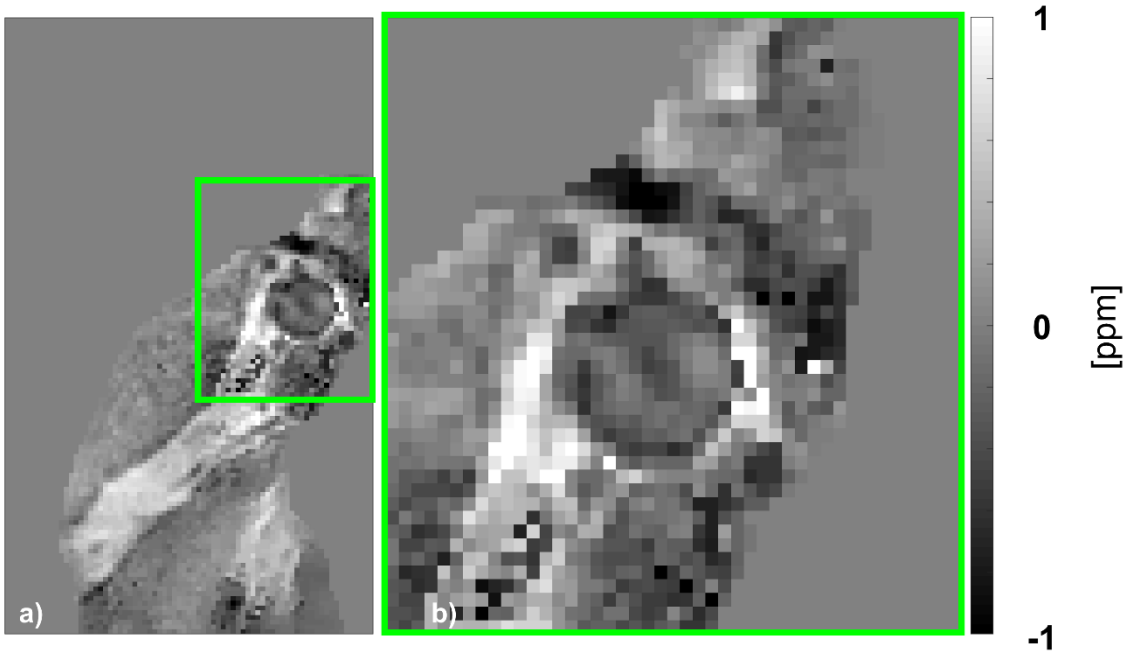


*Figure 1: Susceptibility map of a healthy volunteer*

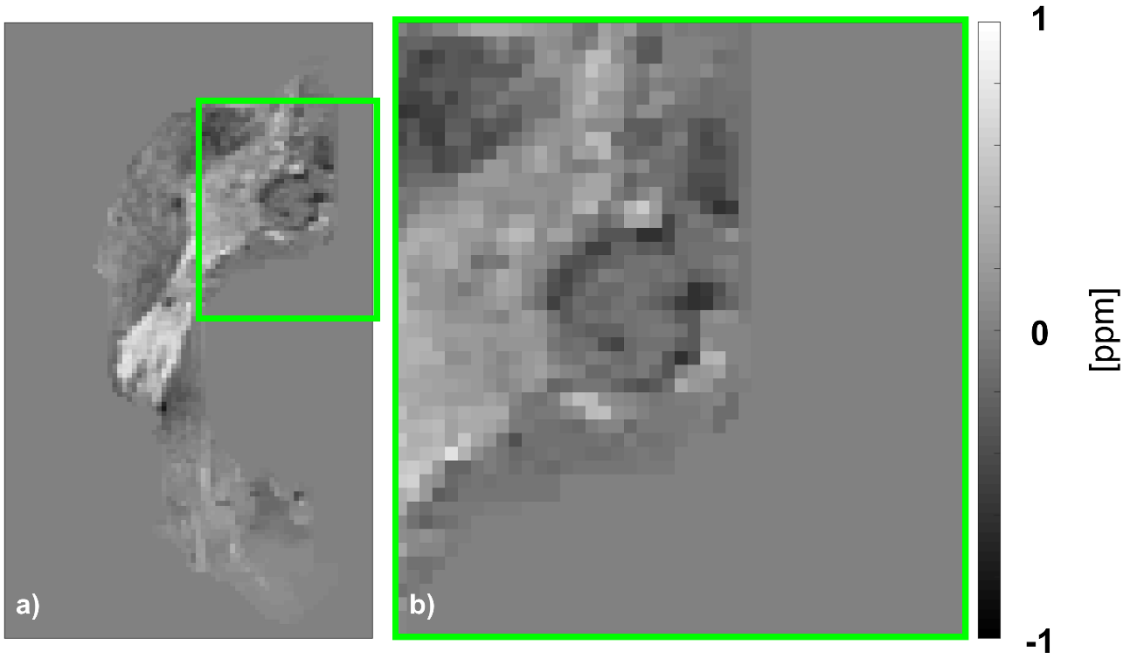


*Figure 2: Susceptibility map of a healthy volunteer*

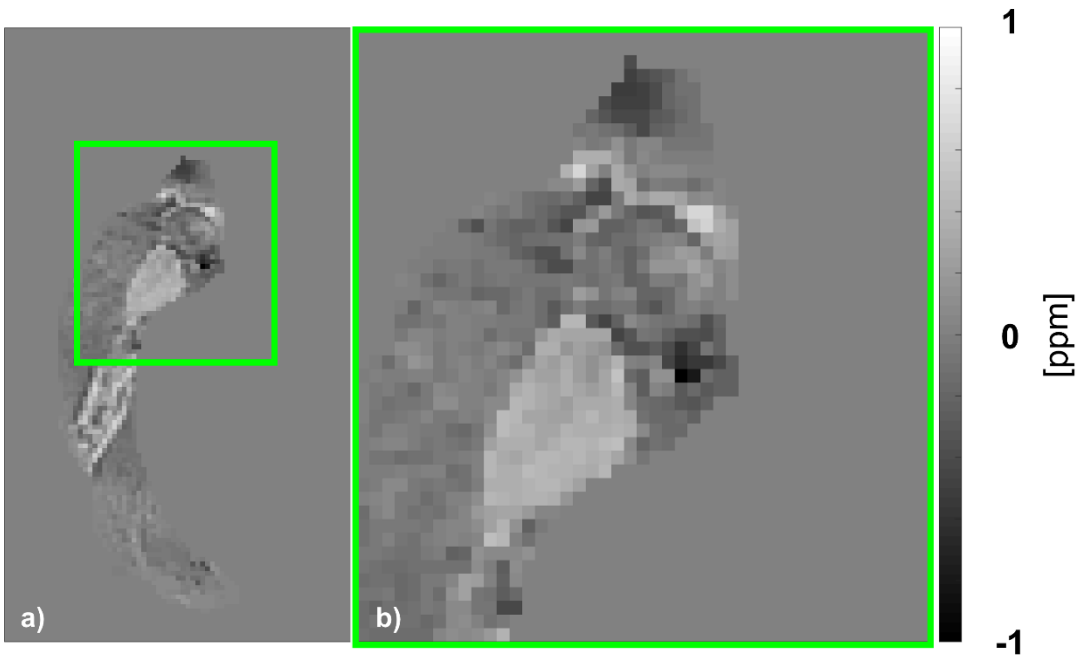


*Figure 3: Susceptibility map of a healthy volunteer*

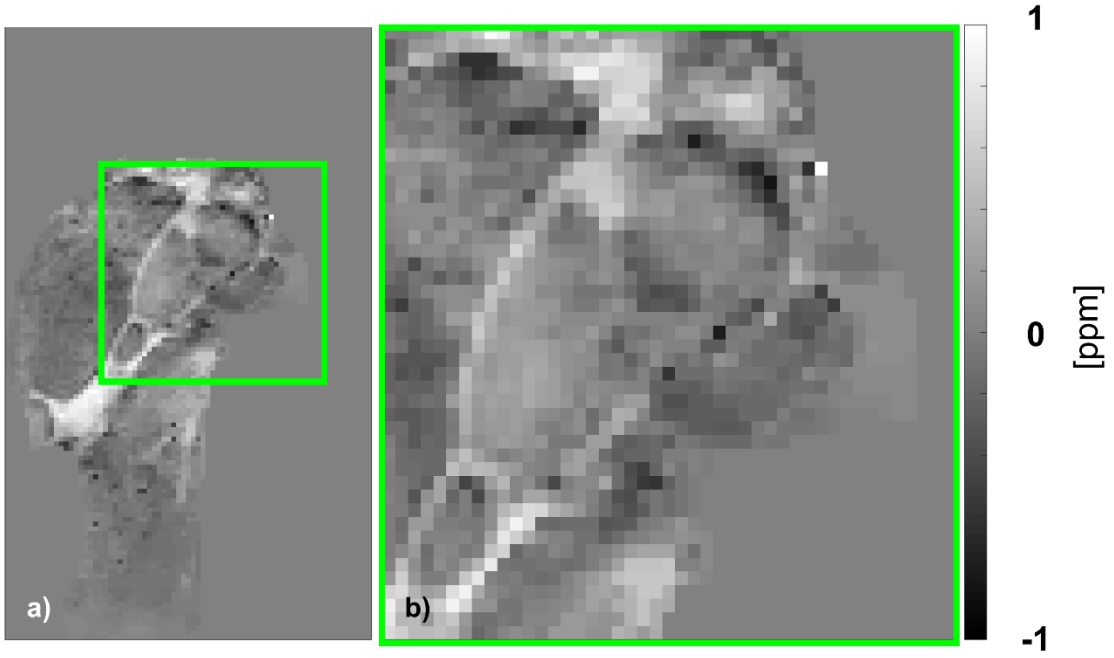


*Figure 4: Susceptibility map of a healthy volunteer*

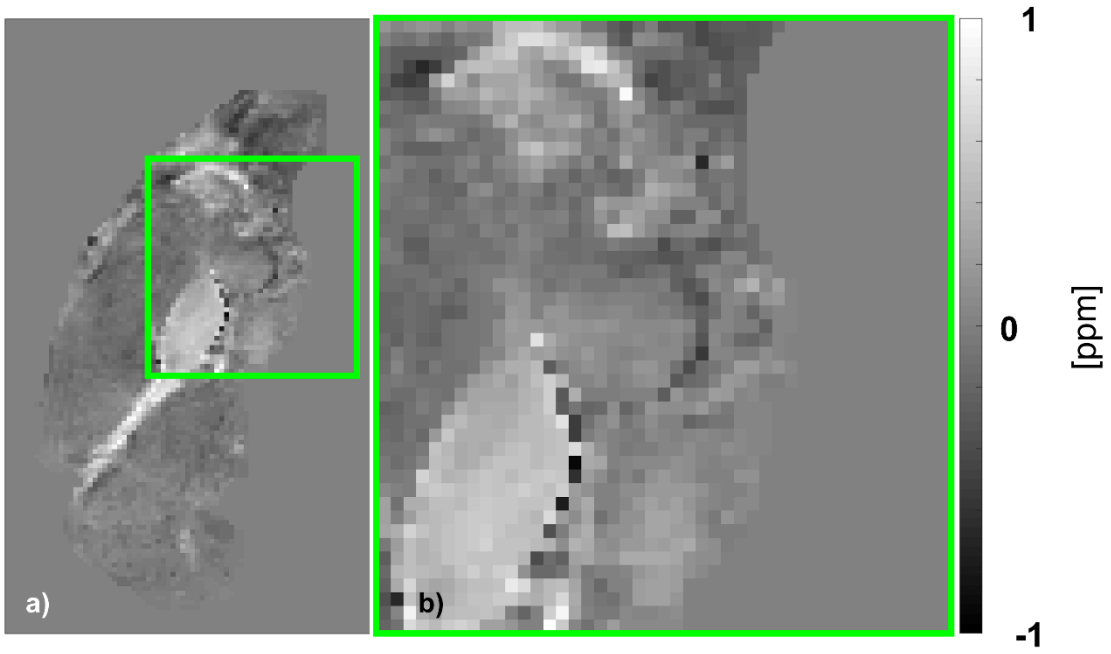


*Figure 5: Susceptibility map of a healthy volunteer*

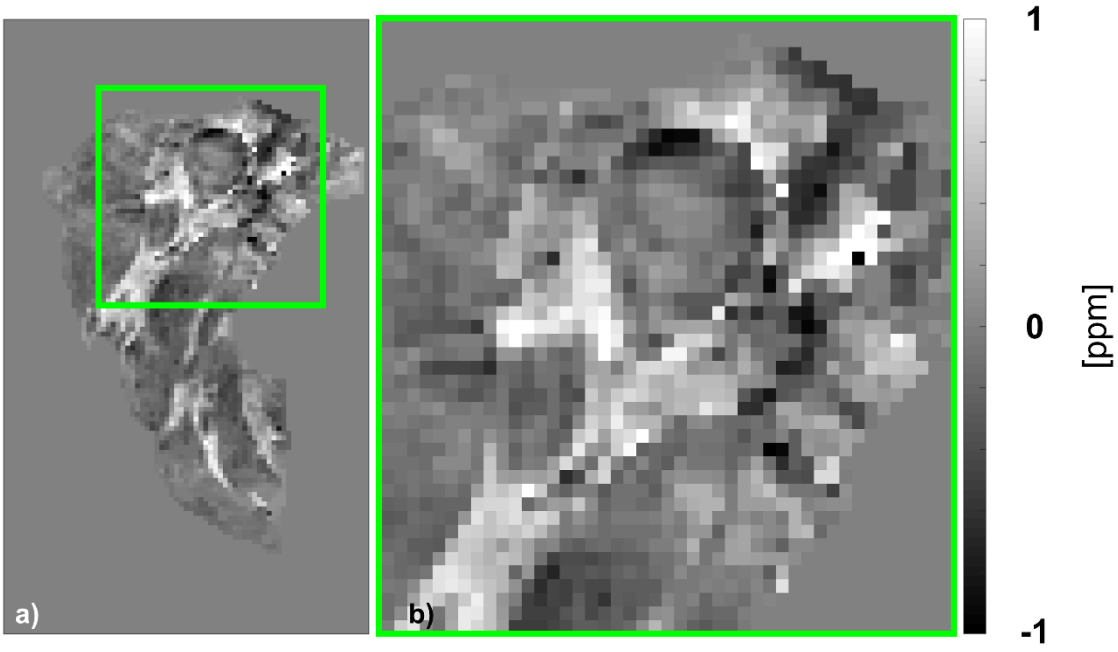


*Figure 6: Susceptibility map of a healthy volunteer*

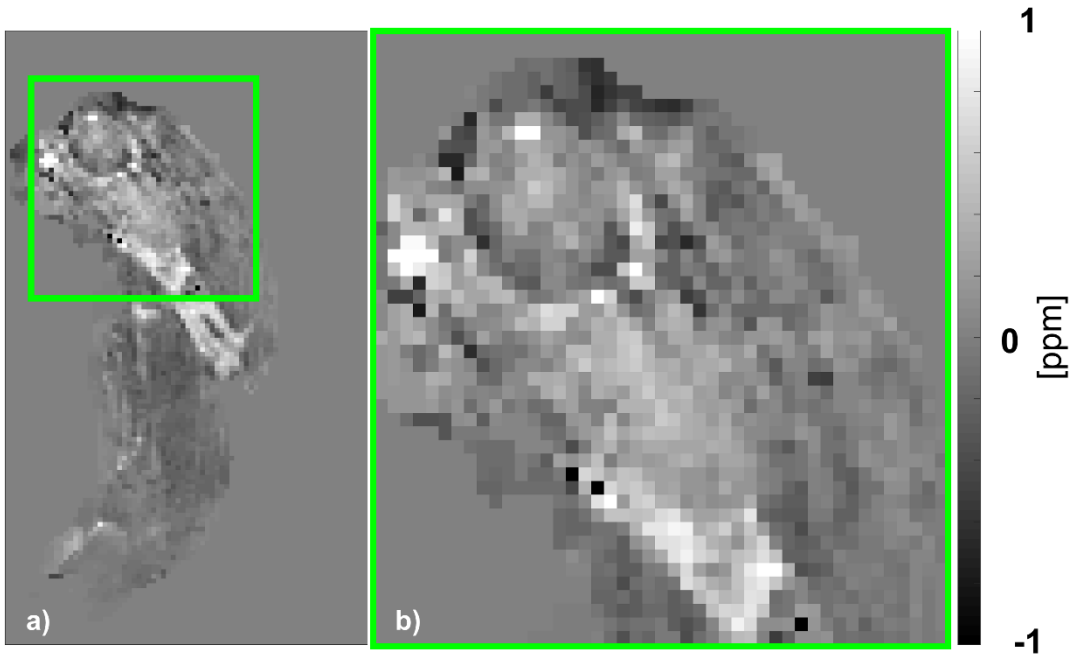


*Figure 7: Susceptibility map of a healthy volunteer*

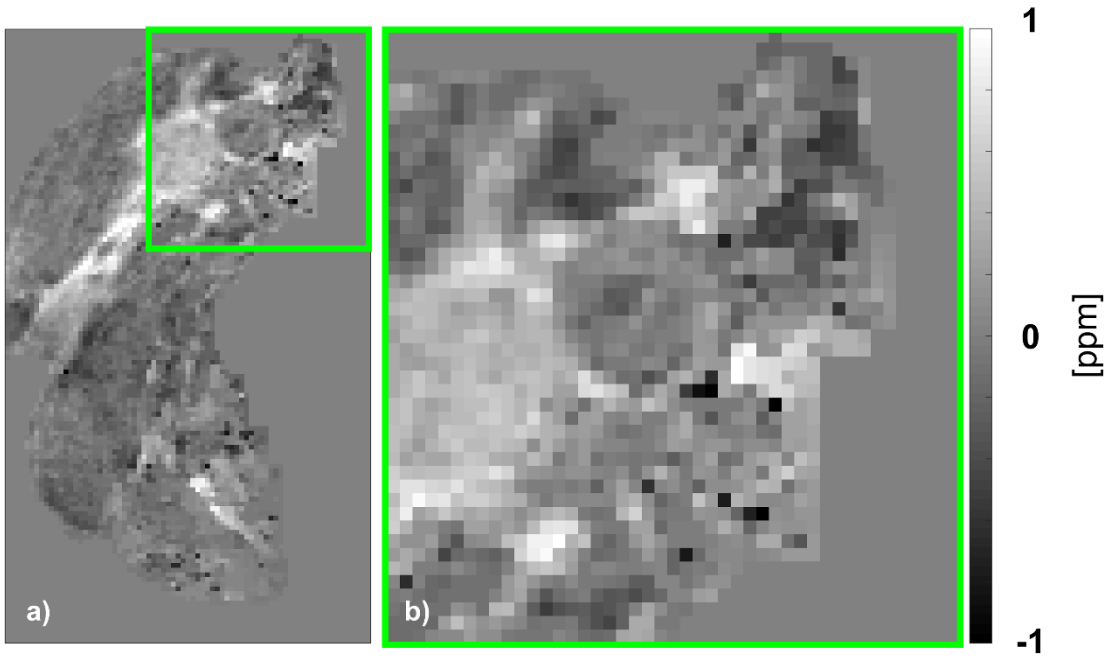


*Figure 8: Susceptibility map of a healthy volunteer*

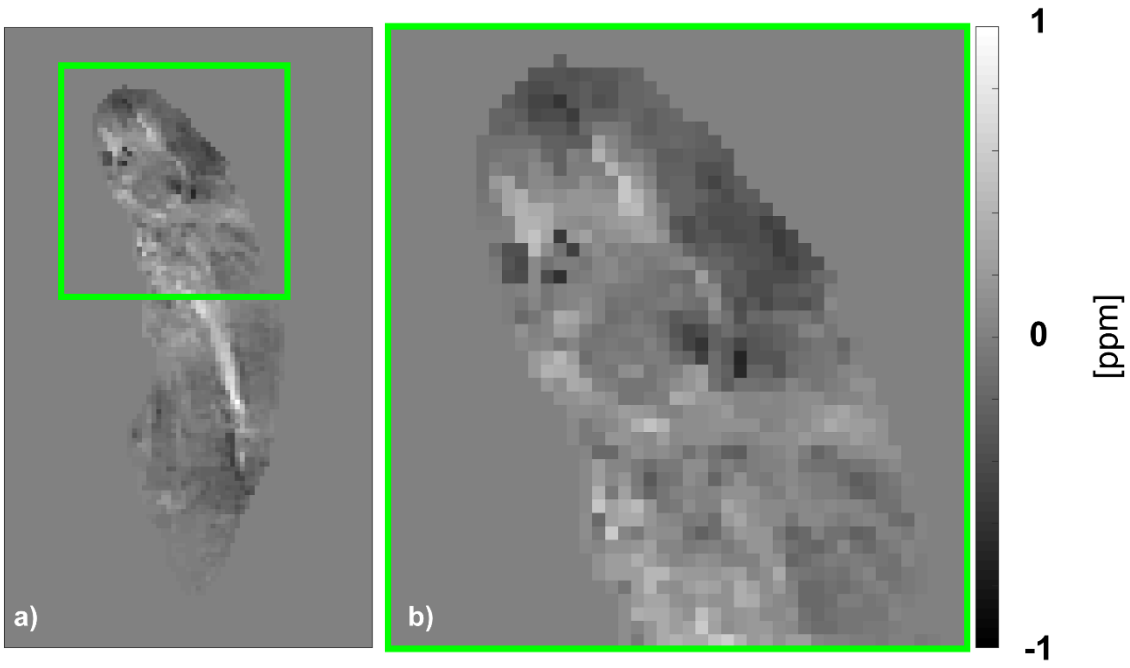


*Figure 9: Susceptibility map of a healthy volunteer*

# Appendix B

The remaining susceptibility maps from the volunteer scans presented in chapter 6 using bipolar readouts.

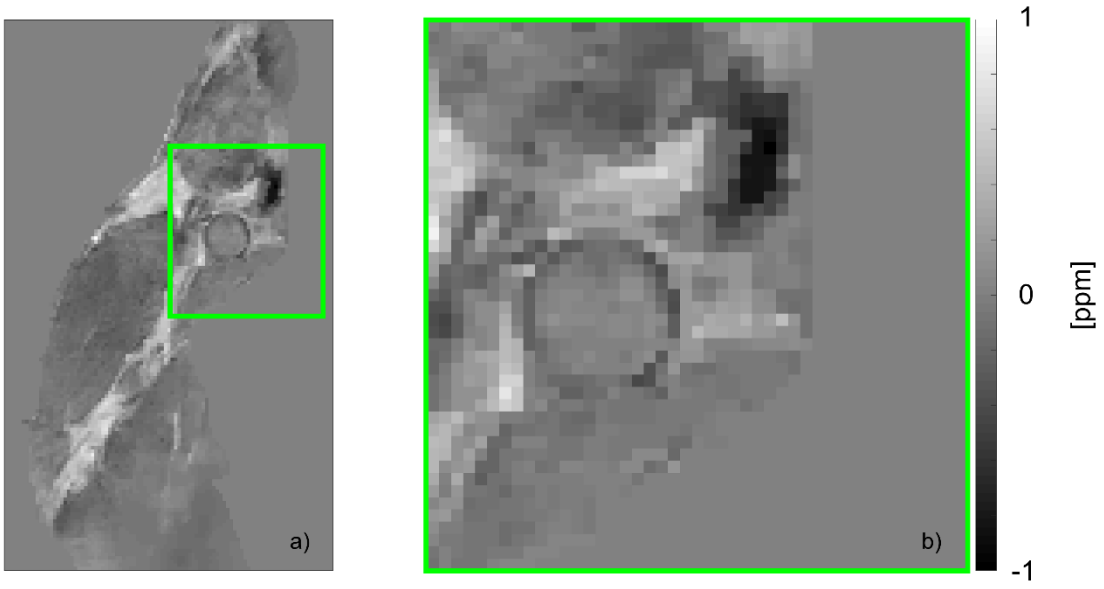


*Figure 1: Susceptibility map of a healthy volunteer*

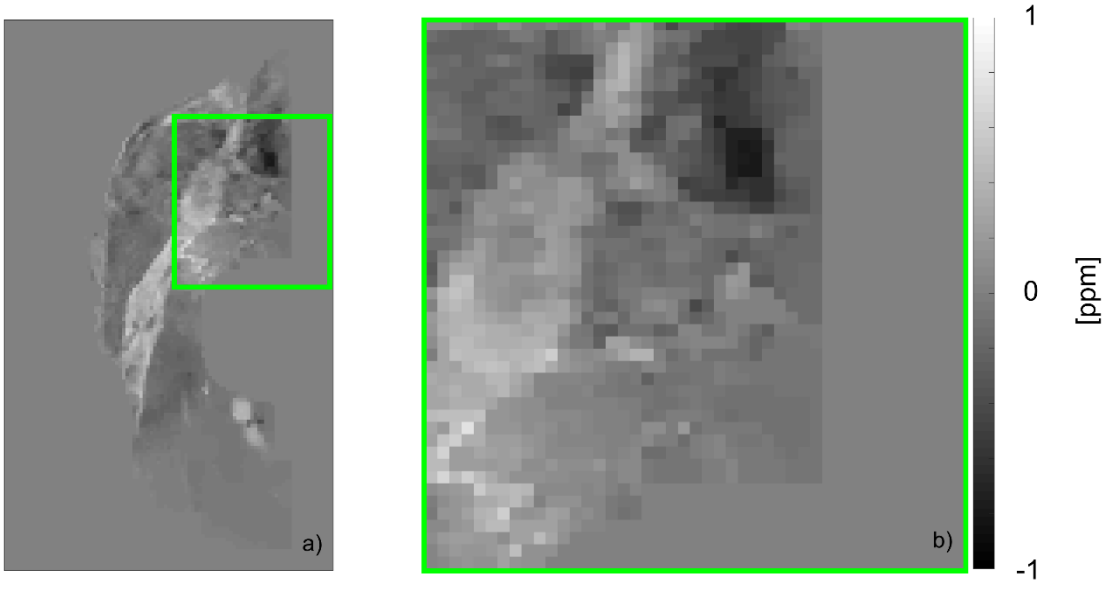


*Figure 2: Susceptibility map of a healthy volunteer*

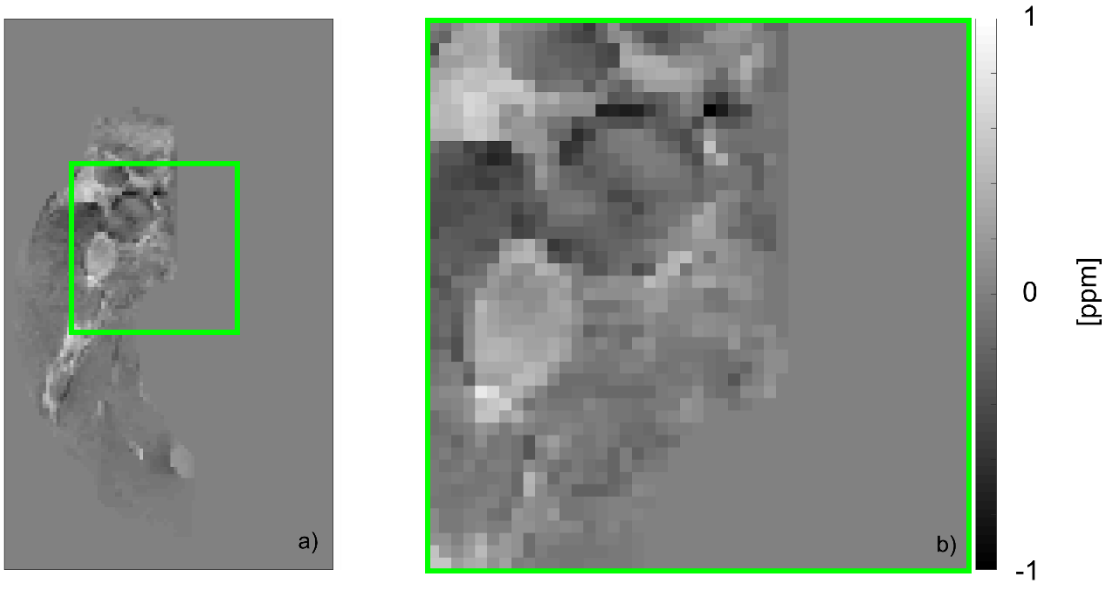


*Figure 3: Susceptibility map of a healthy volunteer*

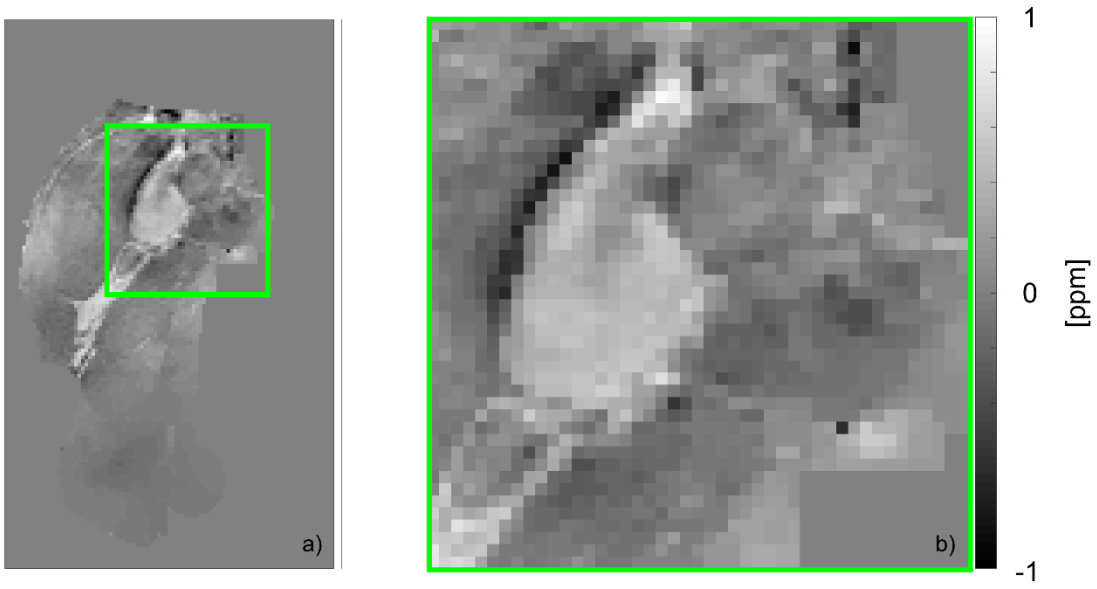


*Figure 4: Susceptibility map of a healthy volunteer*

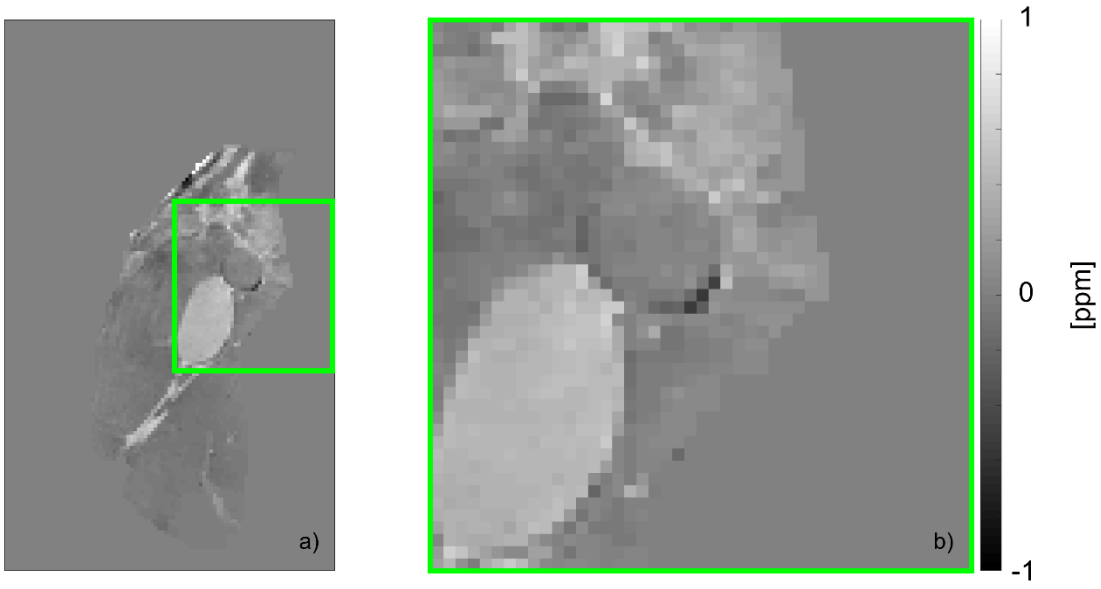


*Figure 5: Susceptibility map of a healthy volunteer*

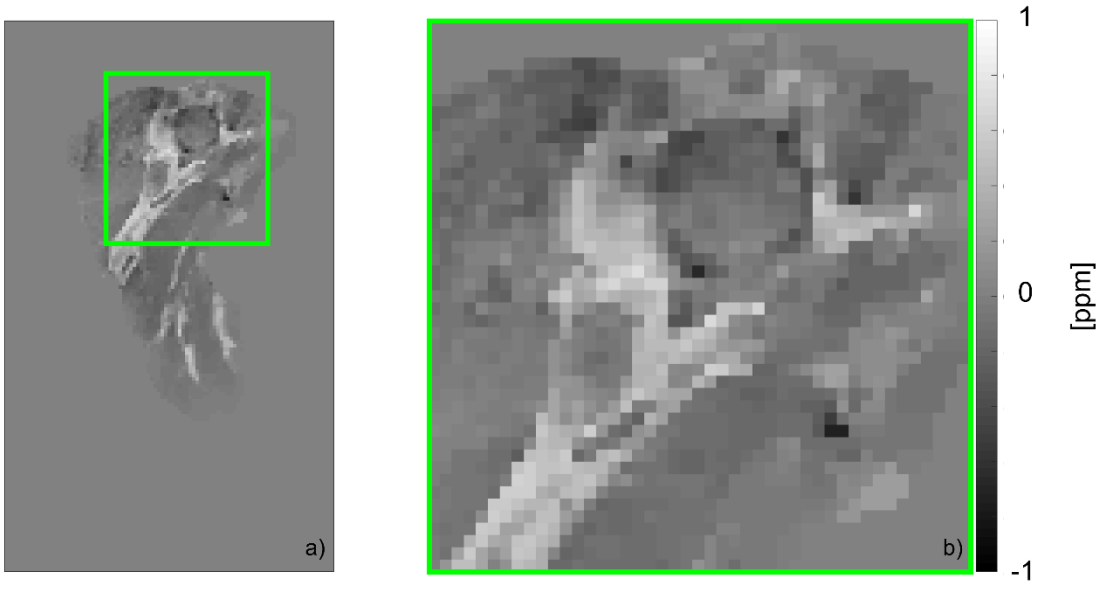


*Figure 6: Susceptibility map of a healthy volunteer*

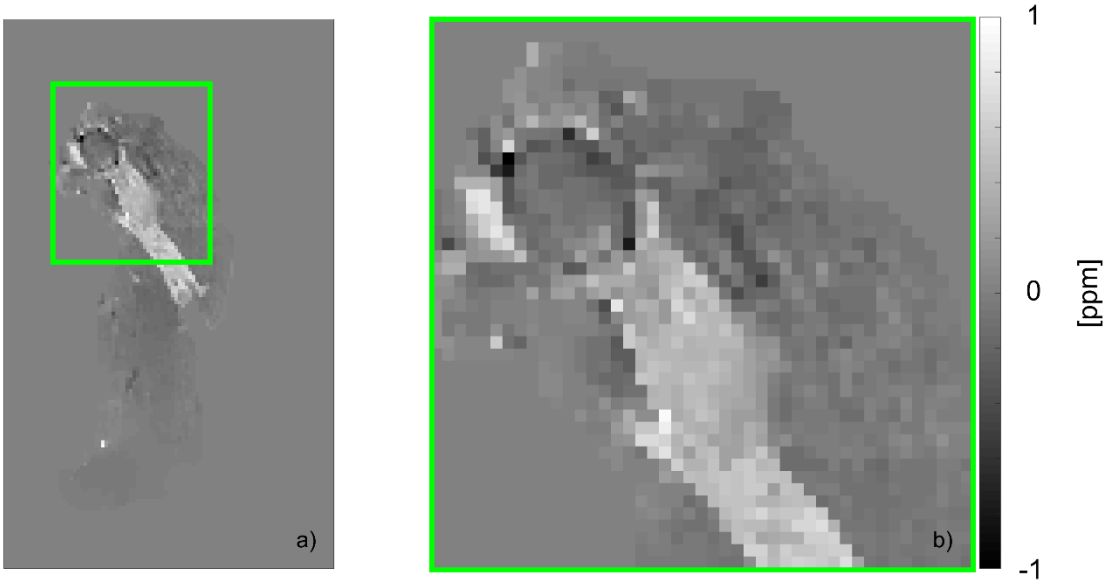


*Figure 7: Susceptibility map of a healthy volunteer*

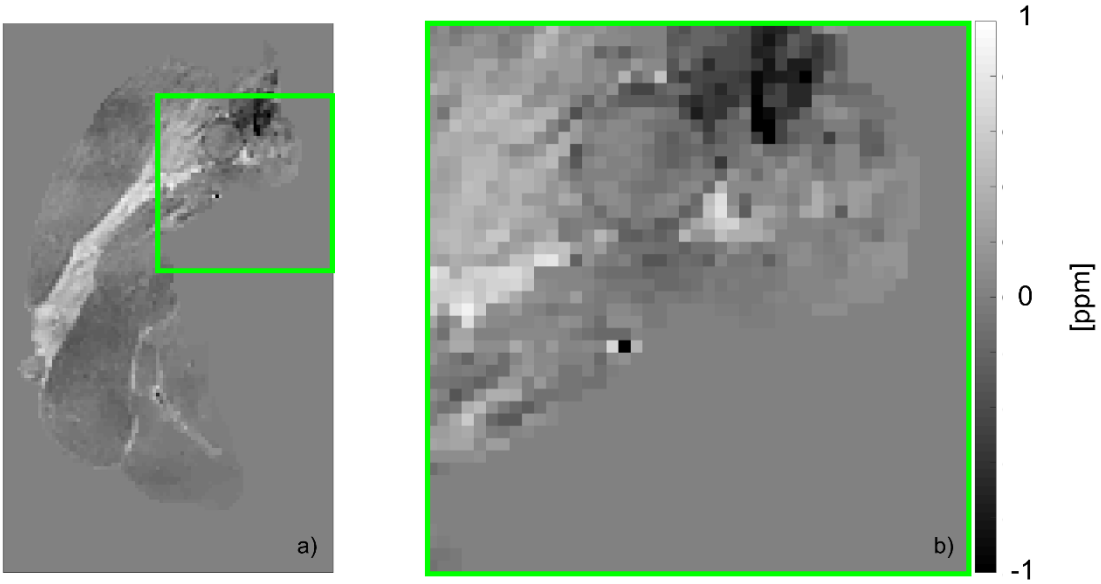


*Figure 8: Susceptibility map of a healthy volunteer*

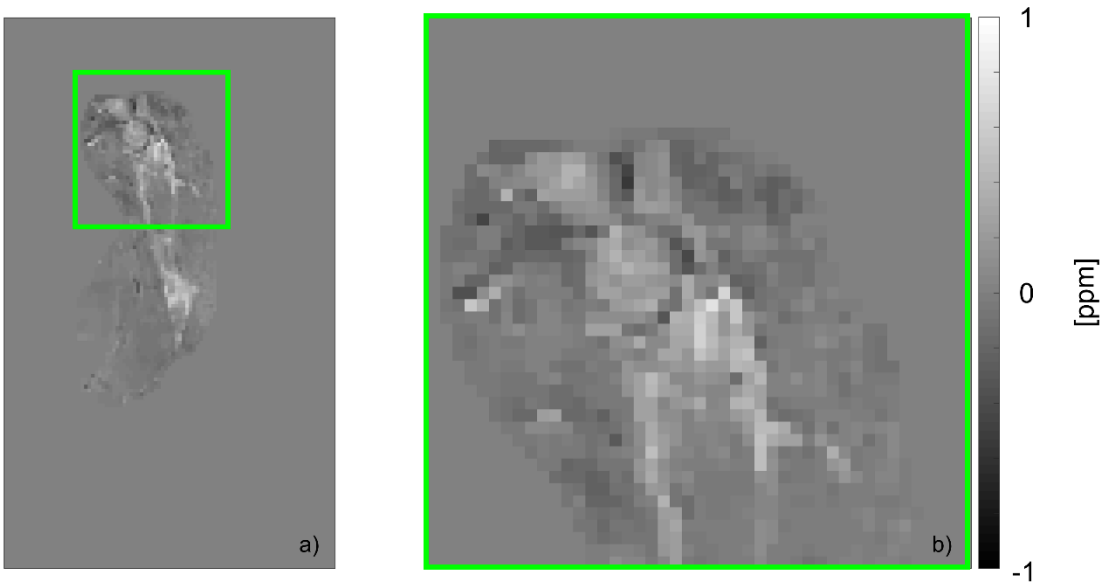


*Figure 9: Susceptibility map of a healthy volunteer*

# Appendix C

The remaining susceptibility maps from the patient scans presented in chapter 6:

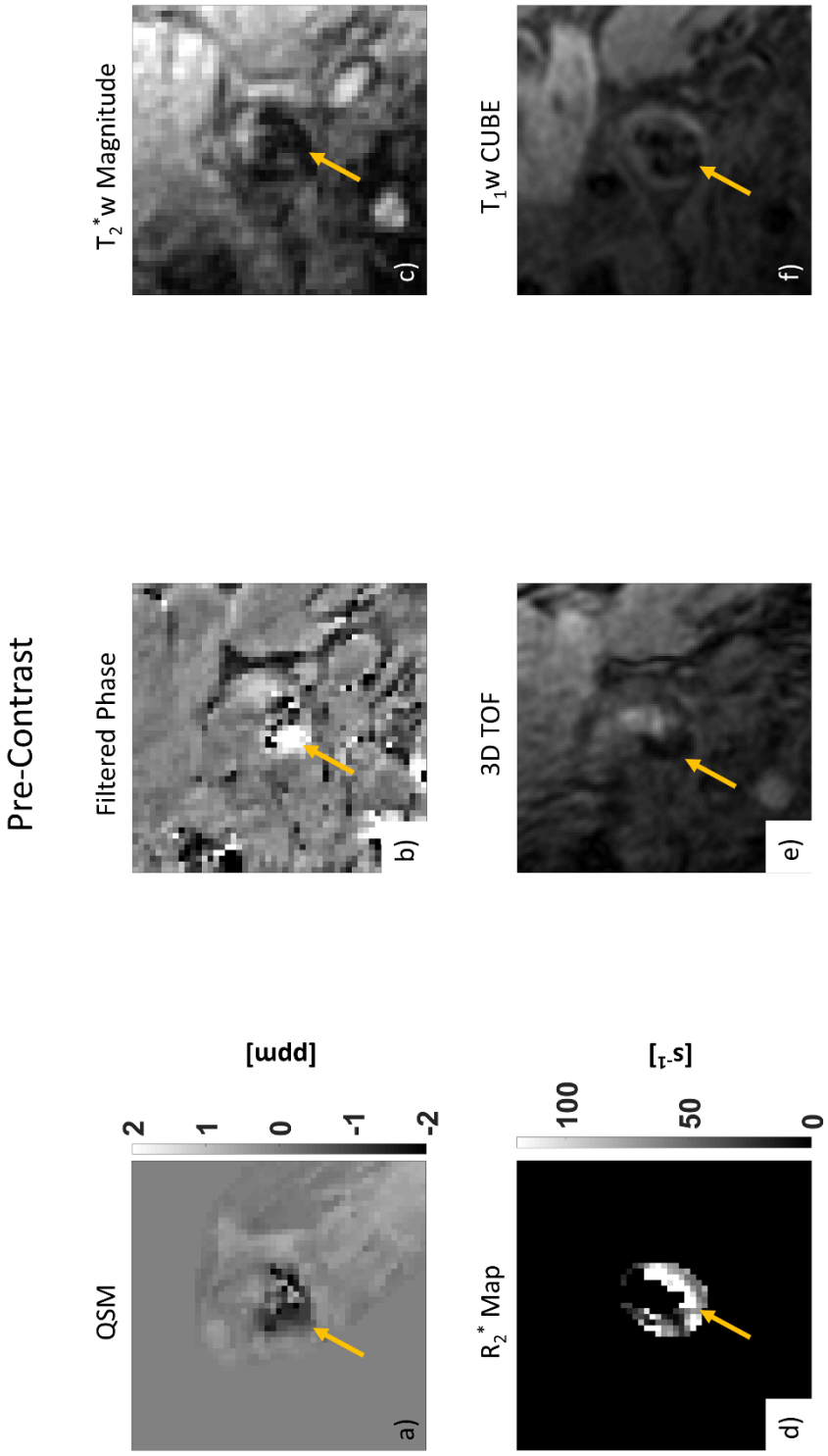

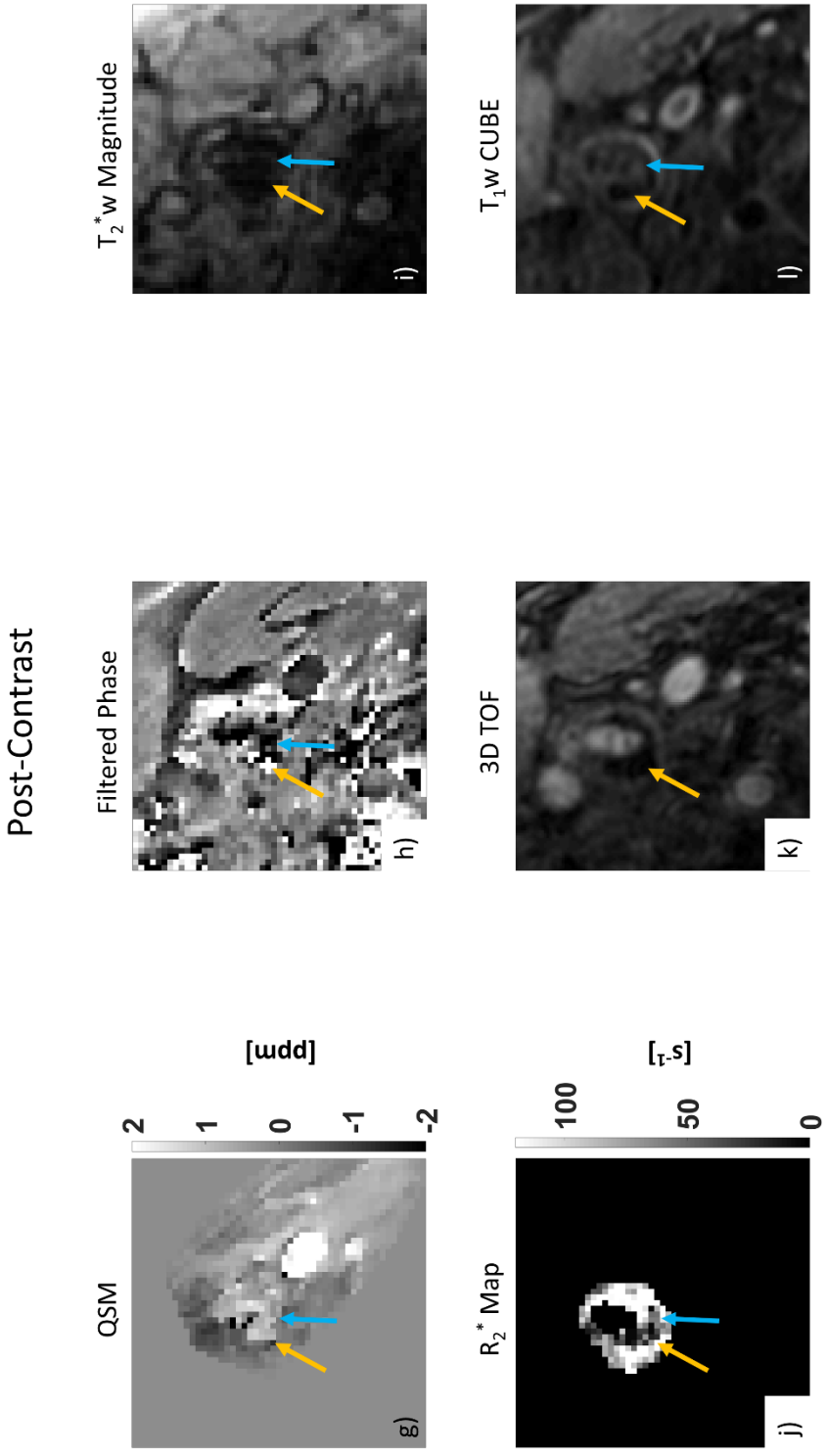


*Figure 1: Pre- and post-contrast QSM of a patient with a carotid artery plaque (calcification is indicated by the yellow arrow, USPIO-uptake by the blue arrow)*

Post-Contrast

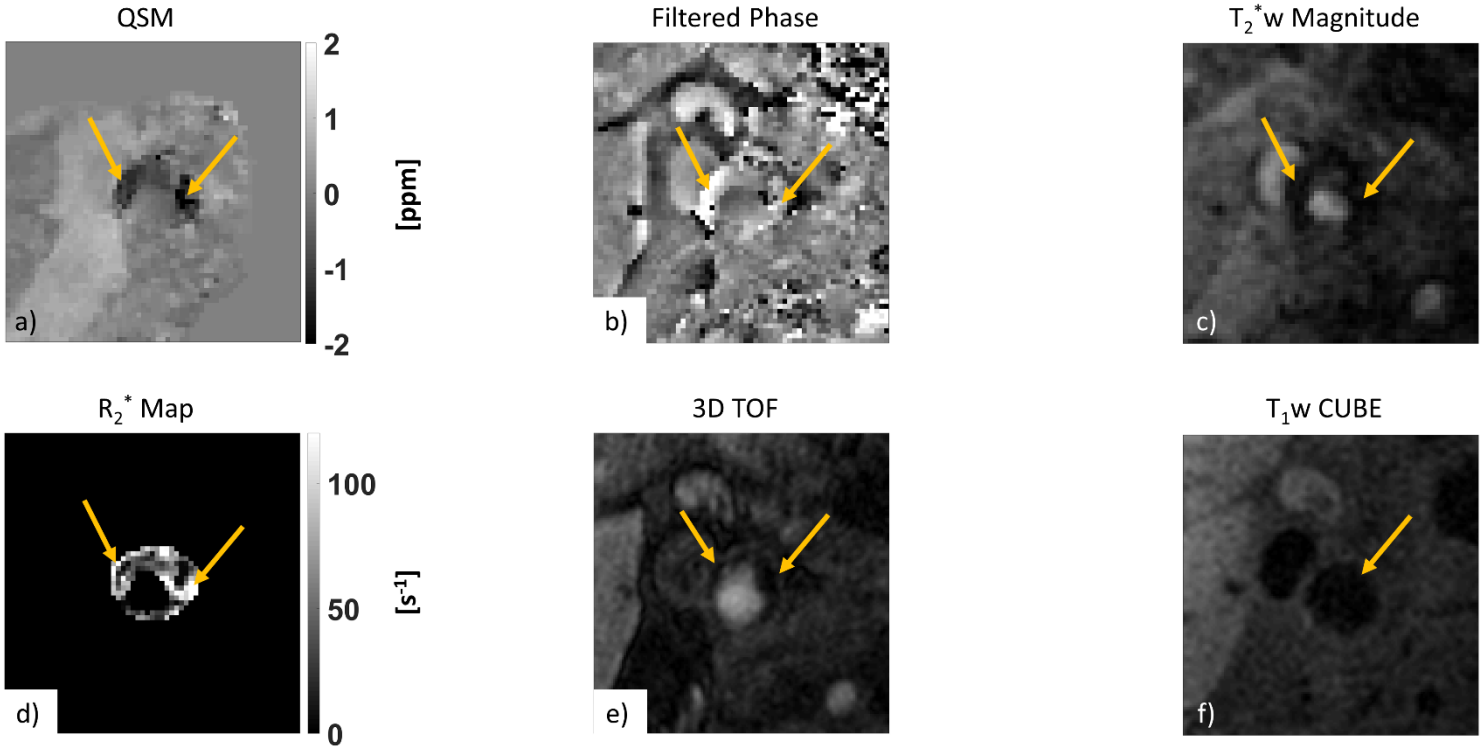

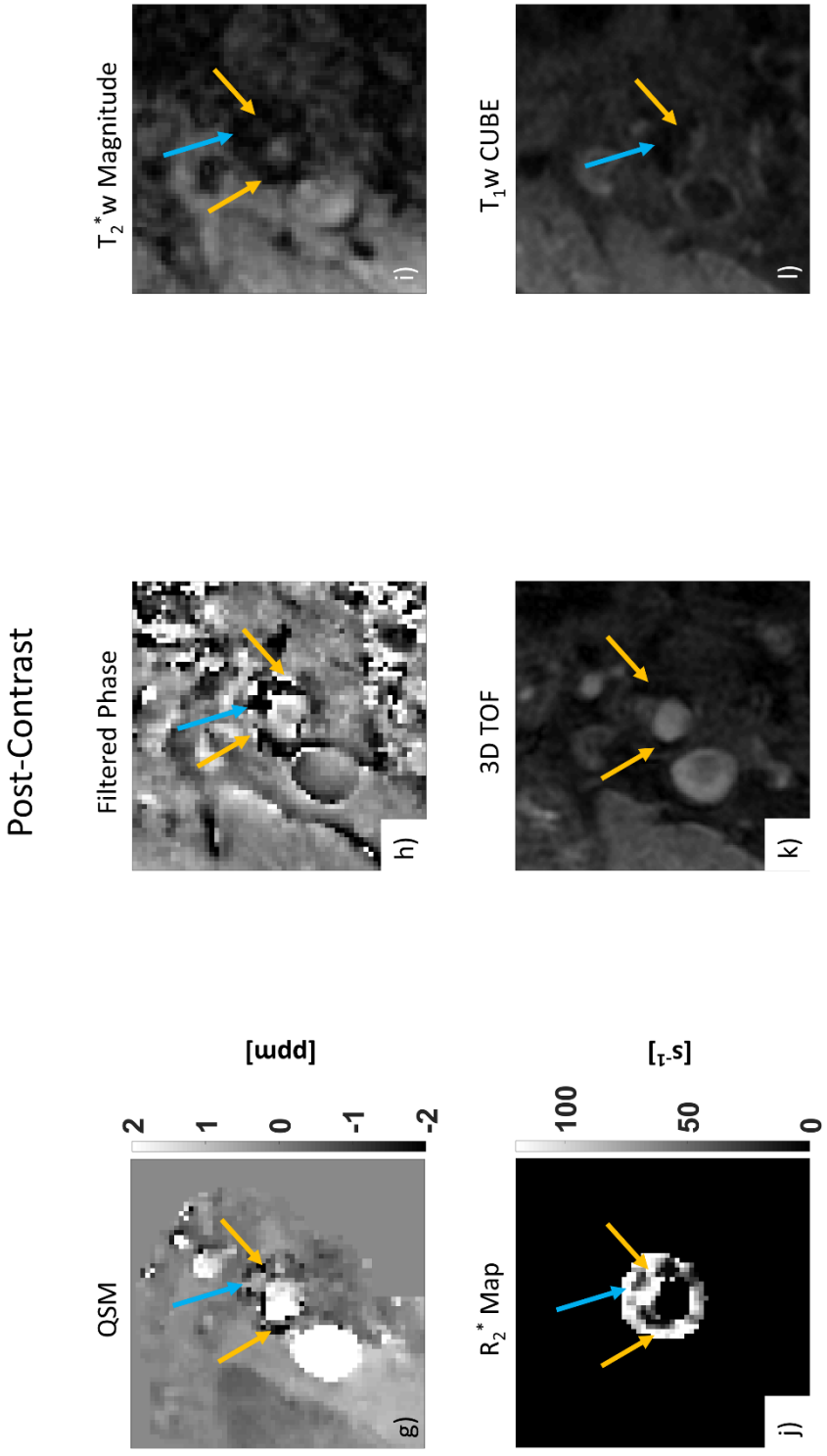


*Figure 2: Pre- and post-contrast QSM of a patient with a carotid artery plaque (calcification is indicated by the yellow arrow, USPIO-uptake by the blue arrow)*

Pre-Contrast

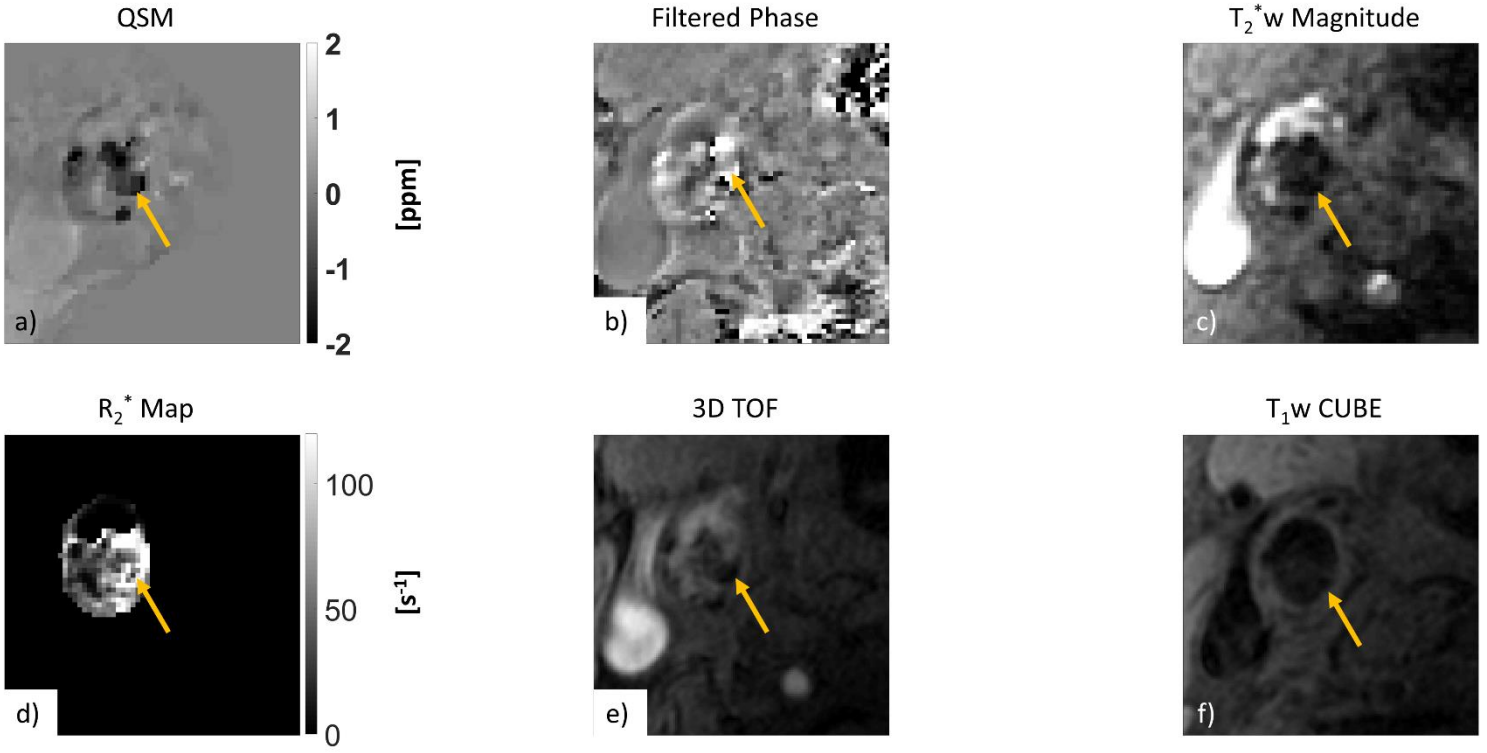

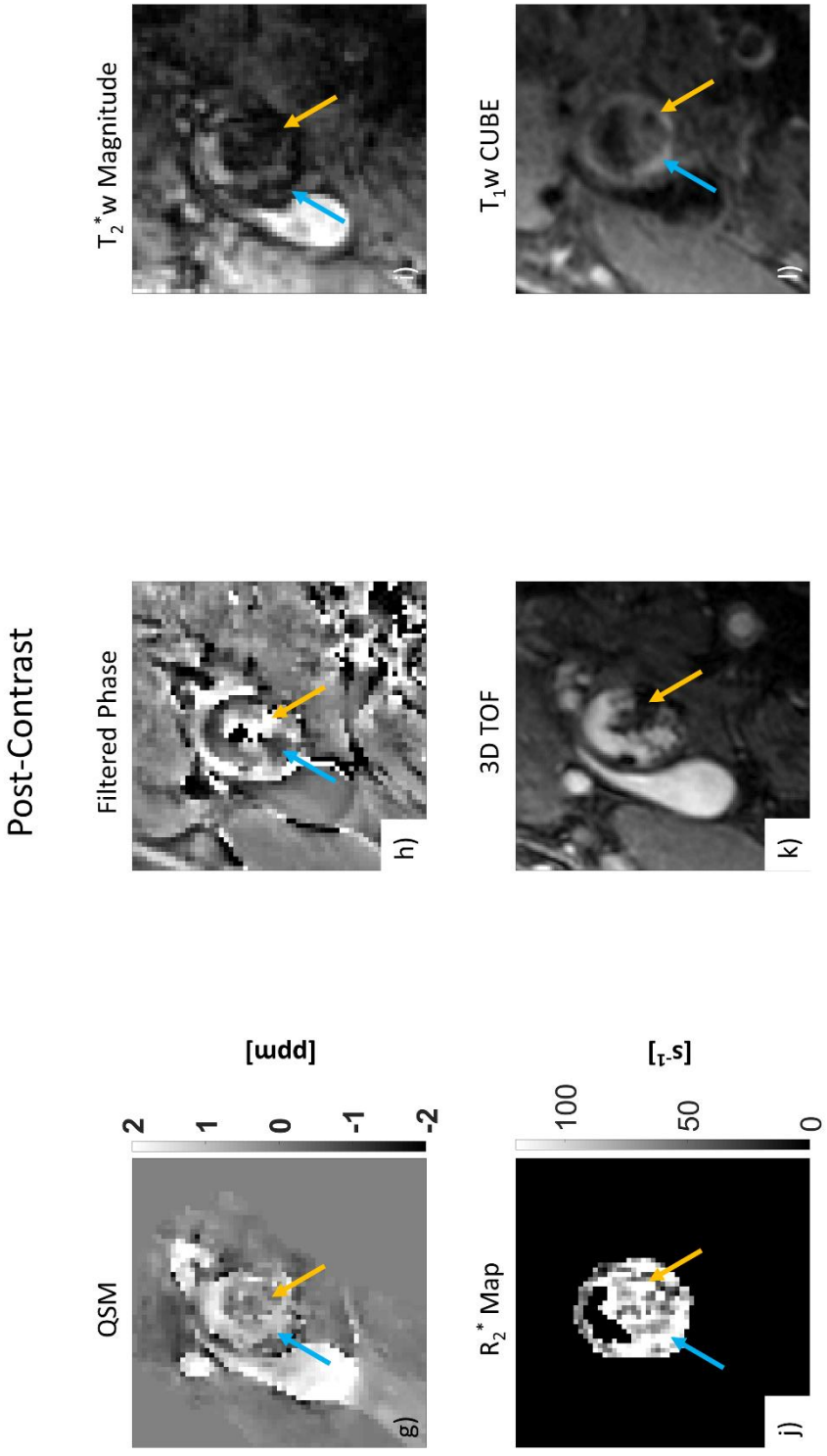


*Figure 3: Pre- and post-contrast QSM of a patient with a carotid artery plaque (calcification is indicated by the yellow arrow, USPIO-uptake by the blue arrow)*